João Bruno Canelas Cascão

Master's of Science in Bioorganic

Application of NMR RDC's, Relaxation and Self-Diffusion for the Study of Dynamic Processes of Small Molecules in Solution

Dissertation to achieve a Master's Degree in Bioorganic

Adviser: Doutor Eurico José da Silva Cabrita, Professor Auxiliar, FCT-UNL

Jury:

President: Doutora Ana Maria Ferreira da Costa Lourenço, Professora Auxiliar FCT-UNL

Examinor: Doutor Eurico José da Silva Cabrita, Professor Auxiliar, FCT-UNL

Examinor: Doutor João Carlos dos Santos Silva e Pereira de Lima, Professor Associado, FCT-UNL

FACULDADE DE CIÊNCIAS E TECNOLOGIA
UNIVERSIDADE NOVA DE LISBOA

Setembro 2014

Application of NMR RDC's, Relaxation and Self-Diffusion for the Study of Dynamic Processes of Small Molecules in Solution

Agradecimentos

Gostaria de agradecer ao meu orientador Prof. Eurico Cabrita por me permitir desenvolver a tese de mestrado no seu laboratório.

Os meus agradecimentos estendem-se também aos meus colegas de laboratório Dr. Ângelo Figueiredo, Dr. Filipa Marcelo, Dr. Marta Corvo, Dr. Ana Sofia, por todas as discussões construtivas. Não esquecendo os juniores quero também agradecer ao, Micael Silva, João Silva, Ricardo Martinho e Tiago Paiva.

Um agradecimento a todos os colegas e amigos, em especial aos que mais me apoiaram directamente nesta jornada, sem os quais tal não teria sido possível, de seu nome: André Dias, Catarina Fernandes, Carmen Gómez, Fausto Queda, Helena Coelho, João Lino, Joaquim Fonseca, Pedro Henriques, Tiago Pascoa e Válter Frade.

Em último lugar, e de tudo o mais importante, quero expressar a minha gratidão à minha família pelo apoio e suporte.

Este trabalho foi parcialmente financiado pela Fundação para a Ciência e a Tecnologia através dos projetos através da rede nacional de RMN (RNRMN) pelo projeto RECI/BBB-BQB/0230/2012.

Resumo

Relaxação "spin-lattice", coeficientes de difusão e acoplamentos residuais dipolares (RDC'S) são a base da bem estabelecida técnica de ressonância magnética nuclear para o estudo físico-químico de moléculas pequenas (geralmente compostos orgânicos e produtos naturais com MW <1000 Da), por terem provado ser uma potente e complementar fonte de informação sobre os processos dinâmicos estruturais em solução. O trabalho desenvolvido nesta tese consiste na aplicação das técnicas de RMN anteriormente mencionadas para explorar, analisar e sistematizar padrões de comportamento dinâmico molecular de pequenas moléculas selecionadas em condições experimentais particulares. Dois sistemas foram escolhidos para investigar o comportamento dinâmico molecular por estas técnicas: a dinâmica de formação de par-iónico e interação de iões em líquidos iónicos (LI) e a dinâmica de reorientação molecular quando as moléculas são colocadas em fases orientadas (meios de alinhamento).

A aplicação de medições de relaxação "spin-lattice" e difusão de RMN foram utilizadas para estudar a dinâmica molecular de rotação e de translação do LI: 1-butil-3-metilimidazólio tetrafluoroborato [BMIM] [BF_4]. O estudo da dinâmica catião-anião em solução pura e misturas IL-água foi sistematicamente investigada por uma combinação de técnicas multinucleares de relaxação de RMN com os dados de difusão (usando espectroscopia de RMN de H^1, C^{13} e F^{19}). As experiências de tempo de relaxação "spin-lattice" (*T*1), coeficientes de difusão e efeito nuclear Overhauser foram combinadas para determinar as condições que favorecem a formação de pares-iónicos de longa duração de [BMIM][BF_4] em água. Para este efeito, e utilizando os coeficientes de difusão de catiões e de aniões como sonda, diferentes composições de LI-água foram verificadas (a partir do LI puro até infinito de diluição) para encontrar as condições em que ambos catião e anião apresentassem coeficientes de difusão iguais (fração de água 8% a 298 K). Esta condição, bem como o LI puro e a diluição infinita foram, em seguida, ainda estudados através de RMN de relaxação de ^{13}C, a fim de determinar os tempos de correlação (τ_c) para o movimento de reorientação molecular, usando um procedimento matemático iterativo e dados experimentais obtidos num intervalo de temperatura entre os 273 e 353 K. O comportamento dos dados de difusão e relaxação obtidos nas nossas experiências apontam para os parâmetros combinados fracção molar de 8% e temperatura de 298 K como a condição mais favorável para a formação de pares-iónicos de longa duração.

Quando as moléculas são submetidas ao movimento anisotrópico suave ao serem colocadas em alguns meios especiais, acoplamentos dipolares residuais (RDCs), podem ser medidos, por causa do alinhamento parcial induzido por estes meios. RDCs estão a emergir como uma poderosa ferramenta de rotina empregue na análise conformacional, pelo facto de complementar e ainda superar as abordagens clássicas baseadas em NOE ou J^3 de RMN. Neste trabalho, três meios de alinhamento diferentes foram caracterizados e avaliados em termos de integridade utilizando espectroscopia de RMN-1D de ^1H e ^2H, nomeadamente, o gel de extensão e compressão de PMMA, e os cristais líquidos liotrópicos CpCl / n-hexanol / salmoura e cromolina / água. A influência que os

diferentes meios e graus de alinhamento têm sobre as propriedades dinâmicas de várias moléculas foi explorada. Açúcares de diferentes tamanhos foram utilizados e sua difusão foi determinada, bem como características de conformação usando RDCs. Os resultados obtidos indicam que nenhuma influência é sentida pelas características de difusão e de conformação das pequenas moléculas estudadas, usando graus de alinhamento de 3, 5 e 6% CPCL / n-hexanol / salmoura para difusão e 5 e 7,5% CPCL / n-hexanol / salmoura para conformação. Também foi possível determinar que a difusão de pequenas moléculas verificada nos meios de alinhamento apresentou valores próximos aos observados em água, reforçando a ideia de não-condicionamento das propriedades moleculares em tais meios.

Abstract

Spin-lattice Relaxation, self-Diffusion coefficients and Residual Dipolar Couplings (RDC's) are the basis of well established Nuclear Magnetic Resonance techniques for the physicochemical study of small molecules (typically organic compounds and natural products with MW < 1000 Da), as they proved to be a powerful and complementary source of information about structural dynamic processes in solution. The work developed in this thesis consists in the application of the earlier-mentioned NMR techniques to explore, analyze and systematize patterns of the molecular dynamic behavior of selected small molecules in particular experimental conditions. Two systems were chosen to investigate molecular dynamic behavior by these techniques: the dynamics of ion-pair formation and ion interaction in ionic liquids (IL) and the dynamics of molecular reorientation when molecules are placed in oriented phases (alignment media).

The application of NMR spin-lattice relaxation and self-diffusion measurements was applied to study the rotational and translational molecular dynamics of the IL: 1-butyl-3-methylimidazolium tetrafluoroborate [BMIM][BF_4]. The study of the cation-anion dynamics in neat and IL-water mixtures was systematically investigated by a combination of multinuclear NMR relaxation techniques with diffusion data (using by H^1, C^{13} and F^{19} NMR spectroscopy). Spin-lattice relaxation time (T_1), self-diffusion coefficients and nuclear Overhauser effect experiments were combined to determine the conditions that favor the formation of long lived [BMIM][BF_4] ion-pairs in water. For this purpose and using the self-diffusion coefficients of cation and anion as a probe, different IL-water compositions were screened (from neat IL to infinite dilution) to find the conditions where both cation and anion present equal diffusion coefficients (8% water fraction at 25 ºC). This condition as well as the neat IL and the infinite dilution were then further studied by ^{13}C NMR relaxation in order to determine correlation times (τ_c) for the molecular reorientational motion using a mathematical iterative procedure and experimental data obtained in a temperature range between 273 and 353 K. The behavior of self-diffusion and relaxation data obtained in our experiments point at the combining parameters of molar fraction 8 % and temperature 298 K as the most favorable condition for the formation of long lived ion-pairs.

When molecules are subjected to soft anisotropic motion by being placed in some special media, Residual Dipolar Couplings (RDCs), can be measured, because of the partial alignment induced by this media. RDCs are emerging as a powerful routine tool employed in conformational analysis, as it complements and even outperforms the approaches based on the classical NMR NOE or J^3 couplings. In this work, three different alignment media have been characterized and evaluated in terms of integrity using ^2H and ^1H 1D-NMR spectroscopy, namely the stretched and compressed gel PMMA, and the lyotropic liquid crystals CpCl/n-hexanol/brine and cromolyn/water. The influence that different media and degrees of alignment have on the dynamic properties of several molecules was explored. Different sized sugars were used and their self-diffusion was determined as well as conformation features using RDCs. The results obtained indicate that no influence is felt by the small

molecules diffusion and conformational features studied within the alignment degree range studied, which was the 3, 5 and 6 % CpCl/n-hexanol/brine for diffusion, and 5 and 7.5 % CpCl/n-hexanol/brine for conformation. It was also possible to determine that the small molecules diffusion verified in the alignment media presented close values to the ones observed in water, reinforcing the idea of no conditioning of molecular properties in such media.

Table of Contents

Index of Figures

Abbreviations, Acronyms and Symbols

CSA	Chemical Shift Anisotropy
B_0	Magnetic field
CPMG	Carl-Purcel-Meiboom-Gill
DC	Dipolar Coupling
DD	Dipolar Coupling
FID	Free Inducing Decay
FT	Fourier Transform
HSQC	Heteronuclear Single Quantum Coherence
IL	Ionic Liquid
INEPT	Insensitive Nuclei Enhanced by Polarization Transfer
LLC	Lyotropic Liquid Crystal
NMR	Nuclear Magnetic Resonance
PFG	Pulsed Field Gradient
PFGSE	Pulsed Field Gradient Spin Echo
QC	Quadrupolar Coupling
RDC	Residual Dipolar Coupling
RTIL	Room-Temperature Ionic Liquid
SAG	Strain Induced Alignment in a Gel
SM	Small Molecules
SR	Spin Rotation
T1	Longitudinal Relaxation
T2	Transversal Relaxation

Objectives

The aim of this work is to explore the use of advanced NMR techniques to determine, analyze and systematize patterns of molecular dynamics of small molecules in solution. For this purpose two different systems have been chosen as study object to probe molecular dynamic processes such as translation, rotation and conformational variability: ionic liquids and alignment media (liquid crystals and gels). The systems were chosen due to their properties, both dynamical and spectroscopic, that make them suitable to better explore the spectroscopic technique elected (NMR spectroscopy).

The study is organized around three main objectives:

- The study of the dynamics of ion-pairing for one ionic liquid, 1-buthyl-3-methyl imidazolium tetrafluoroborate, $BMIMBF_4$: the neat IL and water mixtures were studied using for this purpose self-diffusion, spin-lattice relaxation (T_1) and spin-spin relaxation (T_2) measurements;
- The characterization of different types of alignment media, used for the determination of residual dipolar couplings, namely liquid crystals and cross-linked polymer gels, associated with different solvents, namely water and chloroform;
- The study of the relation between the alignment properties of the media and the translational properties of selected molecular standards (saccharides markers and aromatic markers) achieved by the determination of their diffusion coefficients in different alignment media and conditions;
- Finally, and conjugated with the three previous topics, the approximate conformational determination using residual dipolar couplings made for the organic compounds previously employed (saccharides markers, BMIM+ and aromatic markers) in the distinct alignment conditions.

Chapter 1 - Introduction

1.1 – NMR Spectroscopy

Nuclear magnetic resonance spectroscopy (NMR spectroscopy), based on the discovery and development of Nuclear Magnetic Resonance[1] by the end of 1930s-beginning of 1940s, consists in a powerful and widely recognized research technique that makes use of the interaction between nuclear spins ($I \neq 0$) and electromagnetic radio frequency (RF) pulses to permit the "visualization" and consequent study of molecules at atomic scale (< angstrom)[2,3]; which process of development has been awarded with three Nobel prizes in physics (one in 1944 for Rabi, and two in 1952 for Bloch and Purcell) in the last century. In this way, as the research progressed, it became possible to determine physicochemical properties of the atoms and molecules, as well as detailed information about structure, dynamics, reactions state and chemical environment, making use of different NMR parameters and techniques governed by quantum theory.[4]

Historically Rabi, Purcell and Bloch observed that magnetic nuclei such as ^{1}H, ^{13}C and ^{31}P could absorb RF energy when placed in a magnetic field when the RF was of a frequency specific to the identity of the nuclei. When this absorption occurs, the nucleus is described as being in resonance. Different atomic nuclei within a molecule resonate at different radio frequencies for the same magnetic field strength. The resonant frequency, energy of the absorption and the intensity of the signal are proportional to the magnetic field strength. Theoretically the possibility to distinguish between different "elements" (atomic nucleus) and regions of molecules arise from the fact that atoms and molecules are composed of electrons and these inevitably generate an electric and a magnetic field by their movement which will be different depending on the position in the molecule, causing that each has an individual frequency of resonance and thus giving access to the electronic structure of a molecule and frequently its identity.[4]

Nowadays NMR spectroscopy fits into the field of structural analysis and finds its main application in the field of chemistry and biochemistry investigation, presenting routines with standard material and procedures, whether the purpose is determining the exact structure of a molecule, or determining the interaction between two molecules of different sizes, or even to determine the dynamic of molecules in different states of matter as it can be applied to any sample that contain detectable nuclear spins. Study samples may include compounds from small size such as methanol or ethanol, to complex chiral structures such as natural products, to large and heavy molecules such as proteins or nucleic acids. Each type of molecule depending on its composition, size and configuration, requires different kind and number of experiments and techniques. For example, for the determination of structure of very complex organic compounds and biomolecules normally is necessary to use a variety of 2D correlated experiments.[5] The importance and impact that NMR has been demonstrating in science is enormous because it has enabled the study of innumerous samples

(including solutions and solids) and the acquiring of large amounts of information that couldn't be done by other techniques and methodologies.[4]

A known disadvantage is related with the fact that NMR timescale is relatively long and thus it is not appropriate for observing fast phenomena, producing only an averaged spectrum. Another drawback of this spectroscopy is related with impurities, since NMR is inherently not very sensitive and so it is never assured the purity level.[4]

The NMR tools used in this work that allowed the verification and determination of the expected results were the spin-lattice relaxation time (T1), spin-spin relaxation time (T2), self-diffusion and the residual dipolar couplings (RDC's). The relaxation and self-diffusion measurements to study molecular rotational and translational motions in solution are well established procedures. Measurement of dipolar couplings applied to small molecules (residual dipolar couplings), supported by the achievement of weak alignment media has emerged as a recent advance that allows the configurational and conformational study of these compounds in solution. The combination of these techniques gives a plethora of information that can be used to understand, characterize and systematize nearly all the molecular behaviour in solution.

1.2 – Motional Studies with NMR

As have been uncovered previously, NMR spectroscopy represents nowadays a fairly understood and explored tool in the study of all kinds of molecules. Since its basic assumption is the multiple $I \neq 0$ nuclei detection by the use of radiofrequencies, at the foreground infinitude of nuclei features may be considered to explore. Subsequently, since nucleus are included in complex and highly variable structures called molecules, another infinitude of added features may be regarded using NMR, justifying its great significance and wide application in modern science.[4]

Hereupon, considering that NMR spectroscopy detects nucleus and these are included in molecules, and taking into account that this detection may be performed in different time- and frequency-scales, it has been legitimate to imagine that not just spin but also complex molecular dynamics could be detected and studied with this powerful spectroscopic tool. Within the long list of conceivable molecular dynamic features arises a very intuitive and interesting one, which is the diffusion. Diffusion corresponds, such as the macroscopic concept indicates, to the translational motion that molecules may perform in any kind of sample, especially in liquids. Another predictable motion event that would characterize molecules in general, associated with the previously referred translational motion, is the rotational motion. Just like diffusion, rotation, such as the macroscopic concept indicates, corresponds in NMR to molecular reorientation in the presence of the external magnetic field B_0. As previously suggested the possibility of studying these two types of motion arises from the basic nuclear detection.[4]

On the other hand, since motion occurs over time it only becomes a significant physicochemical property if it may be detected during this period. In that way, techniques and experiences had to be developed over the course of NMR evolution, based on the principle of detecting changes in the nuclear spin Hamiltonian, which enable the detection of different molecular motional effects that happen in distinct time-scale ranges. The range of time-scales that NMR spectroscopy is able to detect goes from the picoseconds (10^{-12} seconds) to several seconds (Figure 1). As can be imagined, different types of motion are associated with different time-scales, as for example: molecular rotation and microscopic diffusion (the two types of motion explored in this work) are detected normally (in liquids) in the range between several picoseconds to nanoseconds; while macroscopic diffusion, flow, mechanical motion and chemical exchange may be detected in the range of milliseconds to seconds (Figure 1).[4]

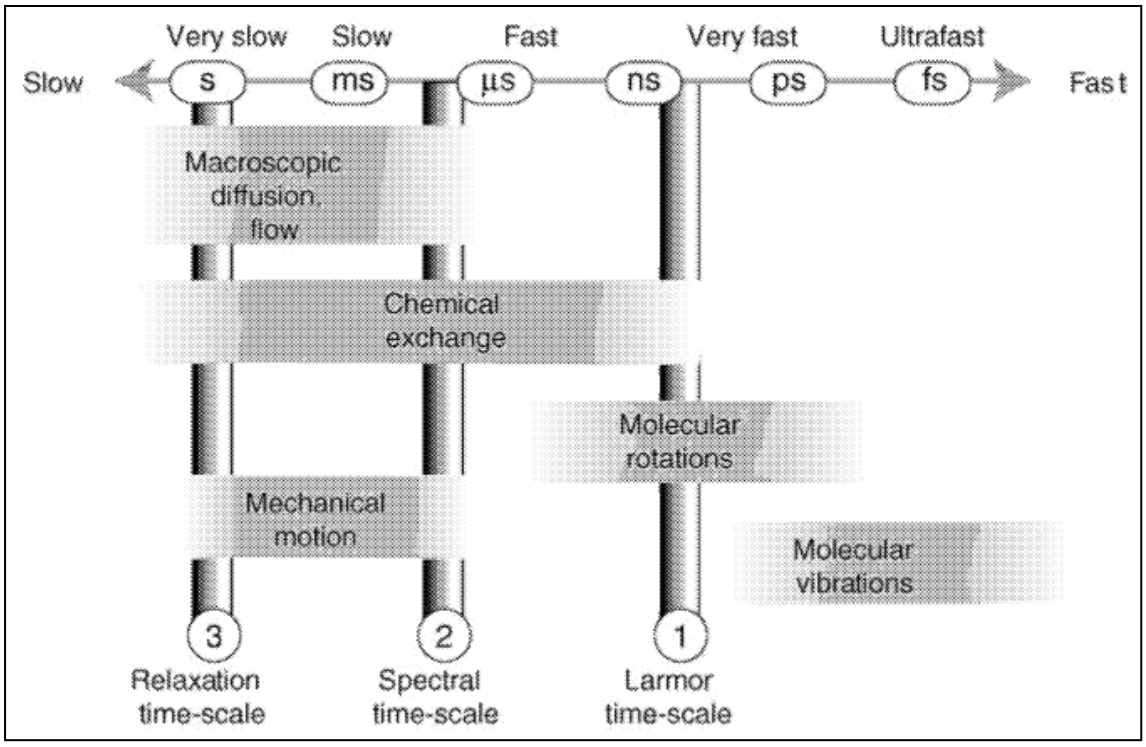

Figure 1 – Representation of the most important NMR timescales. Reproduced from reference [4].

The possibility of detecting such events, as molecular motion from picoseconds to seconds, is related with the closeness that these events may show in relation to the three characteristic nuclear spins spectroscopic manifestations, which are: the Larmor frequency; the spectral time; and the relaxation time (Figure 1). While the Larmor frequency, which consist in the time required for the spins to precess through 1 radian in the magnetic field, is typically situated in the range from picoseconds to nanoseconds, the spectral time, measured in frequency units, is typically situated in the range from microseconds to milliseconds, and finally the relaxation time, which consists in the time required for the recovery of spins to the thermal equilibrium position, is typically situated in the range from milliseconds to seconds. Of course these characteristic nuclear spins spectroscopic manifestations

are dependent of many conditions, such as the sample state, the isotope and physical parameters as the magnetic field and the temperature (Figure 1).[4]

However, despite the temporal proximity to these three characteristic nuclear spins spectroscopic manifestations, some motional processes occurs in a shorter time-scale than these events, the so-called processes that happens faster than the NMR time-scale, which conducts to its averaging over the detection time and results in global values that neglects intermediate events. Interesting examples of these averaged processes are the tensorial averaged NMR secular interactions, such as the dipolar coupling, quadrupolar coupling and chemical shift, and the averaged NMR non-secular event such as the internuclear distance (r_{is}) variation. The averaged NMR secular interactions and its particularities will be further developed in Chapter 3 (Figure 2).[4]

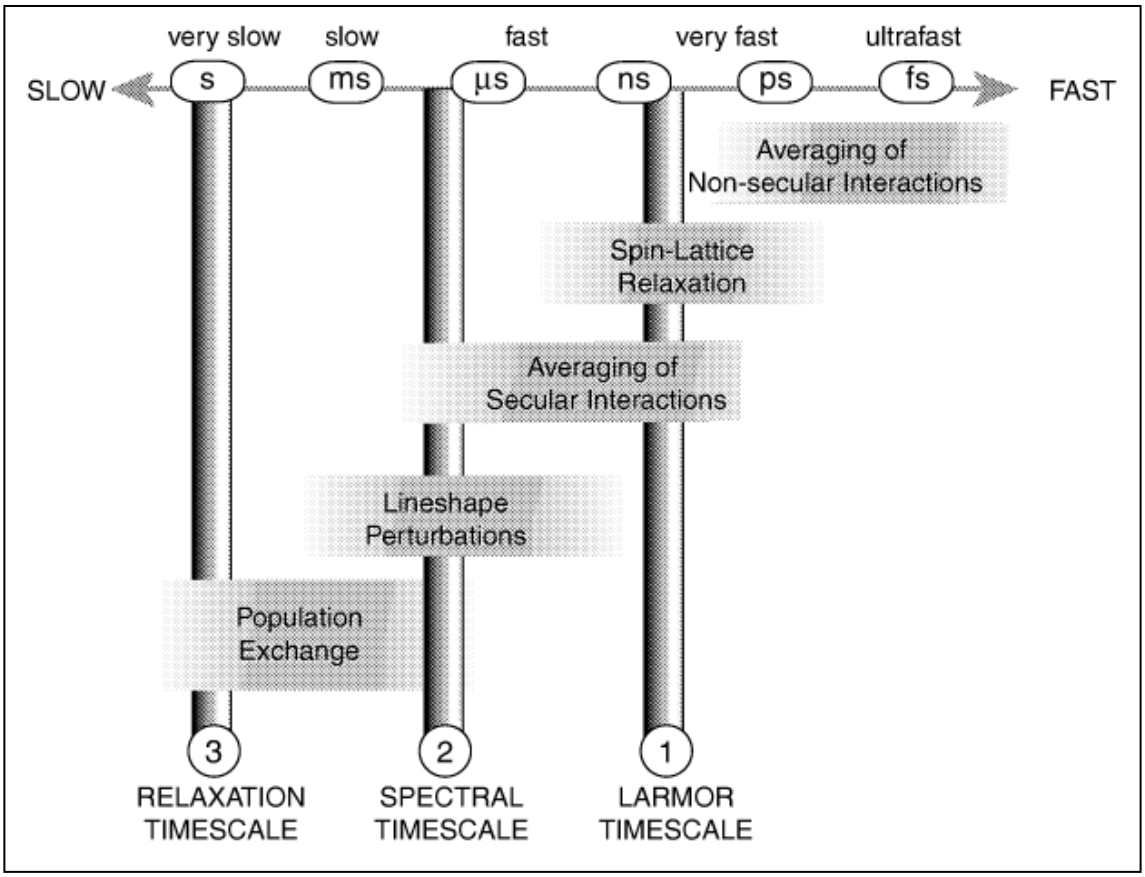

Figure 2 - The effects of motion time-scale on the nuclear spin dynamics. Reproduced from reference [4].

1.2.1 – NMR Relaxation

As highlighted above, relaxation plays a major role in the NMR spectroscopy, namely in detection and spin investigation processes, since it is associated with the observation (or not) of certain events. The relaxation concept, which is frequently used in physical science, aims to describe the process of reestablishment of a thermal equilibrium standard situation that normally corresponds

to an isotropic situation. On contrary, in NMR the so-called thermal equilibrium corresponds to a situation where, in this case, the spin polarizations are distributed anisotropically along an external magnetic field.[4]

As pointed out earlier, relaxation consists in the time required for the recovery of spins to the thermal equilibrium position (Figure 4). This recovery, physically (in terms of spin states) corresponds to the imposed transition of spin population in the excited states (high energy, β) to the ground states (low energy, α) due to external magnetic field influence that holds a small difference between states, process which occurs in a very slow manner when comparing to other spectroscopic techniques (Figure 3).[4]

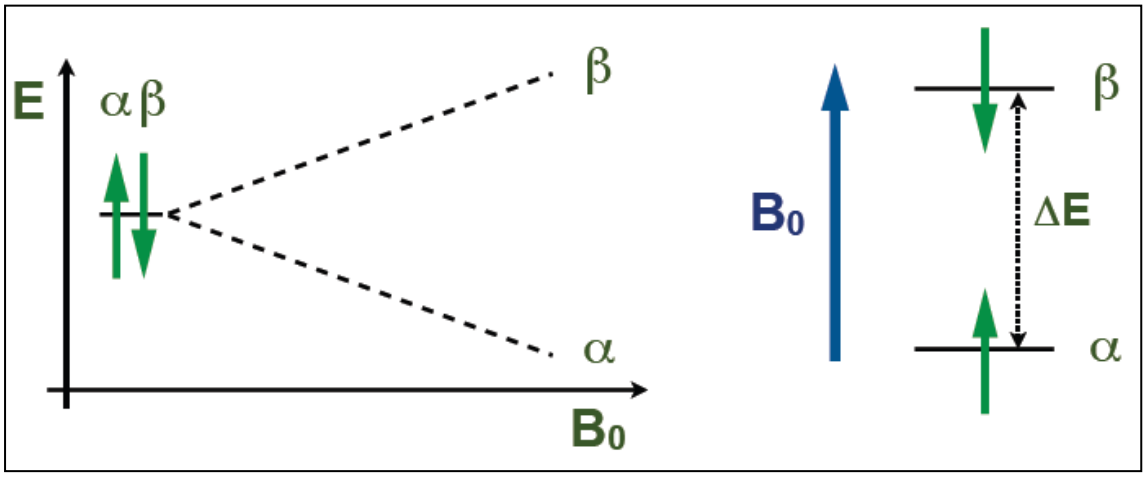

Figure 3 – Representation of the Zeeman effect in the energy states separation in NMR spectroscopy.

This phenomena is driven by several different processes that in many ways cause the spins (globally) to gradually recover from the direction in which they are oriented (after a RF stimulation) to the one of the equilibrium, which in NMR spectroscopy corresponds to the external magnetic field direction (defined as z-axis). In this work it will be discussed spectroscopic techniques, such as inversion-recovery that measure spin-lattice relaxation and CPMG that measure spin-spin relaxation, that makes use of this relaxation rate values to extract structural information, namely related with motion.[4]

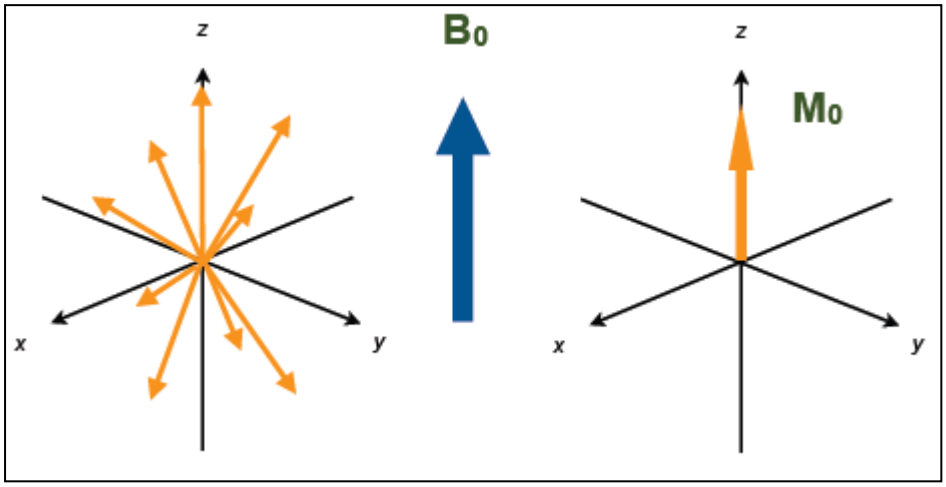

Figure 4 - Net magnetic moment on thermal equilibrium along the external magnetic field.

The two previously referred relaxation processes, namely spin-lattice relaxation (T_1) and spin-spin relaxation (T_2), which in a simple way correspond to the longitudinal relaxation (relaxation in the z-axis) and to the transversal relaxation (relaxation in the x,y-plane), respectively, when considering the referential axis system where the external magnetic field is positioned along the z-axis, will be further introduced hereafter.[4]

1.2.1.1 - Longitudinal Relaxation Time (T1)

The longitudinal relaxation time process, normally known as spin-lattice relaxation time, owe the "longitudinal" denomination to the fact that this process was defined as being the one in which the magnetization builds up alongside (parallel) to the direction for which the external magnetic field is pointing (z-axis) (Figure 6).[4]

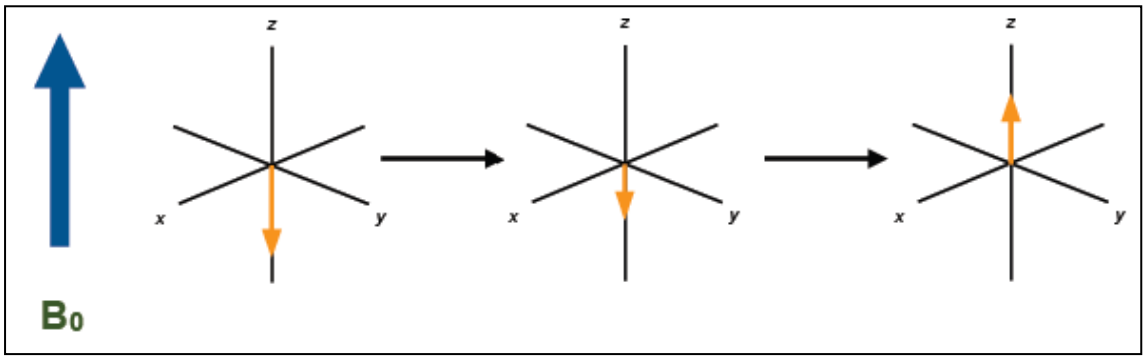

Figure 5 - Returning of the longitudinal magnetization.

As previously introduced, longitudinal relaxation process corresponds to the one already described as being the reestablishing of normal population distribution of α and β spin states. This is caused by different physical relaxation processes and happens in correspondence to the external magnetic field influence that in turn generate a sufficient energy difference between spin states (α and

β) that holds a permanent small population difference between α and β. In NMR spectroscopy T_1 is always associated with acquisition time, since it is the longest and slower event, being always superior or equal to T_2.[4]

Considering now the building up process equation of the longitudinal magnetization, is given by equation 1:[4]

$$M_z^{nuc}(t) = M_{eq}^{nuc}\left[1 - \mathrm{e}^{\left(-\frac{t-t_{on}}{T_1}\right)}\right] \quad \textbf{(1)}$$

- M_z^{nuc} is the anisotropic macroscopic nuclear magnetization pointing in z direction;
- M_{eq}^{nuc} is the isotropic macroscopic nuclear magnetization;
- T_1 is the spin-lattice relaxation time;
- t is the total time;
- t_{on} is the external magnetic field application moment.

In Figure 6 is possible to observe the common situation where the external magnetic field is turned on at t_{on} and is verified the exponential progression of the build up curve of the anisotropic macroscopic nuclear magnetization (M_z^{nuc}), which relaxes coming from the isotropic state (M_{eq}^{nuc}).[4]

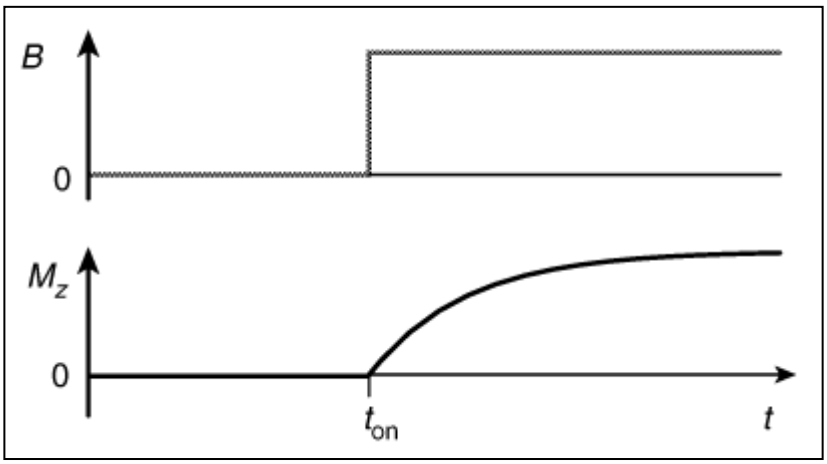

Figure 6 - The build-up of longitudinal spin magnetization, after the magnetic field is turned on. Reproduced from reference[4].

Considering now the decay process equation of the longitudinal magnetization, is given by equation 2:[4]

$$M_z^{nuc}(t) = M_{eq}^{nuc} e^{\left[-\frac{t-t_{off}}{T_1}\right]} \quad \textbf{(2)}$$

In this opposite situation, where the external magnetic field is turned off at t_{off} it is verified in Figure 7 that the anisotropic macroscopic nuclear magnetization (M_z^{nuc}), which initially present a value different of 0, relaxes then gradually to a value equal to 0 that corresponds to the isotropic state (M_{eq}^{nuc}) of spin magnetization.[4]

These two situations could be experienced and measured in a situation where first (Figure 6) it is inserted the sample on the NMR external magnetic field and later (Figure 7) the same is removed from the presence of the external magnetic field. [4]

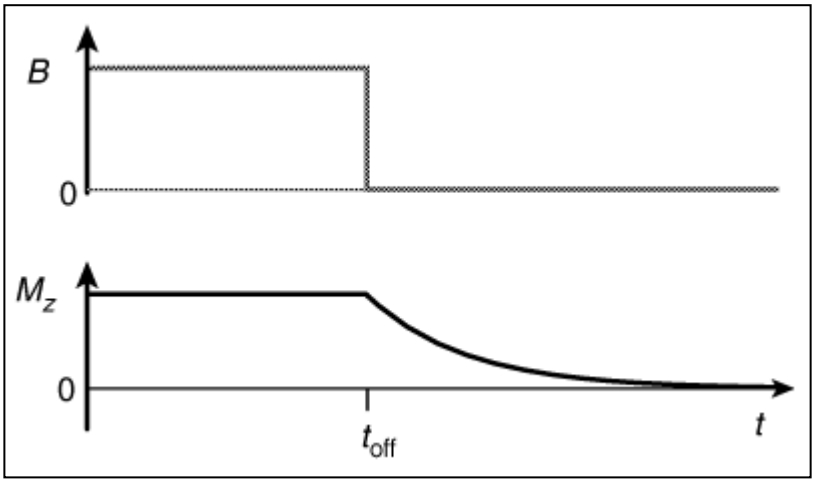

Figure 7 - The decay of longitudinal spin magnetization, after the magnetic field is turned off. Reproduced from reference [4].

As has already been uncovered, the characteristic longitudinal relaxation profile is influenced by many factores, among them viscosity and temperature, parameters that will be integral part of this work as it will be seen in Chapter 2 and 3. This relaxation process is normally comprehended in the time-scale between milliseconds to seconds, as also already referred, determining in this way the shortest possible time between NMR acquisitions.[4]

A description of the most common technique to measure T1 is presented in Annex 1.1.

1.2.1.2 - Transversal Relaxation Time Constant (T_2)

Differently to the previous, the transversal relaxation time, also known as spin-spin relaxation time, consists in the process of lose phase coherence in the x,y-plane (Figure 8). The importance of transversal relaxation (T_2) is related with signal acquisition, since during an NMR experience is necessary to place the magnetization in the so-called x,y-plane of the referential axis system, because only in this plane is possible to detect magnetization, and turns it in spectral data.[4]

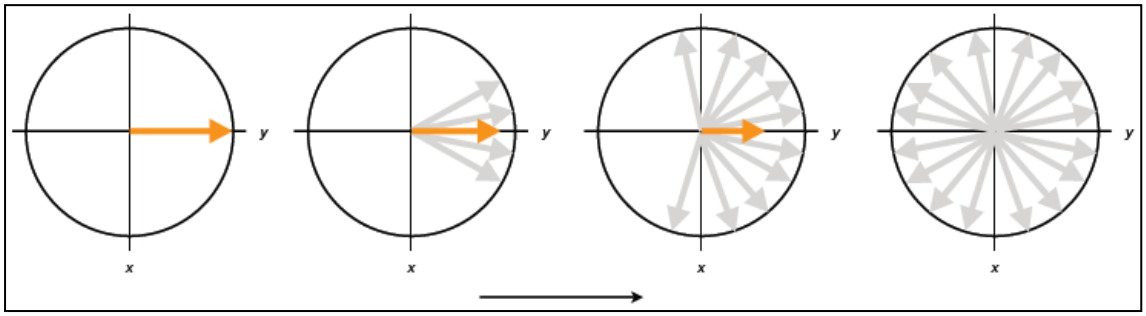

Figure 8 - Precession of the transverse magnetization.

The magnetization rotation by $\pi/2$ radians (Figure 9) from the z-axis to the x,y-plane is made through the application of a radiofrequency pulse (excitation), which orient the bulk magnetization in one major direction (x, y, -x or -y) by the physical principles of electric field rotation, consisting like the longitudinal magnetization in an imposed preferential orientation. Since this imposed preferential orientation is temporally restricted by spin dynamics, with time evolution is observed the loss of this bulk magnetization (Figure 8). This process of bulk magnetization loss with time corresponds to the so-called process of loss of phase coherence in the x,y-plane, which in turn corresponds to the transversal relaxation time (T_2) (Figure 8). The bulk magnetization, or net magnetization, which has been represented in Figure 4, when placed in the x,y-plane corresponds to the transverse magnetization because of its perpendicular relation to the external magnetic field (Figure 8 and Figure 9).[4]

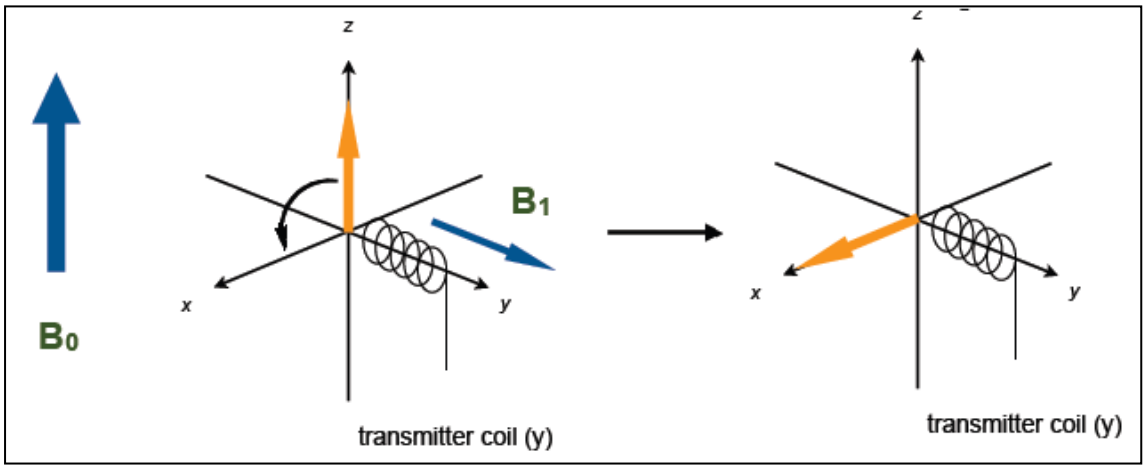

Figure 9 - Rotation of a spin around the y-axis. Reproduced from reference [4].

The practical and visual manifestation of the transversal relaxation (T_2) in NMR spectroscopy is the spectral line width, since, has already been said, x-y plane magnetization is directly related with NMR signal appearance (Figure 10).[4]

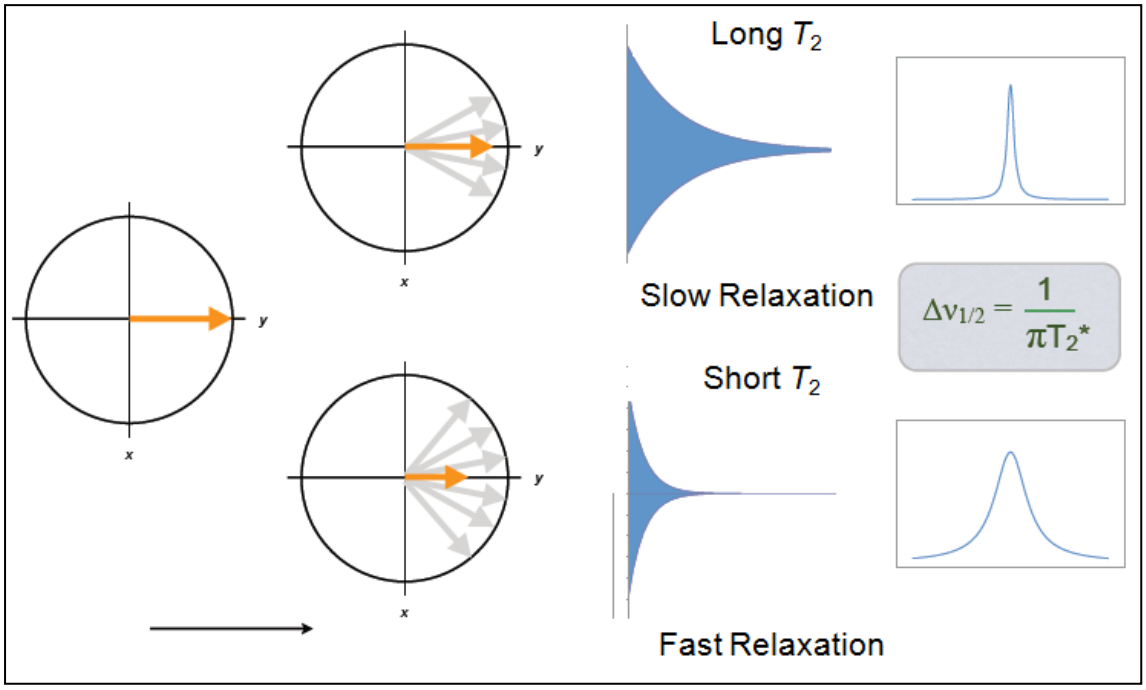

Figure 10 – Effect of different transverse relaxation processes on NMR signal aspect.

The transverse magnetization, which is composed by the several spin orientations that globally form a bulk directional magnetization in the x,y-plane, is known to be only effective during the RF pulse application time, and that subsequently spins relax transversely losing coherence. This transverse relaxation process, as represented in Figure 8, is gradually executed by the precessional motion of the bulk magnetization in both directions of the x,y-plane with time, consequence of the individual spins precession. Considering the precession of the individual spins that compose the bulk magnetization, it is known that its precession is performed at the nuclear Larmor frequency (ω^0) (equation 3):[4]

$$\omega^0 = -\gamma B^0 \quad \textbf{(3)}$$

Considering the bulk magnetization evolution during *t* after the π/2 pulse on the different axes (x and y), is given by equations 5 and 6, respectively:[4]

$$M_y^{nuc}(t) = -M_{eq}^{nuc}\cos(\omega^0 t)\, e^{\left(\frac{-t}{T_2}\right)} \quad \textbf{(4)}$$

$$M_x^{nuc}(t) = -M_{eq}^{nuc}\sin(\omega^0 t)\, e^{\left(\frac{-t}{T_2}\right)} \quad \textbf{(5)}$$

In Figure 11 is possible to observe the slow decay of the transverse magnetization with time. The relaxation process associated with this phenomenon, as also the case for longitudinal relaxation, is explained by the establishment in sample of tiny fluctuations in the local magnetic fields felt by spins due to several events, which first individually and then globally originate relaxation and the subsequent decay (Figure 11). The permanent magnetic synchronization is not achievable in real

systems and further, this transverse magnetization decay represents an irreversible process. In practice this process is observed in the NMR spectral acquisition and is explained by equation (4).[4]

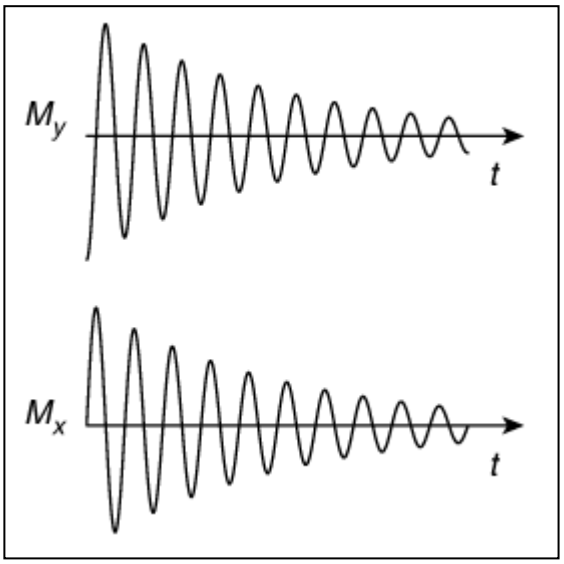

Figure 11 - Decay and oscillation of the transverse magnetization. Reproduced from reference [4].

This transversal magnetization frequency dephasing process consists in a homogeneous process and in this way is called in NMR as homogeneous decay. Because it may possess many structural relevant information, as uncovered above, is crucial in NMR practice, namely in measuring spin-spin relaxation time T_2 values.[4]

In liquid NMR samples of small molecules, T_2 and T_1 exhibit close relaxation time values, that in such cases is in the order of several seconds. This means that spins during this time execute, without losing synchrony, around tens of millions of Larmor precession cycles. However, in such a different situation as the macromolecular NMR or solid state NMR, the transverse relaxation time constant T_2 comes to be as short as milliseconds.[4]

1.2.1.3 - Relaxation Mechanisms

As has been seen so far, relaxation plays a major role either in spin detection as in spin dynamics comprehension. It was uncovered earlier in this work the main features of the two types of nuclear spin relaxation, and has also been referred the importance and the possibility of studying by NMR the molecular dynamics, namely motion. It is crucial to refer that both are intrinsically connected in many ways. However, the relaxation mechanisms and its nature have not been explained and revealed yet.[4]

The relaxation, briefly, consists in the process of spins orientation recovery to the thermal equilibrium, following the physicochemical principle of preferential positioning at the lower energy state, from a previous imposed situation of spin excitation that was forcing it to point in a different

orientation, which in NMR is caused by RF pulses. Although it might seem a spontaneous process, relaxation of coupled spins implies many physical conditioning mechanisms, for example: dipolar coupling, chemical shift anisotropy, spin rotation and quadrupolar coupling in spins with I > ½.[4]

Dipolar coupling (Figure 12) consists in the through space interaction between two nucleus. This type of interaction is space dependent and increases with spins proximity, consisting in the predominant relaxation process of molecular spins (with I = ½) in liquid samples. Dipolar couplings may happen either by intramolecular via, when spins of the same molecule are coupled, or by intermolecular via, if spins of separated molecules are coupled. The source of relaxation in this case is related with the own magnetic field presented by each spin, which is consequence of nuclear electronic dynamic generated by orbiting electrons (Figure 12). Since each spin has its own magnetic field is logical to imagine that the interaction of two different spins, and consequently two different magnetic fields, will cause consequences in both spin states. However, not only the distance explains the relaxation phenomenon. Since dipolar couplings are also dependent on the angular relation with the magnetic field, and as is known already, because molecules are in permanent rotational motion in solution this factor will also contribute for the magnitude of the interaction.[4]

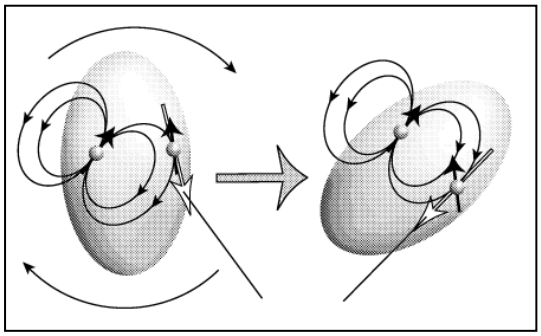

Figure 12 – Representation of the local dipolar field by molecular motion.[4]

Chemical shift anisotropy consists in other significant relaxation mechanisms. Chemical shift, which is materialized in the "chemical shift" of NMR spectroscopy spectral data, corresponds to the interaction between the applied external magnetic field and the molecular spin electrons. This interaction between the applied external magnetic field and the molecular spin electrons that consists in the induction of current in the seconds (molecular spin electrons) culminates in the generation of a local magnetic field in the spin surrounding (Figure 13). This consists in an important relaxation mechanism, especially for higher external magnetic fields. It is important to refer that the chemical shift anisotropy, just like the dipolar coupling, consists in a tensorial property that is orientation dependent, and so its angular relation with the external magnetic field will be taken in consideration for magnitude of the effect. In this way, considering that molecules in liquids present motional dynamics, while these tumble in solution the direction and consequently the magnitude of these local fields is expected to change.[4]

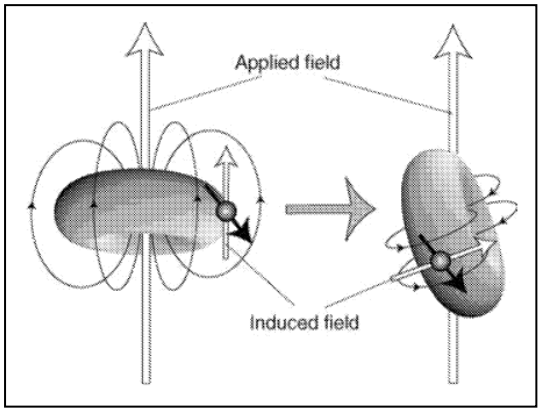

Figure 13 - Representation of the chemical shift interaction by molecular rotation.[4]

When these local effects are considered in the interpretation of the external magnetic field effect, it is obtained that along the sample there are multiple magnetic field fluctuations (differences in value that change with time). These fluctuations are also related to another relaxation mechanism that consists in the spin rotation, which, as the previous two, is also related with molecular motion and consequently with spin dynamics. As molecule rotates the local magnetic field is influenced by circular motion of electrons, leading to changes in the magnitude of the same (Figure 14). Spin rotation has normally decreased importance, comparatively with CSA and dipolar coupling, with exception for small molecules in gases and non-viscous liquids.[4]

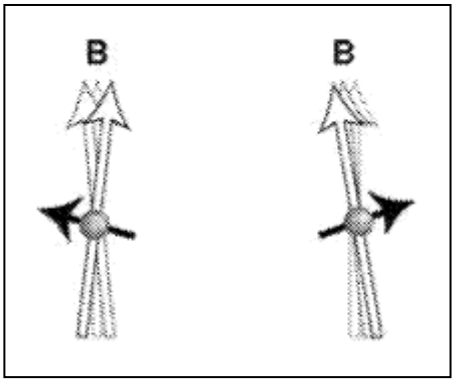

Figure 14 - Wobbling of the total local field.[4]

The normal order of relaxation processes for I = ½ is: first, the dipolar coupling; second, the CSA; and third the spin-rotation. Although this is the normal order, situations there are where one or more of these of these contributions are ineffective, leading to scale inversion.[4]

On the other hand, in I > ½ nucleus other relaxation source gains prominence, which is the quadrupolar coupling. The quadrupolar coupling is the main relaxation source in nucleus with I > ½. This relaxation effect arises from the fact that quadrupolar nucleus, contrary to I = ½ nucleus, the nuclear charge distribution presents to be non-spherical, consisting in an oblate or prolate spheroid. In consequence, in the presence of the sample electric field gradients these nucleus exhibit great torque susceptibility. Because quadrupolar relaxation mechanism, as dipolar and CSA, consist in a tensorial

property i.e., dependent on the relative orientation, its magnitude will be greatly dependent on this factor. [4]

In sum, it is possible to affirm that there are several relaxation mechanisms, also depending on the type of nuclei I, and these mechanisms are globally modulated by molecular reorientation or tumbling, since this motion is modulating orientation-dependent spin interaction energies. In this context, relaxation processes caused by orientation-dependent spin interaction energies over time may be visualized as the progressive summation of transitions between the nuclear spin states α and β. [4]

1.2.2 – NMR Diffusion-Ordered Spectroscopy (DOSY)

As have been already introduced, diffusion as one of the motional properties of molecules represents a significant dimension in molecular dynamics understanding. As also referred, NMR spectroscopy, differently to other spectroscopic techniques, has the ability of monitoring and study the molecular dynamics, including diffusion, through its multiple sequence possibilities and the already introduced relaxation phenomenon. The study of diffusion with NMR stills an actual and widely utilized method.

The study of diffusion with NMR has originated a technique, the so-called diffusion-ordered spectroscopy (DOSY), which through the use of pulsed field gradient spin echoes (PFGSE) or stimulated echo (STE) experiments is capable to provide diffusional data such as diffusion coefficients of individual signals in a spectrum that in this way become not just possible to determine translational motion but also to distinguish between signals of different compounds in a mixture. Although the practical application of PFGSE spectrum to analyse mixtures has appeared in 1981[6], the diffusion-ordered concept as technique have only been introduced in 1992[7]. [8,9]

In applications as the above referred determination of diffusion coefficients and consequently translational motion, the data normally appears normally as a 3-D NMR spectrum considering the chemical shift, gradient pulse area and intensity dimensions (Figure 16). On the other hand, if the distinction between signals of different compounds is required, the data normally appears normally as a 2-D NMR spectrum considering the chemical shift and diffusion coefficients dimensions (Figure 17).[8,9]

This technique requires only additional software for the DOSY experimental data analysis and spectrum presentation when compared to other techniques, since for the rest the same spectrometer hardware and sample procedures may be used. DOSY technique, developed in 1992, have been subject of intense theoretical[10,11] and practical[12,13] investigation by NMR spectroscopy community since then, especially in 1990s.[8,9]

The NMR theoretical fundament of DOSY technique consists in the fact that supposedly diffusion acts as a contributor for the signal attenuation in spin echo measurements when this are performed in an inhomogeneous magnetic field. More specifically, the longitudinal spatial encoding along the sample associated with spins longitudinal dislocation (diffusion)(Figure 15) during spin echo experiments will inevitably lead to changes in signal phase and consequently to signal attenuation.[8,9]

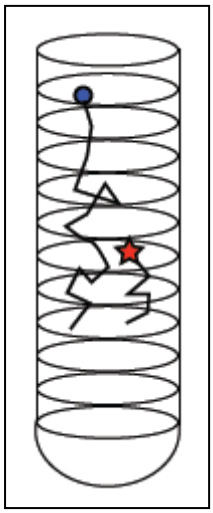

Figure 15 – Representation of translational dislocation of different spins along a NMR tube.

The NMR practical fundament of DOSY technique consists in the acquisition of several spectral measurements using PFGSE, in which through the varying of the evolution time or of the gradient strength diffusion is observed as the attenuation (decay) of the signals (Figure 16). Diffusion coefficients are calculated by the fitting of the signal intensities as function of gradient pulse area (Figure 16).[8,9]

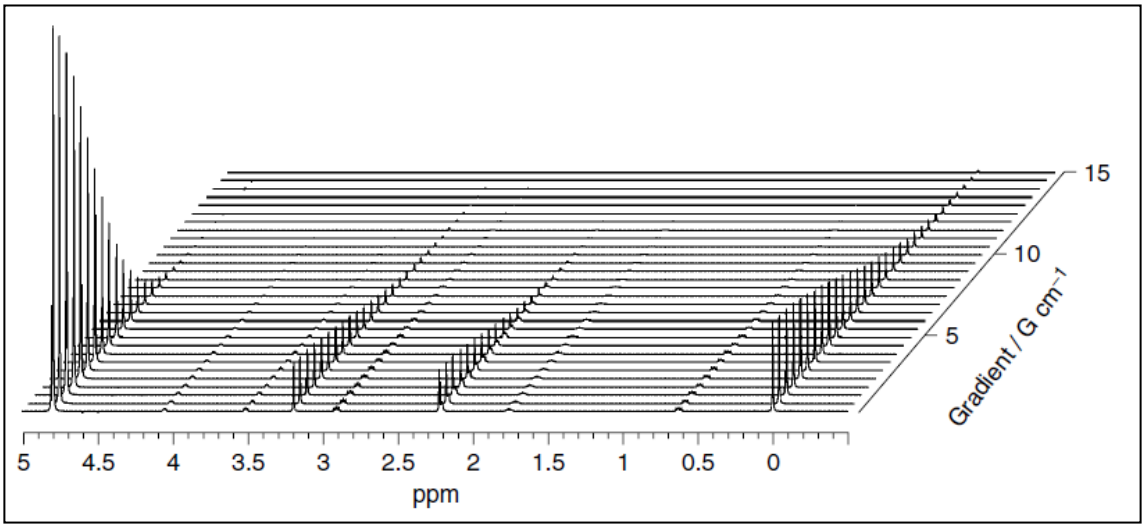

Figure 16 – ^{1}H pulsed field gradient spin echo spectra (500 MHz) for a mixture of acetone, choline, DSS (2,2-dimethyl-2-silapentane-5-sulfonate sodium salt) in D_2O.[9]

As previously mentioned, after diffusion coefficients data calculation a 2-D DOSY spectrum may be produced in order to differentiate different compounds in a mixture, which is achieved by

using the previously determined chemical shift for each signal, diffusion coefficients calculated and a standard error that together allows the positioning a distribution of each signal corresponding diffusion in the new spectrum (Figure 17). Ideally, in such spectrum the signals corresponding to single specie appear in a horizontal line sharing the same diffusion coefficient, allowing the distinction between different species in solution (Figure 17). In any case, this technique is only fruitful when dealing with high resolution NMR spectroscopy, since without resolution in the chemical shift domain signals tend to overlap and no desired information is possible to achieve.[8,9]

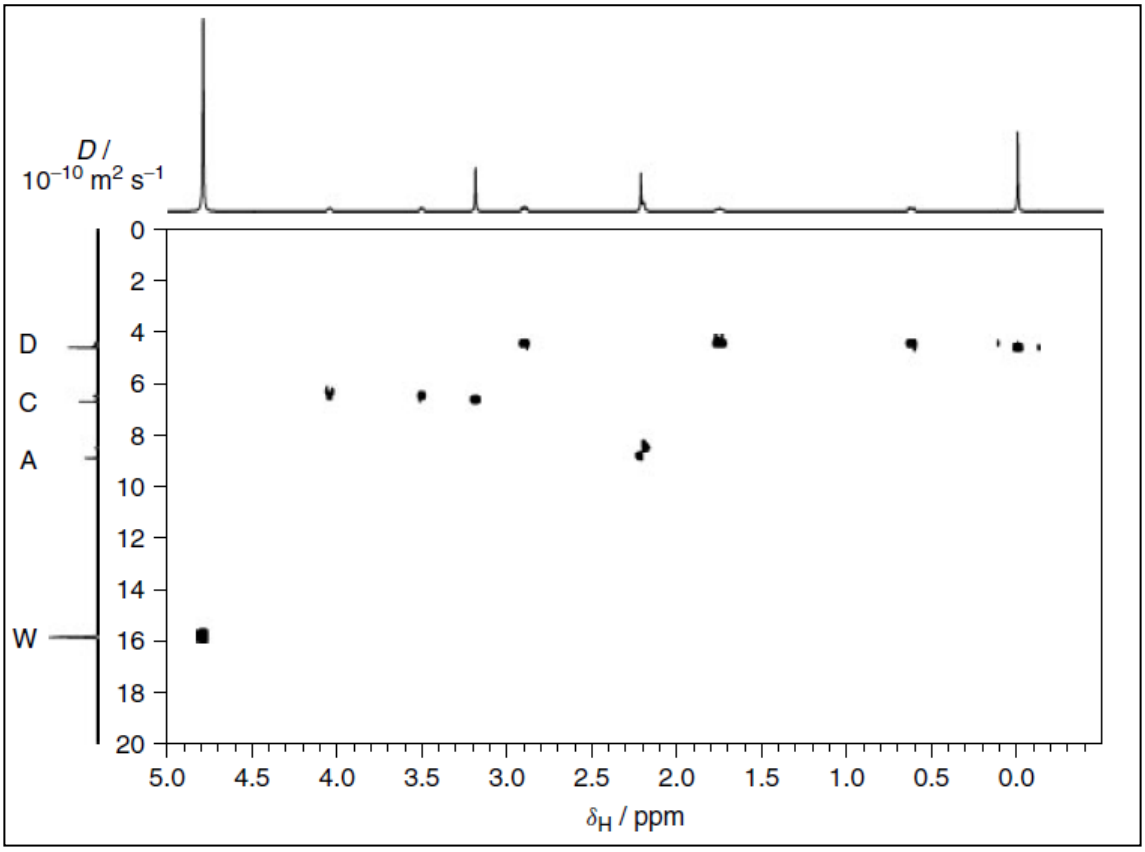

Figure 17 - DOSY spectrum calculated from the data of figure 13.[9]

A description of the most common DOSY techniques is presented in Annex 1.2.

1.3 – Configurational and Conformational Determination with NMR

Besides being able to probe motional dynamics, as previously introduced, NMR spectroscopy also present the ability of probing other molecular dynamics, such as conformation dynamics, and constitutional spatial features, such as configuration. In this way, beyond the traditionally recognized ability to provide information of the chemical environment of an atom, it is also possible with NMR to determine the connection with its neighbours. Experiments that routinely allow the determination of the connection between molecular atoms are the homonuclear and heteronuclear scalar coupling

interactions COSY, TOCSY, HSQC and HMBC. For the determination of molecular three-dimensional arrangement the homonuclear dipolar coupling interactions NOESY and ROESY are normally employed.[14]

The use of ^{1}H-^{1}H and ^{1}H-^{13}C three-bond *J* couplings (^{3}J) NMR data represents nowadays a widely used and consolidated way of studying molecular, mainly small molecules and natural products, relative stereochemistry and in some cases the major conformation in solution, such as for rigid molecules. Because of its inherent particularity, which is the detection of magnetization connecting through bond four sequential atoms, ^{3}J values depend on the dihedral angle between these three bonds, uncovering subsequently part of the spatial arrangement of the molecule.[15] In the analysis of ^{3}J coupling constant of small molecules is nowadays widely used an empiric methodology[16] based on the Karplus equation that includes several molecular parameters, including the electronegativity of the substituents.[14]

On the other hand, nuclear Overhauser effect (NOE), which pioneering application work dates from 1965,[17] consists in one of the most significant and extensively employed NMR data given its ability of providing spatial and consequently also dynamic information, having in this way been used particularly in organic molecules configurational and conformational analysis. Nevertheless, NOE presents a major handicap that is its $1 / r^{6}$ dependence in certain cases, which represents a serious limitation on, for example, the information acquisition of the distance between remotely located protons.[14]

Furthermore, using ^{3}J and NOE, in many cases, ambiguities may arise from the observed data values, given for example the case of different stereoisomeric compounds with equal data values. In such circumstances, the emergent residual dipolar couplings (RDCs) technique present alternative and complementary data that allows, for example, the unambiguous determination of small molecules and macromolecules relative stereochemistry, as it will be seen deeply in chapter 3.[14]

Chapter 2 – Study of Ion-Pair Dynamics in BMIM-BF_4

2.1 – Introduction

2.1.1 – Ionic Liquids and Ion Pairing

As will be further developed, ionic liquids (ILs) represent a very important subject for science today, not just for fundamental physic,[18] materials or chemistry,[19,20] but also for industry[21] and environment purposes.[22]

The physicochemical behavior (individual motion and aggregation) of ionic liquids, as neat or in solution, remains a mystic and widely discussed subject for many research groups.[23–26] The classical concept of ion-pair existence for any kind of salt in solution, reasoned by the opposed charges attraction, seems pretty much changed and disturbed nowadays.[27]

As it will be seen forward in this thesis, one of the possibilities of the NMR spectroscopy is to execute different kind of motion research techniques[2,6] which use relaxation as its basis, namely diffusion, inversion-recovery and spin-lock measurements. In this way, another main objective of this thesis is to do sufficient data acquisition through the previously referred techniques, and subsequent interpretation of the results so it is reasonable the discussion of the possible determination of ion-pairs in ionic liquids.

2.1.2 – Ionic Liquids

Ionic liquids, also called molten salts, ionic melts, liquid salts and fused salts, are a class of substances that correspond to salts which are in the liquid state at temperatures below 273 K.[28] Although the arbitrary temperature for melting point that define and groups this class of substances has been changing since it discovery[28,29] (non-consensual date), there is a more specific and intuitive definition that gathers a smaller group of substances belonging the previous class, that corresponds to the salts that are in the liquid state at room-temperature (298 K), the room-temperature ionic liquids (RTILs)[30]. The principle behind the low melting point of ILs is that ionic bonds are usually stronger than other non-covalent forces such as Van der Waals forces or hydrophobic forces[31]. So, because ILs mixtures usually present bulky cation, instead of small cation that can be closely-packed, they do not consist in regular and geometrical positioning space occupation by ions, which distances and weakens ionic bonds leading to mixtures with reduced melting points.[32] What also makes special this kind of liquids is that while ordinary liquids are predominantly made of electrically neutral molecules, ionic liquids are entirely made of ions and short-lived ion-pairs[33].

In the last few years (since 90s) a great flush of research and development in ILs has began, leading to the establishment of wide range of applications in many distinct areas and purposes[32], such as: analytical chemistry[34–37], batteries and fuel cells[18], electrochemical sensors and biosensors[38], gas detection and electrosynthesis[39], industrial chemistry[21], materials (nano, porous, lubrificants)[40], polymer science[41], green solvents (in synthesis; catalysis; asymmetric synthesis; dissolution, depolymerization and functionalization of carbohydrates, halogenations, etc)[42–58], supercritical fluid[59], and so on; and further the related achievement of lots of spectroscopic information and computational predictions about ILs remarkable and particular physicochemical properties[33], for: reactivity[60,61], solubility[62], solvation[63], stability[64], structural organization[23–26], molecular dynamics[19], fluorine-containing anions[65], viscosity[22], volatility and polarity[66]. Some recent studies indicate that some ILs are associated to certain levels of toxicity[67], contradicting the former idea of pure green chemistry of this research area.

2.1.3 – NMR Studies of ILs Structure and Dynamics

As previously introduced, ionic liquids characteristics consist nowadays in a wide spread and intense field of investigation, reasoned by its numerous possibilities. Justified by the impossibility of total experimental characterization of these substances family features, the spectroscopic route of determining molecular particularities and dynamics arises as fundamental tool, in order to achieve the sufficient understanding of it that allows rational design for different applications. Structure and dynamics presents to be some crucial features in this process.[19]

As also previously uncovered, NMR spectroscopic technique represents nowadays a solid and powerful experimental tool for this purpose, namely the structural and dynamics study of ILs. NMR spectroscopy by allowing the detection and dynamic evaluation of numerous nucleus, such as the spin-1/2 nucleus ^{1}H, ^{13}C, ^{15}N or ^{19}F, and even the quadrupolar (spin > 1/2) nucleus ^{2}H, ^{11}B, ^{14}N or ^{35}Cl, which frequently appear in ILs constitution and for this way represent an added value for information acquisition.[20]

Historically, in the past several years (1980s and 1990s) NMR spectroscopy has already provided crucial and meaningful understanding on different ILs structure and dynamics, namely by self-diffusion coefficients and relaxation times, the two tools employed in this study, and also by chemical shifts and nuclear Overhauser effects, which also take part of this work.

2.1.3.1 – Structural Concepts

Differently to the extended and high degree of order verified in solids, in liquids the order is confined local environment, normally in the scale of Angstroms. The essential distinction between

common liquids and ILs, is that in the second is present a partial ordering caused by charge effects that consists in several types of interaction between the two ions, such as cation-cation, cation-anion and anion-anion, which may be observed by scattering data and MD simulations (Figure 18).[68] Also differently from common liquids, charge-ordering in ILs extends over larger distances, positioning the ILs in terms of ordering between pure solids and pure liquids.[20]

One of the proposed features of such charge-ordering phenomena is the establishment of mesoscopic organization that results from the aggregation, in the nanometres scale, of hydrophilic and hydrophobic domains,[69] which derive from polar heads of the cations mutual interaction and anion segregation from hydrophobic butyl chains. This in many ways observed nanoscopic order of ILs consists in its most curious structural feature, which conditions all of its properties and possible applications.[20]

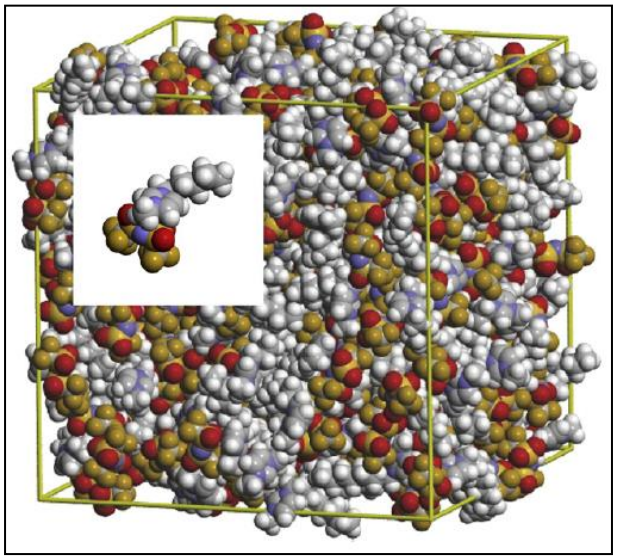

Figure 18 - Nanoscopic structural organization of [BMIM][BF_4] deduced from MD simulations. The relevant white square shows the ion-pair. The following colour code is used: H (white), C (light gray), N (light blue), F (goldenrod) and S (sulphur yellow).[20]

Despite the fact that NMR spectroscopy experimental techniques, such as diffusion-ordered or relaxation, only allows the interpretation of local order insights, it was possible many times to interpret such results as charge-ordering effects and relate to the proposed formation of mesoscopic structures, namely by the spectral determination of H-bonds engaged in H-bonded networks. Although these assumptions are mainly speculative, it can be shown that local ion dynamics strongly suggest an aggregation process associated with structural motifs, which probably are engaged in building blocks that originates such mesoscopic organization.[20]

2.1.3.2 – Hydrogen Bonding

As earlier mentioned, one of major possibilities of the NMR application in ILs structural studies is related with the hydrogen bonding determination between ions. This feature appears in several interpretations of different NMR data parameters, such as in self-diffusion coefficients and relaxation times, the two tools employed in this study, and also in chemical shifts and nuclear Overhauser effects, which also take part of this work. In this NMR studies has been determined that expectedly the ability of donating H-bonds are mainly associated with the cation, while the anion normally acts as H-bond acceptor. The investigators belief consists that the H-bonding network formation leads ion-pairing and the establishment of aggregates and consequently mesoscopic structures.[20]

Even consisting in aprotic species, many IL cations present the possibility of establishing H-bonds with proton-accepting anions. One good example is the C-H···anion bond of 1-alkyl-3-methylimidazolium salts. Comparing with other substances, such as the common molecular solvents, C-H bonds mainly represents no interest for H-bonding. On the other hand, in these aromatic imidazolium salt cations, a feature as the electronic structure gives rise to an acidic C-H bond at the position of carbon C2. In the aromatic ring, also the C4 and C5 carbons present a little acidic behaviour, inferior due to the structural positioning, since the acidity is related with the electro deficit in the two N-C-N bonds, as represented in the figure below (Figure 19). This C-H bonds acidity represents one crucial event for understanding the 1-alkyl-3-methylimidazolium cation ILs properties.[20]

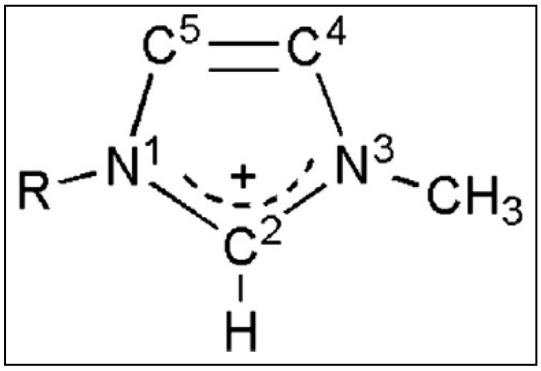

Figure 19 - The electronic structure and numbering of the ring atoms in 1-alkyl-3-methylimidazolium ions.[20]

Historically, it was in end of 1990s that have been initially established the relation between downfield chemical shifts of the ring protons and the strength of the H-bonds caused by the proton-accepting ability of the anions.[70] This was followed by the establishing of another correlation, which was between the ring protons chemical shifts and other spectroscopic properties, such as the quadrupolar coupling of ^{2}H species and vibrational frequencies.[71] The results obtained with such correlations have demonstrated that the referred spectroscopic properties presented similar reactions considering the variations in the C-H bonds chemical environment. One of the main purposes of such correlations establishment is the possibility of achieve estimating processes for predicting spectroscopic properties variation in such phases.[71] The chemical shifts appreciation for H-bonds

existence also includes the anionic nucleus, as for example the ^{35}Cl.[72] Nevertheless, this employed concept of H-bonding, at least for ILs, consists yet in a controversial subject.[20]

2.1.3.3 - Ion-Pairing

The previously introduced H-bonding particularity between the two ion species was a way to introduce a more important question that is the ion-pairing in the ILs. However, in neat systems in which ions are densely populated and cross-connected, the finding and attribution of ion-pairing consists in a difficult or even impossible task. Throughout time, different and dubious interpretations arisen for the explanation of ion-pairing with experimental results.[20]

One of the major evidences, related with conductivity studies, would be the existence of non-conducting ion stages consequent from the charge neutralization by the ion-pair formation. This fact is observed in experimental results that indicate lower electrical conductance by the ILs when compared with fully dissociated systems. A technique that has widely contributed for this question speculation has been the diffusion-ordered (DOSY) spectroscopy, which through the use of multinuclear PFGSE has provided valuable ionic diffusion coefficients that may be related with this ion-pairing problematic.[7374–7677] The obtained results in this way have uncovered many other physicochemical phenomena related with structure and dynamics of the ions in different ILs.[20]

In any case, taking into account the mentioned studies is globally realized that the idealization of perfectly defined ion-pair verification may be unattainable. Even the verification of the main source of ion-pair investigation, which is the conductance reduction observation, has been impossible so far to determine the time-scale in which these events are happening. Suggestions mainly from MD simulations[78] indicate nowadays that these cation-anion correlations only occur in the subpicosecond-to-picosecond time-scale, being in this way undetectable by spectroscopy methods so far. However, this scenario contradicts the intuitive picture of long-lived pairs, which are also supported by conductance behaviour.

Because NMR spectroscopy present limitations related with time-scale detection, other spectroscopic methods ranging different time-scales detection are necessarily considered. Experimental results on C-H vibrations coming from FT-IR spectroscopy indicates that ion-pair interactions may be observed at sub-picosecond time-scale.[79] Other experimental results that come from dielectric relaxation spectroscopy indicates that no such interactions are detected above the nanosecond time-scale.[80] Considering these results it is possible to conclude that the ion-pairing determination possibility only exists in the sub-picosecond time-scale, which, as already introduced, are time-scales out of the detection limits of NMR spectroscopy.[20]

Another equated and applied NMR technique in trying to evaluate ion-pair dynamics in IL solutions have been the NOESY and ROESY methods, by measuring intermolecular NOE values.[27]

However, no continuity has been given to these works recently, with exception of the intermolecular ^{1}H-^{19}F NOE study in $BMIMBF_4$.[87] The main reason the non-continuity with intermolecular NOE studies is related with the fact that to be observed a measurable intermolecular NOE the ion-pair needed to survive sufficient time to result in a notable probability for cross relaxation, condition that would imply that the process occurs at nanosecond time-scale. However, by the obtained NOE results it is proposed that contrary to the other previously referred spectroscopic data, the ion-pairs after all might be long enough to be detected.[80]

2.1.3.4 – Interactions Involving Aromatic Rings

The current perspective on the IL imidazolium aromatic rings-based cations suggests that the interactions between cations are established through three different mechanisms involving the ring, which are the $\pi\cdots\pi$ stacking, the methyl$\cdots\pi$ and the C2-H$\cdots\pi$ interactions in staggered spatial dispositions. The same principles may be applied to anions that present aromatic rings in its constitution. These interactions are mainly predicted by ILs crystal structures, taking into consideration that at least part of these structural patterns remains equal either in solids as in liquids.[23] It was also possible by NMR ^{1}H-^{1}H NOESY to determine close cation-cation encounters by two different ring interactions, which are the ring stacking and T-shaped ring.[81] However, in a subsequent NMR ^{1}H-^{19}F NOE study, in the same salt ($BMIMBF_4$), have not been determined such interactions existence, uncovering the problems that may be found when using NOE data in structural interpretation.[82]

2.1.3.5 – Translational Dynamics

As previously uncovered, IL dynamics, including the translational motion, present many interesting feature. Its motional dynamics understanding is of maximum interest in IL characterization, since it may influence practical properties such as the solvent ability. In this way, recently NMR PFGSE technique has been much requested for multinuclear studies of ions diffusion, with no hard technical adaptation for this purpose. However, has been determined the higher effectiveness of the stimulated-echo pulse sequence over the conventional spin-echo sequence in IL study.[89]

Although currently much research is being done with PFGSE technique studies on specific ILs, giving valuable information, no major results have emerged since the early works on this topic.[7374–7677] On the other hand, significant diffusion studies have been made over extreme temperature ranges, uncovering unexpected results from super-cooled and glassy conditions. In any case, considering that the measurements performed over small temperature ranges reveal specific ambient conditions, they may be informative on basic structural dynamics.[74–76] With the combination

of diffusion and conductance data have been possible the characterization over eight orders of magnitude, from microscopic to macroscopic range.[90]

2.1.3.6 – Rotational Dynamics

Along with the increasing interest in translational dynamic motion of ILs, has emerged the increasing interest also on the reorientational dynamic motion, resulting mainly from the spin-lattice relaxation times T_1 measurement. In this way, NMR, differently to other spectroscopic methods, offers the possibility specific-site reorientational studies through its numerous experiments, namely using different nucleus and/or different peak signals results.[91]

The possibility of studying molecular reorientation in solution NMR is related with the connection of the previously described relaxation times, which are experimental acquired, with the desired reorentational motion of the particles that is given through the calculation of rotational correlation times (τ_c). Besides providing rotational motion, ^{13}C NMR relaxation methods can also give insight on molecular interactions, becoming in this way so important in the present study of ILs.[91]

Considering now the large range of molecular motion, two extreme behaviours may be identified: one that corresponds to the fast molecular motion, and another that corresponds to slow molecular motion. The distinction between the two regimes is highlighted by the previously referred rotational correlation times (τ_c), in which for slow molecular motion this parameter is typically in the range between nanoseconds to milliseconds, and for fast molecular motion this parameter is typically in the range between picoseconds to nanoseconds. The two regimes are traditionally designated as being "within the extreme narrowing region", for the fast molecular motion, or on the other hand being "outside the extreme narrowing region", for the slow molecular motion. This concept is normally employed to differentiate between small sized or non-viscous molecular rotation in solution, and high sized or viscous molecular rotation in solution.[4,83] The rotational correlation time is normally thought of as being the time required for a nucleus to rotate an angle of one radian.[4,84]

As previously introduced, the measured ^{13}C NMR relaxation time is a result of various mechanisms contribution, namely: the more significant the dipolar coupling relaxation and the chemical shift anisotropy (CSA); and the other normally less significant including scalar coupling relaxation, which occurs for nucleus with similar Larmor frequencies; spin rotation, which is only observed for very small molecules; and paramagnetic relaxation, which is frequently due to impurities.[84] Although at low magnetic fields the contribution of CSA may be neglected, since CSA contribution increases with the square of magnetic field, for the same reason when using the modern higher magnetic fields it is often requires an analysis that includes its contribution. Considering that the relaxation values are used in rotational correlation times calculation, is logical to predict that by neglecting CSA contribution considerable errors may be introduced in such calculations. For such

purpose of separating the contribution of the two major relaxation mechanisms (dipolar and CSA) from the overall relaxation, an iterative mathematical approach combining several correlation functions has been devised.[84]

In this thesis such algorithm is explained in a stepwise manner in the experimental section of this chapter.[84]

2.1.3.7 – IL/Water Mixture Studies

As already introduced, ILs are thought to present many degrees of mesoscopic domains in solution. These mesoscopic domains, as already uncovered, are known to present a major role in ILs dynamics and properties, namely in the complex solvation dynamics. In this way, after the existence of cluster entities was first suggested,[75] numerous experimental evidences were collected for structural heterogeneities that are verified over the scale of a few nanometres. As an example, these structural heterogeneities of IL/water mixtures have been recently investigated in BMIM-BF_4/water compositions.[85] Globally, have been possible to determine a correlation between the formation of water clusters and the already mentioned ILs organization into polar networks with hydrophobic tails segregation. With the increasing addition of water, ion-pair interactions are progressively broken, causing in this way the weakening of such structural organization.[86] On the other hand, considering that segregation of the tails depend on the hydrophobic degree of the carbon chains, it is logical to suppose that segregation will progressively decrease as the chains polarity increases.[69] Nevertheless, some questions afterwards appeared in relation to the really existence of such structural heterogeneities.[87]

In this context, the entire BMIM-BF_4/water phase diagram plus temperature variation is herein also re-investigated by means of diffusion[6] and relaxation[88] NMR techniques, to: analyze BMIM-BF_4 possible aggregation process; unambiguously probe the existence of an ion-pair high-content sustainable point of mixing conditions; and, eventually, the progressive disruption of ion-pairs upon increasing the water content.[87]

2.2 – Experimental Section

2.2.1 – Materials

The IL 1-butyl-3methylimidazolium tetrafluoroborate [BMIM][BF_4] was purchased from "io-li-tec" (purity > 99 %). Distilled water was obtained from laboratory facility instruments. Dioxane was purchased from "RPE-ACS" (purity > 99.5 %).

2.2.2 – NMR measurements

All NMR experiments were performed using a Bruker Avance III 400 operating at 400.15 MHz for protons 376.3 MHz for ^{19}F and 100.6 MHz for ^{13}C, equipped with a 5 mm high-resolution BBO probe and with pulsed gradient units, capable of producing magnetic field pulsed gradients in the z-direction of 0.54 $T.m^{-1}$. ^{1}H, ^{19}F and ^{13}C NMR measurements were carried out in water with dioxane (1% IL molar fraction) for referencing, the temperature range from 273 to 353 K (273, 283, 293, 298, 303, 313, 323, 333, 343 and 353 K) was covered for three water molar fraction samples (neat, 8% and 93%) through a Bruker Avance 400 MHz (9.4 T) spectrometer at the operating frequencies of respectively. A standard BVT 3000 variable temperature control unit with an accuracy of +/-0.5 ºC was used.

Diffusion measurements were performed using the stimulated echo sequence using bipolar sine gradient pulses and eddy current delay before the detection (PFGSE). Self-diffusion coefficients were obtained by varying the gradient strength (g) while keeping the gradient pulse length (δ) and the gradient pulse intervals constant within each experimental run. Typically, in each experiment a number of 32 spectra of 16 K data points were collected, with values for the duration of the magnetic field pulse gradients (δ) of 1.0 to 3.0 ms, diffusion times (Δ) of 50 to 1000 ms and an eddy current delay set to 5 ms, the gradient recovery time was 200 μs. The sine shaped pulsed gradient (g) was incremented from 5 to 95% of the maximum gradient strength in a linear ramp.

The data were fitted according to the Stejskal-Tanner equation:

$$\frac{I}{I_0} = e^{(-Dq^2t)} \quad \textbf{(6)}$$

- I and I_0 are the signal intensities, respectively, in the presence and absence of the applied field gradient, $q = \gamma g \delta$ is the so-called scattering vector (γ being the gyromagnetic ratio of the observed nucleus), $t = (\Delta - \delta/3)$ is the diffusion time, Δ is the delay time between the encoding and decoding gradients, and D is the self-diffusion coefficient to be extracted.

Spin-lattice (T_1) relaxation times were obtained by means of the usual inversion recovery (180-τ-90-acquisition) sequence, respectively.

Typically for a T_1 determination a number of 32 spectra of 64 K data points were collected, with 32 τ values in the range of 25 ms to 8 s. A quick T1 estimation was performed for all samples in order to set the appropriate relaxation delay. Relaxation delays varied between 7 s and 46s.

Values of T_1 were obtained by three-parameter;

$$I(\tau) = A - Be^{\left(\frac{-\tau}{T_1}\right)} \quad \textbf{(7)}$$

For the ^{13}C NOE measurements two experiments were executed: the gated decoupled 1D-NMR (pg; power gated) that consist in a decoupled NOE including experiment, since it comprehends the use of decoupling during relaxation time, followed by 90º pulse and acquisition, giving singlet signals with amplified signal intensity (signal amplification occurs during the relaxation time while the transformation of multiplets to singlets occurs during acquisition); and the inverse gated decoupled 1D-NMR (ig) that consist in a decoupled NOE excluding experiment, since it comprehends the use of decoupling during acquisition time, preceded by 90º pulse, giving singlet signals without amplified signal intensity. The NOE factor is obtained by the ratio (I_{pg} - I_{ig}) / I_{ig}.

These experiments were performed with 64K points over a spectral window of 160 ppm (16129 Hz) centred at 80 ppm (8049 Hz). The number of scans was 16 s and the relaxation delay varied between 7 s for the concentrated sample to 46 s for the more diluted.

It deserves pointing out that tetrafluoroborate anion in water slowly hydrolyzes, producing hydrofluoric and boric acids.[89] To overcome this problem, all measurements were performed immediately after sample preparation. Since no precipitate (H_3BO_3 is hardly soluble) was observed and, more importantly, both self-diffusion and relaxation experiments showed a mono-exponential decay, the presence of significant hydrolysis products that could affect the NMR results was ruled out.

For each temperature/water molar fraction the quality of the subsequent experiments was controlled by a close inspection of the ^1H and ^{19}F 1D-NMR experiments to assure the inexistence of impurities and degradation.

2.3 – Results and Discussion

As it has been referred in the beginning of this chapter 2, one of the main targets of this work is the investigation of the ion-pairing formation, during the study of ion-pairing dynamics in the ionic liquid BMIM-BF_4 with NMR. In this context, a specific approach has been outlined consisting first in the determination of self-diffusion coefficients using diffusion-ordered spectroscopy (DOSY), and second in the recording of longitudinal and transversal relaxation measurements to ascertain both translational and rotational motion of neat BMIM-BF_4 and IL/water solutions prepared with different water molar-fractions. While in the case of DOSY measurements, translational motion can be directly observed and interpreted via diffusion coefficients, which results from exponential decaying of the NMR signal as it was explained previously in this chapter, in the case of relaxation measurements, rotational motion can only be determined after a mathematical iteration process that enables a reliable estimation of the correlation time τ_c,[84] which will be presented later in this section. This correlation time parameter is the one that gives directly information about molecular rotational motion. The principle underlying this translational and rotational combined approach is the belief that if the two ionic species are together in a lasting ion-pair combination at some sort of conditions, they must be diffusing and rotating synchronously (with the same parameters values), and therefore it should be detectable by the NMR techniques sensible to these parameters.

Before proceeding, it is crucial to justify the selection of BMIM-BF_4 as a model ionic liquid to perform such investigation. The characteristics that make BMIM-BF_4 so appealing are: first, the fact that it has a vast bibliographic support[74,87,90–92], as many and diverse physicochemical studies have been developed about it; and second, because differently to many other ionic liquids it presents detectable and highly sensitive NMR nuclei (in this case ^1H and ^{19}F) in both ionic species (cation and anion, respectively). This NMR detectable nucleus presence in both ionic species allows that the diffusion coefficients for both ionic species could be independently determined.

Relatively to impurities and concentrations, during the experimental work all the fifteen samples (0 %, 4 %, 8 %, 16%, 24 %, 30 %, 35 %, 37 %, 43 %, 46 %, 50 %, 62 %, 73 %, 83 % and 93 %) were inspected for impurities with ^1H and ^{19}F 1D spectroscopy, presenting no impurities, and besides all the concentrations (molar fractions) were verified and adjusted with signal integration of water, dioxane and BMIM-BF_4 species.

2.3.1 – Translational Dynamics - BMIM-BF_4

Since the DOSY studies allow a direct verification of the dependence of anion and cation diffusion coefficients of water percentage and temperature, the diffusion measurements will be addressed before all the others in this discussion. The two distinct but conjugated conditions for which diffusion has been measured (water percentages and temperature variations) will be presented in two

sub-divisions in order to clarify its distinct results. Thus, even though in the context of this dissertation the dilution and temperature studies may seem sequential these have been performed in an integrated manner (same samples and at the same time), resulting in a combinatorial study that provides better and wider comprehension of the influence of the two factors concurrently.

In all the PFGSE experiments the measuring time (Δ, the big delta, which corresponds to the interval between two gradient pulses) dependency of the self-diffusion coefficients for the different water molar fraction samples and different temperatures was checked, and in the range of Δ from 20 to 100 ms, the self-diffusion coefficients did not show any notable dependency, which suggests that the ion diffusion is the "Fickian" diffusion in the homogeneous fluid and the convection effects can be disregarded in the water molar fraction and temperature ranges studied under the experimental conditions.

2.3.1.1 – Translational Water Molar Fraction Dependence

In this sub-section the results of the whole phase diagram of BMIM-BF_4/water mixture, investigated by means of ^{1}H and ^{19}F PFGSE-NMR experiments performed at room temperature (298 K, 298 K) will be presented.

As it was already known from previous NMR and computational publications[87,90,91,93–95], the inorganic anion and imidazolium-based cation diffusion coefficients do not show continuous linear progression with increasing amount of water and temperature, but an exponential progression, as will be seen next. Furthermore, the diffusion coefficients are not equal for both ions, they even show an intersection-point (close to 10% of water molar fraction) highlighted below in Figure 20, meaning that one of the ions (the anion BF_4^-) begins with lower diffusion coefficient and at a certain moment (of increasing amount of water added) equals the other ion (cation $BMIM^+$) diffusion coefficient, and later turns out to overtake it (Figure 20). During this initial interval of concentration (approximately from neat to 30% molar fraction of water) the diffusional progression of the ions shows a linear relationship as can be seen in Figure 20.

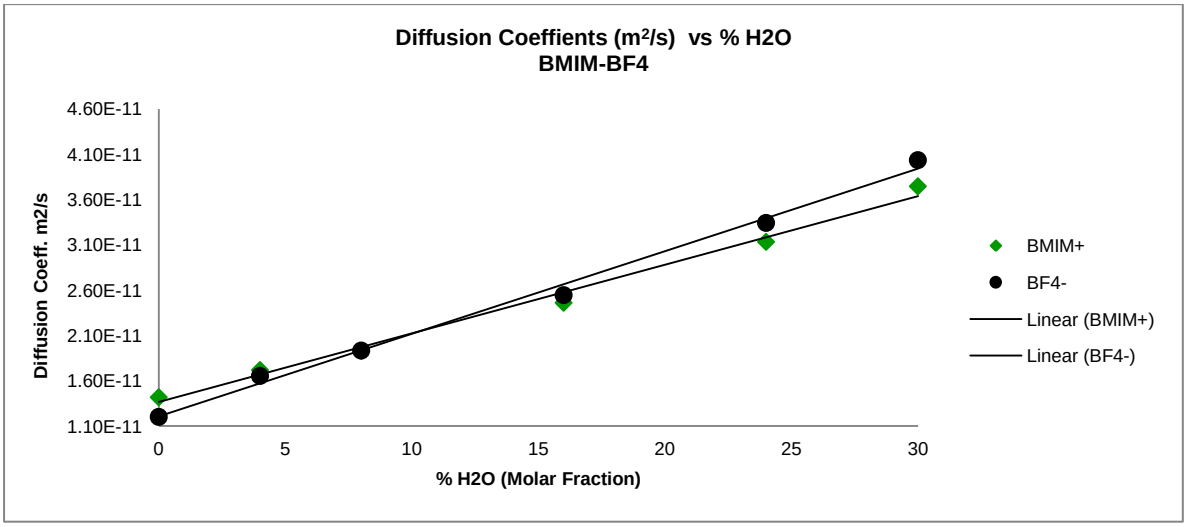

Figure 20 - [BMIM][BF_4] diffusion coefficient values for the water molar fraction range from 0 (neat) to 30 %, highlighting the diffusion coefficients cross-value at 8 %.. Linear regressions are presented to illustrate the apparent linear progression for this range of water molar fraction values (R_{cation}^2 = 0.9913, R_{anion}^2 = 0.9943).

As far as we know, although many diffusional studies had been carried out in ionic liquids/water mixtures, and specifically in BMIM-BF_4, none has had the objective of study the ion-pairing dynamics. In this context, we believe that the previously referred intersection point for the cation and anion diffusion coefficients, represented in Figure 20, represents the stage where both ionic species are diffusing at the same rate, and corresponds possibly to a 1:1 translation motion of the ion-pair in solution. This assumption is realistic since it is known that ionic liquids start from a situation of extensive cluster-aggregation existence in neat (pure ionic liquid sample) and ends up in free-motional ion disposition in infinite dilution sample (water molar fraction above 90%), as supported by motional data.

A basic supervision over the three species (cation, anion and dioxane) diffusion coefficients data from neat IL to 93 % water molar fraction (in Figure 21) reveals that at low water content (8 % water molar fraction) anions and cations share approximately the same self-diffusion coefficient, but above a critical water concentration (30 % water molar fraction) the anions begins to diffuse faster than the cations (in Figure 21). It is also possible to observe that the dioxane presents always higher diffusion coefficient values than the two ionic species, showing closer relation to the anion diffusion at higher water concentrations, which was expected due to similar size of both (in Figure 21).

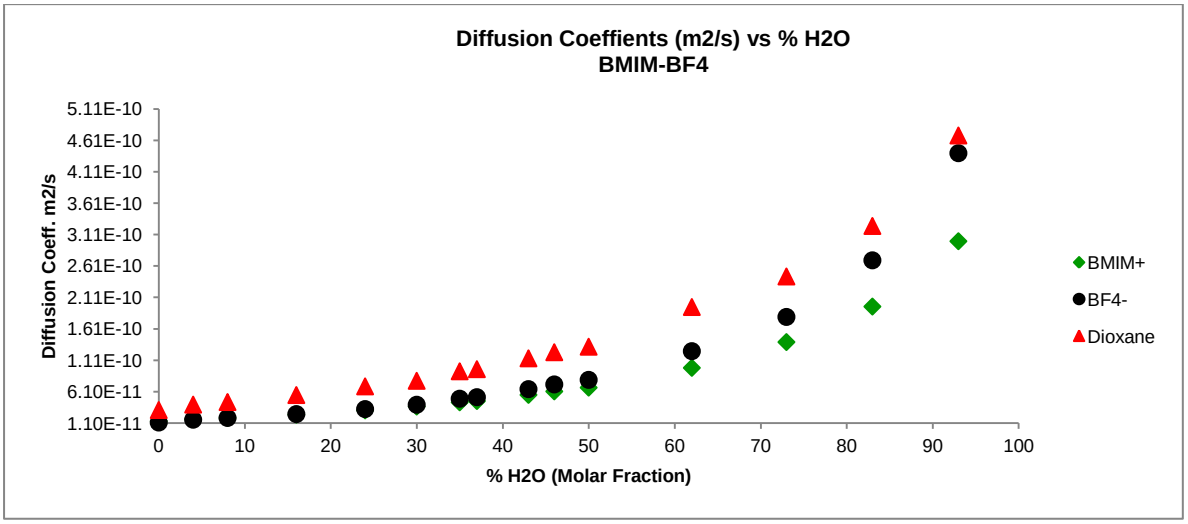

Figure 21 - [BMIM][BF_4] diffusion coefficient values for the total water molar fraction range from 0 (neat) to 93 %, exhibiting the exponential progression of the diffusion with increasing amount of water.

Relevant physicochemical information that can also be derived from the diffusional data collected is the diffusion values that result from the product of diffusion coefficients with molecular concentrations, since it gives the value of mole diffusion over m.s (in Figure 22). Although the apparent similitude to the diffusion coefficient trace, this representation shows that the relative "diffusion flux" (mol/(m.s)) seems to evolve exponentially slower than the diffusion coefficient (the ratio between the progression slopes of diffusion coefficient and diffusion flux is not constant). This "diffusion flux" parameter result confirms that the diffusion exponential progression of both ionic species in solution although influenced by the ionic species concentration factor, which was expected, since this study implies concentration variation, it does not explains all the diffusion coefficient behaviour (in Figure 22). Thus, the inference that must be taken from this result is that other factor, or a conjunction of factors must be in the origin of the diffusional behaviour observed.

By the observation of the plot in Figure 22 it is possible to observe that until the 30 % water molar fraction, the two ionic species behave very closely with "diffusional flux" values almost similar. In this range is possible to observe that there is a first fast progression from the neat to 10 % water molar fraction, followed by a reduced progression until the 20 %, and followed again by a faster progression (in Figure 22). With respect to the dioxane, is possible to verify that its diffusion flux is one order inferior to the two ionic species, fact that is explained by its reduced concentration in solution (in Figure 22).

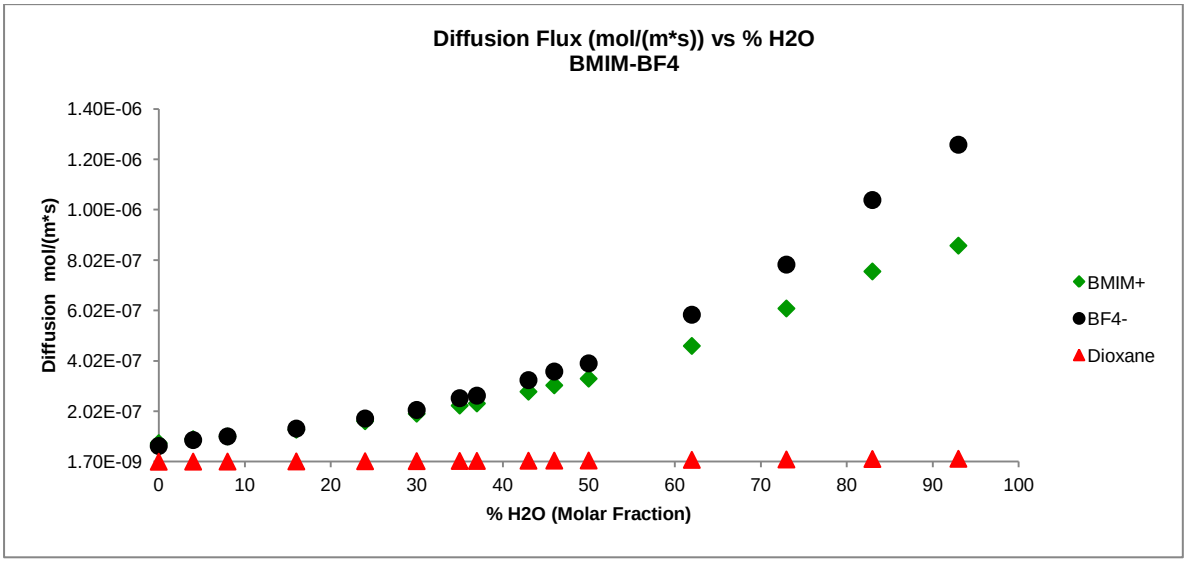

Figure 22 - [BMIM][BF_4] diffusion flux values for the total water molar fraction range from 0 (neat) to 93 %, exhibiting, by the graphical differences to the previously represented figure 18, the influence of the concentration in the diffusion coefficients.

Table 1 and 2 shown below summarizes the diffusion-ordered spectroscopy data versus the molar fraction of water, and even presents some additional information. Within this additional information may be seen the progression slopes columns. These progression slopes values are calculated according to the quotient of the difference between sequential diffusion coefficient values over the difference between sequential molar fractions of water values (in Table 1 and 2). In this way, these progression slope values reflect an average evolution of the diffusion coefficient values during the increase percentage of water molar fraction. It is worth noting two relative minimums and one absolute minimum in the progression slopes function values, which reflects the progression of the ionic species diffusion coefficient values over the increasing amount of water added, in the values corresponding to values of 8 %, 37 % and 50 % water molar fraction for both ion species ($BMIM^+$ and BF_4^-) (in Table 1). While the 8 % sample will be further studied, the other two (37% and 50%) will be sent for future works section.

Table 1 - $[BMIM]^+$ diffusion data values for the total water molar fraction range from 0 (neat) to 93 %.

%H_2O	[$BMIMBF_4$] mol/m^3	[Dioxane] mol/m^3	$D_{dioxane}$ (m^2/s)	Progression Slopes for $D_{dioxane}$	$D_{dioxane}$ x [Dioxane] (mol/(m*s)	D_{BMIM+} (m^2/s)	Progression Slopes for D_{BMIM+}	D_{BMIM+} * [$BMIMBF_4$] (mol/(m*s)	Progression Slopes for D_{BMIM+} x [$BMIMBF_4$]	D_{BMIM+} / $D_{dioxane}$
0	5,33E+03	5,33E+01	3,19E-11		1,70E-09	1,42E-11		7,56E-08		4,44E-01
4	5,30E+03	5,30E+01	4,06E-11	2,16E+00	2,15E-09	1,72E-11	7,53E-01	9,12E-08	3,90E-01	4,24E-01
8	5,28E+03	5,28E+01	4,46E-11	1,02E+00	2,36E-09	1,93E-11	5,28E-01	1,02E-07	2,68E-01	4,32E-01
16	5,23E+03	5,23E+01	5,58E-11	1,39E+00	2,92E-09	2,46E-11	6,64E-01	1,29E-07	3,35E-01	4,41E-01
24	5,18E+03	5,18E+01	6,96E-11	1,73E+00	3,60E-09	3,13E-11	8,41E-01	1,62E-07	4,21E-01	4,50E-01
30	5,13E+03	5,13E+01	7,84E-11	1,48E+00	4,03E-09	3,75E-11	1,02E+00	1,92E-07	4,99E-01	4,78E-01
35	5,09E+03	5,09E+01	9,36E-11	3,02E+00	4,76E-09	4,42E-11	1,34E+00	2,25E-07	6,45E-01	4,72E-01
37	5,04E+03	5,04E+01	9,70E-11	1,70E+00	4,89E-09	4,63E-11	1,05E+00	2,33E-07	4,25E-01	4,77E-01
43	4,99E+03	4,99E+01	1,14E-10	2,88E+00	5,70E-09	5,60E-11	1,63E+00	2,80E-07	7,78E-01	4,91E-01
46	4,95E+03	4,95E+01	1,24E-10	3,23E+00	6,13E-09	6,16E-11	1,86E+00	3,05E-07	8,37E-01	4,97E-01
50	4,91E+03	4,91E+01	1,33E-10	2,20E+00	6,51E-09	6,76E-11	1,49E+00	3,31E-07	6,62E-01	5,09E-01
62	4,66E+03	4,66E+01	1,96E-10	5,27E+00	9,13E-09	9,90E-11	2,62E+00	4,61E-07	1,08E+00	5,06E-01
73	4,35E+03	4,35E+01	2,45E-10	4,42E+00	1,06E-08	1,40E-10	3,73E+00	6,10E-07	1,35E+00	5,73E-01
83	3,85E+03	3,85E+01	3,25E-10	8,04E+00	1,25E-08	1,97E-10	5,65E+00	7,57E-07	1,47E+00	6,05E-01
93	2,86E+03	2,86E+01	4,69E-10	1,44E+01	1,34E-08	3,01E-10	1,04E+01	8,59E-07	1,02E+00	6,41E-01

Table 2 - $[BF_4]^-$ diffusion data values for the total water molar fraction range from 0 (neat) to 93 %.

%H_2O	[$BMIMBF_4$] mol/m^3	[Dioxane] mol/m^3	$D_{dioxane}$ (m^2/s)	Progression Slopes for $D_{dioxane}$	$D_{dioxane}$ x [Dioxane] (mol/(m*s)	D_{BF4-} (m^2/s)	Progression Slopes for D_{BF4-}	D_{BF4-} x $[BF_4^-]$ (mol/(m*s))	Progression Slopes for D_{BF4-} x $[BF_4^-]$	D_{BF4-} / $D_{dioxane}$
0	5,33E+03	5,33E+01	3,19E-11		1,70E-09	1,20E-11		6,41E-08		3,76E-01
4	5,30E+03	5,30E+01	4,06E-11	2,16E+00	2,15E-09	1,65E-11	1,13E+00	8,77E-08	5,92E-01	4,08E-01
8	5,28E+03	5,28E+01	4,46E-11	1,02E+00	2,36E-09	1,93E-11	7,00E-01	1,02E-07	3,59E-01	4,33E-01
16	5,23E+03	5,23E+01	5,58E-11	1,39E+00	2,92E-09	2,55E-11	7,65E-01	1,33E-07	3,88E-01	4,57E-01
24	5,18E+03	5,18E+01	6,96E-11	1,73E+00	3,60E-09	3,34E-11	9,96E-01	1,73E-07	5,01E-01	4,80E-01
30	5,13E+03	5,13E+01	7,84E-11	1,48E+00	4,03E-09	4,04E-11	1,16E+00	2,07E-07	5,66E-01	5,15E-01
35	5,09E+03	5,09E+01	9,36E-11	3,02E+00	4,76E-09	4,99E-11	1,91E+00	2,54E-07	9,35E-01	5,34E-01
37	5,04E+03	5,04E+01	9,70E-11	1,70E+00	4,89E-09	5,24E-11	1,23E+00	2,64E-07	5,02E-01	5,40E-01
43	4,99E+03	4,99E+01	1,14E-10	2,88E+00	5,70E-09	6,52E-11	2,14E+00	3,26E-07	1,03E+00	5,71E-01
46	4,95E+03	4,95E+01	1,24E-10	3,23E+00	6,13E-09	7,27E-11	2,49E+00	3,60E-07	1,14E+00	5,87E-01
50	4,91E+03	4,91E+01	1,33E-10	2,20E+00	6,51E-09	7,99E-11	1,81E+00	3,92E-07	8,08E-01	6,02E-01
62	4,66E+03	4,66E+01	1,96E-10	5,27E+00	9,13E-09	1,26E-10	3,81E+00	5,85E-07	1,61E+00	6,41E-01
73	4,35E+03	4,35E+01	2,45E-10	4,42E+00	1,06E-08	1,80E-10	4,95E+00	7,84E-07	1,81E+00	7,37E-01
83	3,85E+03	3,85E+01	3,25E-10	8,04E+00	1,25E-08	2,70E-10	9,01E+00	1,04E-06	2,56E+00	8,32E-01
93	2,86E+03	2,86E+01	4,69E-10	1,44E+01	1,34E-08	4,41E-10	1,71E+01	1,26E-06	2,20E+00	9,40E-01

As may be seen in Table 1 and 2, as in Figure 21 and Figure 22, the diffusional data includes information about the organic compound dioxane (or 1,4-dioxane). This is justified by the intentional addition of dioxane, in a fixed molar fraction of 1% relative to BMIM-BF_4, to all samples. The importance of adding a regular small amount of dioxane to all samples is related with the necessity of having a diffusion standard to allow the calculation of a "corrected diffusion" for BMIM-BF_4 species, i.e. of obtaining a diffusion value for both ion species ($BMIM^+$ and BF_4^-) that presents dimensionless character and is independent of the medium viscosity. The value of this dimensionless character results from the ratio between the ion specie (cation and anion) diffusion coefficient and the dioxane diffusion coefficient (D_{ion} / $D_{dioxane}$), as described in Table 1 and 2. The choice of dioxane is related with its known miscibility with water and with the ionic liquid in study, BMIM-BF_4. The graphical representation of the corrected diffusion for both ion species, $BMIM^+$ and BF_4^-, is shown below in Figure 23.

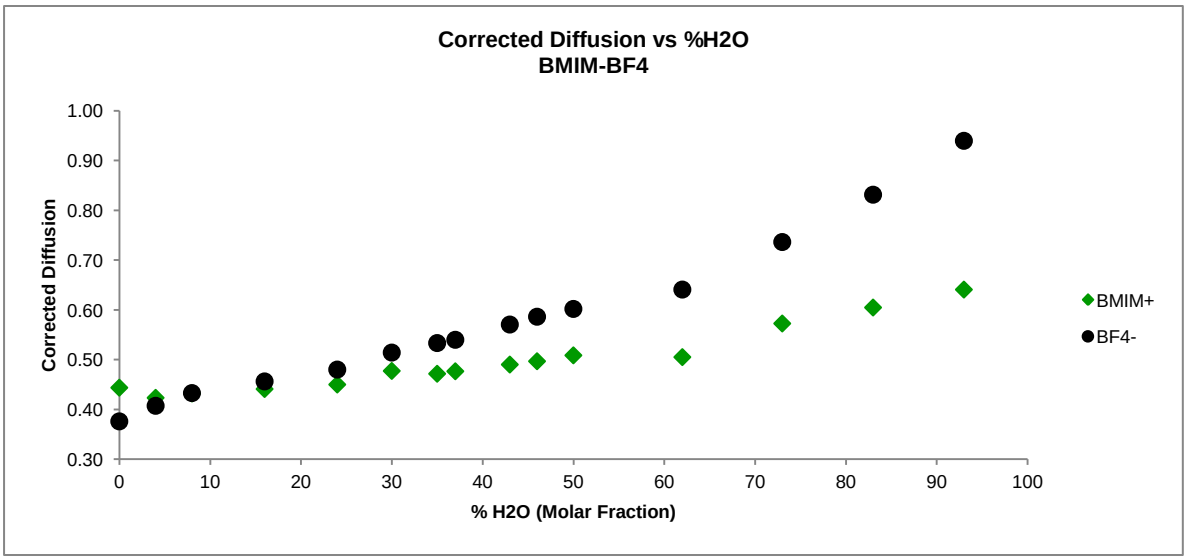

Figure 23 - [BMIM][BF_4] corrected diffusion D_{ion} / $D_{dioxane}$ values for the total water molar fraction range from 0 (neat) to 93 %, highlighting the relative diffusional evolution progression of the two ions in relation to the dioxane diffusion evolution and the diffusion coefficients cross-value at 8 %.

From the observation of Figure 23 and the data in Table 1 and 2 it can be determined that BF_4^- despite presenting always a lower diffusion coefficient than dioxane, has a non-linear and always positive progression of its corrected diffusion.

By the Stokes-Einstein equation it is reasonable to understand the observed relation between the solution viscosity and diffusion of the species:

$$D = \frac{kT}{c\pi\eta a} \quad \textbf{(8)}$$

- D is the diffusion coefficient in m^2/s;
- k is the Boltzmann constant in $Pa.m^3/K$;
- T is the temperature in K;

- c is the theoretical constant for slip and stick boundary conditions, ranging between 4 and 6, respectively;
- a is the hydrodynamic radius of the diffusing specie in m;
- η is the viscosity in Pa.s.

The Stokes law is based on the assumption of a rigid sphere solute diffusing in a continuum of solvent, and in the case of a large solute in a small solvent the factor c can attain the value of 6 (stick boundary condition)[96]. However, if the ratio of the solute size to solvent is increased, especially for highly viscous media, the correlation breaks down, and the value of c in Stokes-Einstein equation is reduced to 4 (slip boundary condition)[96]. In this way, the factor c may help to understand the microscopic ion dynamics in RTILs.[74] In any case, it is known from a variety of investigations on micelles in a variety of solvents that the Stokes-Einstein equation proves quantitative validity[97], and so it is worth to use it in this particular approach of BMIM-BF_4 aggregation dynamics in water, even knowing that has been reported a micellar size of about 10 Å for this RTIL[98].

According to the Stokes-Einstein equation the corrected diffusion value, $D_{ion}/D_{dioxane}$ corresponds to the ratio of the hydrodynamic radius, $a_{dioxane}$ / a_{ion}, of the two species, since for the same solution the same theoretical constant for slip and stick boundary conditions (c) is assumed for all solutes and the viscosity (η) is the same. In this way, and taking into consideration a static dioxane hydrodynamic radius ($a_{dioxane}$), by the observation of the ionic species trace in Figure 23 it is possible to assume that they correspond to the variation of its hydrodynamic radius, namely a_{cation} and a_{anion}. However, in Figure 23 are represented D_{ion} / $D_{dioxane}$, which gives the hydrodynamic relation of $a_{dioxane}$ / a_{ion} that is the inverse of what is physically interesting to understand, which is a_{ion} / $a_{dioxane}$, since it allows the determination of the ionic species aggregation stages, in case of increased a_{ion} / $a_{dioxane}$ relation.

The approach of using an internal diffusion reference, which presumably does not take part in H-bonding, in order to allow the calculation of different species hydrodynamic radius has been described previously.[8] This approach is based on the supposition that changes on the hydrodynamic radius due to aggregation processes can be detected by diffusion NMR, if they occur in the same time-scale.[8]

For this reason the following graphical representation of Figure 24 has been calculated. As it was expected the traces are inverted in relation to Figure 23, By observing Figure 24, assuming static dioxane hydrodynamic radius, is possible to state that at lower water molar fractions the previously detected low diffusion coefficient of the anion may be associated with a higher aggregation state,

since its hydrodynamic radius, in relation to the one of dioxane, is much higher (higher than 2; almost 3 for neat composition) and higher than the one of the cation. With the consequent addition of water is observed the progressive decreasing of the hydrodynamic radius relation for the anion, which is reasonably associated with the aggregation progressive disruption.

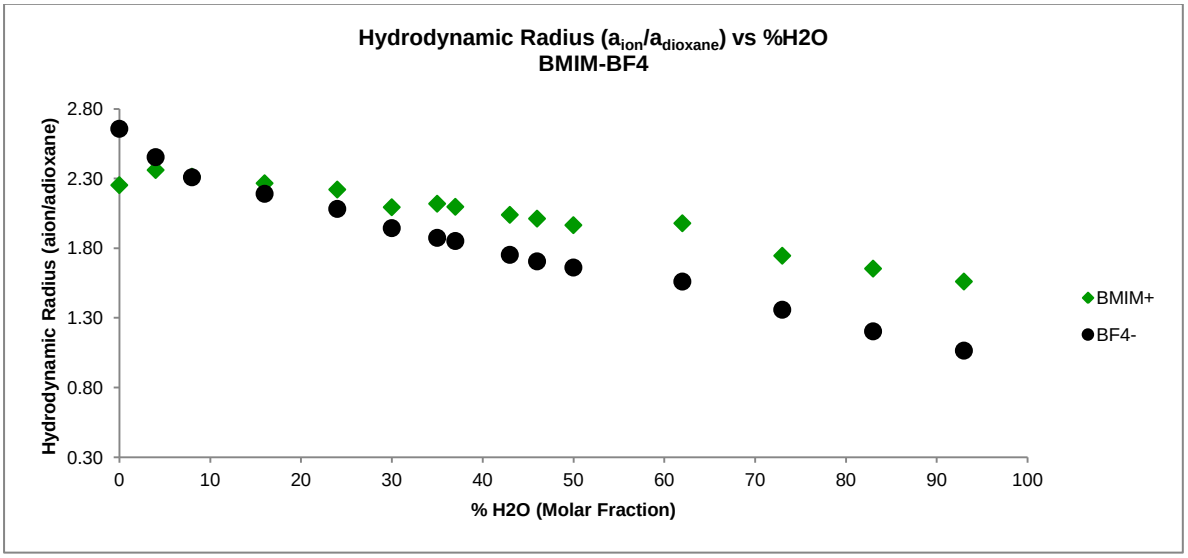

Figure 24 - [BMIM][BF_4] hydrodynamic radius ratio (a_{ion} / $a_{dioxane}$) values for the total water molar fraction range from 0 (neat) to 93 %, highlighting the relative diffusional evolution progression of the two ions in relation to the dioxane diffusion evolution and the diffusion coefficients cross-value at 8 %.

In the case of the cation, in Figure 24 is observed an initial increasing, from neat to 4 %, of the hydrodynamic radius relation, presenting values close to 2.40, which is followed by a progressive decreasing with the addition of water. At 8 % the hydrodynamic radius relation of both ion species intersect at the same value (2.310 approximately). This expected intersection may indicate that physically the two ions are sharing the same hydrodynamic radius because of their involvement in ion-pairing. This data proposes that the cation aggregates increase in a first moment with the addition of water, and begins to separate subsequently. One possible explanation for this result is that with the first addition of water, the more hydrophobic sections of the cation, namely the aliphatic chain, tend to aggregate, giving rise to higher aggregates.

Finally, at the higher water molar fraction compositions is possible to observe the true hydrodynamic radius relation, which strongly support this results, indicating that the anion and the dioxane share approximately the same hydrodynamic radius (a_{anion} / $a_{dioxane}$ = 1) and the cation presents a hydrodynamic radius 3/2 times higher than both dioxane and the anion (a_{cation} / $a_{dioxane}$ = 1.5) (in Figure 24).

Another frequently procedure for diffusion data analysis is to represent the difference D_{BF4-} - D_{BMIM+} versus the water content. This data show particularly well the effect of increasing water percentage on the differentiation of the individual ionic diffusivities. As it has been referred before, above a determined threshold of water added the anions begins to diffuse faster than the cations, and

it is believed that that composition corresponds to the one at which the ion-pairs start an accelerated dissociation. That threshold for us corresponds to the water molar fraction value of 16 % (for us the ion-pair composition lies close to 8 %) since it is clear that only above 16 % this difference deviates significantly from zero. What is observed in the remaining solutions is that further water addition continues to drive the equilibrium (between ion-pairs and free ions) towards dissociated ions, until above a certain water concentration the system will behave as a classical electrolyte solution.[87]

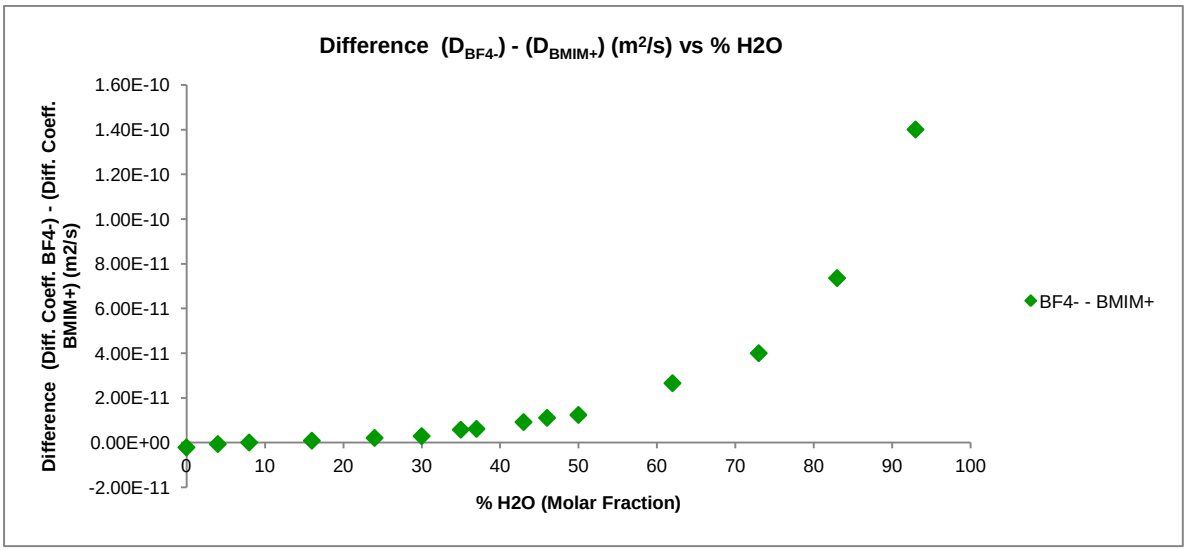

Figure 25 - Diffusion difference between ion species for the total water molar fraction range from 0 (neat) to 93 %, highlighting the ions diffusion coefficients detachment at approximately 20 %.

The low ionic diffusivity of the ionic liquids, in comparison with other commonly used organic solvents, is well justified in terms of their high viscosity (from 40 to 182 mPa.s at 303 K). The much lower ion diffusion coefficients and higher viscosity for the ionic liquids may be attributable to the very strong Coulombic forces among each ionic species in the ionic liquids.[74]

A similar study of the influence of water in the diffusion of BMIM-BF_4 has been reported before.[87] A significant result of that study was the relation established between diffusion coefficients and solution viscosity values. In that study[87] the relation observed was not a linear one, as it was not predictable from the Stokes-Einstein equation (D = const x η^{-1}). Instead the two ionic species obey to the power law:[87]

$$D = const \times \eta^{-\alpha} \quad \textbf{(9)}$$

In this fractional power formulation of the Stokes-Einstein equation, the exponent must be $\alpha < 1$. Analogous behavior was observed in a large number of systems (polymers, glass-formers, water, hydrocarbons, etc.) when the size of the tagged particle is less than a few nanometers and the fluid viscosity increases over several orders of magnitude.[87] In this context, another significant achievement from this previous study is that for low water content (high viscosity) the two ion species have the same diffusion coefficient versus viscosity relation (same α, α = 0.78).[87] In agreement with

our previously discussed self-diffusion results, this finding evidences once again that the ion-pair dissolution begins at low water content.

In any case, the major result from that previous study[87] was that when they applied the diffusion data to the fractional power formulation of the Stokes-Einstein equation to estimate the hydrodynamic radius for different water molar fractions, they obtained the following graphical result:

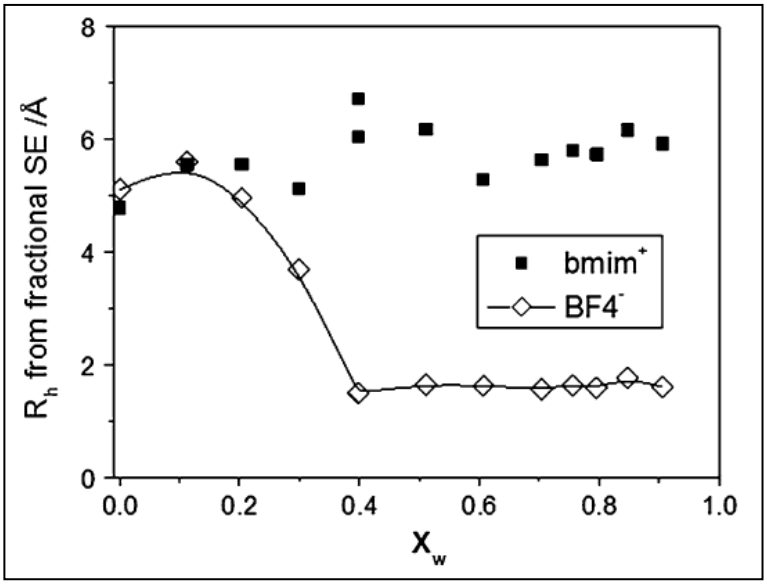

Figure 26 - Hydrodynamic radius calculation for the two ions for the total water molar fraction range.[97]

This result strongly suggests three inferences: first, that cations experience some form of association (with increasing amount of water); second, the cation size is unaffected by water addition; and finally, the anion size undergoes a dramatic drop, beginning at approximately 10 % water molar fraction, which is the water molar fraction that we have determined as the ion-pair formation peak.[87]

In any case, comparing with the hydrodynamic radius estimation obtained in this work, represented in Figure 24, the two results appear to be quiet distinct. While in this work are obtained progressive decreasing of the two ion species hydrodynamic radius, in the reference study is verified that the cation presents no hydrodynamic radius significant variation. Additionally, the anion hydrodynamic radius, in the reference study, presents a much more pronounced decrease in the 20 to 40 % water molar fraction range than our results. Considering these results, two hypotheses arise: one is the defective approach employed in the reference study; and the second is the unexpected dioxane hydrodynamic radius variation, which may be influencing the two species hydrodynamic radius relation results. Nevertheless, our results are in much agreement with several literatures that propose, at least, cation aggregation manifestations.

Globally, these first results reflect the known behavior of the two ionic species that compose these imidazolium-based ionic liquids. Initially, in neat, the cationic specie presents higher diffusion coefficient, which is inverted with the addition of water and consequent lowering of the solution viscosity, fact that present higher influence in the anion diffusion coefficient.[87] Although normally

cations present higher self-diffusion values than their smaller anion pairs in neat, it has been already shown that this is not a universal phenomenon for all ionic liquids.[75] In practice, the relative diffusivity of the cation and anion of ionic liquids seems to be determined both by the ionic size and the shape, i.e. the nature of the ions themselves influences the relationship between cation and anion self-diffusivities.[74,75] Apparently the imidazolium-based cations are favored in terms of self-diffusion by the structural planar shape. It is also known that increasing the alkyl chain length serves to hinder cation diffusion in these systems reducing its diffusion coefficients.[75] With the increasing amount of water the opposite ionic species begin to separate themselves from each other, i.e. increases the distance between ions in solution, and thereafter, naturally, the self-diffusion coefficient becomes being governed by molecular size, which favors the self-diffusion rates of the smaller anionic species.

Considering the objective of this work, which is the study of ion-pairing dynamics, after the analysis of the diffusional studies executed for increasing water content, it is possible to define three compositions in which ion-pairs present for sure different dynamics: first, the neat situation, where due to the exclusive existence of ions in solutions it is believed in the existence of a complex aggregation-clustering disposition of the ion matrix in solution; second, the situation where the closer values for the diffusion coefficients of both ion species (cation and anion) has been found, which we believe that may be the closer of a 1:1 ion-pair situation in solution; and third, the infinite dilution situation, where it is expected, and has been already partial confirmed by the previous diffusion results, that the ion species present a free-motional behaviour in solution which prevents the spatial close relation expected in a lasting ion-pair in solution.

2.3.1.2 – Translational Temperature Dependence

Another widely employed method to characterize physicochemical properties and molecular dynamics in ionic liquids is the variation of diffusion upon temperature.[73–75,92,99,100] Making use of one of the technical possibilities of the NMR instrumentation, in this study, for the same water molar fraction value sample, the temperature is changed, and for defined values in a specific range (273 - 353 K) DOSY experiments are executed and treated in the same way as has been explained in the beginning of this chapter.

As it has been referred before in this discussion three interesting compositions were identified to explore the ion-pairing dynamics of BMIM-BF_4. Those were defined as: neat, for pure ionic liquid sample; ion-pair, for the solution that presented closer values of diffusion coefficients for both ion species; and infinite dilution, for the solution with higher water molar fraction (93%).

In this sub-division of this discussion, the diffusion data of each composition will be presented and discussed individually in sequential sub-sections for better clarification.

2.3.1.2.1 – IL in Neat Composition

Variable temperature diffusion measurements using BMIM-BF_4[74] have been reported before. Nevertheless in this work due to the context of the study of ion-pair dynamics it is justified to repeat the studies in the already mentioned compositions, and compared them with the previous literature results.

The variation of the diffusion coefficients versus temperature is represented in Figure 27. In contrast to the results for diffusion versus water molar fraction, the temperature dependence for the neat ionic liquid presents a strictly exponential behavior. In this case also the diffusion coefficients of both ion species ($BMIM^+$ and BF_4^-) present a very similar progression, from 273 K to 353 K. Nevertheless, it is verified again that at a certain point there is a crossing point in the diffusion of the cation and anion (343 K), where BF_4^- associated with the lower diffusion coefficient overtakes $BMIM^+$. Differently to the previously reported results, the moment determined by us for the overtaking by the anionic diffusion coefficient is at 343 K and for the previous publication it happens at 353 K.[74] One conclusion that can be taken from the results so far is that the addition of water has much more dramatic effect on differentiating the cationic and anionic diffusion coefficients in solution than temperature.

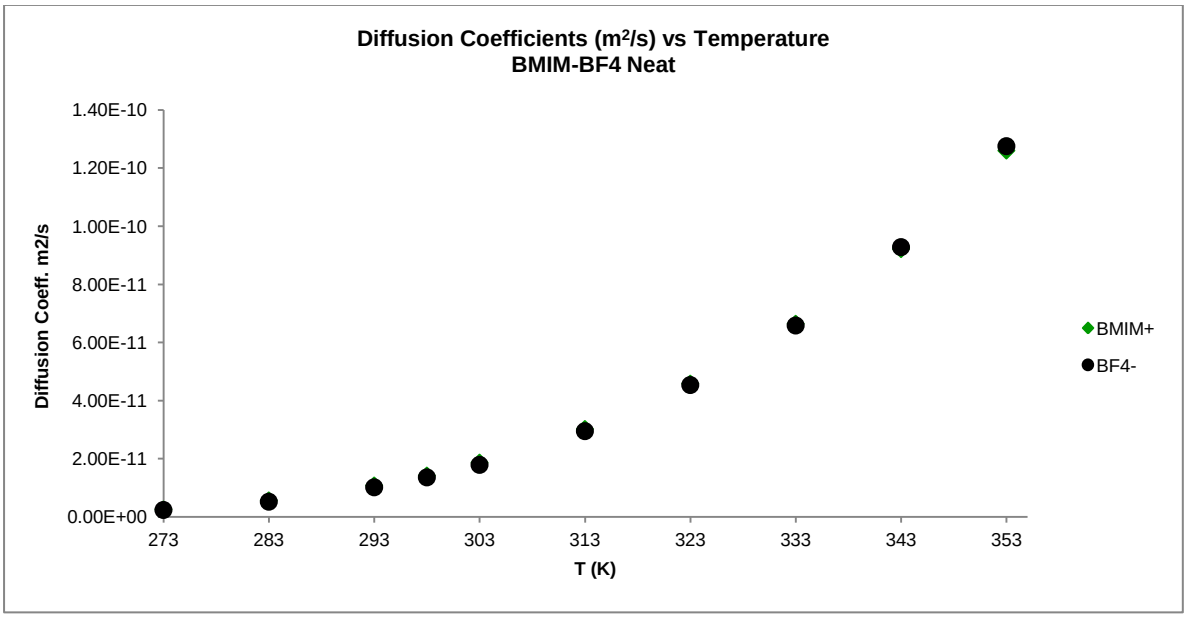

Figure 27 - [BMIM][BF_4] neat diffusion coefficient values for the temperature variation range from 273 to 353 K, exhibiting the exponential progression of the two species diffusion with increasing temperature.

It has been show previously for BMIM-BF_4,[74] that the dependence of diffusion and viscosity on temperature is linear. This indicates that the ionic diffusivity in BMIM-BF_4, and globally in ionic liquids, basically obeys to Stokes-Einstein equation.[74]

Another commonly used parameter to interpret diffusion versus temperature data is the apparent cationic transference number (Figure 28), which consists in the ratio between the diffusion

coefficient of the cationic specie and the summation of the cationic plus the anionic diffusion coefficients (D_{cation} / (D_{cation} + D_{anion})). This result reflects the contribution of the cationic ($BMIM^+$) diffusion for the total diffusion of ionic species in solution ($BMIM^+$ and BF_4^-), and also indicates that the cation is diffusing faster than the anion, as it has been reported in previous publications, even if the anionic specie (BF_4^-) is the one that presents the smaller hydrodynamic radius.[74]

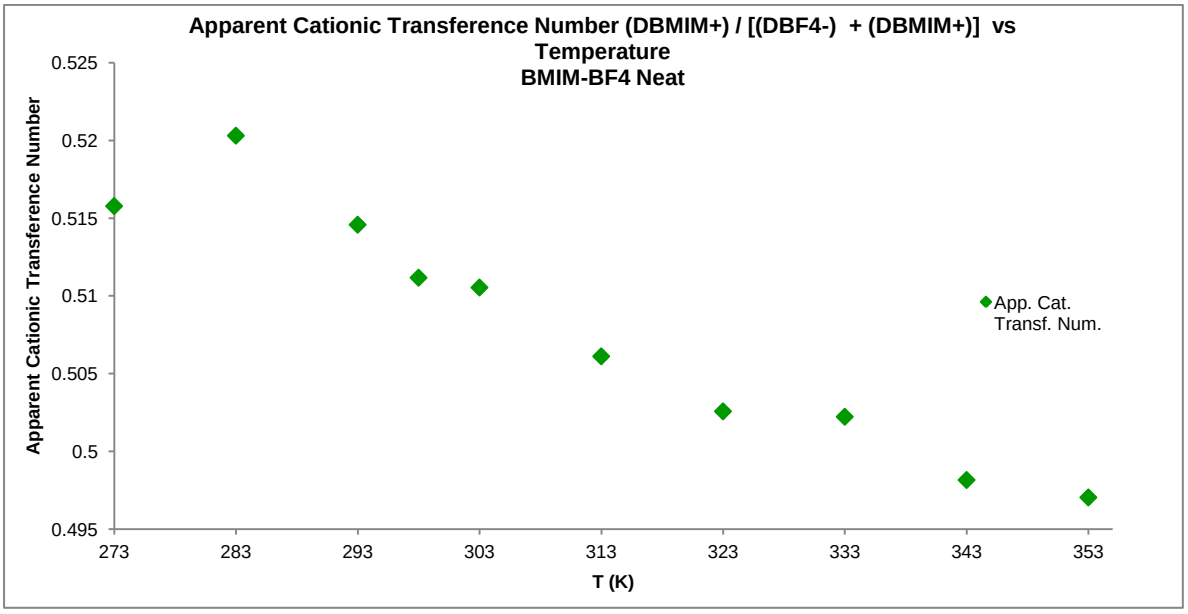

Figure 28 - [BMIM][BF_4] neat apparent cationic transference number values for the temperature variation range from 273 to 353 K, highlighting the progressive decreasing of the cation diffusion coefficient in relation to the total ionic diffusion coefficient (D_{cation} + D_{anion}).

In contrast with the referred previous publication[74], our results show that the apparent cationic transference number doesn't decrease "almost linearly with increasing temperature" (Figure 28), at least during the temperature range studied (273 – 353 K), presenting a progression inversion at 283 K, characterized by a maximum value at this point. This maximum indicates that at 283 K the cation specie in solution experience a "diffusion jump" not accompanied by the anion specie, i.e. the cation specie reacts independently to the counter ion, meaning that the ion-pairs shows no stability at this point.

With this graphical result (Figure 28) is possible to state that the temperature range in which the ion-pair shows better diffusion stability is between 323 K and 333 K, first because of the almost constant value of the apparent cationic transference number, and also because of the apparent transference number value approximately equal to 0.5 (equal diffusion coefficient for both ionic species). This constant level (stage) at which the diffusion coefficients present lasting proximate values may also indicate the possibility of stable ion-pair relation between the two ionic species at certain conditions in the neat sample. In any case the same conclusion is obtained with respect to the evolution of the two species, that there is a relatively higher thermal acceleration of the anionic diffusion compared with the cationic diffusion, meaning that the activation energy for the diffusion of the anionic specie is superior to the cationic specie.

To confirm this suspicion we moved to the calculation of the diffusion activation energies for the two ionic species for its temperature dependence (Figure 29). This simple and meaningful calculation can be executed with the help of the Arrhenius equation, substituting the original rate constant k by the experimental diffusion coefficients D:

$$D = Ae^{\left(\frac{-E_A}{RT}\right)} \quad \textbf{(10)}$$

- R is the universal gas constant in J/(mol.K);
- A is a pre-exponential factor with the same units as the diffusion coefficient, m^2/s.

After this step, in order to achieve a possible linear regression (Figure 29), this expression is converted in its logarithmic form ($\log(D) = \log(A) - E_A/RT$), and then a linear relation is established between the $\log(D)$ and the $1/RT$. Experimentally, the diffusion coefficient values that have been converted in its logarithmic correspondents, are plotted against $-1/RT$ in a graphical representation. The resulting linear regression slope corresponds to the desired activation energy (E_A) in joule per mole (J/mol). The plot obtained for the neat BMIM-BF_4 in the temperature range under study is represented in (Figure 29).

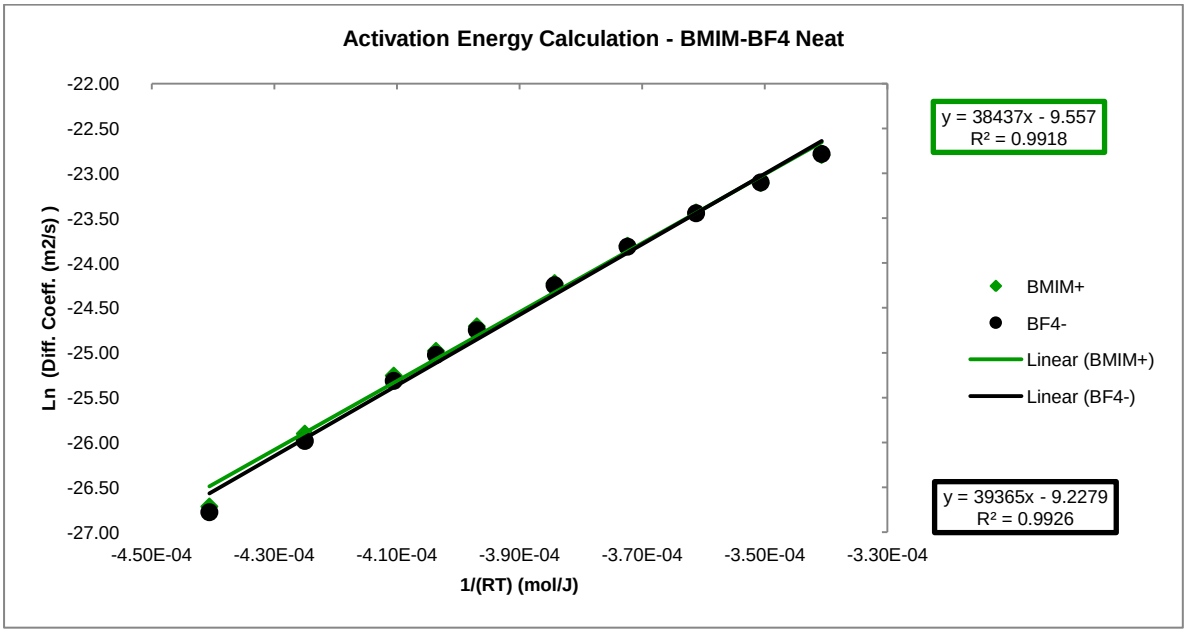

Figure 29 - [BMIM][BF_4] neat activation energy calculation for the temperature variation range from 273 to 353 K, with 38.437 KJ/mol for the cation and 39.365 KJ/mol for the anion (R^2 = 0.9918 for the cation and R^2 = 0.9926 for the anion).

The smaller activation energy is observed for the cation, 38,5 (kJ/mol) while for the anion, as it was expected from the diffusion behavior, a higher value is observed, 39,4 (kJ/mol).

Relatively to the R^2 values of the regression, although they seem quite adequate (R^2_{cation} = 0.9918 and R^2_{anion} = 0.9926) the progression of the graphical points indicate that the Arrhenius equation-based linear regression may not be the more accurate way to describe and calculate

activation energies in ionic liquids, in this case for BMIM-BF_4. This situation will be verified for the following preparations, presenting progressive worst fittings, as it will be seen. However, this question will not be discussed here but will be sent for future works section as a suggestion.

In this study with varying temperature we have also applied similar graphical treatments as those applied in the section for the water composition variation.

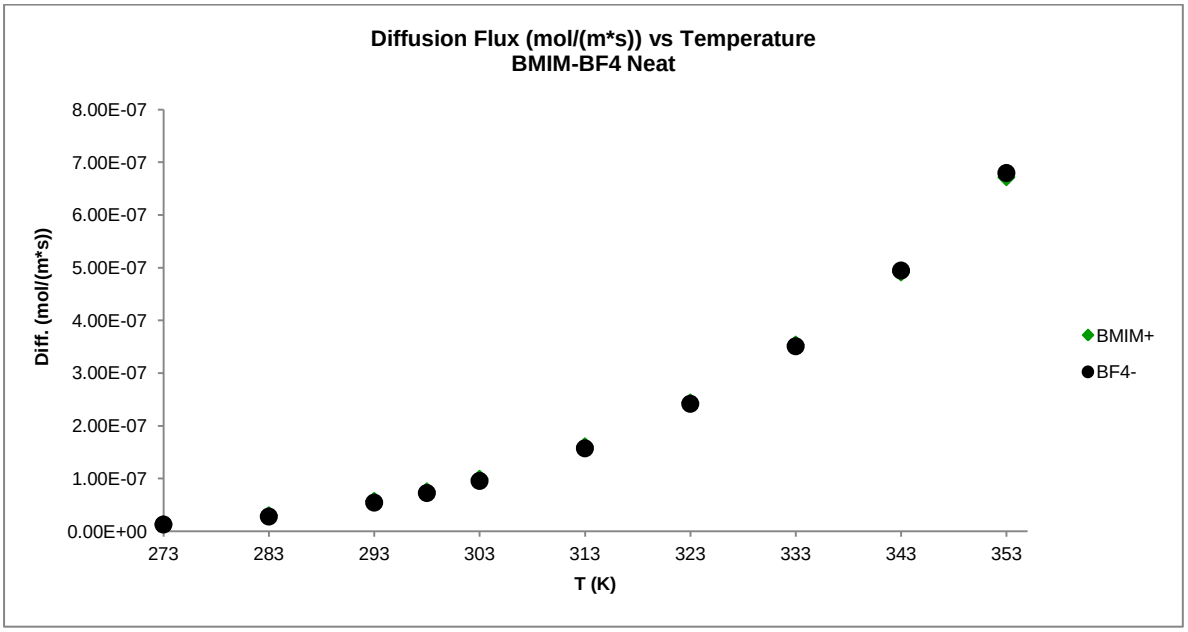

Figure 30 - [BMIM][BF_4] neat diffusion flux values for the temperature variation range from 273 to 353 K, exhibiting, by the graphical similarity to the previously represented figure 23, the same progression as the species diffusion coefficient.

One of those is the neat "diffusion flux" (Figure 30) versus the temperature variation graphical representation. In this graphical representation is possible to observe an exclusively exponential diffusion flux behavior for the two ionic species, equal to the observed in diffusion coefficient behavior (the ratio between the progression slopes of diffusion coefficient and diffusion flux is constant). Through this data is possible to determine that the two ionic species start at 273 K with an approximately $1.3x10^{-8}$ mol per meter.second diffusion flux, and end at 353 K with an approximately $6.75x10^{-7}$ mol per meter.second diffusion flux.

The other graphical result is the neat corrected diffusion versus the temperature variation. As it has been referred before, dioxane has been added intentionally in 1% molar fraction of BMIM-BF_4 with the purpose of providing the ability of measuring the dimensionless corrected diffusion parameter. Differently from the earlier presented corrected diffusion in the water molar fraction variation, in this study the diffusion behavior of the two ionic species of BMIM-BF_4 does not show an increasing mobility relative to dioxane, in accompanying the increasing diffusion coefficient. On the contrary, for the initial temperature ranges, 273 K to 293 K, the diffusion of the two ionic species decrease, in relation to dioxane, from a close diffusion value (with higher diffusion value of the cation) to less than half, which means that dioxane has a lower activation energy for diffusion in this solution.

In the following temperature range the two ionic diffusion values tend to the same value, as it was observed in the diffusion coefficient plot, which represents half of the diffusion coefficient of dioxane.

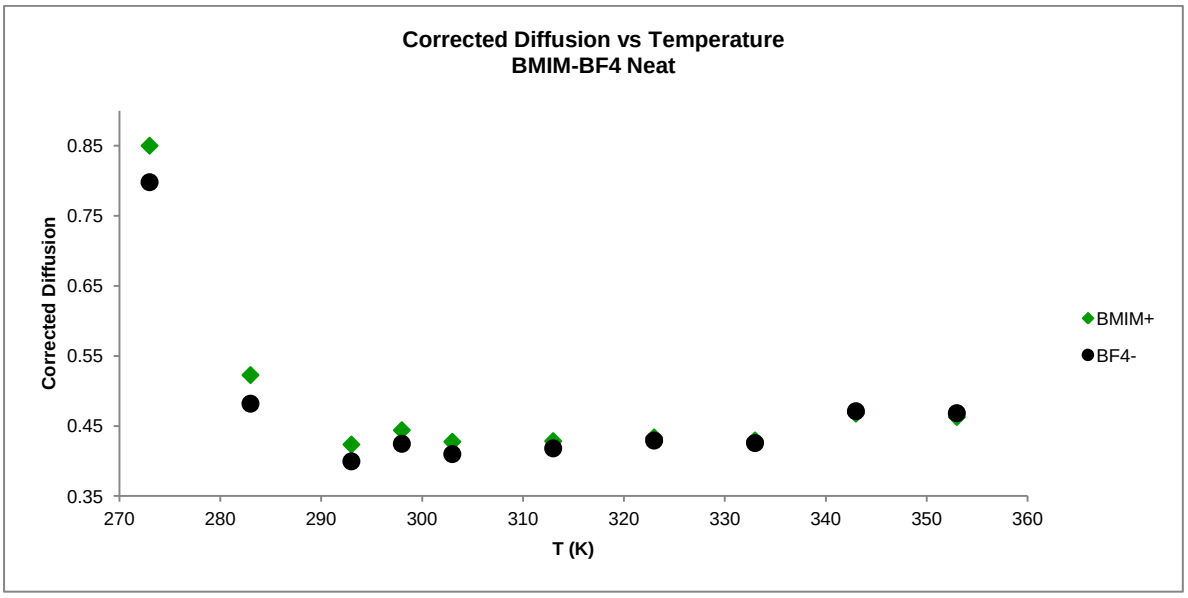

Figure 31 - [BMIM][BF_4] neat corrected diffusion values for the temperature variation range from 273 to 353 K, highlighting the relative diffusional evolution progression of the two ions in relation to the dioxane diffusion evolution and the attachment of the two species diffusion starting at 343 K.

This result (Figure 31) indicates that from 293 K the diffusion of the species appears to be ruled by the solution viscosity, since the two ion species present constant values, differently to what has been verified in the water molar fraction plot (Figure 23). A fundamental characteristic of dioxane that influenced its choice for this temperature variation study was its boiling point (101.1 ºC), which is predictable that does not interfere on results.

The result of the hydrodynamic radius relation of the two ion species with dioxane was again plotted, this time for neat composition.

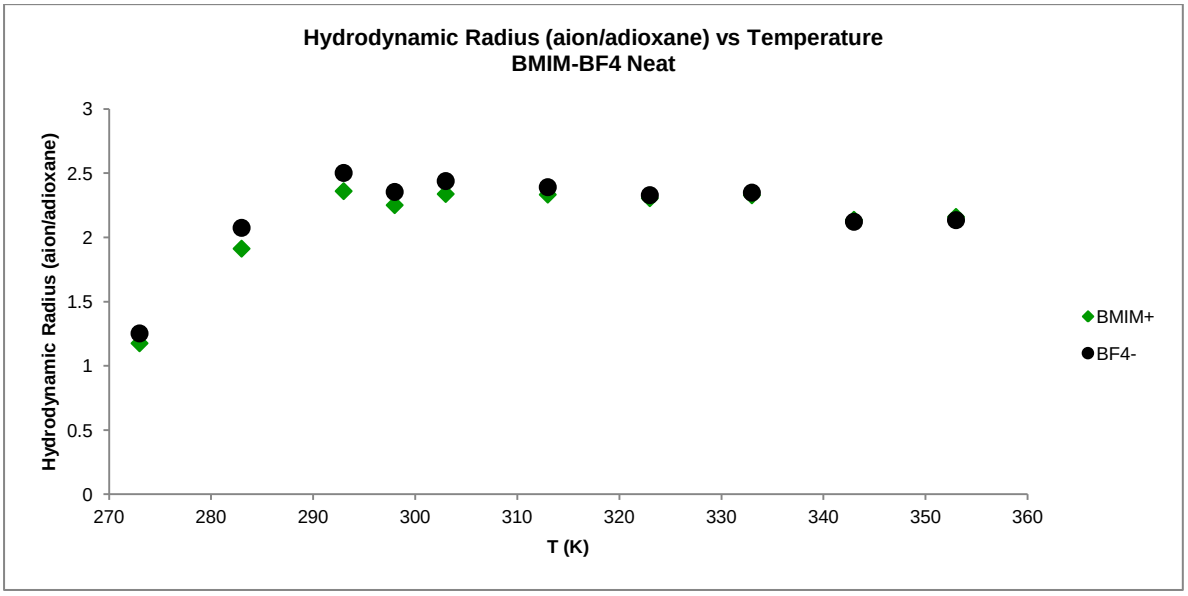

Figure 32 - [BMIM][BF_4] neat hydrodynamic radius ratio (a_{ion} / $a_{dioxane}$) values for the temperature range from 273 to 353 K.

By the plot observation (Figure 32) is determined that both ion species present at 273 K close hydrodynamic radius relation with dioxane (approximately the same value), and that from 273 to 293 K an accentuated value increase of the same is verified, which remains with increasing temperature. The simultaneously hydrodynamic radius increase for the two species may indicate a common aggregation phenomenon. The hydrodynamic radius relation values (both species) of 2.5 suggests the same. Considering that the hydrodynamic radius relation of the cation with dioxane at infinite dilution (composition at which is expected individual ions diffusion and then individual hydrodynamic radius) is 1.5 and the hydrodynamic radius relation of the anion with dioxane at the same composition is 1, the 2.5 value appear to match with the two values summation. The initial (273 K) similitude between ion species and dioxane hydrodynamic radius may be attributed to some kind of dioxane hydrodynamic radius conditioning that is influencing its real value by increasing it.

Globally, the results from neat sample temperature variation study indicates that cationic and anionic species share closely the same diffusion behavior along the measurements performed, with slight differences in terms of extreme temperature conditions (cation with higher diffusion coefficient at 273 K; anion with higher diffusion coefficient at 353 K); the anionic specie presents a higher activation energy for the temperature range studied; and both species present a distinct behavior to the molecular probe dioxane, which indicates a motional heterogeneity within the miscibility of the two substances.

2.3.1.2.2 – IL in Ion-Pair Composition

In the case of the "ion-pair" sample, as it has been referred earlier, this approach consists in studying the temperature dependence of the diffusion coefficients on the previous determined "ion-

pair" composition, which corresponds to the 8 % water molar fraction sample composed by BMIM-BF_4/H_2O/dioxane. The particular characteristic of this sample was the fact that both ionic species in solutions presented the same diffusion coefficient, which in our interpretation could correspond to the sought ion-pair of this IL BMIM-BF_4. However, as was seen before for the neat sample the ions diffusion is temperature dependent and there is way to predict what should be the behavior of the ions diffusion coefficient with temperature for this composition. Seeking this answer and the comprehension of motional physicochemical properties of this specific BMIM-BF_4/water mixture, we moved to perform diffusion measurements that will be presented in this sub-section.

Beginning once again with the plot of the diffusion data for the range of temperatures studied (Figure 33), it is notorious that the two ionic species diffusion values present very close relation during all the range from 273 K to 353 K.

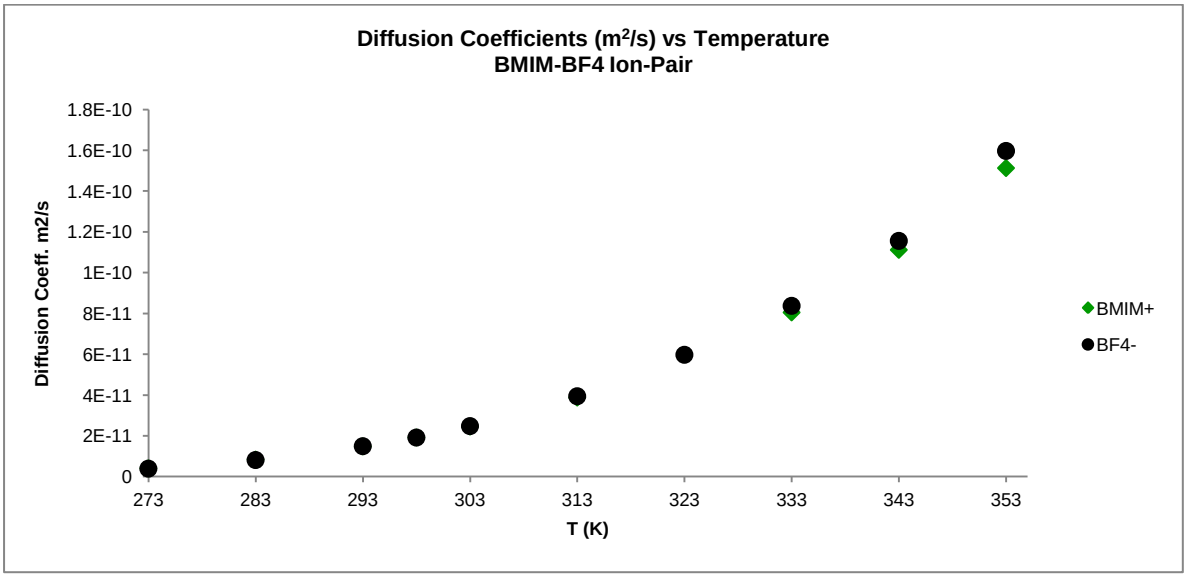

Figure 33 - [BMIM][BF_4] ionic-pair diffusion coefficient values for the temperature variation range from 273 to 353 K, exhibiting the exponential progression of the two species diffusion, higher for the anion, with increasing temperature.

Another treatment that has been applied in the interpretation of the data for the neat IL and that may also be used here is the determination of the apparent cationic transference number. As it has been referred before, this number consists in a diffusion dimensionless parameter that reflects thoroughly the cation diffusion progression relative to the total ionic species diffusion progression (Figure 34).

As seen in Figure 34, the cationic diffusion behavior may be described as progressively downward in relation to the total ionic species diffusion (D_{cation} + D_{anion}), which reflects the previously determined major increasing of anionic diffusion. However, this downward progression evidences an interesting relative minimum at 293 K, which is conjugated with a consequent relative maximum at 298 K that corresponds to the determined ion-pair situation (equal diffusion coefficients for both cation and anion species) from the water molar fraction variation study. By a more dedicated observation it is possible to distinguish three distinct moments: fist, in the range between 273 and 283 K, where there

is an apparent number > 0.5 (higher cationic diffusion); followed by the range between 293 and 313 K, where the apparent number is close to 0.5 (whereas this value is matched at 298 K); and finally the range between 333 and 353 K, where the apparent value is inferior to 0.5 (higher anionic diffusion), presenting the range from 333 – 343 K a constant value of approximately 0.49.

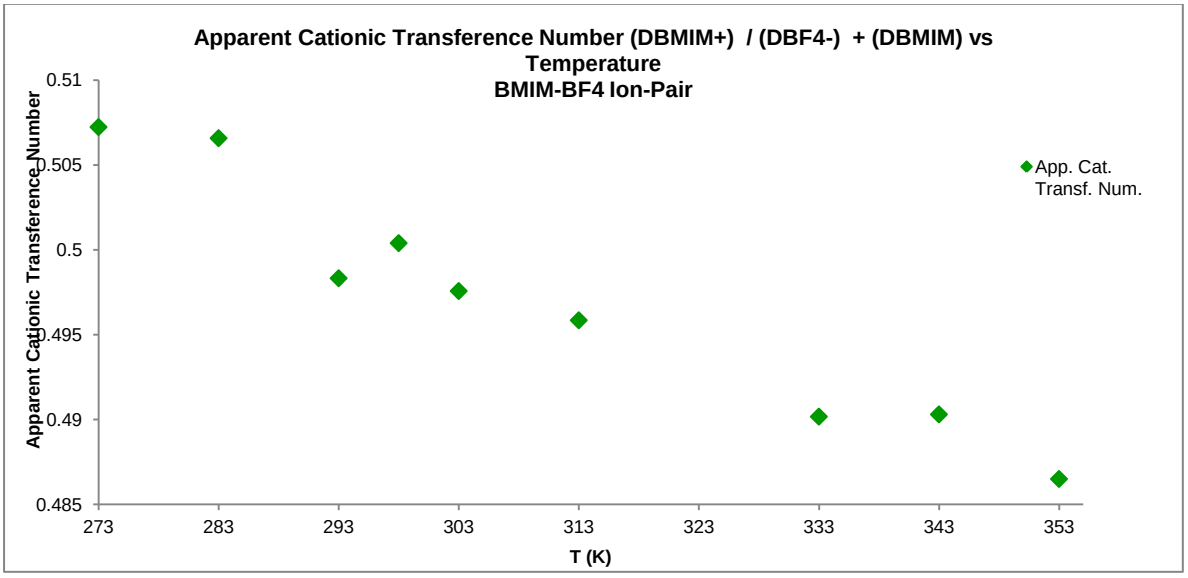

Figure 34 - [BMIM][BF_4] ionic-pair apparent cationic transference number values for the temperature variation range from 273 to 353 K, highlighting the progressive decreasing of the cation diffusion coefficient in relation to the total ionic diffusion coefficient (D_{cation} + D_{anion}) and the relative maximum value at 298 K that may correspond to the ionic-pair formation.

Particularizing now in Figure 34 the interesting presence of a relative minimum at 293 K followed by a relative maximum at 298 K (298 K), it must be referred that this result might be a favorable suggestion of high ion-pair content formation in solution at this point. The reason for this inference is related with two facts: first, because of the subtle inversion in the apparent cationic transference number, i.e. inversion in the progressive detachment between the cationic and the anionic diffusion coefficients; and second, because this inversion converges exactly to the 0.5 apparent cationic transference number, which corresponds to the situation of equal diffusion coefficient of both anion and cation. This conjugation of factors strongly suggests that something at the structural level is making that the initial progression of the anionic diffusion coefficient is being delayed, such that the cationic diffusion coefficient catch it again (note that have to have another apparent cationic transference number equal to 0.5 between 283 and 293 K), expectedly in a different structural organization frame. A possible interpretation is that in this range, a temperature increase of 5 K (293 - 298 K) provides the necessary activation energy for the total disruption of the cationic proposed aggregation structure[98] (hydrophobic cation-cation aggregation), and therefore is favored the ionic interaction, which pulls the cationic diffusion to be synchronized with the one of the anion (same diffusion coefficient), establishing the ion-pair at 298 K.

Following the same procedure presented for the neat solution, the activation energy has been calculated by the Arrhenius modified equation (Figure 35). Confirming what has been said above, in the range of temperatures considered (273 to 353 K) the activation energies for the two ionic species

present a small difference between them, with higher value for the anionic specie (Figure 35). The values of 35.5 kJ/mol for the cation and 36.4 kJ/mol for the anion in conjugation with the graphical observation reflects, as expected, the divergence of the diffusion values of the two ionic species at the higher temperatures in the chosen temperature range, oppositely to what has been verified for the neat solution (where the divergence happens at lower temperatures). This diffusion divergence at higher temperatures might be the reason for such activation energy difference that is comparable to the energy difference verified for the neat solution (aprox. 1 kJ/mol). Nevertheless, the lower activation energy values obtained for ion-pair composition when compared to the neat composition, indicates the relative easier diffusion effort of the two ion species in the ion-pair composition. We find this activation energy difference between the two ionic species higher than was expected for the ion-pair solution. Yet, this result might not be representative due to the large temperature range.

Another problematic procedure question is the earlier verified (for neat solution) not accurate linear regression, despite the high R^2 values of 0.9944 for the cation and 0.9943 for the anion, which might be a negative influence to the establishment of objective activation energy values for the two ionic species in this solution.

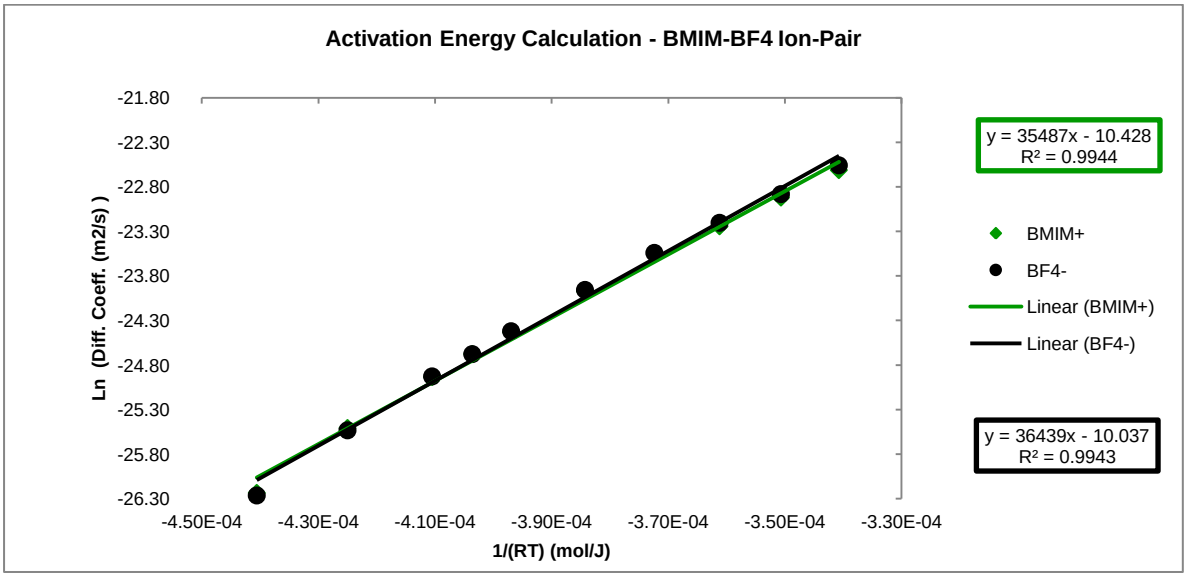

Figure 35 - [BMIM][BF_4] ionic-pair activation energy calculation for the temperature variation range from 273 to 353 K, with 35.487 KJ/mol for the cation and 36.439 KJ/mol for the anion (R^2 = 0.9944 for the cation and R^2 = 0.9943 for the anion).

The diffusion flux was also determined for this "ion-pair" solution and the plot versus temperature is represented in Figure 35.

As it was predictable this diffusion flux follows an exponential progression just like the diffusion coefficient progression. Through this data is possible to determine that the two ionic species start at 273 K with an approximately 2.1×10^{-8} mol per meter.second diffusion flux, and end at 353 K with an approximately 8.2×10^{-7} mol per meter.second diffusion flux, which in comparison with previous neat results shows very poor diffusion flux increase that reflects the similitude of the global solution compositions and diffusion dynamics.

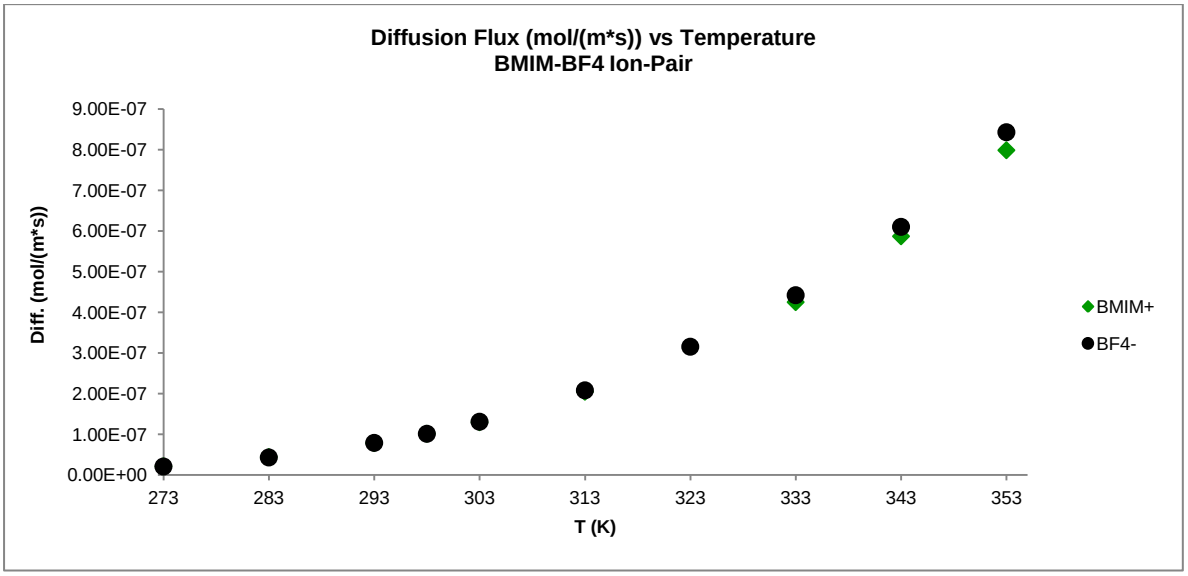

Figure 36 - [BMIM][BF_4] ionic-pair diffusion flux values for the temperature variation range from 273 to 353 K, exhibiting, by the graphical similarity to the previously represented figure 28, the same progression as the species diffusion coefficient.

From the observation of the plot of the corrected diffusion (Figure 37), it is possible to determine and compare significant information. From Figure 37 it is observed that from 273 to 293 K there is an initial pronounced decrease of the two ions diffusion coefficient with respect to that of dioxane, this had already been verified for the neat IL in a very similar way. This decrease is more accentuated for the anion diffusion, which had superior value. Contrary to the corrected diffusion data for the neat solution, in this case the cation and anion diffusion come together, with respect to the dioxane, at 293 K and remain close until 303 K. After this period the two ionic species begin a soft increasing process, in which the anion presents superior positive slope, from 313 to 353 K. With this initial increase and final decrease behavior the result is a subtle minimum, which may give relevant information and corroborate the "ion-pair" hypothesis.

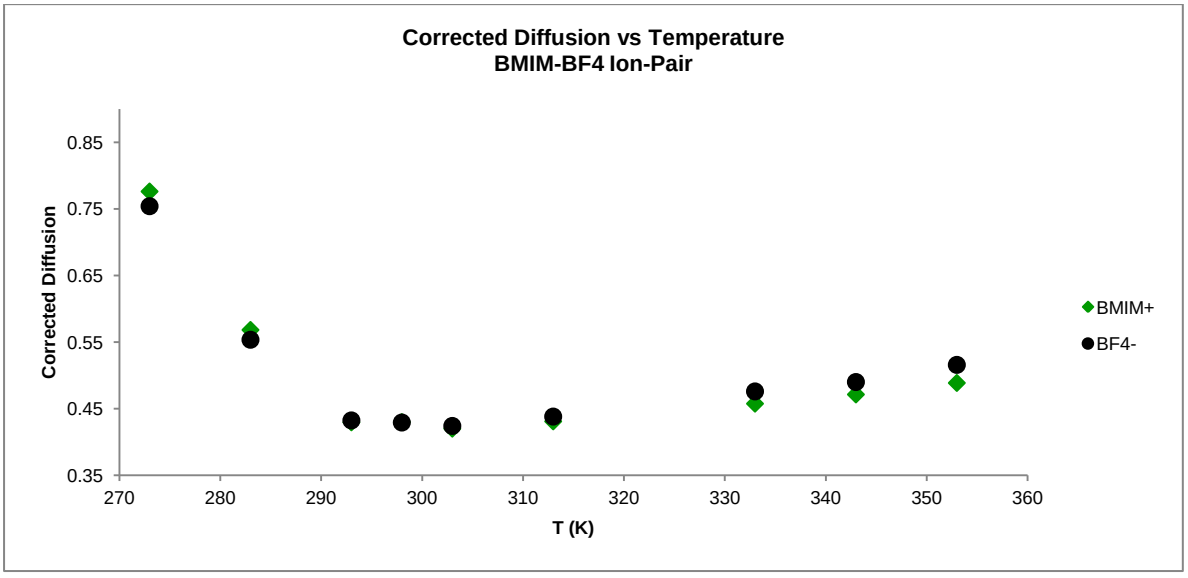

Figure 37 - [BMIM][BF_4] ionic-pair corrected diffusion values for the temperature variation range from 273 to 353 K, highlighting the relative diffusional evolution progression of the two ions in relation to the dioxane diffusion evolution and the attachment of the two species diffusion during the temperature range from 293 to 303 K.

The initial decrease of the ions diffusion coefficients, with respect to the dioxane, with increasing temperature (273 to 293 K), as was seen for the neat solution (Figure 31), may be interpreted as the beginning of the disruption of the already referred IL-cluster aggregates[98], where the cation show higher diffusion. With the continuing increase of temperature (293 to 303 K) it is proposed that the two ionic species presents some oscillations supposedly due to the ion-pair formation as has been referred above in the apparent cationic transference number discussion (Figure 34), which corresponds to the constant period in Figure 37 (that includes the minimum value). The positive slope section (313 to 353 K) of Figure 37 corresponds to an increase in the free-motion dynamics of the two ions, which due to the differences in the activation energy for the individual ion diffusion motion will slowly increase its independent diffusion process. Summing up, this result is significant to understand what is happening with the diffusion of the three water miscible participants, and consequently to the organizational dynamics, in this 8 % water molar fraction solution within the temperature range from 273 to 353 K.

Considering now the hydrodynamic radius plot (Figure 38) it is observed the previous (Figure 37) inverted relation.

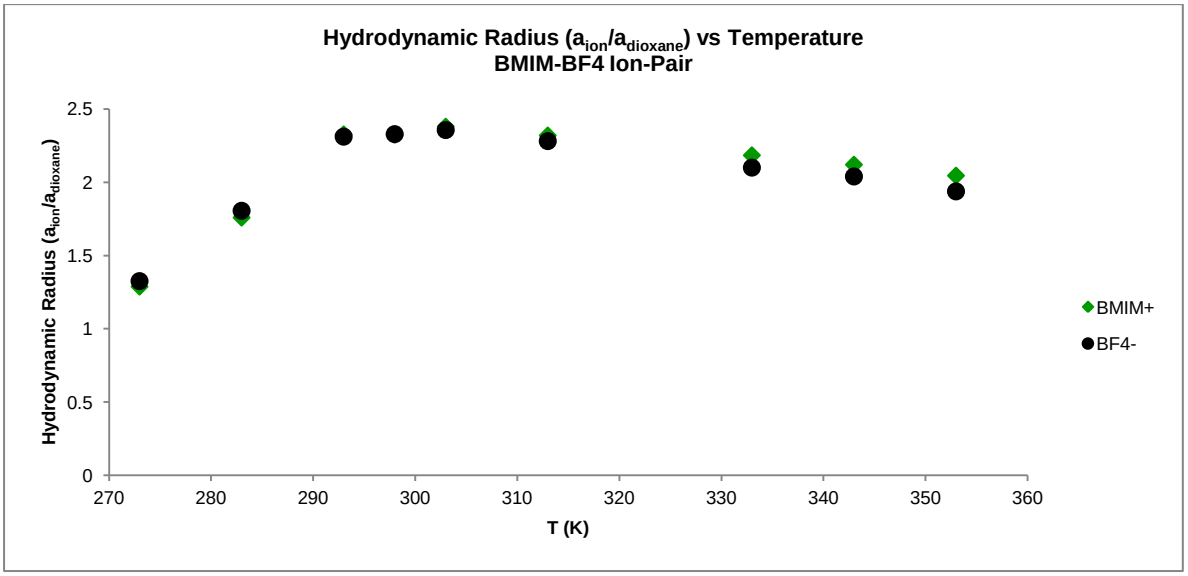

Figure 38 - [BMIM][BF_4] ion-pair hydrodynamic radius ratio (a_{ion} / $a_{dioxane}$) values for the temperature range from 273 to 353 K.

Comparing the hydrodynamic radius results of ion-pair (Figure 38) and neat (Figure 32) compositions, it is possible to establish a relationship. In both results are verified an initial hydrodynamic radius values increase from 273 to 293 K, which leads to a 2.5 hydrodynamic radius value for both ion species. As previously referred, this value matches the hydrodynamic radius summation of the two ion species in relation to the dioxane hydrodynamic radius. Differently from the neat composition (Figure 32), the two ions hydrodynamic radius relation values decrease at higher temperatures may indicate some kind of aggregation disruption not verified in the first (Figure 32). The more accentuated decrease of the anion hydrodynamic radius in this plot is in accordance to the same behavior verified in the water molar fraction plot (Figure 24). As verified in neat composition (Figure 32) the initial (273 K) similitude between ion species and dioxane hydrodynamic radius may be attributed to some kind of dioxane hydrodynamic radius conditioning that is influencing its real value by increasing it.

Globally, the results obtained for this sample from this study with temperature indicate that cationic and anionic species experience the three possible organizational structural stages, which are: for low temperatures, the stage of IL-cluster aggregates and its disruption; for intermediate temperatures a stage where the two ionic species share the same diffusion coefficient, which is believed to be the ion-pair period; and for high temperatures, the stage where the two ionic species begin to diffuse independently and progressively faster. These three stages are proposed in comparison, and contrast, to the behavior observed for neat solution, since in neat solution in the temperature range studied it is believed that only the initial stage of IL-cluster existence is observed, and the beginning of the second, namely with the anion overcoming the cation in diffusion coefficient. In this way, it is possible that we have found interesting organizational dynamics with this combined concentration/temperature variation study, which must be complemented with more information from other techniques.

2.3.1.2.3 – IL in Infinite Dilution Composition

At last, the previous discussed experiments for neat and "ion-pair" compositions have also been applied to the infinite dilution solution. This composition presents the opposite extreme of motional dynamics comparing with the neat IL, since neat sample supposes no water existence, and infinite dilution sample supposes almost exclusive water existence. Comparing these two systems studied in the same temperature range, is expectable to allow detecting and understanding the possible extreme motional dynamics that BMIM-BF_4 can present due to concentration and temperature variation. In the context of the main purpose of this study, which is the determination and evaluation of ion-pair formation, the comparison of the data for this sample with the one of the "ion-pair" composition will allow to corroborate or contradict any idea previously discussed. In any case it will provide additional information for the comprehension of ILs behavior in different media conditions.

The expected results for this system motional behavior were that: the two ionic species would present much higher diffusion coefficient values, since the solution viscosity has qualitatively decreased substantially; the anionic diffusion would present higher diffusion values for all the temperature range, since it is expected that this system, particularly (in contrast to the neat and ion-pair solutions where the cation starts diffusing faster), follows the Stokes-Einstein determination and then, because of the smaller size of the anionic specie it diffuses faster; the diffusion flux would follow the same behavior of diffusion coefficients, since there is no expected concentration variation; and finally, the corrected diffusion would exhibit an approximately constant behavior for the two species.

In accordance with the previous stated expectations, by the observation of the plot of the diffusion coefficients versus temperature in Figure 39, it is possible to verify that the two ionic species present diffusion coefficient values one order of magnitude (x10) higher than those measured for the ion-pair and neat samples, confirming that even at low temperatures (273 K and 283 K) the diffusion of the two species is comparable to the diffusion values measured for the higher temperatures (343 K and 353 K) of the other compositions. In terms of the previously referred stages, this indicates that, even for low temperatures, at infinite dilution composition the two ionic species begin to diffuse independently and progressively faster. It is also possible to verify that although almost similar at to the cation at lower temperature, the anionic specie presents higher diffusion coefficient values in all the temperature range studied. In any case the initial small difference must be discussed, so, in this way, the hypothesis that this data may suggest at first sight is that for low temperatures the electrostatic interactions (ionic interactions) reveal to be more significant than what was expected. Thus, the diffusion coefficients of the two ionic species start from an approximate value and progressively increase, with different progression slopes (higher for the anion), almost in a linear way during the temperature range from 273 to 343 K. From 343 to 353 K the diffusion coefficients of the two species seem to reach the limit of increasing progression.

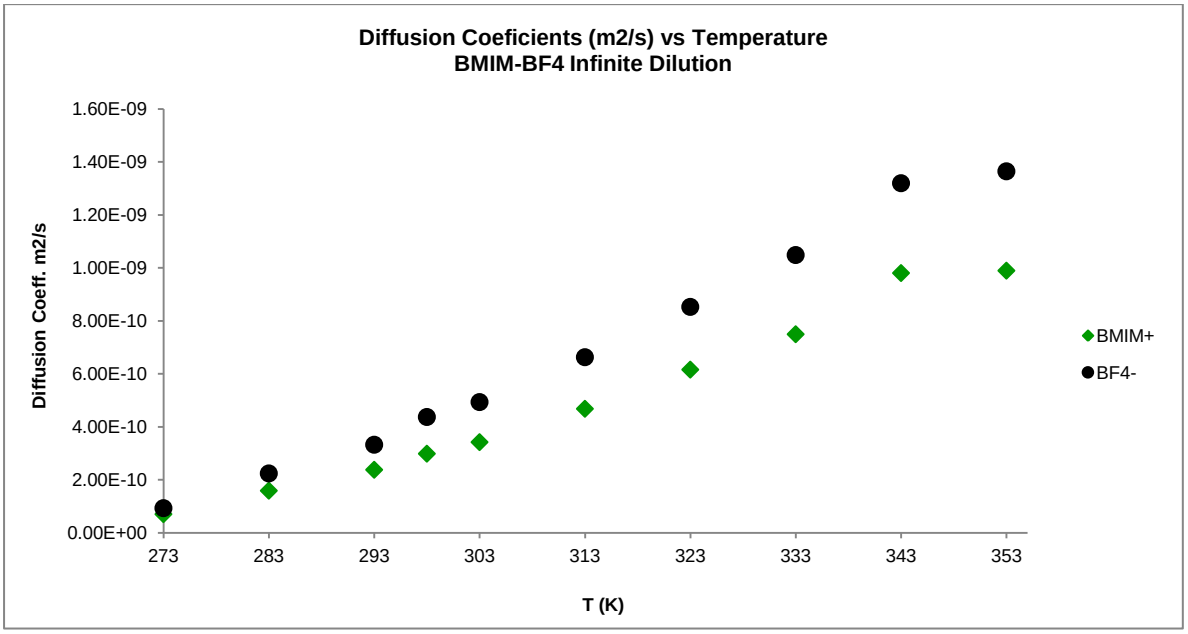

Figure 39 - [BMIM][BF_4] infinite dilution diffusion coefficient values for the temperature variation range from 273 to 353 K, exhibiting the almost linear progression, from 273 to 343, of the two species diffusion, higher for the anion, with increasing temperature.

The apparent cationic transference number is again used in this infinite dilution solution (Figure 40). Two initial indications may be inferred from a first appreciation of the graphical data, which are: first that the anionic diffusion is superior to the cationic diffusion during the temperature range studied; and second that the progression of cationic and anionic diffusion along the temperature range is full of small fluctuations, even knowing that the apparent number only oscillates between 0.43 and 0.405 approximately. Subtly, what may be denoted in this apparent cationic number evolution is that: initially it decreases from 273 to 298 K, because of the anionic faster diffusion increasing derived from the breaking of the electrostatic interactions and the anion smaller size; from 298 to 323 K the apparent cationic number increase probably due to diffusion activation energy cross, which may be related with cationic organizational modifications; and finally it is observed a sinusoidal constant behavior around 0.42, probably due to anionic and cationic structural fluctuations.

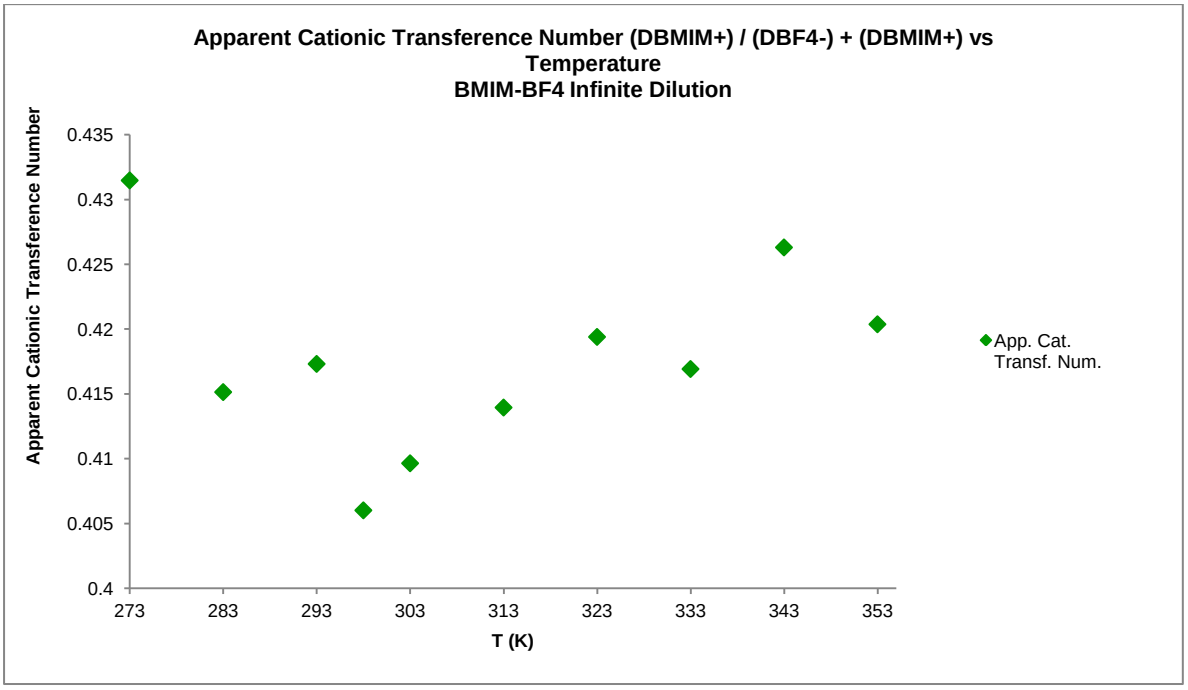

Figure 40 - [BMIM][BF_4] infinite dilution apparent cationic transference number values for the temperature variation range from 273 to 353 K, highlighting the oscillating progression of the cation diffusion coefficient in relation to the total ionic diffusion coefficient (D_{cation} + D_{anion}).

The activation energy for diffusion has been calculated the same way as for neat and ion-pair solution compositions. The values obtained reflect quite well what was expected and the difference to the other two compositions (neat and ion-pair), since the similar values of 25.4 kJ/mol for the cation and 25.3 kJ/mol for the anion represent a fall of 10 000 J/mol in comparison to the diffusion activation energy verified in ion-pair solution. In any case, the R^2 factors begin to reflect very poor correlation, 0.96 for the cation linear regression and 0.9486 for the anion linear regression, particularly for the extreme temperature values of diffusion, and therefore this value is not valuable as it could. Anyway, the similar values of activation energy reflect the low viscosity of the solution in study.

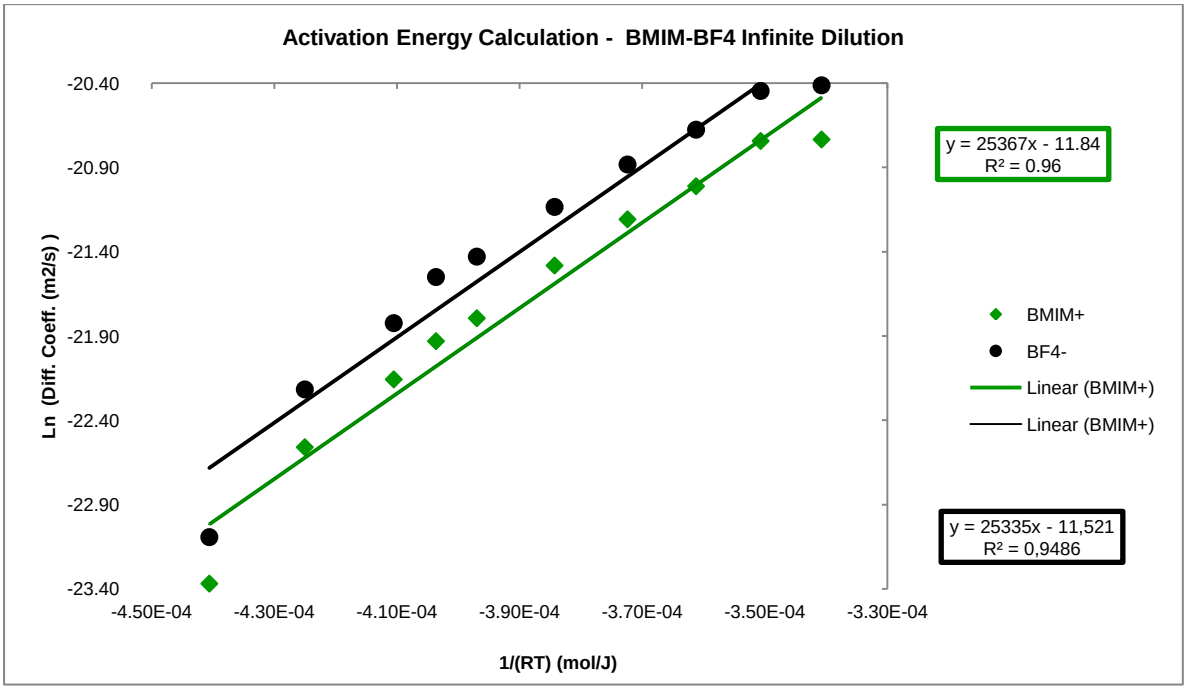

Figure 41 - [BMIM][BF_4] infinite dilution activation energy calculation for the temperature variation range from 273 to 353 K, with 25.367 KJ/mol for the cation and 25.335 KJ/mol for the anion (R^2 = 0.96 for the cation and R^2 = 0.9486 for the anion).

Regarding the diffusion flux data, an equal graphical representation and order jump (10 times) is verified in relation to the diffusion coefficients data (Figure 39).

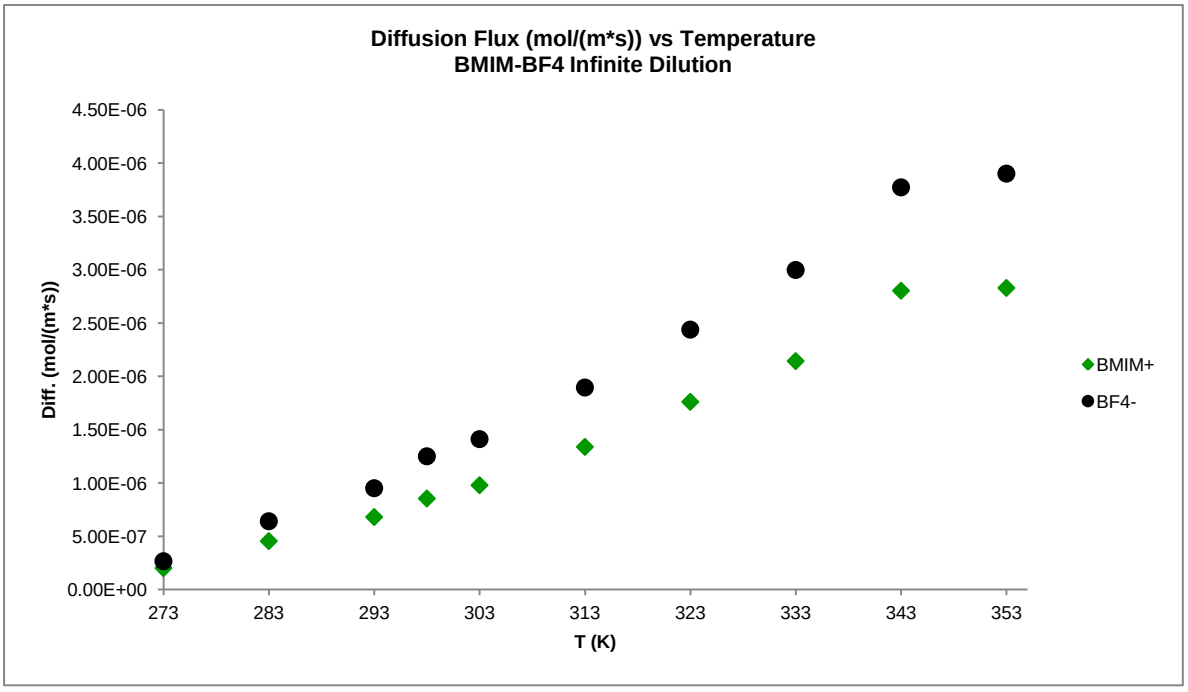

Figure 42 - [BMIM][BF_4] infinite dilution diffusion flux values for the temperature variation range from 273 to 353 K, exhibiting, by the graphical similarity to the previously represented figure 33, the same progression as the species diffusion coefficient.

Regarding the corrected diffusion data below (Figure 43), is also partially confirmed the expectations stated before. It is said partially because besides the approximately constant profile of the two species diffusion from 298 to 353 K, it is verified that initially, from 273 to 298 K, occurs a progressive increment of corrected diffusion of the two species, with different rates. This progressive increment of the two ionic species may be justified by the existence of an initial interaction (electrostatic interaction) that is delaying the diffusion progression of the two ionic species with respect to the dioxane progression.

The higher progression of the anionic specie, that almost reaches the diffusion value of the dioxane, is consequence of its smaller size (similar to the dioxane).

The observable convergence of the two ionic species corrected diffusion values at lower temperatures (below 298 K) proves the lasting of the electrostatic interaction between both even at infinite dilution solutions, and demonstrates the temperature variation effect on it. Contrary to the verified for the apparent cationic transference number (Figure 40), the fluctuations that occurs simultaneously and with equal profile for the two ionic species, must be related with dioxane diffusion variations instead of ionic specie ones.

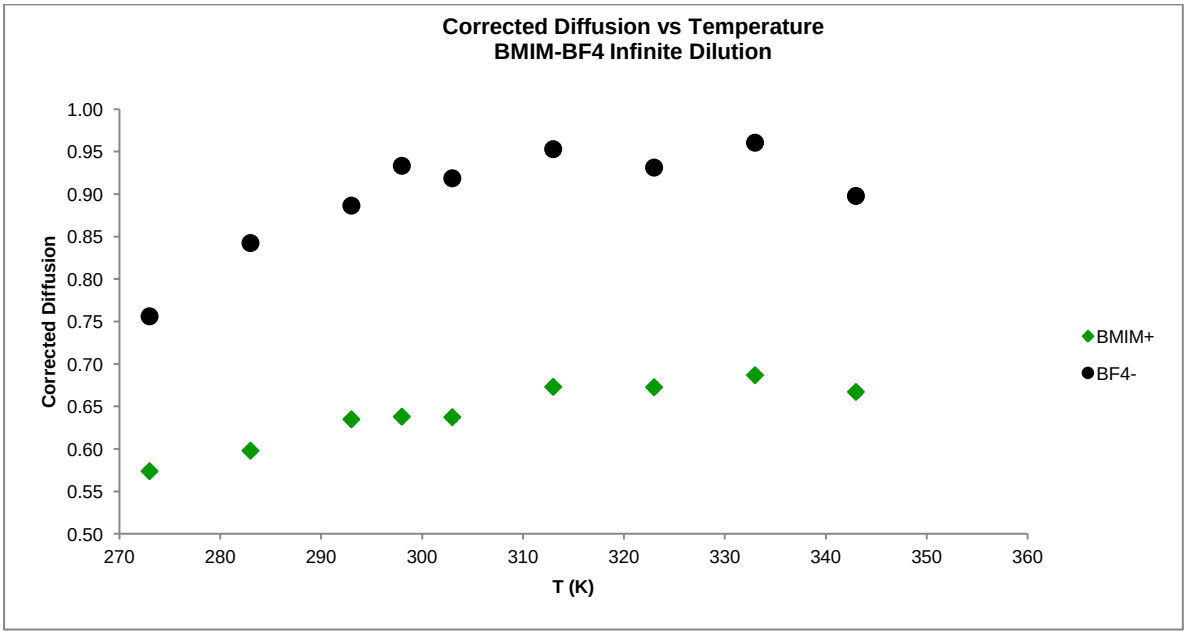

Figure 43 - [BMIM][BF_4] infinite dilution corrected diffusion values for the temperature variation range from 273 to 353 K, highlighting the relative diffusional evolution progression of the two ions in relation to the dioxane diffusion evolution and the free-motion regime of the two species.

Considering now in Figure 44 the hydrodynamic radius plot with temperature for the infinite dilution composition, is primarily possible to observe an almost constant profile. This result indicates that differently to the other compositions (Figure 26 and Figure 32), the hydrodynamic radius of the two ion species in this composition does not present much variation (0.2 over the temperature range for the two species), as it was previously expected. Such value of hydrodynamic radius is compatible with the suggested free-motional regime of the two ions. Additionally, the hydrodynamic radius

relation verified probably establish the real relation between the individual ions and the dioxane, giving as expected a similar hydrodynamic radius for the anion and the dioxane (value of approximately 1), and a value of approximately 1.5 for the cation hydrodynamic radius relation with dioxane (Figure 44).

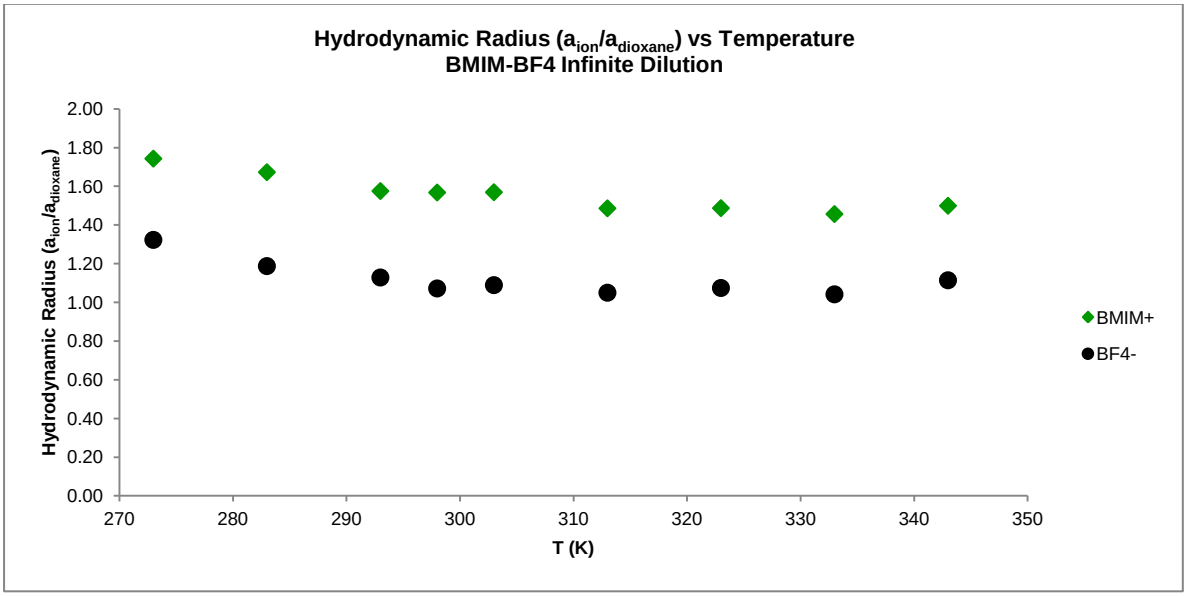

Figure 44 - [BMIM][BF_4] infinite dilution hydrodynamic radius ratio (a_{ion} / $a_{dioxane}$) values for the temperature range from 273 to 353 K.

Globally, with these results it is determined that at the infinite dilution composition we can only detect the diffusion of separate ionic species. The expectations are globally confirmed, with the interesting lasting of the believed electrostatic interactions with relative significance at lower temperatures. The Stokes-Einstein equation is applicable, since the diffusion data reveals the influence of size in the expression of lower diffusion of the cation, in contrast to the neat and half of the ion-pair compositions. The confirmation of the electrostatic interaction influence in the two ionic species diffusion is very important for the purpose of this study, which is the study of ion-pair dynamics in BMIM-BF_4, because it proves the reliability of all the data discussed until this moment.

2.3.2 – Rotational Dynamics - BMIM-BF_4

The study of the rotational dynamics was performed with the purpose of exploring the relation between the two kinds of dynamics and, eventually, the probing of possible ion-pair formation manifestation on rotation, as has been verified for diffusion. The possibility of studying rotational dynamics by NMR arises from the fact that the reorientation of spins in the presence of moderate magnetic fields provides rotational information through nuclear relaxation mechanisms, which may be quantified by several techniques, as has been introduced before in this chapter.

In this section will be discussed the results obtained from inversion-recovery (ir), spin-echo (se), inverse gated (ig) and power gated (pg) ^{13}C NMR techniques versus temperature variation, which together allowed the calculation of several correlation time τ_c values by an iterative process[84] for all BMIM-BF_4 carbons of the cation $BMIM^+$. This parameter gives direct insight on molecular rotational motion, and specifically segmental rotational motion (individual carbons correlation time). The results will be presented as tables and graphical representations of different parameters versus temperature, encompassing all the information resulting from the iterative process realized. Although this consists in the first study for BMIM-BF_4, there have been publications on a similar IL (BMIM-PF_6)[83,101], for neat conditions, which will be used for data comparison.

In contrast to the diffusion study where the two ionic species were considered as one entity each, in this rotational dynamics study there is the possibility, as has been said above, of segmental calculation of individual correlation times for the different carbons for $BMIM^+$. For this reason the cationic structure is presented below (Figure 45) with the numbering used to identify the carbon atoms used in the following discussion.

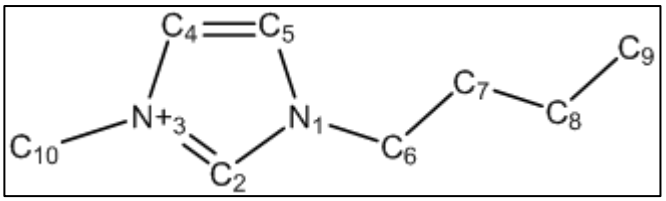

Figure 45 - $[BMIM]^+$ structure and numbering of the ion atoms.

2.3.2.1 – Methodology for τ_c and $R_1^{dipolar}$ calculation

2.3.2.1.1 – Correlation Equations

The correlation equations describe rotational molecular motion and its relationship with intra-molecular events. Dipolar relaxation can be directly related to rotational motion with the use of spherical harmonic functions. Solution of the resulting autocorrelation functions produces spectral density functions, assuming exponential decay. The spectral density equations are correlation time dependent at a set frequency.[4] These equations describe spin-lattice and spin-spin relaxation mechanisms. The algorithm described herein is concerned only with spin-lattice relaxation that is typically determined by inversion-recovery methods.

2.3.2.1.2 – ^{13}C NMR Relaxation Analysis

The relaxation of ^{13}C in medium-sized molecules at moderate magnetic fields is usually caused by dipolar interactions with directly bonded protons. When the relaxation times are measured

under ^{1}H decoupling conditions, the cross-relaxation term vanishes, and the intra-molecular dipolar longitudinal (spin-lattice) relaxation rate ($R_1 = 1 / T_1)_i$ for the relaxation of ^{13}C nucleus i by N_H protons j is connected to the molecular reorientations by:

$$\left[\frac{1}{T_1}\right]_i = \left(\frac{1}{20}\right) N_H \left(2\pi D_{ij}\right)^2 [J(\omega_c - \omega_H) + 3J(\omega_c) + 6J(\omega_c + \omega_H)] \quad \textbf{(11)}$$

- Dipolar coupling constant $D = (\mu_0/4\pi)\gamma_C\,\gamma_H\,(h/2\pi)r_{ij}^{-3}$, μ_0 is the permeability of vacuum, γ_C and γ_H are the gyromagnetic ratios of the ^{13}C and ^{1}H nuclei, respectively, and r_{ij}^{-3} is the length of the internuclear vector between i and j (C-H = 1.09 Å). $J(\omega)$ is the spectral density, with ω_C and ω_H the resonance frequencies of the ^{13}C and ^{1}H nuclei, respectively.

2.3.2.1.3 – Nuclear Overhauser Effect

The nuclear Overhauser (NOE) factor η_i of carbon atom i relaxed by N_H protons j is given by:[102]

$$n_i = \gamma_H \frac{\sum \sigma_{ij}}{[\gamma c \sum(\rho_{ij} + \rho_i^*)]} \quad \textbf{(12)}$$

- $\sum$ includes from j = 1 to N_H, σ_{ij} is the cross-relaxation rate, ρ_{ij} is the dipolar relaxation rate, and ρ_i* is the leakage term that represents the contribution of all other relaxation mechanisms to the relaxation of a ^{13}C nucleus i, thus reducing the NOE factor. Usually, intermolecular dipolar contributions can be neglected for ^{13}C nuclei with directly bonded protons. Under ^{1}H decoupling conditions, the sum of ρ_{ij} over all N_H interacting protons gives the dipolar spin-lattice relaxation rate $R_1^{Dipolar} = 1 / T_1^{Dipolar}$. The relaxation of ^{13}C exclusively via intra-molecular dipolar interaction implies a leakage term ρ_i* = 0. Thus the NOE factor reaches its ,maximum value and depends only on reorientational molecular dynamics:[102]

$$n_{i,max} = \frac{\gamma H[6J(\omega_c + \omega_H) - J(\omega_c - \omega_H)]}{\gamma C[J(\omega_c - \omega_H) + 3J(\omega_c) + 6J(\omega_c + \omega_H)]} \quad \textbf{(13)}$$

2.3.2.1.4 – Spectral Densities

Assuming isotropic tumbling, the spectral densities can be connected to be effective correlation times, τ_c, for reorientation of the corresponding internuclear ^{13}C-^{1}H vectors by:

$$J(\omega) = \frac{2\tau_c}{[1 + (\omega\tau_c)^2]} \quad \textbf{(14)}$$

In theory τ_c is the time required for a molecule (i.e., vector connecting the interacting nuclei) to rotate through an angle of one radian. However, in fact, the correlation time is the integral with respect to time from 0 to ∞ of the normalized autocorrelation function and is actually τ_2, the time constant for the exponential decay of the second-rank Legendre polynomial P_2. In the extreme narrowing case (low viscosity solutions, unlike ionic liquids) the product of $\omega.\tau_c$ is much less than unity and $J(\omega) = 2\tau_c$. Also, $\eta_{i,max}$ becomes a maximum value and is:

$$\eta_{i,max} = \left(\frac{\gamma_H}{\gamma_C}\right)\left(\frac{10_{\tau_c}}{20_{\tau_c}}\right) = 1.988 \quad \textbf{(15)}$$

2.3.2.1.5 – Chemical Shift Anisotropy (CSA)

Aromatic and aliphatic ^{13}C nuclei relax even in moderate magnetic fields partially via the chemical-shift anisotropy (CSA) mechanism. The corresponding longitudinal relaxation rate of ^{13}C nucleus *i* is given by:

$$R_1^{csa} = \left(\frac{1}{15}\right)\gamma_C^2 H_0^2 (\Delta\sigma_i)^2 \left[1 + \left(\frac{\eta_{csa}^2}{3}\right)\right] J(\omega_c) \quad \textbf{(16)}$$

- With the magnetic field strength H_0, the chemical shift anisotropy $\Delta\sigma$ for an axially symmetric chemical shift tensor, and the asymmetry parameter η_{CSA}. The [1 + η_{CSA}^2 / 3] term usually represents a correction factor of less than 5% and is therefore ignored.

2.3.2.1.6 – Stepwise Solution of the Combined Dipolar and NOE Equations

The basic assumption in this analysis is that the maximum value of the ^{13}C NOE is determined by the dipolar rotational correlation time obtained from the measured relaxation rate. It is also assumed that dipolar relaxation and chemical shift anisotropy make up the overall relaxation rate:

$$R_1^{total} = R_1^{Dipolar} + R_1^{CSA} \quad \textbf{(17)}$$

The ^{13}C dipolar and chemical shift anisotropy spin-lattice relaxation rates for those carbons bonded to hydrogen may be obtained by iterations of the following steps 1 through 4, followed by step 5. Although in the original publication the authors have used Mathcad Plus, version 6 professional, in this work these calculations have been executed in Microsoft Office Excel, yielding comparable results.

1. The experimental T_1 values are assumed to be completely dipolar and equation (11) is solved for a pseudo rotational correlation time as follows:

$$\tau_c = \left[\frac{10}{T_1 N_H (2\pi D_{ij})^2}\right] \times \left[\left(\frac{1}{[1+(\omega_c-\omega_H)^2\tau_c^2]}\right) + \left(\frac{3}{[1+\omega_c^2\tau_c^2]}\right) + \left(\frac{6}{[1+(\omega_c+\omega_H)^2\tau_c^2]}\right)\right] \quad \textbf{(18)}$$

In equation (18), values for ω_C, ω_H, N_H, and D_{ij} are known. Experimental values for T_1 are measured. Values of τ_c were calculated by successive approximation steps by setting τ_c on the right-hand side of equation (18) equal to the previously calculated value. The initial value of τ_c was set at 0.01 ns. A constant value of τ_c was obtained after approximately 5 successive steps. However, the value after approximately 40 successive steps was utilized. This result affects the determination of the relative contributions of both the dipolar and chemical shift anisotropy relaxation rates as shown in a later section.

2. Equations (11) and (13) are combined, thus eliminating the term [J (ω_C - ω_H) + 3 J (ω_C) + 6 J (ω_C + ω_H)] from equation (19). The experimental values of T_1 and the pseudo rotational correlation time's τ_c from equation (18) were used in equation (19) to calculate η_{max}. If these values of η_{max} were greater than 1.988, η_{max} was set equal to 1.988, the limiting value established in equation (15).

$$\eta_{max} = N_H \left(\frac{T_1^{DD}}{20}\right)\left(\frac{\gamma_H}{\gamma_C}\right)^2 (2D_{ij})^2 (6J_+ - J_-) \quad \textbf{(19)}$$

- Where J_+ = [2τ_c / [1 + (ω_C + ω_H)^2 τ_c^2]] and J_- = [2τ_c / [1 + (ω_C - ω_H)^2 τ_c^2]] and $T_1^{Dipolar}$ = 1 / $R_1^{Dipolar}$ as defined in equation (11) and (20) below.

3. The η_{max} value is then used to calculate $R_1^{Dipolar}$ from equation (20).

$$R_1^{Dipolar} = \frac{\left(\frac{\eta}{\eta_{max}}\right)}{T_1^{total}} \quad \textbf{(20)}$$

4. $R_1^{Dipolar}$ is used to calculate a new τ_c as outlined in step 1 above. The new τ_c is then used as outlined in step 2 above to determine a new $\eta_{i,max}$, and the iterative process is repeated until a final self-consistent τ_c and $R_1^{Dipolar}$ are obtained.
5. Finally, the aromatic carbon chemical shift anisotropy (R_1^{CSA}) spin-lattice relaxation rates are determined from equation (17). Equation (16) can then be used to calculate the chemical shift anisotropy for an axially symmetric chemical shift tensor ($\Delta\sigma$) (not used).

2.3.2.2 – Rotational Temperature Dependence

As referred earlier, the study of the temperature dependence of the ILs relaxation and rotational dynamics has been reported before by different groups[101,103–105]. In practice temperature dependence studies have been used since the conception of the original relaxation theory[88]. Temperature is known to have influence on viscosity, and since viscosity is known to influence

molecular rotation, specifically in terms of the correlation time τ_c values (which are commonly thought of as the time required for a nucleus to rotate an angle of one radian). The accurate determination of rotational correlation times can provide physical information that relates to molecular dynamics, and in particular, such information can provide a useful description of phase changes, changes in molecular structure and other possible events as a function of temperature, as for example the ion-pair formation. Because these rotational correlation times are obtained from dipolar spin-lattice relaxation rates they are also called dipolar rotational correlation times. Therefore is expected that this study may contribute for eventual determination of distinct rotational dynamic behavior related with ion-pair formation. In this way, the neat and infinite dilution compositions will serve as extreme situations term of comparison of rotational dynamics with the ion-pair composition of interest, and the neat composition will also serve as initial comparison term with the bibliographic data. The ion-pair composition will be discussed with reference to the diffusion data, so that it is possible to achieve any kind of correlation that point towards the ion-pair formation.

In this sub-division of this discussion, the rotational values of each solution composition will be presented and discussed individually in sequential sub-sections for better clarification.

2.3.2.2.1 – Neat IL

As has been said before, the reason for choosing the neat IL as the starting point for this discussion concerns the fact that it is the only composition for which other rotational dynamic studies have been already reported for other ionic liquids. The data that will be presented here in this section consists:

- first, the experimental T_1 values which are directly obtained from processing data from ir experiments, in the form of total relaxation rate values ($R_1 = 1/T_1$), which includes contribution from dipolar relaxation and chemical shift anisotropy (CSA);
- second the corrected maximum NOE factors (η_{max}), calculated (by equation 19; formed by combination of equations 11 and 13) from an iteration process (in section 2.3.2.1) using the experimental T_1 ($1/T_1^{experimental}$), NOE values determined from the ig and gd ^{13}C NMR experiments data and an initial estimation of the correlation times (τ_c);
- third the correlation times (τ_c), which are calculated by an initial estimation, are progressively adjusted by difference minimization between $1/T_1^{calculated}$ (by equation 11) and $1/T_1^{experimental}$ (progressively substituted by new $1/T_1$ values coming from equation 20) in the same iteration process mentioned before in section 2.3.2.1;

T_1 values are sensible to certain parameters, such as viscosity or molecular weight. In practice, T_1 values are longer (higher values) (Figure 46) for small molecules in non-viscous solvents, that present fast molecular reorientational tumbling (small correlation time values – corresponding to the extreme narrowing condition; for example 10^{-12} s), characterized by molecular rotation at a higher frequency than the nuclear Larmor frequency (frequency of detection). This condition leads to a small

fraction of motions at the proper frequency of the relaxation pathway, and consequently inefficient relaxation (see also sections 1.2.1 for relaxation introduction and 2.1.3 for NMR IL studies).

With increasing solution viscosity, or molecular weight, the reorientational rates become progressively slower, and consequently relaxation becomes more efficient (shorter T_1) (Figure 46) due to synchronization of molecular rotation with the nuclear Larmor frequency. In this evolution there is a point of inversion, because at some point molecular rotation becomes slower than Larmor frequency and T_1 becomes longer again (Figure 46). The inversion point is physically very interesting, because it represents approximately the point where the molecular correlation time matches the inverse of the Larmor frequency ($\tau_c = 1/\omega_0$). Although this characteristic point is frequently used for the determination of the correlation time[103], it will not be used in this work. Instead, correlation times were calculated by the iteration process previously explained in the section 2.3.2.1 above.

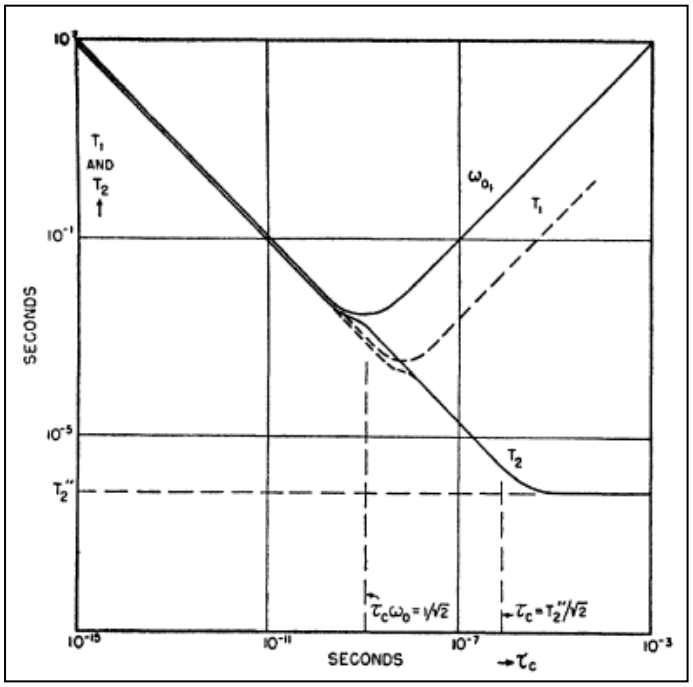

Figure 46 - Dependence of T_1 and T_2 upon τ_c, according to the simplified theory in which all interactions are assumed to have the same correlation time.[88]

2.3.2.2.1.1 - Plot Description - Figure 47

In order to establish the relation between the T_1 relaxation time data with the one actually used in this discussion, which is the relaxation rate R_1 data ($R_1 = 1 / T_1$), it is presented in the next plot the dependence of the neat experimental T_1 values with temperature (Figure 47, page 66).

The temperature in this study is responsible for the solutions viscosity variation, whose microscopic structural implications we aim to understand. As previously introduced in this Chapter 2 (section 2.1.3.6, page 25), ^{13}C NMR relaxation data has emerged as a huge contribution for this

purpose, since it allows the detection of distinct rotational dynamics for each structural carbon nuclei, which for $BMIMBF_4$ are: C2, C4 and C5 the imidazolium ring carbons; C10 the imidazolium adjacent methyl carbon; C6, C7 and C8 the aliphatic chain methylene carbons (order of distancing from the imidazolium ring); and C9 the aliphatic chain terminal methyl carbon (molecular structure in Figure 45, page 60).

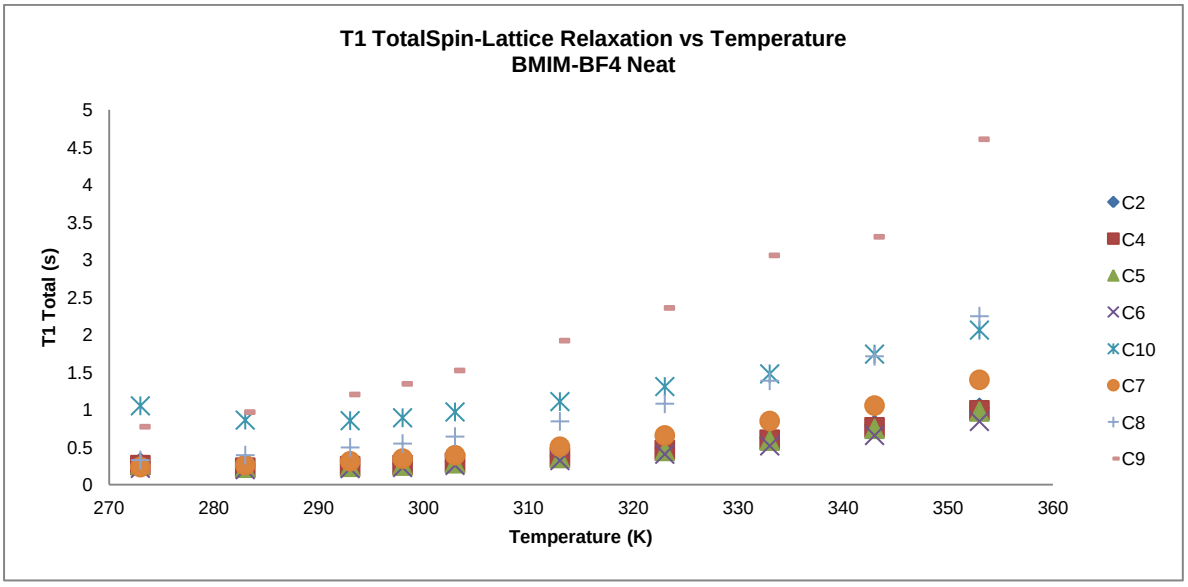

Figure 47 - Experimental total spin-lattice relaxation time values for the neat IL of the 8 $[BMIM]^+$ carbons for the temperature range 273 to 353 K, highlighting the extreme narrowing regime limit for the imidazolium ring carbons (C2, C4 and C5) at 283 K, associated with the minimum value.

As it may be seen roughly in the plot (Figure 47) a minimum is obtained for the imidazolium ring (C2, C4 and C5), and for the immediately adjacent methyl (C10) and methylene (C6) carbons at 283 K, which produces similar T_1 results to the ones observed by Bloembergen, Purcell and Pound when plotted T_1 against correlation times (τ_c) (which depend directly from the solution viscosity or/and molecular size) in Figure 46. These absolute minimum values, and corresponding absolute maximum values of R_1, of the imidazolium (C2, C4 and C5) and near carbons (C10 and C6) corresponds theoretically to the extreme narrowing region ($\tau_c = 1/\omega_0$), from which in both directions (increasing or decreasing viscosity/molecular size) the T_1 values will always increase (Figure 46 and Figure 47), and oppositely the R_1 values will always decrease.

Considering the plot of Figure 47, is possible to determine that while the referred carbons show an absolute minimum value at 283 K, the other aliphatic chain carbons (C7, C8 and C9) show monotonic T_1 decrease with decreasing temperature, for the temperature range studied. This known situation (section 2.1.3.6) allows the separation of the $BMIM^+$ carbons in two distinct groups: one composed by the carbons that present T_1 minimum (respective R_1 maximum), which correspond to the ones that supposedly present reduced rotational mobility; and the other is composed by the carbons which T_1 values present monotonic decrease (or monotonic increase of R_1 values) with decreasing temperature.

2.3.2.2.1.2 - Structural Insight

These distinct relaxation times T_1 (Figure 47) are associated with different segmental rotation dynamics of each carbon in the molecule, uncovering the possibility of individual carbon monitoring for conditions dependence. In this way, it is also possible to distinct which parts of the molecules are subjected to each rotational regime (into extreme narrowing or outside extreme narrowing), for example by the absolute minimum detection. In this case, the evidenced imidazolium ring carbons minimum values indicate rotational conditioning of the same, especially when compared with the aliphatic carbons of the same molecule ($BMIM^+$) (Figure 47).

In fact, this distinction between cation carbons based on the presence or absence of an absolute minimum value (or maximum for R_1) during the temperature range studied, is not entirely justified by the imidazolium ring higher conditioning. In practice, the absence of similar minimum value for the aliphatic chain carbons is also quiet intriguing, since it could be expected that the entire molecule (every carbon) would progressively lose rotational mobility for the same conditions (Figure 47).

This is apparently explained by the fact that aliphatic chain carbons are connected by sigma bonds, which per se allow a much higher degree of rotational freedom than the rigid aromatic π-bonds (see Figure 45 for $BMIM^+$ structure). In this way, it has been proposed that these aliphatic chain carbons observed relaxation rates R_1 (Figure 48), reflect a combined contribution of overall rotational motion (entire molecule) and local segmental rotational motion, justifying the distinct carbons R_1 values.[106]

Considering this proposal, the overall rotational contribution respects the imidazolium aromatic ring, which for being the slower rotating part represents the whole molecule rotation, and the additional local part respects the individual carbon degree of segmental rotational freedom, namely the aliphatic chain carbons (C6, C7, C8 and C9) and the imidazolium adjacent methyl C10. The sum of these two parameters corresponds to the observed results for the carbons relaxation and subsequent correlation time calculated values by iterative process (see section 2.3.2.1), as will be discussed further.

In any case it is also known that the imidazolium aromatic carbons are involved in inter-ionic interactions at least in neat composition (cation-cation and cation-anion), which is supported by the cation charge (+) positioning at this structural section (imidazolium ring N's), and the existence of hydrogen bonding between C2 aromatic carbon and BF_4^- Fluor atoms.

2.3.2.2.1.3 - Plot Description - Figure 48

Figure 48 represents the experimental longitudinal relaxation rate R_{1total} ($1/T_{1total}$) for the temperature range studied, as determined for all the carbon atoms of the $BMIM^+$ in the neat IL.

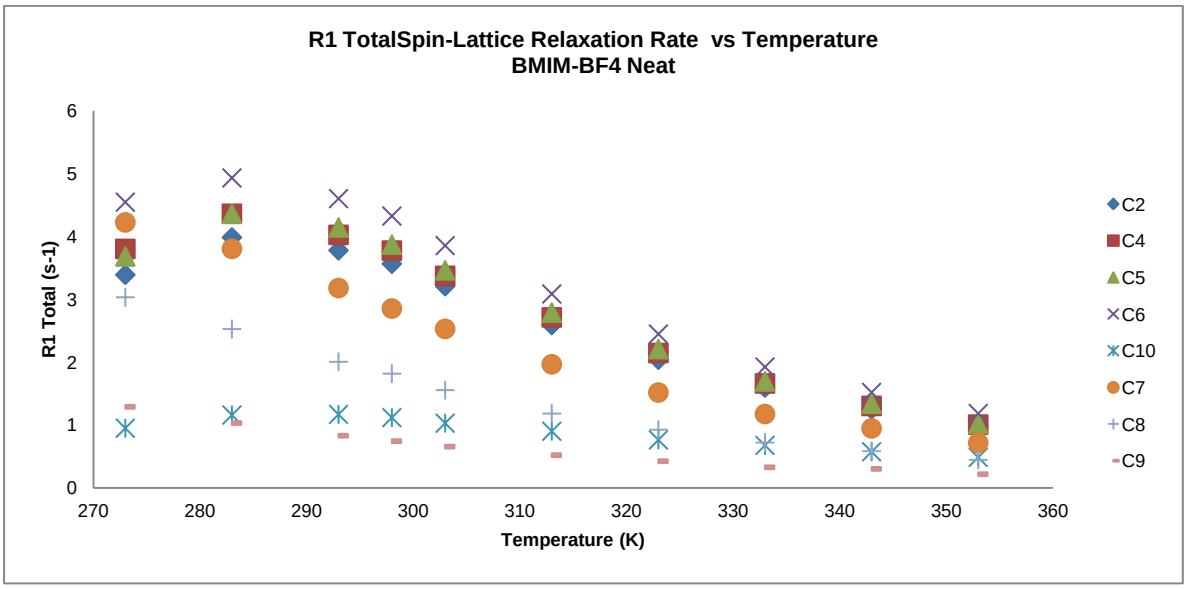

Figure 48 - Experimental total spin-lattice relaxation rate values for the neat IL of the 8 $[BMIM]^+$ carbons for the temperature range 273 to 353 K, highlighting the extreme narrowing regime limit for the imidazolium ring carbons (C2, C4 and C5) at 283 K, associated with the maximum value.

2.3.2.2.1.4 - Structural Insight

Despite the maximum value observed for C10, the constant short R_1 value indicates that this methyl group keeps a rapid rotation even at low temperatures, and suggests that C10 methyl group R_1 value results from a the contribution of two distinct dynamics: the own rapid segmental dynamic (internal rotation) of the methyl group, which causes large T_1 and consequently short R_1; and a soft influence of the slower dynamic, at low temperatures (283 – 293 K), of the imidazolium ring to which the methyl group is adjacent (overall rotation). This interpretation and mathematical separation of these two contributions for methyl group C10 have already been done in a previous publication[106].

The higher values of R_{1total} are verified for the C6 carbon of the butyl chain, adjacent to the imidazolium ring. This relaxation behaviour is commonly explained by the close relation with the imidazolium ring, which is slow rotating, and possible segmental rotation inhibition by the faster rotating adjacent carbon C7. All the other carbons (C7, C8 and C9 of the butyl chain) do not present a maximum in temperature range studied for the R_{1total} data, which means that even for low temperatures the butyl chain is having fast free-segmental rotation, increasing in the direction of the end of the chain, which were already expected.

2.3.2.2.1.5 - Plot Description - Figure 49

As has been already introduced in this chapter (see section 2.1.3), the primary contributions to the ^{13}C NMR R_{1total} are the dipolar and CSA relaxation mechanisms. From moderate magnetic fields CSA relaxation contribution for the total relaxation gains increasing importance since it increases with the square of the magnetic field. Therefore in order to avoid considerable errors in the calculation of rotational correlation times using R_{1total} it becomes necessary to calculate an accurate value for the CSA contribution, which was done using the methodology explained in section 2.3.2.1.

Although CSA relaxation rates (^{13}C NMR R_{1CSA}) are commonly just calculated for imidazolium aromatic ring carbons[106], we have calculated for every carbon of the cation.

Figure 49 represents the calculated R_{1CSA} dependence with temperature, as determined by the iterative procedure explained in section 2.3.2.1. R_{1CSA} is calculated by equation 17 as a subtraction of $R_{1dipolar}$ from R_{1total}. In this way is understandable the complementarity between R_{1CSA} and $R_{1dipolar}$ in forming R_{1total}. $R_{1dipolar}$ calculation process is explained in the next page (see section 2.3.2.1).

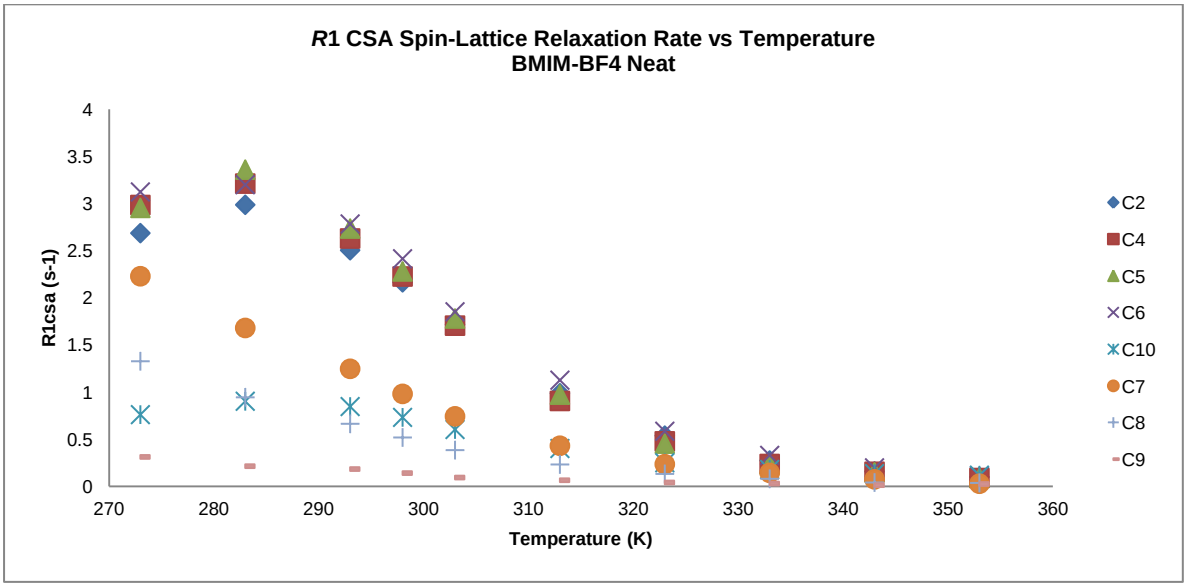

Figure 49 - Calculated neat CSA spin-lattice relaxation rate values of the 8 $[BMIM]^+$ carbons for the temperature range 273 to 353 K, highlighting its high contribution for the imidazolium ring carbons (C2, C4 and C5) total relaxation rate at lower temperatures.

By the observation of Figure 49, the values of R_{1CSA} versus temperature confirm that the aromatic ring carbons have in general higher values of CSA relaxation rates (^{13}C NMR R_{1CSA}) than the butyl chain carbons C7, C8, C9 and C10. However, carbon C6 exhibits a CSA relaxation rate value as high as the aromatic carbons, which represent more than half of its total relaxation rate R_{1total} (Figure 48), which indicates that the decomposition of the total relaxation rate R_{1total} (equation 17) at least for this case could also be necessary. Comparing Figure 49 with Figure 48 is easy to determine that the maximum point observed for R_{1CSA} (283 K) coincides with the previously observed for R_{1total}, indicating

the significant contribution of CSA relaxation mechanism for the total relaxation (Figure 48). The same is true for carbon C10 CSA relaxation rate presenting a coincident maximum with R_{1total}, between 283 K and 293 K.

2.3.2.2.1.6 - Plot Description - Figure 50

Figure 50 represents the calculated $R_{1dipolar}$ ($1/T_{1dipolar}$) dependence with temperature. Although $1/T_{1dipolar}$ is obtained finally from equation 20, it is calculated, as explained in section 2.3.2.1, from an initial estimation of the correlation time (τ_c), which is involved indirectly (through *J*+ and *J*-, based on equation 14, defined in section 2.3.2.1) in the calculation of η_{max} by equation 19, which in turn is included in equation 20 with experimental NOE and $1/T_1$ values to give $1/T_{1dipolar}$ values.

This process is repeated n times (until maximum minimization of $1/T_{1calculated}$ with respect to $1/T_{1dipolar}$) in an iterative manner, where the $1/T_{1dipolar}$ values obtained by equation 20 (as explained above) are computationally approached (by least-square minimization) by $1/T_{1calculated}$ (calculated by equation 11; alteration of τ_c values for minimization) giving new correlation time (τ_c) values, which initiates again the process explained above that culminates with the final $1/T_{1dipolar}$ after approximately 40 iterations (see section 2.3.2.1). Those values for each temperature of each carbon are presented in Figure 50 below.

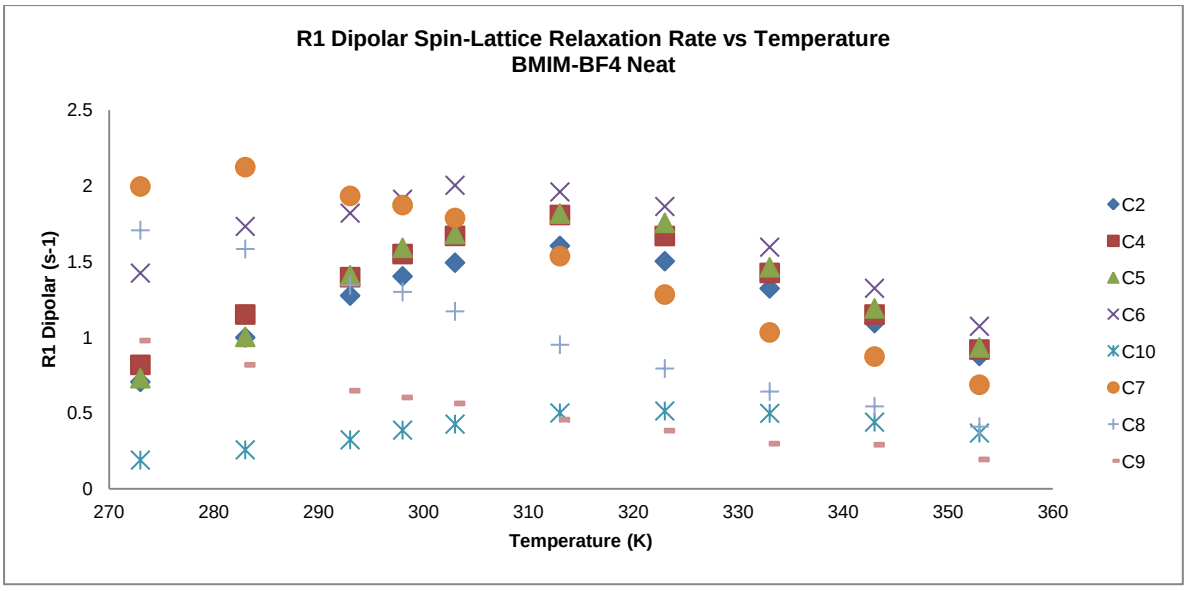

Figure 50 - Calculated neat dipolar spin-lattice relaxation rate values of the 8 $[BMIM]^+$ carbons for the temperature range 273 to 353 K, highlighting the displacement of the imidazolium ring carbons (C2, C4 and C5) extreme narrowing regime limit from 283 to 313 K taking into account the total relaxation rate represented in figure 41.

From the observation of the plot in Figure 50 it is easy to identify different features when compared with R_{1total} (Figure 48). The most obvious is the displacement of the maximum values towards higher temperature values for the previously referred carbons (C2, C4, C5, C6 and C10), and

also the appearance of a maximum for C7 at 283 K that was not observed for R_{1total} data (see Figure 48), which must be consequence of the combination of experimental NOE and $1/T_1$ values in equation 20 of the methodology used (see section 2.3.2.1).

From this observation is possible to conclude that the dipolar and CSA relaxation mechanisms (see section 1.2.1.3) have different contributions at different temperatures, whereas the dipolar relaxation mechanism is dominant for higher temperatures (lower viscosity) the CSA relaxation mechanism is dominant for lower temperatures (higher viscosity).

This information indicates that CSA and dipolar relaxation mechanisms (see section 1.2.1.3) have more efficiency in different conditions associated with different motional regimes (rotation rates) and that for this reason it will be probably possible to observe particular motional conditionings if both independent relaxation mechanisms are analysed separately, proving the importance of R_{1total} decomposition (by equation 17, see section 2.3.2.1). This result is very interesting for the purpose of the study of the ion-pair dynamics of BMIM-BF_4 in solution, since it provides another parameter that may be sensible to the ion-pair formation and dynamics even in the presence of other competing factors.

2.3.2.2.1.7 - Plot Description - Figure 51

In addition to the total spin-lattice relaxation values (T_1), experimental $\{^1H\}^{13}C$ NOE values were also measured. These values are determined by the combination of two different experiments, the already referred pg (power gated) and ig (inverse gated) ^{13}C NMR experiments. These two are similar ^{13}C NMR directed experiments with singlet signals (due to proton decoupling), which difference consists in the presence or not of NOE, whereas pg includes NOE effect, ig does not. While in the pg experiment the decoupler is kept on during a delay period when the NOE enhancement builds up and turned off during acquisition of the FID, in the ig the decoupler is on only during the acquisition time and off otherwise. The experimental value of NOE effect for each carbon atom can be determined by a simple mathematical operation using the signal intensities of the two experiments, $(I_{pg} - I_{ig}) / I_{ig}$.

The results for the experimental NOE effect obtained for the neat IL may be observed in Figure 51. As previously referred, experimental NOE values are employed in the calculation of $R_{1dipolar}$ by equation 20 in the iterative process described in section 2.3.2.1.

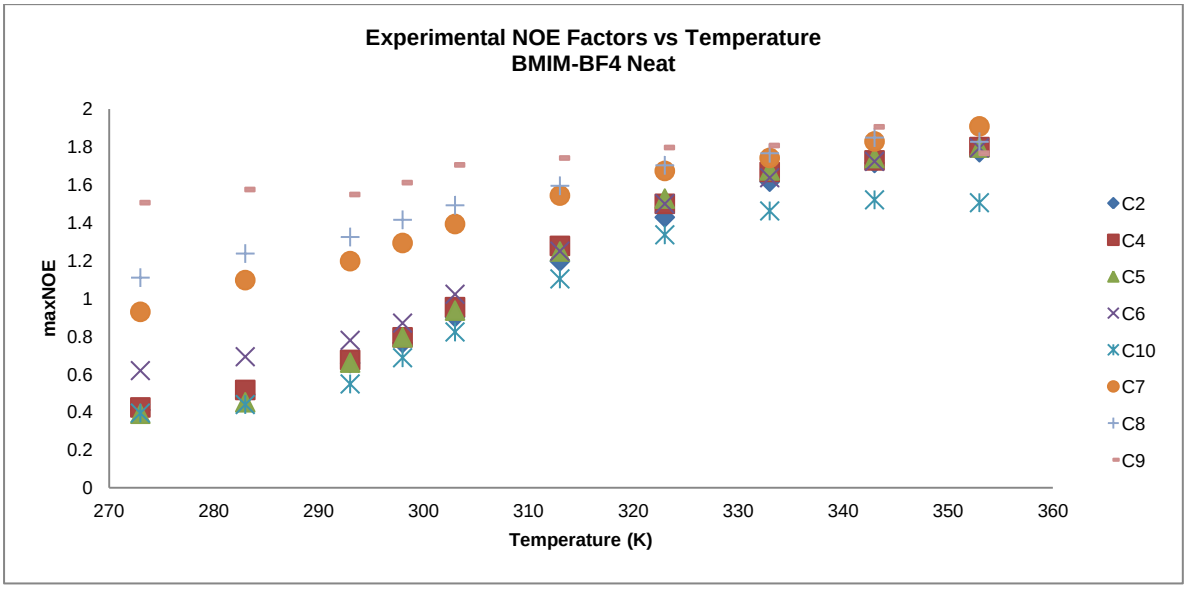

Figure 51 - Experimental NOE factor values for neat IL of the 8 $[BMIM]^+$ carbons for the temperature range 273 to 353 K, highlighting the permanent increasing with increasing temperature.

By the observation of the data in Figure 51 is possible to determine that for every carbon the NOE value is increasing progressively with temperature starting at 273 K. The carbons that present lower values for low temperatures are the imidazolium ring carbons (C2, C4 and C5) and the adjacent ones (methyl C10 and methylene C6). These results uncover the influence of experimental NOE values (by equation 20) on the calculated relaxation rates (dipolar in Figure 50 and CSA in Figure 49), and are in good agreement with reported data, except for the minimum NOE determination, which in the bibliographic data occurs at 263 K, and is out of the temperature range studied in this work[101,106].

2.3.2.2.1.8 - Structural Insight

Such temperature dependence of the NOE factor (Figure 51) is explained by a slowing down of the global reorientational (rotational) dynamics and the leaving of the extreme narrowing region ($\omega_0\tau_c >> 1$) at low temperatures for the imidazolium ring and adjacent carbons, in accordance with the occurrence of the maxima in the R_{1total} versus temperature (Figure 48).

The values of all ^{13}C nuclei, with the exception of the methyl carbon C10, almost reach the theoretical maximum limiting value of 1.988 for the extreme narrowing region at high temperatures (Figure 51). At the lowest temperatures the limiting value of 0.154 for $\tau_c >> 1/\omega_0$ was not observed, which is a consequence of the occurrence of fast internal (segmental) reorientations. The deviation of the NOE factors for the methyl C10 from the maximum value of 1.988 in the extreme narrowing region could be explained by increasing importance of the spin-rotation relaxation mechanism.[106]

2.3.2.2.1.9 - Plot Description - Figure 52

In this context, another resulting data from the iterative process to the determination of the correlation time consists in the determination of corrected maximum NOE factors (η_{max}) (Figure 52). The maximum NOE factors (η_{max}) as referred earlier derive from an iterative process in such a way that first they are calculated by the experimental T_1 values (according to equation 19, in section 2.3.2.1), and with iteration progress the relation between these calculated maximum NOE factors and the experimental NOE factors will recursively determinate the decomposition of the R_{1total} into $R_{1dipolar}$ and R_{1CSA} (according to equations 20 and 17, respectively, in section 2.3.2.1), and generate new values for maximum NOE factors itself.

The basic assumption is that the maximum value of ^{13}C NOE is determined by the dipolar rotational correlation time (see section 2.3.2.1). The purpose of all this process from which derives these corrected maximum NOE factor values (equation 19) is the accurate calculation of corrected dipolar rotational correlation times.

Figure 52 represents the calculated maximum NOE factors (equation 19) after convergence of the iteration process (see section 2.3.2.1). By the graphical observation (Figure 52) is possible to determine that the corrections to the maximum NOE factors in the neat solution of BMIM-BF_4 are quite minimal (in relation to the maximum value in extreme narrowing condition).

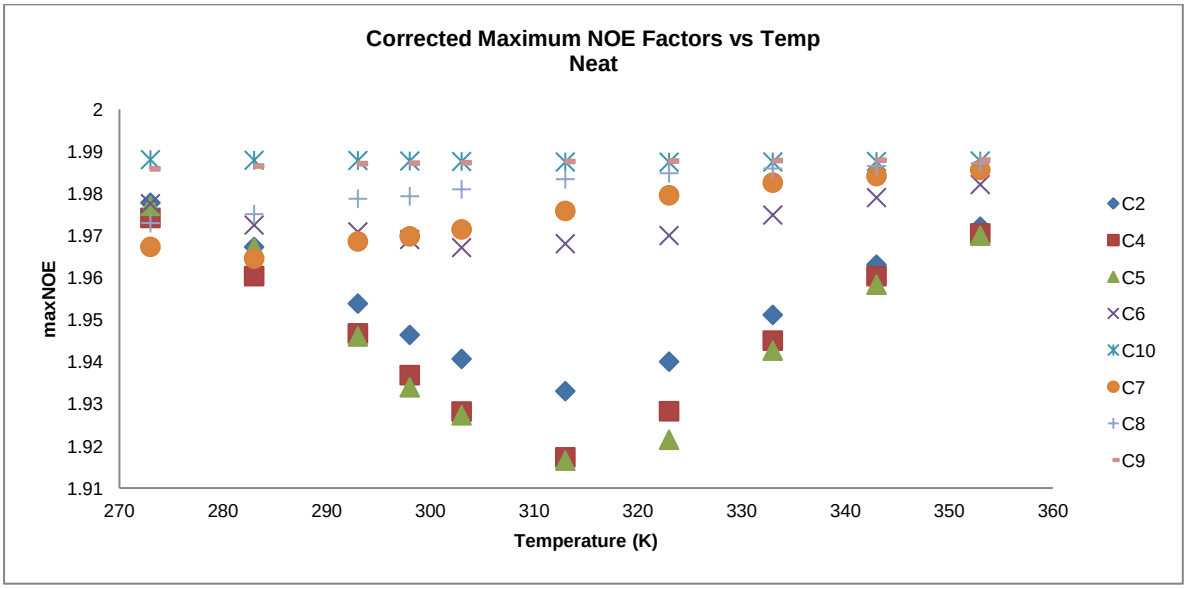

Figure 52 - Calculated maximum NOE factor values for neat IL of the 8 $[BMIM]^+$ carbons for the temperature range 273 to 353 K, highlighting the complementary with the dipolar relaxation rate reasoned by the mathematical iterative process, presenting a minimum value at 313 K for the imidazolium ring carbons (C2, C4 and C5).

The more significant corrections are for the imidazolium ring carbons (C2, C4 and C5) and for the adjacent methylene carbons (C6 and C7), justified by the departure of these carbons motional dynamics from the extreme narrowing region, which is related with progressive decreasing of

experimental NOE effect and even vanishing (Figure 51). The matching observed at the temperatures for the minimums of the corrected maximum NOE factors (Figure 52) and the maximum of dipolar spin-lattice relaxation rates ($R_{1dipolar}$ Figure 50) is only a fortuitous consequence of the combined equations 19 and 20 used in the iterative process to obtain the parameters values (see section 2.3.2.1). Although there is no particular explanation to that fact, it may serve as a useful check on the correct application of the process.

2.3.2.2.1.10 - Plot Description - Figure 53

As it is already known, the ^{13}C rotational correlation time, which is commonly thought of as the time required for a nucleus to rotate an angle of one radian, provide a useful guide in determining relative nuclear mobility within a given molecule.

As referred above for neat relaxation rate R_1, in section 2.3.2.2.1.2, in accordance to relaxation distinct values for different carbons in the molecule, is also possible to discriminate distinct correlation times for different carbons.

The importance of determining such distinction is associated with the fact that despite the individual carbons present different correlation time values due to its different parts segmental dynamics, associated for example with the type of chemical bonds, the distance to the imidazolium ring or even the number of Hs, every carbon must present two contributions, which are the one from the overall molecular rotational motion and one from its own segmental rotational motion.

The overall rotational motion precisely corresponds to the correlation time for the molecule rotate about itself. In this way, it is logical to suppose that the slow rotation of the molecule corresponds directly to the slower rotating part of the molecule, which in this case is the imidazolium ring. It is also logical to suppose that the differences between the imidazolium ring carbons (C2, C4 and C5) and the other $BMIM^+$ carbons (C6, C7, C8, C9 and C10) are associated with the segmental contributions, which the imidazolium ring doesn't show for being rigid (imidazolium ring carbons present always the same profile as each other).

These correlation times, as previously mentioned, result from the same iterative methodology (defined in section 2.3.2.1) used in the separation of total relaxation rates (Figure 48) into dipolar relaxation rates (Figure 50) and CSA relaxation rates (Figure 49). Actually, the iterative process is initiated by introducing estimated values for correlation times, which are involved indirectly (through *J*+ and *J*-, defined in section 2.3.2.1) in the calculation of maximum NOE factors (η_{max}) by equation 19, which in turn is included in equation 20 with experimental NOE and $1/T_1$ values to give $1/T_{1dipolar}$ values. This process is repeated n times in an iterative manner as explained above (see section 2.3.2.1). It is crucial to refer that the estimated initial values used in this case (root1) were in the order of 0.01 nanoseconds, as proposed in the reference work. A particularity about this iterative process to

determine the correlation times is that the corrected (final) rotational correlation times are shorter (numerically inferior) than the initial rotational correlation times (see equation 18 in section 2.3.2.1), as the total relaxation rates (Figure 48) are now separated into both dipolar relaxation (Figure 50) and a CSA contribution (Figure 49). The correlation times determined by this process are represented in Figure 53.

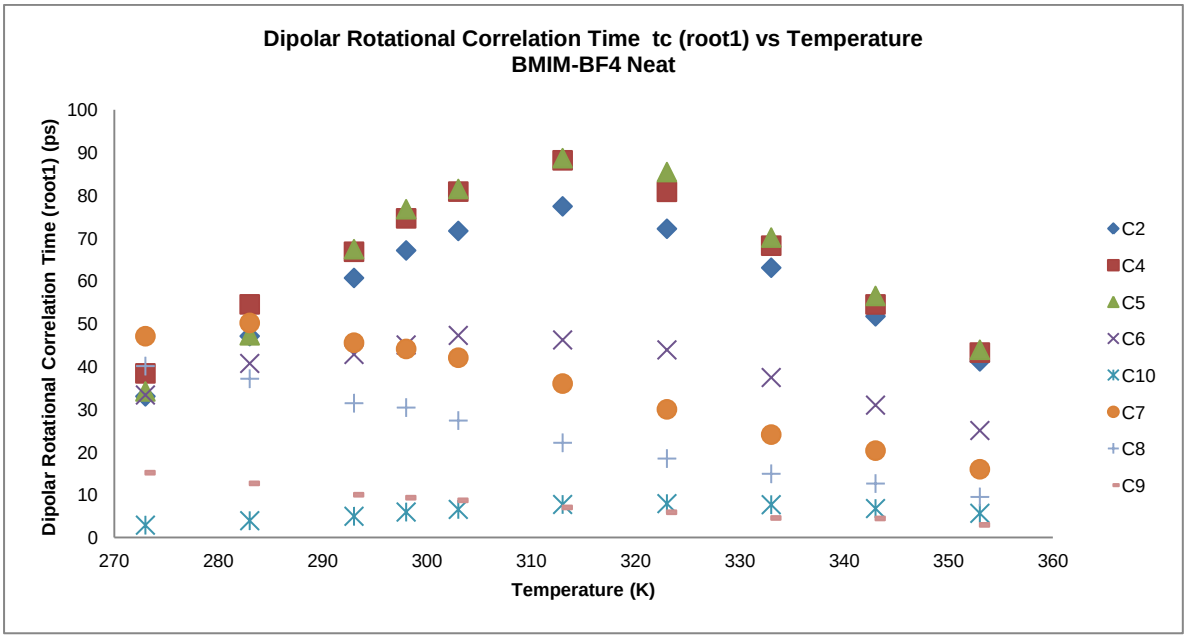

Figure 53 - Calculated correlation times (root1) values for neat IL of the 8 $[BMIM]^+$ carbons for the temperature range 273 to 353 K, highlighting the correspondence with the dipolar relaxation rate reasoned by the mathematical iterative process, presenting a maximum value at 313 K for the imidazolium ring carbons (C2, C4 and C5).

By the observation of the data in Figure 53 is possible to determine the maximum rotational correlation time for the imidazolium ring carbons (C2, C4 and C5) at approximately 313 K, thus matching the $R_{1dipolar}$ maximum (Figure 50) and the minimum in the corrected maximum NOE factors plot (Figure 52) as it was expected due to the mathematical iterative process (conjugation of equations 11, 19 and 20 in section 2.3.2.1). Is also possible to identify the same matching for the adjacent methyl and methylene carbons (C10 and C6, respectively), and also for the aliphatic C7 carbon.

2.3.2.2.1.11 - Structural Insight

However the direct influence of $R_{1dipolar}$ (Figure 50) is obvious in the behaviour described by the dipolar rotational correlation times (Figure 53), its relative values reflect accurately the expected differences for the particular rotational dynamics of the distinct segmental regions of the cation. Therefore, the higher rotational correlation time values for the imidazolium ring carbons (C2, C4 and

C5; approx. 30 to 90 picoseconds) for almost all the temperature range studied, indicates the known relative reduced mobility of this segment in comparison with the aliphatic chain (Figure 53).

Even the relative high rotational correlation time values for the aliphatic near-imidazolium carbons C6, C7 and C8 indicates the strong influence of the ring carbons reduced mobility in these carbons segmental dynamics, and uncovers the possible participation of such carbons in structural motifs, such as aggregation in neat solution (Figure 53).

The lower values for the aliphatic terminal methyl C9 and for the ring adjacent methyl C10 indicate the high segmental rotational dynamics expected (Figure 53). However, the discrete maximum value verified for the adjacent methyl carbon C10, near coincident with the aromatic carbons maximum, indicates the influence of the imidazolium ring restriction effect on the adjacent methyl partial mobility (Figure 53).

2.3.2.2.1.12 – Methodology Considerations

While in the extreme narrowing region the dipolar rotational correlation times are physically in accordance with classical mechanics given by the Stokes-Einstein-Debye (SED) equation (Figure 53):

$$\tau_c = \frac{4\pi a^3 n}{3kT} = \frac{V\eta}{kT} \quad \textbf{(21)}$$

Its behaviour outside the extreme narrowing region that begins at 313 K and follows with decreasing temperature, for the aromatic carbons, is against to what was predictable by the same theory, which was the increasing of dipolar rotational correlation times with increasing viscosity (decreasing temperature) (Figure 53).

The explanation for this feature is that upon the iterative decomposition process (see section 2.3.2.1) of the total spin-lattice relaxation rates (Figure 48) the rotational correlation times (Figure 53) have also been separated in dipolar rotational correlation rates (Figure 50) and CSA rotational correlation rates (Figure 49). As has been already referred, the graphical behaviour of the dipolar rotational correlation times (Figure 53) follows exactly the same behaviour as dipolar spin-lattice relaxation rates (Figure 50), which happen because of the direct related sources of the two values (equations 11, 19 and 20) in the iterative process (see section 2.3.2.1).

In this way, with this method (section 2.3.2.1), the result behaviour verified for the dipolar rotational correlation time (Figure 53) of ring carbons (non-monotonous τ_c decreasing with increasing temperature) is only justified by the presence of a large contribution of the chemical shift anisotropy (CSA), which are not considered in dipolar rotational correlation time values (Figure 49).

2.3.2.2.1.13 - Plot Description - Figure 54

However, by means of mathematical investigation, instead of one root (one result from the iterative process) two roots have been determined as answers for dipolar rotational correlation times (two results from the iterative process) for the same dipolar spin-lattice relaxation rate (Figure 50) with this approach (see section 2.3.2.1). The determination of the second root occurred by setting the initial estimated values in the order of 10 nanoseconds into the iterative (indirectly into equations 11 and 19) process explained before (see section 2.3.2.1), differently to the previous 0.01 nanoseconds used in obtaining root 1. The values of correlation times (τ_c) for each minimization process is represented below in Figure 54.

These two roots present distinct value ranges: the first root (root1, presented in Figure 53) presents values in the range of dozens of picoseconds; while the second root (root2, presented in Figure 54) presents values in the range of dozens of nanoseconds.

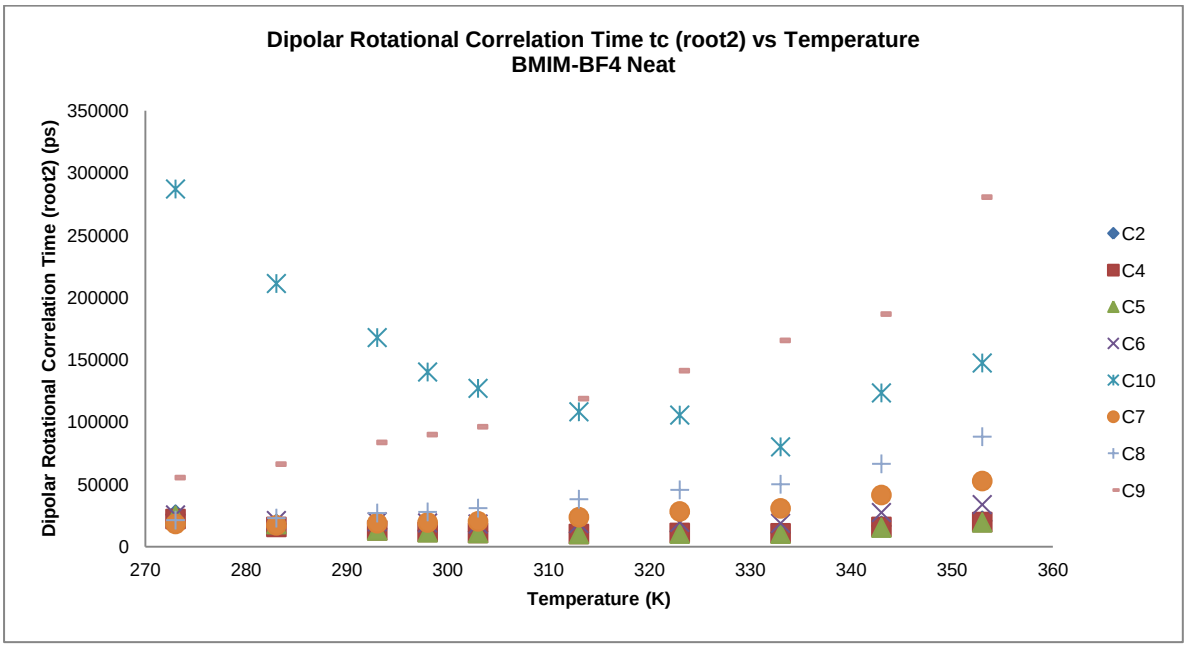

Figure 54 - Calculated correlation times (root2) values for neat IL of the 8 $[BMIM]^+$ carbons for the temperature range 273 to 353 K, highlighting the symmetric correspondence with the dipolar relaxation rate reasoned by the mathematical iterative process, presenting a relative minimum value at 313 K for the imidazolium ring carbons (C2, C4 and C5).

The particular importance of this discovery (in Figure 54) is that: first, nanoseconds are a much more accepted scale for the imidazolium ionic liquids rotational correlation times; second, for the initial temperature range of the graphical data many carbons, including the imidazolium ring ones, present decreasing values of rotational correlation time with increasing temperature, which were expected and didn't happen in root1 derivation (in Figure 53).

2.3.2.2.1.14 – Methodology Considerations

The second point is related with the previous referred classical mechanic question of the Stokes-Einstein-Debye (SED) equation (21) (decreasing of correlation times with increasing temperature).

Nevertheless, not all is positive in this new derivation (root2) (in Figure 54), for example: first, the fact that the aliphatic carbons C7, C8 and C9 present increasing correlation times with increasing temperature is not understandable, since these should be the faster rotating carbons at the cation due to increased free-chain-rotation; second, is not reasonable that the imidazolium ring carbons have lower correlation time values than methyl C10 (adjacent to the ring; should present segmental dynamics) and specially methyl C9 (aliphatic methyl end); third, makes no sense that all carbons present correlation time increasing for the highest temperatures range (333 to 353 K) (in Figure 54).

The justification for this neat dipolar rotational correlation time's (root2) (Figure 54) behaviour is reasoned again by the neat dipolar spin-lattice relaxation times (Figure 50) behaviour, since the graphical representation of both seem to be the inverse from each other (and additionally root2 the inverse of root1), sharing same temperature values for the minimums of correlation times (Figure 54) and maximums of dipolar relaxation (Figure 50).

In conclusion, both obtained roots (Figure 53 and Figure 54) of dipolar rotational correlation times miss in providing accurate and reliable information about cation $BMIM^+$ rotational dynamics.

2.3.2.2.1.15 - Plot Description - Figure 55

In contrast, the reliable approximate behaviour of rotational correlation time for imidazolium cations of ionic liquids has been obtained with the use of an alternative (simpler) methodology, published during the course of this thesis.[105] Following this procedure we have calculated new rotational correlation times (Figure 55).

This new methodology consists in a much simpler approach that ignores the CSA spin-lattice relaxation rate contribution based on experimental evidences that suggest that this relaxation rate is negligible for all imidazolium carbons, and consider dipolar spin-lattice relaxation rate the only contribution to the total spin-lattice relaxation rate (Figure 48). In this way, no iterative process is necessary, and no NOE experimental data is used.

The mathematical resolution is only based on the BPP (Bloembergen-Purcell-Pound)[88] theory applied to ^{13}C nuclei. The equation (derived from equation 11) also considers some practical approximations and a constant A_0 which does not depend on temperature and frequency, and includes an order parameter S. The results of this simpler approach are presented in figure 48.

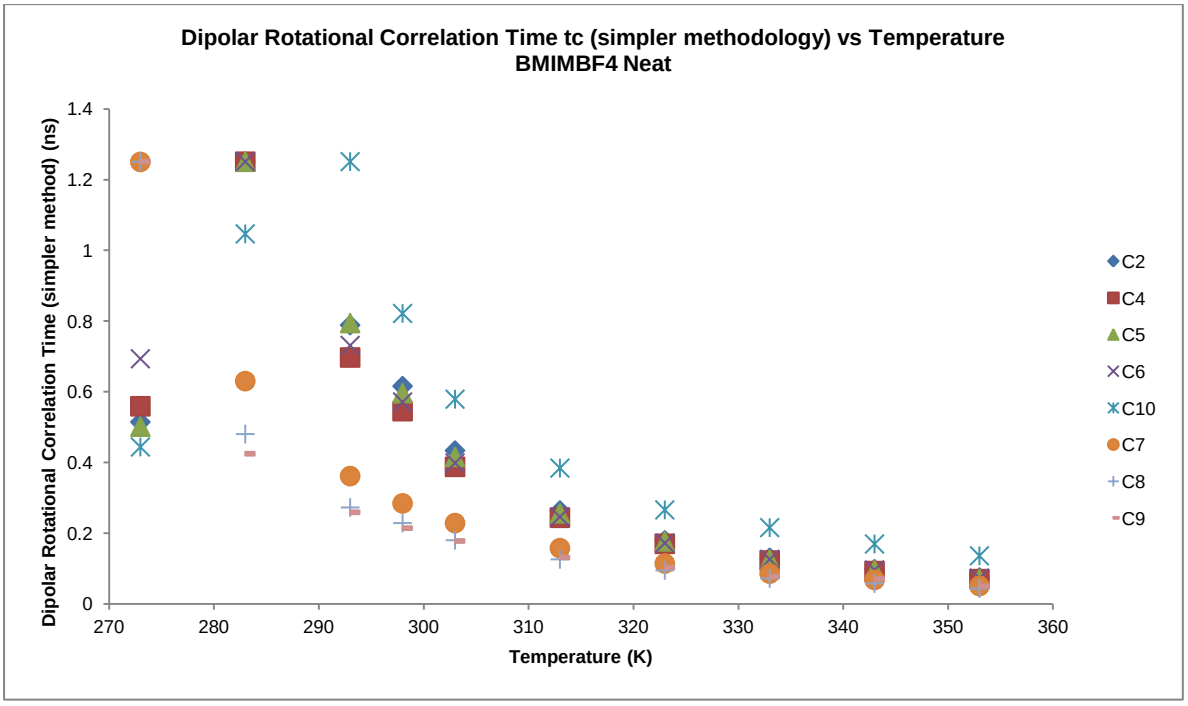

Figure 55 - Calculated correlation times (simpler methodology) values for neat IL of the 8 $[BMIM]^+$ carbons for the temperature variation range from 273 to 353 K, highlighting the correspondence with the total relaxation rate reasoned by the mathematical procedure utilized, presenting a maximum value at 283 K for the imidazolium ring carbons (C2, C4 and C5).

By the observation of the dipolar rotational correlation time results (in Figure 55) of this simpler methodology is possible to determine two good indicators about its reliability: first's the so-called time-scale which is in the nanoseconds scale; and second the monotonic decreasing profile of cation aliphatic carbons (C7, C8 and C9) correlation times with increasing temperature (Figure 55).

In any case, for the imidazolium ring carbons (C2, C4 and C5) and for the adjacent carbons methyl and methylene (C10 and C6, respectively) it is still being verified the non-monotonic profile (Figure 55), whose maximum has been shifted to lower temperatures (283 K; and 293 K for carbon C10) because of its mathematical relation now with total relaxation rate (considered exclusively dipolar) (Figure 48).

Considering the temperature dependence profile (Figure 55): first, to refer that the maximum is reasoned by the relaxation rate dependency of correlation times from the BPP-type approach, which is explained by the fact that in this range of temperatures is possible to observe the inversion between the two T_1 (and inversely R_1) regimes (into the extreme narrowing or outside the extreme narrowing limit), which in turn is explained simply by the change in solution viscosity with temperature.

2.3.2.2.1.16 - Structural Insight

The reason for only imidazolium ring carbons and adjacent ones present a maximum (Figure 55) is related with the aliphatic carbons are still presenting high rotational segmental dynamics even for imidazolium aggregation profile at low temperatures (responsible for increased viscosity). This result also suggests that imidazolium adjacent methyl carbon C10 may be involved in aggregation processes, being the first losing segmental rotational dynamics and reaching the maximum at 293 K.

2.3.2.2.1.17 – Neat Composition Considerations

In sum, with this BMIM-BF_4 IL neat composition study has been possible to determine that although rotational correlation times derived with the first methodology (Figure 53 and Figure 54) cannot be considered, the other parameters calculated ($R_{1dipolar}$, R_{1CSA} and maximum NOE factors) may still provide useful descriptions of phase changes, changes in molecular structure and other possible events as a function of temperature, since they are derived from the R_{1total} (Figure 48) and NOE experimental (Figure 51) values. For this reason, the calculations made with decomposition of total spin-lattice relaxation rates into dipolar and CSA contributions will continue to be used for the next compositions, namely ion-pair and infinite dilution, as they may enclose crucial information and clues for molecular dynamic change.

2.3.2.2.1.18 – Neat Comparative Analysis between Rotation and Diffusion Data

Considering the combined diffusion and rotation results from $BMIMBF_4$ neat composition dependence with temperature, it is possible to establish a connection between both.

In first place, considering that the overall cation rotation increase with increasing temperature (not counting the C2, C4, C5 and C6 correlation time inversion associated with R_1 inversion), it is possible to state that both diffusion and rotation increase with increasing temperature, observed in diffusion coefficients (Figure 27) and correlation time (Figure 55) plots. While diffusion increases progressively faster with increasing temperature (exponentially), rotation increases greatly until approx. 313 K and then starts to progress slowly.

In second place, with respect to structural organization, by observing the $BMIM^+$ hydrodynamic radius diffusion data (Figure 32), which exhibits an initial increasing from 273 to 293 K, it is possible to find relation with the elevated C10, C2, C4, C5 and C6 correlation time values (Figure 55), which present correlation time maximums at this range. This relation indicates possibly some kind of phase transition in this range (273 to 293 K), which is associated for one side with different stages of $BMIM^+$ segments aggregation (C10 maximum at 293 K; C2, C4, C5 and C6 maximums at 283 K), and also reflected on the other side by relative diffusion increasing of dioxane when compared with $BMIM^+$.

During the rest of the temperature range studied is possible to state that $BMIM^+$ preserves a diffusional state of aggregation, considering its constant hydrodynamic radius relative value (Figure 32), even observing the progressive increasing for the overall cation diffusional and rotational motions acceleration (Figure 55).

2.3.2.2.2 – IL in Ion-pair Composition

In accordance with the previously verified similarity between the neat IL and ion-pair composition regarding the diffusion studies, relaxation studies also reveal common features.

2.3.2.2.2.1 - Plot Description - Figure 56

When concerning the total spin-lattice relaxation rate (R_{1total}, Figure 56), a similar behavior as the one verified for neat IL (Figure 48) is now observed for ion-pair composition (compare Figure 56 with Figure 48). This means that similar individual carbon relaxation is verified for all carbons and also approximately the same values for R_{1total} (Figure 56) are determined for every carbon.

The only physical meaningful different result obtained consists in the higher value verified for the imidazolium ring carbons (C2, C4 and C5) plus the methyl and methylene adjacent ones (C10 and C6, respectively) at the minimum temperature (273 K) (Figure 56).

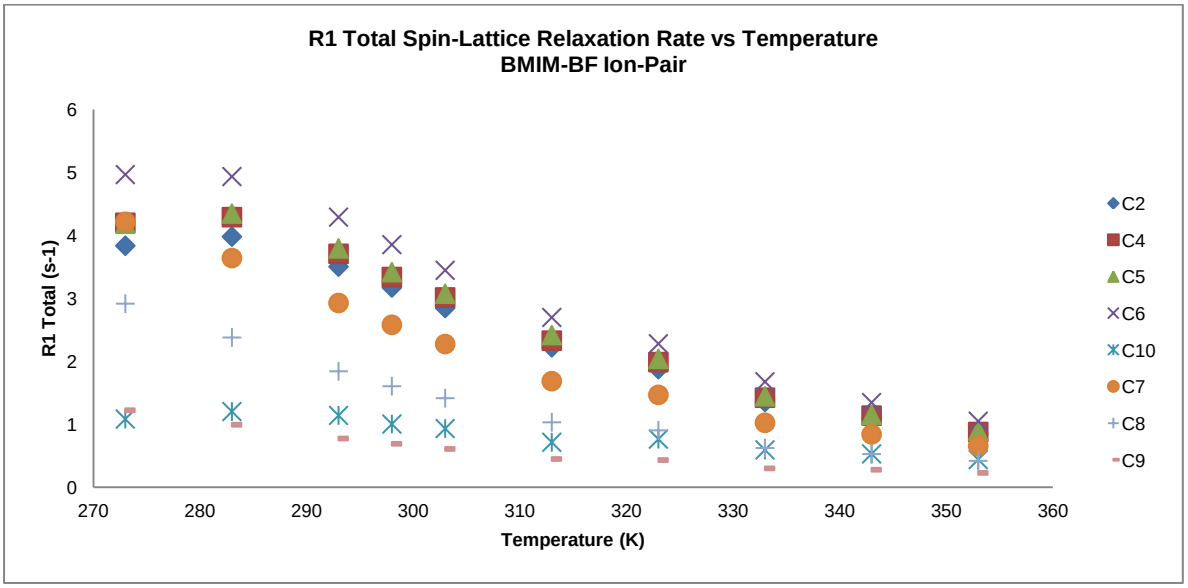

Figure 56 - Experimental total spin-lattice relaxation rate values for the ion-pair composition of the 8 $[BMIM]^+$ carbons for the temperature range 273 to 353 K, highlighting the extreme narrowing regime limit for the imidazolium ring carbons (C2, C4 and C5) at 283 K, associated with the maximum value.

This behavior may be justified by the lower viscosity of ion-pair solution comparing with neat,[104] since higher values of R_1 means lower values of T_1. In this case, higher values of R_1 (Figure 56) means higher mobility comparing with the neat R_1 values (Figure 48) at the same temperature (273 K).

2.3.2.2.2.2 - Plot Description - Figure 57

The data for the CSA spin-lattice relaxation (R_{1CSA}) is plotted on Figure 57. This data corresponds to the values obtained for individual carbons of $BMIM^+$ by using the previously referred methodology (see section 2.3.2.1) with a conjugation of equations (11 - 20) that ultimately by equation 17 allows the separation of R_{1total} into R_{1CSA} and $R_{1dipolar}$, as explained before in neat composition.

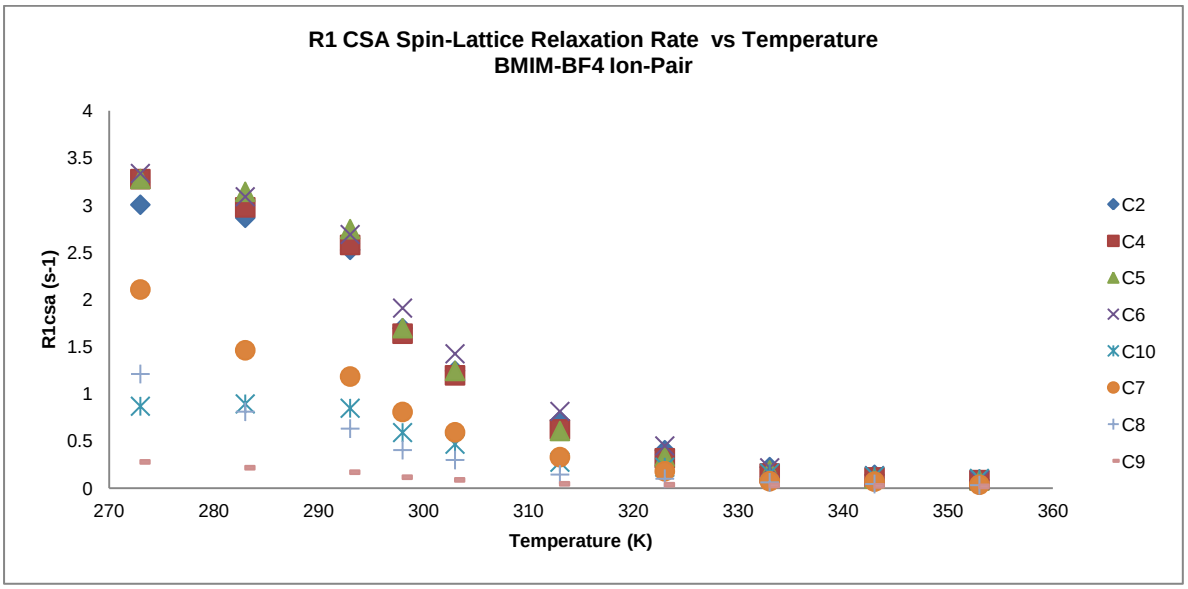

Figure 57 - Calculated CSA spin-lattice relaxation rate values for the ion-pair composition of the 8 $[BMIM]^+$ carbons for the temperature range 273 to 353 K, highlighting its high contribution for the imidazolium ring carbons (C2, C4 and C5) total relaxation rate at lower temperatures.

By the observation of this figure is possible to check the exact same behavior as verified for the neat IL (compare Figure 57 with Figure 49). From the data in Figure 56 and Figure 57 and its comparison with the same data for the neat IL (Figure 48 and Figure 49) it follows that the higher value observed for the total relaxation (Figure 56) at 273 K when compared to the neat IL, is mainly justified by the contribution of CSA relaxation mechanism (Figure 57) (see section 2.3.2.1, equation 17).

Both the high values of CSA relaxation (Figure 57) and this significant contribution for total relaxation (Figure 56) at low temperatures is in accordance to what was expected with this methodology (see section 2.3.2.1), which is the probation of large contribution of CSA (Figure 57) at low temperatures, based on the low experimental NOE values (Figure 59 and equation 20 in section 2.3.2.1) for this same temperature range.

2.3.2.2.2.3 - Structural Insight

This result also indicates that the water presence is contributing to influence the imidazolium ring relaxation by increasing rotational motion freedom, which is also associated with the observed lowering of composition viscosity (Figure 57).

2.3.2.2.2.4 - Plot Description - Figure 58

As was done before we have next analyzed the dipolar spin-lattice relaxation rates data ($R_{1dipolar}$) as represented in Figure 58. This data corresponds to the values obtained for individual carbons of $BMIM^+$ by using the previously referred methodology (see section 2.3.2.1) with a conjugation of equations (11 - 20) that ultimately by equation 20 allows the calculation of $R_{1dipolar}$ from an initial estimation of correlation times (τ_c) (affecting equations 11 and 19) and the use of experimental NOE and T_{1total} values.

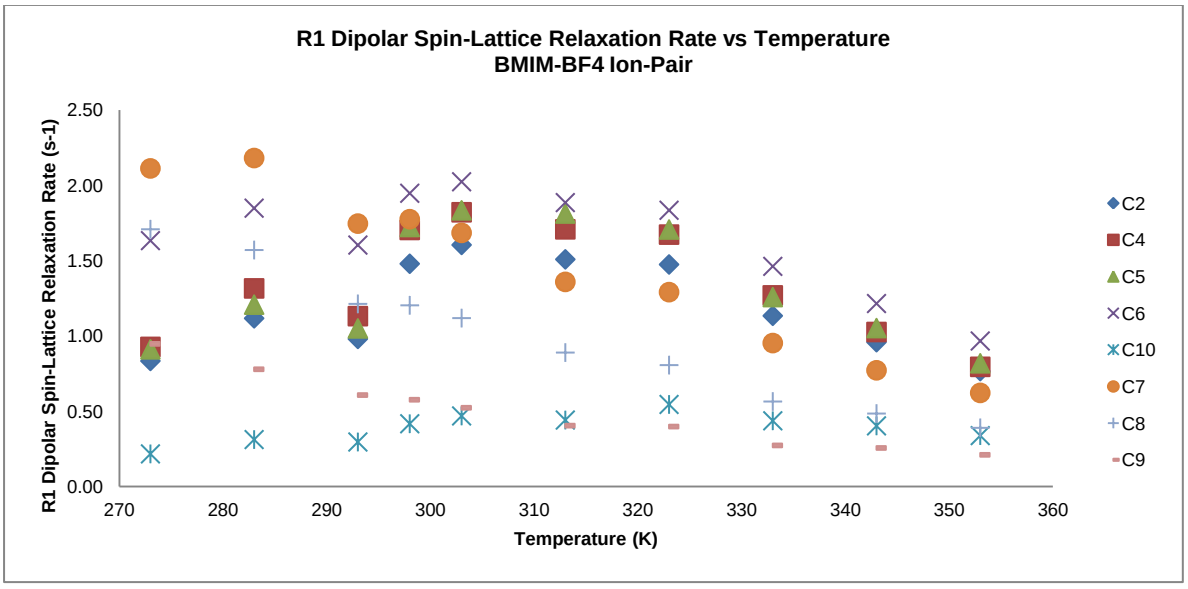

Figure 58 - Calculated dipolar spin-lattice relaxation rate values for the ion-pair composition of the 8 $[BMIM]^+$ carbons for the temperature range 273 to 353 K, highlighting the two relative maximums at 283 and 303 K that correspond to the cation-cation and cation-anion aggregation increasing periods, respectively.

From the plot in Figure 58 it is possible to realize the complementarity of dipolar relaxation rates (Figure 58) and CSA relaxation rates (Figure 57) to the total relaxation rates (Figure 56) (see equation 17 in section 2.3.2.1), which in essence is given by $R_{1total} = R_{1dipolar} + R_{1CSA}$. In this way, and by the previous observation of CSA relaxation rate data (in Figure 57) and the dipolar relaxation rate (in Figure 58), is obvious the contribution of dipolar relaxation at higher temperatures.

Taking into account the fact that according to the diffusion studies (Figure 23 and Figure 34) this composition consists in the one where there is a high probability (or life-time) of existence of ion-pairs, the irregularities verified (especially at room temperature) for the carbons relaxation deserve further analysis.

Globally, is possible to state that dipolar relaxation rate (Figure 58) behaviour for this composition (ion-pair) is very close to the one observed for the neat IL (Figure 50), also sharing close relaxation rates values for some temperatures (273 K to 283 K and 298 K to 353 K). The major difference is related with the dipolar relaxation rate value close to 293 K (Figure 58). At this point (293 K) the dipolar relaxation rate (Figure 58) presents an unexpected relative minimum of carbon $R_{1dipolar}$ values close to the ones observed at 273 K. This relative minimum (Figure 58) is especially pronounced for the imidazolium ring carbons (C2, C4 and C5) and the methyl and methylene adjacent carbon atoms, C10 and C6, respectively, which are known to be the principal participants in ionic and general polar interactions of the cation.

2.3.2.2.2.5 - Structural Insight

Although dipolar relaxation presents higher importance at higher temperatures, it is on the lower/medium temperature range that the most interesting irregularities are observed (Figure 58).

In terms of dynamics, this relative minimum (Figure 58) could represent either an increase or decrease in molecular rotation (being inside or outside the extreme narrowing region, respectively; remember BPP equation 11 in section 2.3.2.1, and R_1 relation with τ_c). The possibility of such decrease (Figure 58 and Figure 61) in the molecular rotation rate implies that with increasing temperature, from 273 K to 293 K, in the presence of low content of water, the cation would re-aggregate losing mobility. This hypothesis doesn't seem to be very likely.

Otherwise, if we consider that molecular rotation is increasing (Figure 58 and Figure 61) due to quick disruption of ion-pair aggregation, associated with the raise in temperature and preferential interaction of water with the charged portions of ILs at low water contents[104], it seems a much more appealing explanation and hypothesis.

Consequently, this minimum is followed by an increase of the relaxation rates (Figure 58) with temperature that indicates that the cation loses rotational mobility again. This loss of rotational mobility at higher temperature (298 K) after mobility gain (293 K) as probed by the relaxation is probably the best indication of ion-pair formation until this moment. The profile of the relaxation rate values (Figure 58) evolution in the temperature range (298 K to 353 K) can be associated with progressive ion-pair dissociation and consequently increase in the cation rotational mobility.

2.3.2.2.2.6 - Plot Description - Figure 59

As it is remembered, dipolar relaxation rates (Figure 58) irregular behaviour result largely from the experimental NOE values (Figure 59), which cannot be refuted to have physical motional meaning. As previously referred, experimental NOE values are employed in the calculation of $R_{1dipolar}$ by equation 20 in the iterative process described in section 2.3.2.1.

In conjugation with all the previously discussed diffusion indicators for ion-pair formation (Figure 23 and Figure 34), the addition of this NMR relaxation information is experimental evidence that supports this hypothesis.

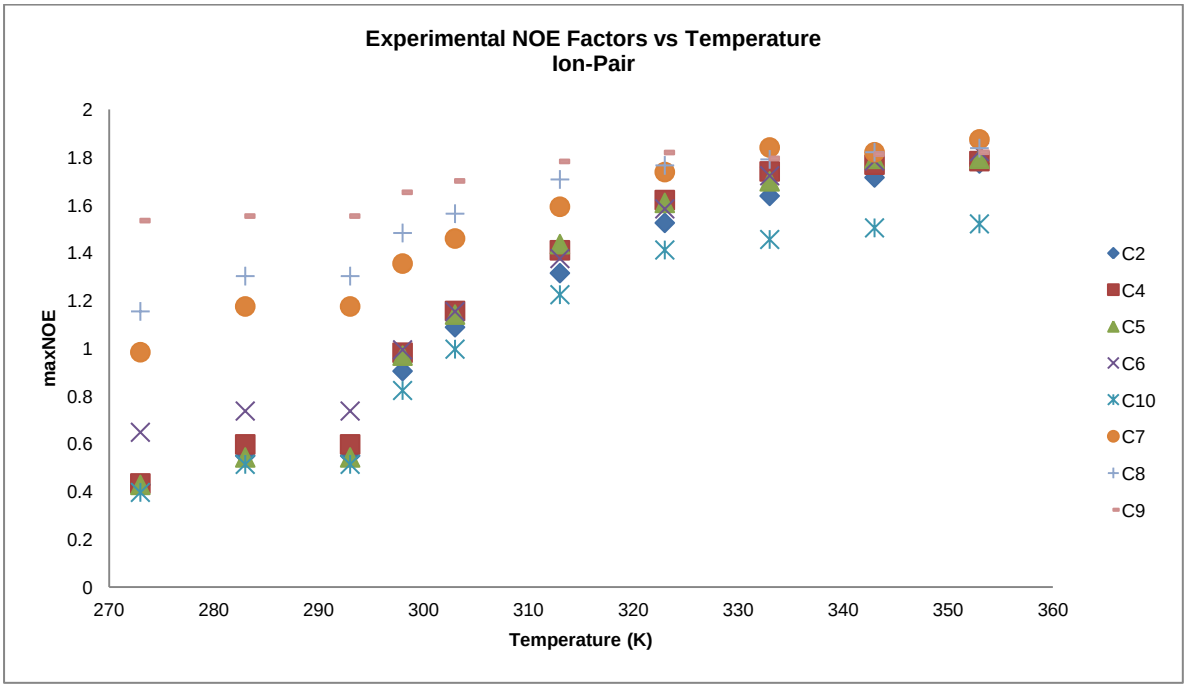

Figure 59 - Experimental NOE factor values for the ion-pair composition of the 8 $[BMIM]^+$ carbons for the temperature range 273 to 353 K, highlighting the relative minimum observed at 293 K that also matches the calculated dipolar relaxation rate minimum.

Looking now to the experimental NOE data (Figure 59), which has been acquired directly from the NMR experiments as explained previously in sections 2.2.2 and 2.3.2.2.1.7, is possible to verify that globally it present close similarity to the one observed for neat IL (Figure 51). However, although the global similarity between both datasets (Figure 59 and Figure 51), it is possible to observe that at 293 K a relative minimum value for all cation carbons is observed, especially pronounced for the imidazolium ring (C2, C4 and C5) and for the methyl and methylene adjacent carbons (C10 and C6, respectively), which is not verified for the neat IL (see Figure 51).

The correspondence of these minimum at the temperature 293 K (Figure 59), with the one verified for dipolar relaxation rate values (Figure 58) proves the relation between the two results (equation 20, section 2.3.2.1). The temperature of 323 K corresponds to the one where the experimental NOE (Figure 59) for almost every carbon atom evidences a decline in the positive

progression slope of its values. In this way, it is shown the relation between the experimental NOE (Figure 59) and the dipolar relaxation rate data (Figure 58).

2.3.2.2.2.7 - Plot Description - Figure 60

Another result derived from the iterative process (by equation 19, section 2.3.2.1) is the maximum NOE value (Figure 60). As it has been already mentioned, these maximum NOE values reflect entirely the common origin of the dipolar relaxation rates (equation 11, 19 and 20, section 2.3.2.1) (Figure 58) previously discussed, presenting total correspondence of its relative maximums and minimums with dipolar relaxation rates (Figure 58) minimums and maximums, respectively.

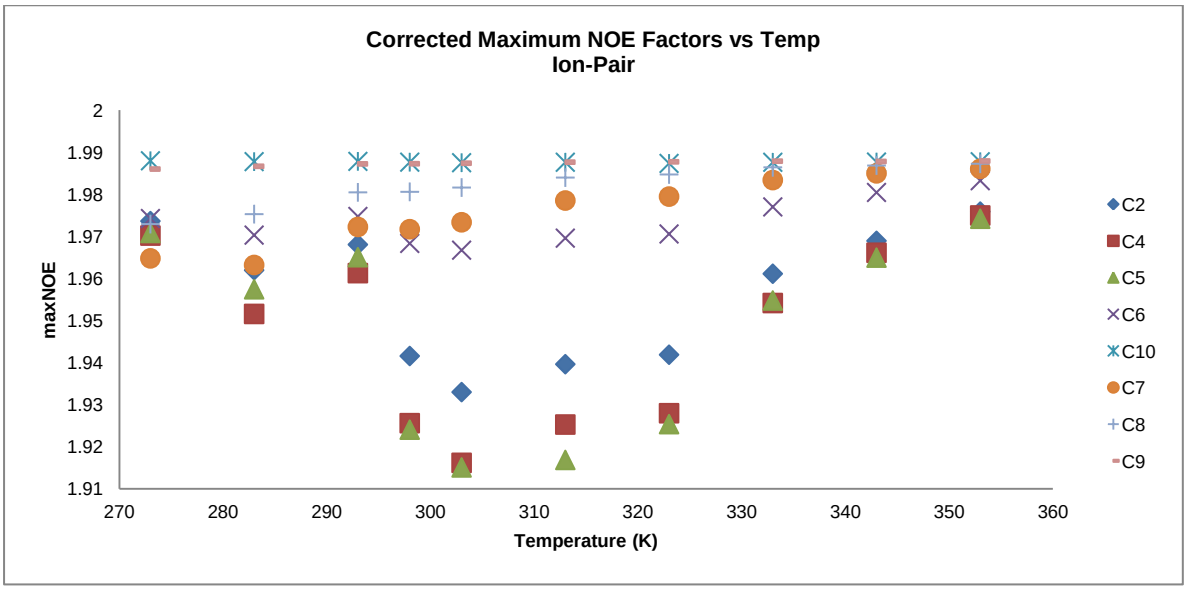

Figure 60 - Calculated maximum NOE factor values for the ion-pair composition of the 8 $[BMIM]^+$ carbons for the temperature range 273 to 353 K, highlighting the complementary with the dipolar relaxation rate reasoned by the mathematical iterative process, presenting a relative maximum value at 293 K for the imidazolium ring carbons (C2, C4 and C5).

As can be observed in Figure 60, and by comparison with Figure 52, these maximum NOE factor values, just like the relaxation rates values (Figure 56, Figure 57 and Figure 58), present close relation with the ones obtained for neat IL (Figure 48, Figure 49 and Figure 50), fundamentally regarding the range of determined values (1.92 to 1.97 for imidazolium ring carbons; 1.97 to 1.98 for C6; 1.96 to 1.988 for C7; 1.97 to 1.988 for C8; and 1.988 for C10 and C9).

2.3.2.2.2.8 - Structural Insight

Apparently, the maximum NOE values (Figure 60) reflect distinctively the segmental dynamics of each carbon atom, because of the highest values for the two methyl carbons, known for its rapid

segmental dynamics, and the detachment of the values presented for the ring carbon C2 in comparison to other ring carbons C4 and C5. The relevance of this observation (Figure 60) is the possibility of discrimination of the known higher influence of hydrogen bonding of water with the ring carbon C2, than with ring carbons C4 and C5.[91]

2.3.2.2.2.9 - Plot Description - Figure 61

In Figure 61 the correlation time corresponding to the first root (initial estimated values equal to 10 picoseconds in equation 11) of the iteration process (see section 2.3.2.1) is depicted as before. In accordance to the previous discussed data, especially dipolar relaxation rates (Figure 58), experimental NOE factors (included in equation 20) (Figure 59) and corrected maximum NOE factors (calculated by equation 19) (Figure 60), the rotational correlation time (changed for least square minimization of $1/T_{1calculated}$ with respect to $1/T_{1dipolar}$ by equation 11) (Figure 61) reflect the behavior of these parameters.

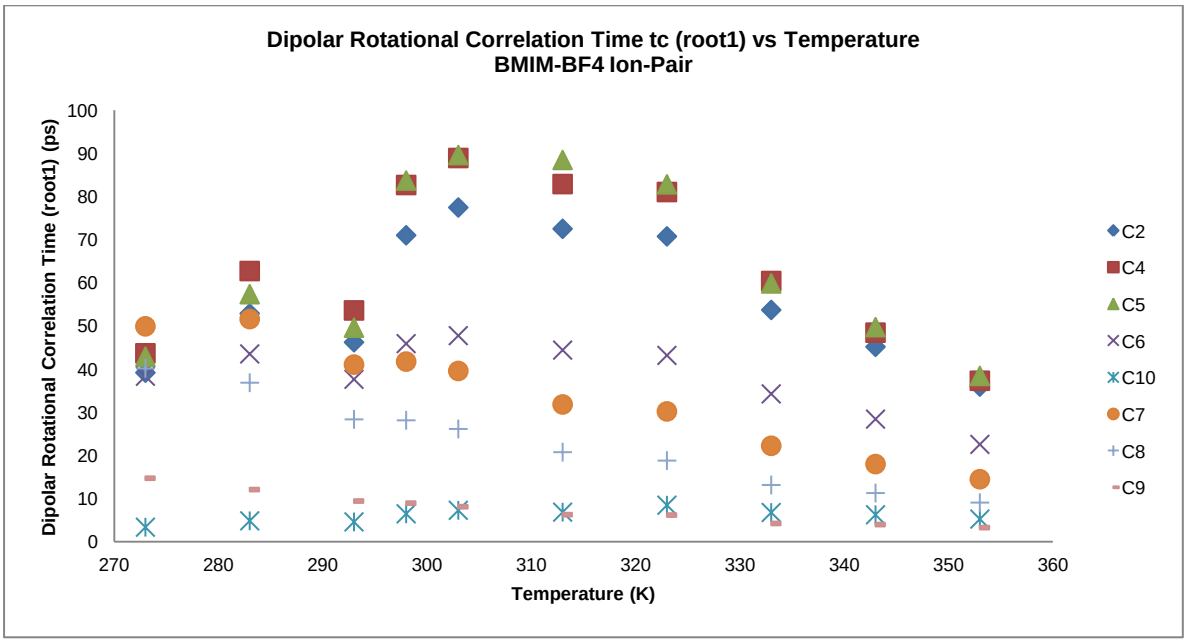

Figure 61 - Calculated correlation times (root1) values for the ion-pair composition of the 8 $[BMIM]^+$ carbons for the temperature range 273 to 353 K, highlighting the correspondence with the dipolar relaxation rate reasoned by the mathematical iterative process, presenting a relative minimum value at 293 K for the imidazolium ring carbons (C2, C4 and C5).

Again, globally, this result (Figure 61) presents also close relation with the results observed for the neat IL (Figure 53), including an initial tendency for an increase of the correlation time (Figure 61) with temperature for the imidazolium ring carbons (C2, C4 and C5), reaching one relative maximum at 283 K and a absolute maximum (for the temperature range studied) at 303 K. Following the absolute maximum (Figure 61) a progressive decreasing of correlation time is observed, first with soft slope and from 323 K with a steeper slope.

The methylene carbon C6, with lower correlation time value (higher rotation rate) presents a similar behavior (Figure 61). The three aliphatic carbons C7, C8 and C9 present an almost monotonic decrease with increasing temperature, with soft fluctuations matching the minimums and maximums verified for the imidazolium ring carbons. Since these fluctuations are explained by the matching dipolar relaxation rate (see equation 11 in section 2.3.2.1) (Figure 58) fluctuations, they would disappear for these carbons (aliphatic chain) if it was consider no contribution by the CSA relaxation mechanism (see equation 17 in section 2.3.2.1) (Figure 57) to the total relaxation rate (Figure 56), as proposed in the literature.

2.3.2.2.2.10 - Structural Insight

The imidazolium adjacent methyl carbon C10 with lower correlation time values (Figure 61) of the whole cation (higher rotation rate; at lower temperatures), presents an almost constant evolution over the temperature range, demonstrating its permanent fast rotating regime in the molecule at any condition. This fact is associated with the referred contribution of the local segmental fast rotation characteristic of the methyl groups, explained for example by the contribution of the spin-rotation relaxation mechanism, typical for such groups.

As in the case of the neat IL (Figure 53) this dipolar correlation time (Figure 61) presents many inaccuracies, as the questions of too high molecular rotation rates (picoseconds per radian) for all carbons and the verification of correlation time values decreasing for low temperatures, which is incompatible with mechanical classics and Stokes-Einstein-Debye equation.

2.3.2.2.2.11 - Plot Description - Figure 62

Because of the previous stated reasons the dipolar rotational correlation times of root1 (Figure 61) cannot be considered reliable and accurate. In this way, just like in the case of the neat IL (Figure 53), we calculate the dipolar rotational correlation times with the solution corresponding to root2 (Figure 62) of the same methodology[84] (initial estimated values equal to 10 nanoseconds in equation 11, see section 2.3.2.1).

Figure 62 represents the results obtained for root2.

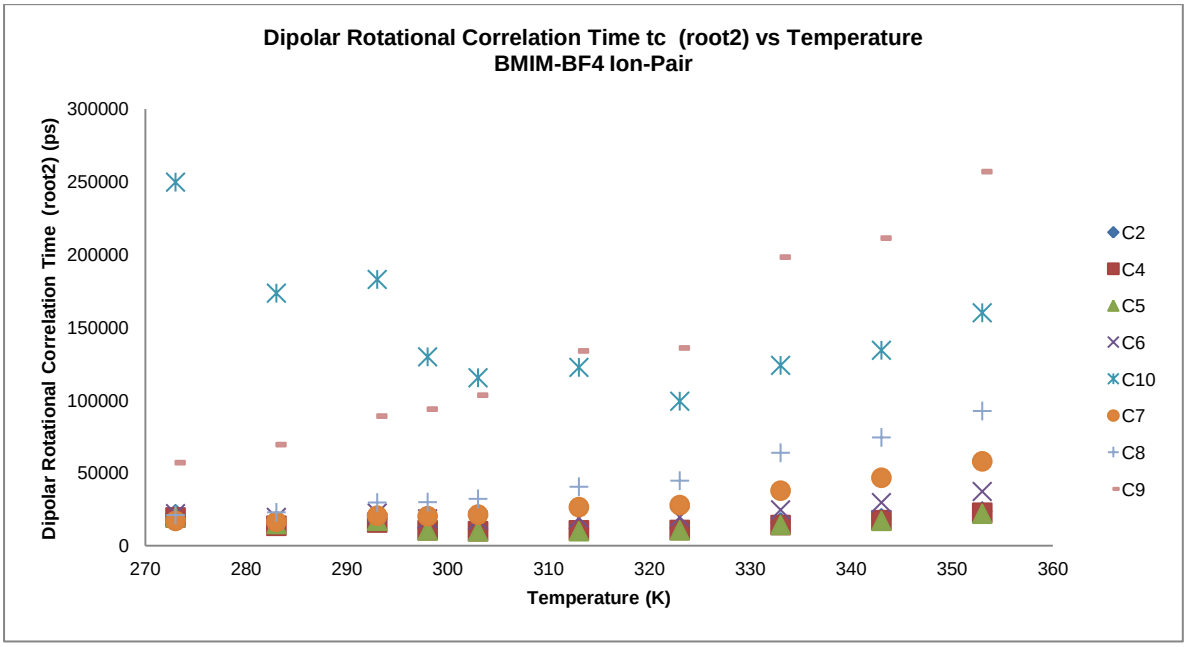

Figure 62 - Calculated correlation times (root2) values for the ion-pair composition of the 8 $[BMIM]^+$ carbons for the temperature range 273 to 353 K, highlighting the symmetric correspondence with the dipolar relaxation rate reasoned by the mathematical iterative process, presenting a relative maximum value at 293 K for the imidazolium ring carbons (C2, C4 and C5).

By the observation of the graphical data representation for root2 (Figure 62) a close relation to what was observed and discussed for root2 of the neat IL (Figure 54) is verified. The global trace for all carbons is described the same way as it was done for the root2 result for the neat IL (Figure 54), with exception for the relative maximums and minimums (Figure 62).

Regarding the evidenced maximums and minimums (Figure 62) is possible to find a match between them and the ones previously verified for the graphical representations of dipolar spin-lattice relaxation rates (Figure 58), maximum NOE factors (Figure 60) and experimental NOE factors (Figure 59), which means that this root2 (Figure 62) result is explained by the correlation of the different parameters through the iterative process (equations 11, 19 and 20 in section 2.3.2.1), just as in the case of the neat IL (Figure 54).

2.3.2.2.2.12 - Structural Insight

Although the correlation times (Figure 62) are in the nanoseconds scale, the observed temperature dependence has no relation with classic mechanics and SED equation. Therefore, just as in the case of neat IL (Figure 54), the results have no reliability and accuracy.

2.3.2.2.2.13 - Plot Description - Figure 63

Figure 63 represents the dipolar rotational correlation times obtained by the simpler methodology as explained before (by a derivation of equation 11, see section 2.3.2.1). A first observation is that the result is very similar to the one obtained for the neat IL (see Figure 55).

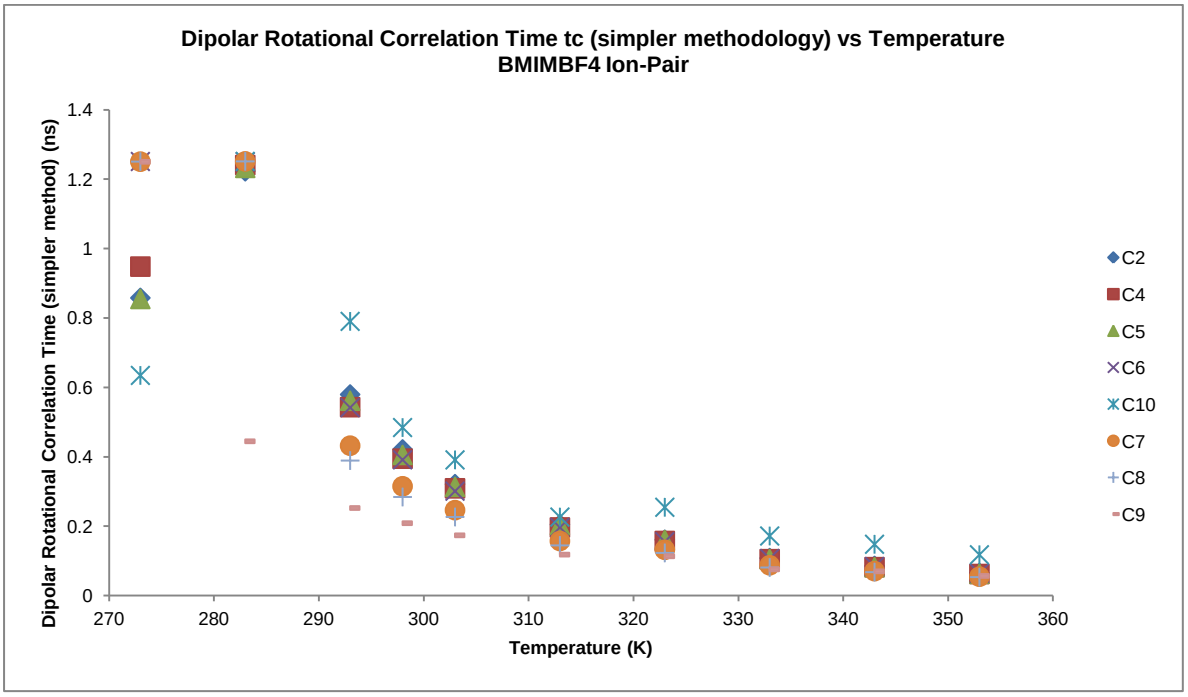

Figure 63 - Calculated correlation times (simpler methodology) values for the ion-pair composition of the 8 $[BMIM]^+$ carbons for the temperature range 273 to 353 K, highlighting the correspondence with the total relaxation rate reasoned by the mathematical procedure utilized, presenting a maximum value at 283 K for the imidazolium ring carbons (C2, C4 and C5).

In comparison to the neat IL (see Figure 55), two additional maximums for carbons C7 and C8 of the aliphatic chain are observed (Figure 63), as well as the matching of the methyl carbon C10 maximum with the other maxima at 283 K.

2.3.2.2.2.14 - Structural Insight

This data (Figure 63) is very interesting, because it suggests that with the addition of water (8% molar fraction) it seems to be possible to "homogenise" the cationic individual carbon rotation, with the exception of the aliphatic methyl carbon C9 that maintains its high rotational dynamics due to the contributions of high segmental dynamics of methyl carbons, plus the higher aliphatic chain mobility.

The profile obtained for C9 (Figure 63) matches exactly the one obtained for the neat IL (see Figure 55), indicating that segmental dynamics is much more effective for C9 "total rotational dynamics". The shifting of the carbon C10 maximum from 293 K in neat IL to 283 K in the ion-pair composition (compare Figure 63 with Figure 55) indicates that the addition of water probably

prevent/disrupt the initial aggregation process at 293 K that was believed to be highly related with imidazolium adjacent methyl C10, or any kind of particular interaction, which was decreasing its mobility, which it was establishing previously in the neat IL (Figure 55).

Another curious fact is the extension of the maximum value for aliphatic chain carbons C7 and C8 from 273 to 283 K (compare Figure 63 and Figure 55), which might be associated with a decreasing of the aliphatic chain mobility due to more effective hydrophobic tail segregation caused by water addition.

2.3.2.2.2.15 – Ion-Pair Comparative Analysis between Rotation and Diffusion Data

Considering the combined diffusion and rotation results from $BMIMBF_4$ ion-pair composition dependence with temperature, it is possible to establish a connection between both.

By observing the diffusion coefficients (Figure 33) and the correlation times (Figure 63) plots for this composition, it is possible to state that is verified a progressive increasing in $BMIM^+$ diffusional and rotational motions with increasing temperature. While diffusion increases progressively faster with increasing temperature (exponentially), rotation increases greatly until approx. 313 K and then progresses slowly, becoming almost constant.

As was the case for neat composition, with respect to structural organization, by observing the $BMIM^+$ hydrodynamic radius diffusion data (Figure 38), it exhibits an initial increasing from 273 to 293 K. It was then possible to find relation with the elevated correlation time values (root1 and simpler methodology) of all $BMIM^+$ carbons (with exception for C9) (Figure 61 and Figure 63), which present correlation time maximums at 283 K. This relation indicates possibly some kind of phase transition in this range (273 to 293 K), which is associated for one side with alterations in $BMIM^+$ state of aggregation reflected by the overall rotational motion, and is also reflected on the other side by the relative diffusion increasing of dioxane when compared with $BMIM^+$. (root1 results are considered in this case due its relation with experimental NOE values)

Considering rotation and diffusion on ion-pair formation, there are three indicators that support this notion, which are: the equal value (approx. 2.50) of the hydrodynamic radius (Figure 38) for both ion species in the temperature range of 293 to 303 K; the equal diffusion coefficient (Figure 28) for both ion species during this range (at 298 K); and the correlation time absolute maximum at 298 K (root1) after a relative minimum at 293 K (Figure 61), indicating re-aggregation (cation-anion formation; 298 K) after aggregation disruption (of cation-cation; 293 K).

All data indicates that from the temperature of 303 K $BMIM^+$ starts progressively losing the diffusional state of aggregation, considering its decreasing in hydrodynamic radius relative value (Figure 38), and the observed progressive increasing of the overall cation diffusional and rotational motions acceleration (Figure 61 and Figure 63).

2.3.2.2.3 – IL in Infinite Dilution Composition

Proceeding now to the analysis of the infinite dilution composition is expected to observe different results in comparison to the ones discussed until now for the neat IL and ion-pair composition.

2.3.2.2.3.1 - Plot Description - Figure 64

Starting with the observation of the total spin-lattice relaxation rate experimental values profile (Figure 64) is immediately possible to realize that the lower temperature values obtained for the R_{1total} are similar to the values obtained for the other compositions (Figure 48 and Figure 56) but at high temperatures and that almost every carbon presents a steeper decrease (higher slopes) of R_{1total} in the low temperature range (from 273 to 283 K).

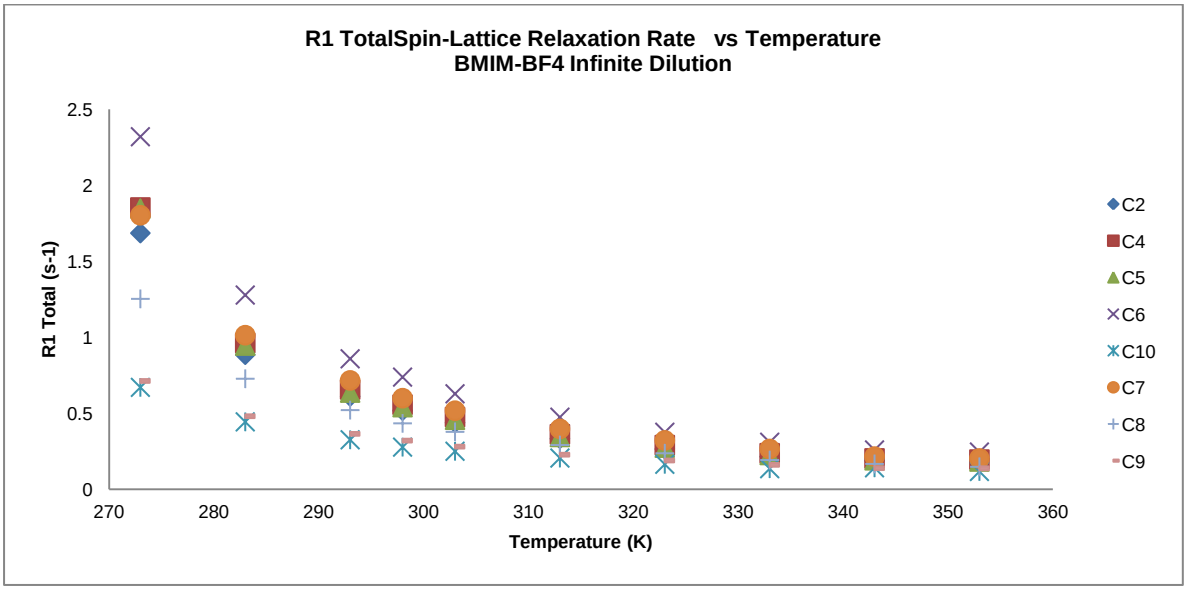

Figure 64 - Total spin-lattice relaxation rate values for the infinite dilution sample of the 8 $[BMIM]^+$ carbons for the temperature range 273 to 353 K, highlighting the progressive value decreasing associated with increasing molecular mobility.

This experimental profile (Figure 64) is in accordance to what was expected, since the infinite dilution sample implies a large amount of water and consequently a decreased viscosity when compared to the other two composition (Figure 48 and Figure 56). This lower viscosity implies a high higher rotational dynamic freedom of the overall molecule present in solution.

Initially is observed higher relaxation rate (Figure 64) values at low temperatures for aromatic carbons C2, C4 and C5, methylene carbon C6 and aliphatic chain carbon C7 and C8. At higher temperatures is observed that every carbon share almost the same relaxation rate (Figure 64).

2.3.2.2.3.2 - Structural Insight

The initial values (Figure 64) are justified by the known lower mobility of the imidazolium ring and adjacent carbons at lower temperatures, and the final values (Figure 64) represent total accelerated free motional behavior of the whole imidazolium that indicates the disruption of any possible chemical interaction, such as the ones discussed until now (ionic interaction and hydrogen bonding).

The initial accentuated decrease in the R_{1total} (Figure 64) for the lower temperatures indicates also that possible interactions between cation-water, cation-anion or cation-cation that may exist at these temperatures are quickly disrupted from 273 to 283 K, as has been verified already by diffusion data.

2.3.2.2.3.3 - Plot Description - Figure 65

Considering now the CSA spin-lattice relaxation rate values (Figure 65), it is possible to determine that it presents a similar profile as the total relaxation rate (Figure 64), since it decreases sharply from 273 to 283 K, a little less from 283 to 293 K, and after 298 K it takes an almost constant profile (equation 17, section 2.3.2.1).

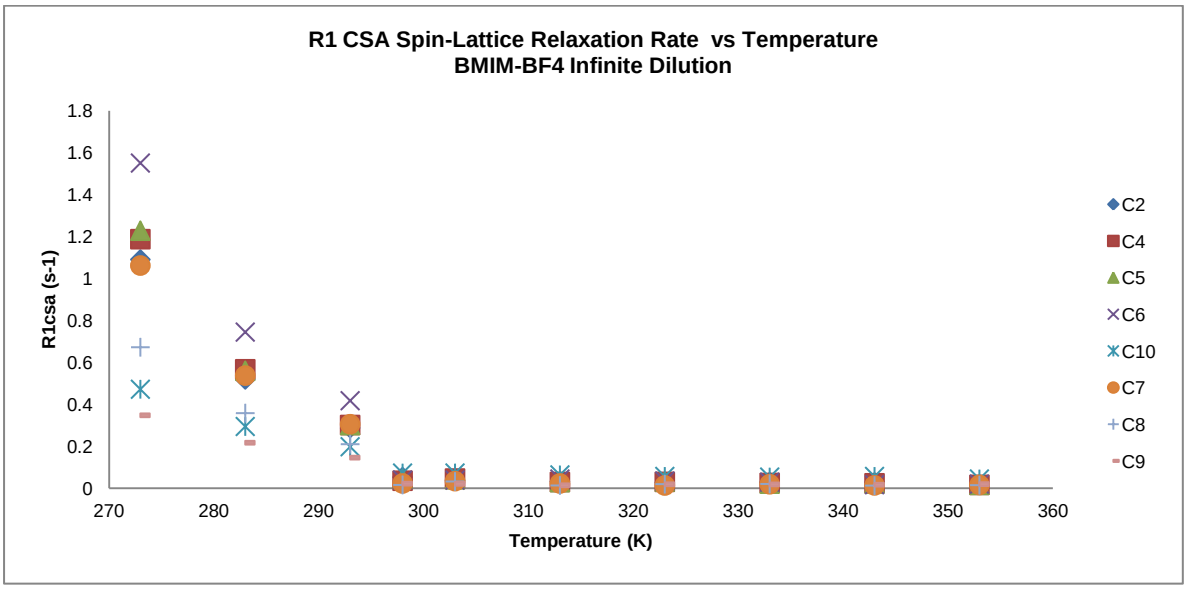

Figure 65 - CSA spin-lattice relaxation rate values for the infinite dilution sample of the 8 $[BMIM]^+$ carbons for the temperature range 273 to 353 K, highlighting its high contribution for the imidazolium ring carbons (C2, C4 and C5) total relaxation rate at lower temperatures.

Important to notice again that CSA relaxation rate (Figure 65) is part of the contribution to the total relaxation rate (equation 17, section 2.3.2.1) (Figure 64), which means that some complementarity is expected in dipolar relaxation rate (Figure 66).

2.3.2.2.3.4 - Plot Description - Figure 66

As it was expected by the observation of a CSA relaxation rate minimum at 298 K (Figure 65), a complementary relative maximum is observed for dipolar spin-lattice relaxation rate at the same temperature (equation 17, section 2.3.2.1) (Figure 66). Beyond this mark, is possible to observe a complementary profile of dipolar relaxation rates with respect to the total relaxation rates profile (compare Figure 65 and Figure 66).

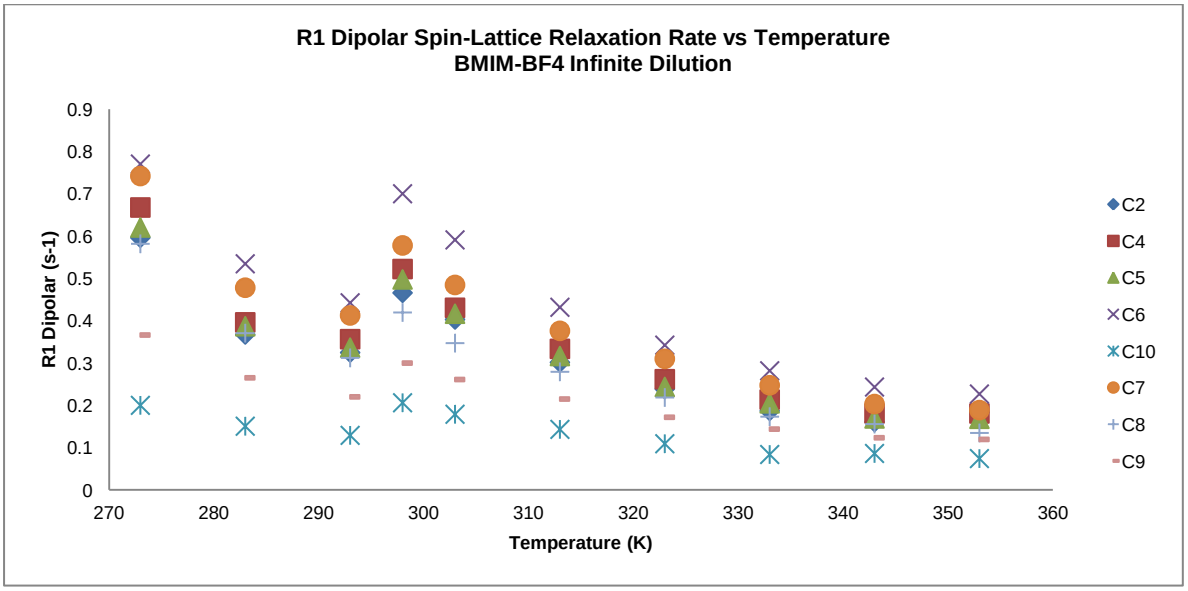

Figure 66 - Dipolar spin-lattice relaxation rate values for the infinite dilution sample of the 8 $[BMIM]^+$ carbons for the temperature range 273 to 353 K, highlighting the almost permanent decreasing values, except for the relative maximum at 298 K that is caused by the mathematical relation with the experimental NOE values in the iterative process.

The initial relative low values of dipolar relaxation rate (Figure 66), as in the other compositions (Figure 50 and Figure 58), are explained by the initial (low temperatures) elevated CSA relaxation rate values (equation 17, section 2.3.2.1) (Figure 65), which in turn are both explained by the integration of the experimental NOE factor values (equation 20) (Figure 67) in the iterative process (equations 11, 19 and 20, section 2.3.2.1), as it will be seen next. After the relative maximum at 298 K, all the cation carbons dipolar relaxation rates tend to converge for the same limiting value with increasing temperature, the same behavior as with CSA relaxation (Figure 65) and total relaxation rate (Figure 64).

2.3.2.2.3.5 - Plot Description - Figure 67

The experimental NOE values (Figure 67), as it has already been referred, are the second experimental source of values of the iterative process (equation 20, section 2.3.2.1). For this reason, together with total spin-lattice relaxation rates (Figure 64), they are the conditioning parameters that give to all the other parameters the evolution profile and specific behaviors (equation 20, section 2.3.2.1), such as maximums and minimums. In this way, and because of the continuous profile of total relaxation rates observed before (Figure 64), the sudden alterations in the graphical traces of the parameters resultant of the iterative process (see section 2.3.2.1), namely dipolar relaxation (Figure 66) and CSA relaxation rate (Figure 65), have to be associated with experimental NOE factor values (Figure 67).

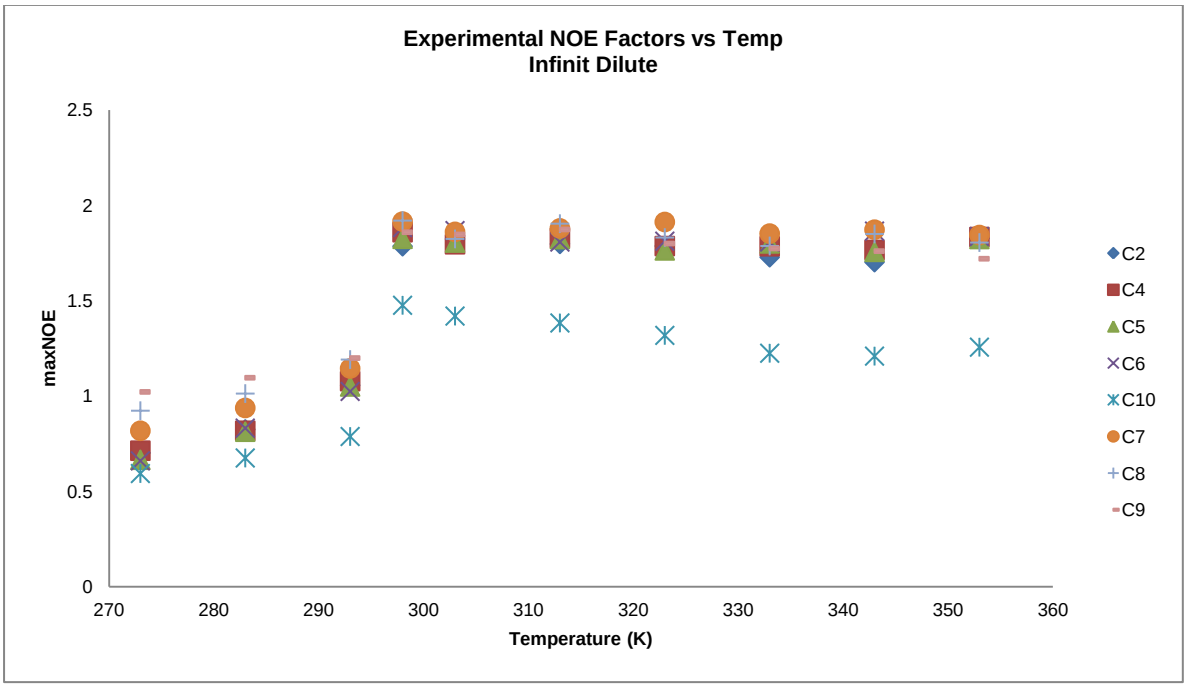

Figure 67 - Experimental NOE factor values for the infinite dilution sample of the 8 $[BMIM]^+$ carbons for the temperature range 273 to 353 K, highlighting the relative maximum observed at 298 K that also matches the calculated dipolar relaxation rate maximum.

By the observation of the plot of the experimental NOE factors in Figure 67, the origin of the maximum (of dipolar relaxation rate, Figure 66) and minimum (of CSA relaxation rate, Figure 65) of the previous results at 298 K can be explained, which is the experimental NOE maximum at the same temperature (equations 20 and 17, section 2.3.2.1) (Figure 67). This graphical representation shows yet a soft increasing of experimental NOE factors from 273 to 293 K, a huge increase from 1 to 1.988 (maximum value) for almost every carbon (exception of imidazolium adjacent methyl C10) from 293 to 298 K, and a constant progression in the following temperature range (298 to 353 K) (Figure 67).

2.3.2.2.3.6 - Structural Insight

This sudden increase of NOE factors experimentally determined from 293 to 298 K (Figure 67) may be associated with some kind of solution phase change, which could be associated with the previously referred total disruption of the remaining cation-cation aggregates, proposed in diffusion and, recently, in the discussion of the total relaxation rate value (Figure 64).

2.3.2.2.3.7 - Plot Description - Figure 68

The maximum NOE factor is represented in Figure 68. Just as in the case of the previous compositions (neat in Figure 52 and ion-pair in Figure 60), the profile of the maximum NOE factor (Figure 68) totally corresponds to the profile of the parameters involved in its calculation (equations 11, 19 and 20, section 2.3.2.1) (total relaxation rate in Figure 64 and experimental NOE factor in Figure 67), and also in the other resultant parameters discussed until now (dipolar in Figure 66 and CSA relaxation rate Figure 65).

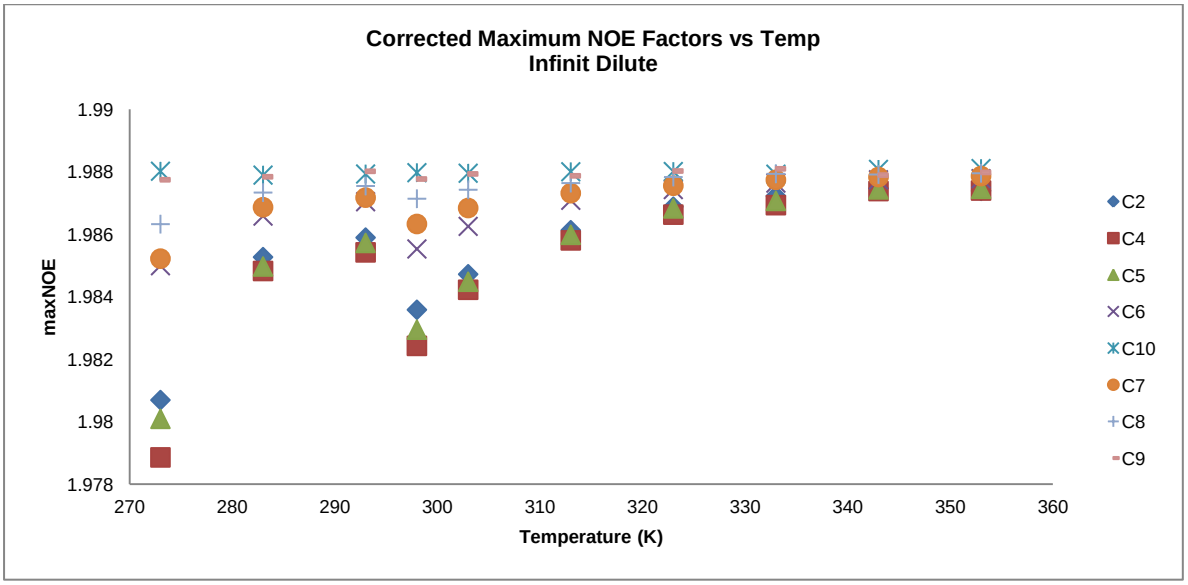

Figure 68 - Calculated maximum NOE factor values for the infinite dilution sample of the 8 $[BMIM]^+$ carbons for the temperature range 273 to 353 K, highlighting the complementary with the dipolar relaxation rate reasoned by the mathematical iterative process, presenting a relative minimum value at 298 K for the imidazolium ring carbons (C2, C4 and C5).

Due to the relation between the parameters, maximum NOE (Figure 68) values and dipolar relaxation rate (Figure 66) have a complementary profile, every maximum or increase in one plot corresponds to a minimum or decrease in the other. All these relations and complementarities are justified by the common source of the parameter values, which is the iterative process previously presented (equations 11, 19 and 20, section 2.3.2.1).

2.3.2.2.3.8 - Plot Description - Figure 69

Figure 69 represents the result for the first root of the iterative process (initial estimated values equal to 10 picoseconds in equation 11) for the dipolar rotational correlation time. It is possible to observe that again this parameter is being influenced by the values obtained for the other parameters (equations 11, 19 and 20, section 2.3.2.1). In this way, the root1 correlation time profile obtained (Figure 69) matches perfectly with the one verified for dipolar relaxation rate profile (Figure 66), as it has been verified for the other compositions (compare Figure 50 with Figure 53 and Figure 58 with Figure 61).

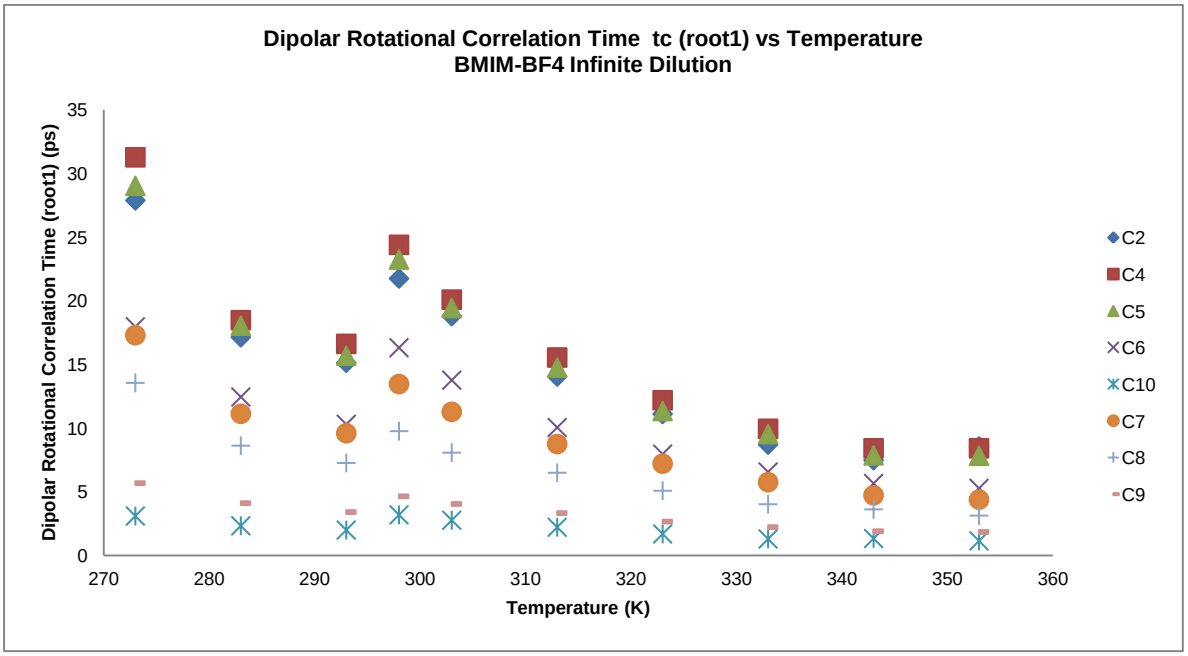

Figure 69 - Calculated correlation times (root1) values for the infinite dilution sample of the 8 $[BMIM]^+$ carbons for the temperature range 273 to 353 K, highlighting the correspondence with the dipolar relaxation rate reasoned by the mathematical iterative process, presenting a relative maximum value at 298 K for the imidazolium ring carbons (C2, C4 and C5).

Although at first sight the correlation time profile of root1 (Figure 69) may seem credible, the fact is that the time scale (picoseconds) of the rotational correlation time, as the case for the same root1 result of the other compositions (Figure 53 and Figure 61), is physically not expected and then not very reliable. In addition, the eventual decreasing of carbons rotational dynamics (higher correlation time; maximum value) at 298 K (Figure 61) associated with the hypothesis of aggregates disruption is not very sustainable.

2.3.2.2.3.9 - Plot Description - Figure 70

Taking into account the above facts about root1 result discrepancies (Figure 69), root2 (Figure 70) was also calculated (initial estimated values equal to 10 nanoseconds in equation 11, see

section 2.3.2.1), as for neat IL (Figure 54) and ion-pair (Figure 62). The root2 result of dipolar rotational correlation times is presented in Figure 70. For this composition the discrepancies are even more prominent, since all the carbons tend to decrease their rotational dynamics for higher temperatures (Figure 70).

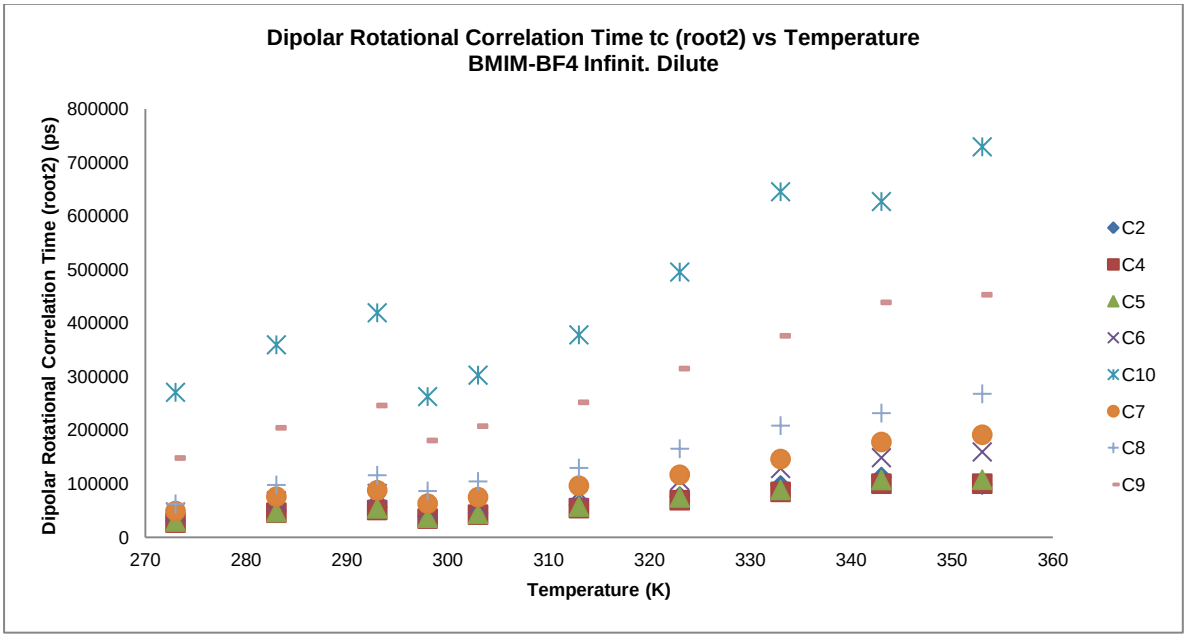

Figure 70 - Calculated correlation times (root2) values for the infinite dilution sample of the 8 $[BMIM]^+$ carbons for the temperature range 273 to 353 K, highlighting the symmetric correspondence with the dipolar relaxation rate reasoned by the mathematical iterative process, presenting a relative minimum value at 298 K for the imidazolium ring carbons (C2, C4 and C5).

This representation of the results for root2 in Figure 70, present the expected symmetric profile relative to root1 (Figure 69), and the only virtue is the expected time scale, which is the nanoseconds scale for rotational correlation times.

2.3.2.2.3.10 - Plot Description - Figure 71

Considering now the direct calculation of the dipolar rotational correlation time by simpler methodology (derived from equation 11, in section 2.3.2.1), represented in Figure 71, it is possible to observe two important features that may be significant to justify previous interpretations.

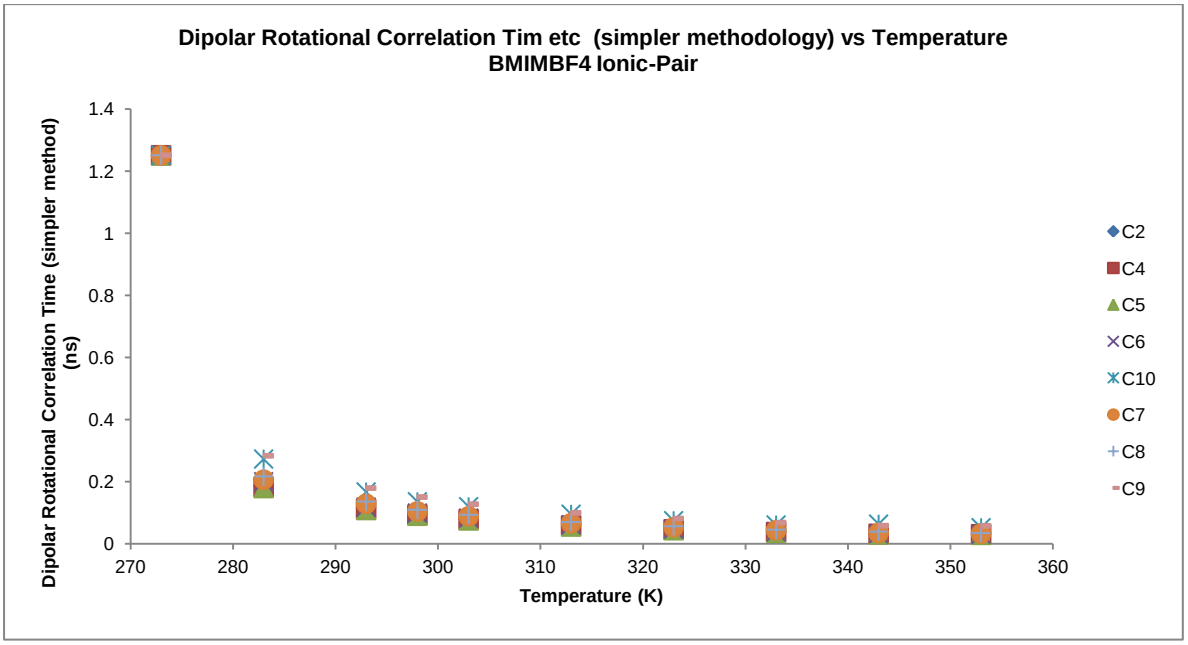

Figure 71 - Calculated correlation times (simpler methodology) values for the infinite dilution sample of the 8 $[BMIM]^+$ carbons for the temperature range 273 to 353 K, highlighting the correspondence with the total relaxation rate reasoned by the mathematical procedure utilized, highlighting the progressive value decreasing associated with increasing molecular mobility for the imidazolium ring carbons (C2, C4 and C5).

First of all the carbons have similar rotational dynamics, which is expected due to high water content (> 90% water molar fraction) and low viscosity of the solution, but two more facts are important: the first consists in the fact that for lower temperature (273 K) the rotational correlation times (Figure 71) are of equal value as the one for neat (Figure 55) and ion-pair (Figure 63) maximums (approximately 1.2 nanoseconds), which have been associated with aggregation phenomena; the second is the major decrease of dipolar correlation times (Figure 71) from 1.2 nanoseconds to almost the final value of 0.1 nanoseconds from 273 to 283 K.

2.3.2.2.3.11 - Structural Insight

This data (Figure 71) corroborates the previously mentioned hypothesis of clusters at low temperatures for infinite dilution composition, and the quick disruption of the same by raising the temperature above 283 K.

2.3.2.2.3.12 – Infinite Dilution Comparative Analysis between Rotation and Diffusion Data

Considering the combined diffusion and rotation results from $BMIMBF_4$ ion-pair composition dependence with temperature, it is possible to establish a connection between both.

Initially is immediately possible to observe two features that are: the almost linear soft increasing of $BMIM^+$ diffusional motion with increasing temperature (from 273 to 343 K) (Figure 39); and the abrupt initial (273 to 283 K) of $BMIM^+$ rotational motion increase (Figure 71), followed by stabilization (almost constant value from 283 to 353 K); uncovering the fact that rotational motion increases much faster than diffusional motion.

In terms of structural organization there are results that support the existence of residual $BMIM^+$ aggregation forms at the initial temperature range (from 273 to 293 K), for example: the $BMIM^+$ hydrodynamic radius data (Figure 44), which present a decrease during this range; and the previously referred abrupt initial increase of $BMIM^+$ rotational motion (Figure 71).

The temperature range that goes from 293 K to 353 K present constant profile for rotational motion and relative hydrodynamic radius (calculated from diffusion data), indicating constant structural organization, which supposedly consist of individual free-ion accelerated dynamics (diffusion and rotation; although diffusion coefficients only stabilize from 343 K).

2.4 – Conclusions and Future Work

Through this multinuclear NMR approach it has been possible to investigate thoroughly both the $BMIMBF_4$/water phase diagram and its dependence from temperature.

The most important conclusion from the combined diffusion and relaxation study is that it is possible to find a particular solution composition and temperature in the water/ILs phase diagram, where many indicators truly suggest a high-content of long lived ion-pairs.

There are two main results obtained from both studies (self-diffusion and relaxation) for a specific composition (8% water molar fraction and 298 K) that together represent major evidences for the high-content of ion-pair at this point, which are: first, the verification of the same self-diffusion coefficient values for cationic and anionic species, suggesting that at least the two ionic species are diffusing at the same rate; and second, the verification of abnormal reorientational behavior with decreased rotational mobility, which strongly suggests ion-pair formation after cluster disruption verification (from 283 to 293 K). These results have been determined after extensive analysis of relaxation and NOE experimental data, which have processed with a mathematical iterative methodology in order to obtain supposed meaningful parameters, such as the dipolar rotational correlation time and the maximum NOE factor. In any case, the dipolar rotational correlation time obtained with this methodology revealed very poor reliability and accuracy, therefore another simpler and direct mathematical approach was used, yielding better correlation time results.

Overall it is concluded that in these conditions the ion-pair consists in a relatively "long-lived" specie, sufficiently to be detectable by relaxation measurements and to affect diffusion coefficients in the milliseconds to nanoseconds time-scale, which can be verified in a particular composition (8% water molar fraction and 298 K) with reduced interval of conditions endure, consisting probably in a rapid exchange process between ion-pair and free ion, coexisting in solution, and driven by sample conditions alterations, which displace the equilibrium either for ion-pair high content formation, or for ion-pair disruption. In the extreme situations of neat and infinite dilution samples the equilibrium is shifted for the second.

In the context of other reported works, the same conclusions were obtained in this work concerning the neat IL and for low water content, such as: the cation/anion abnormal diffusion relation, which is against the Stokes-Einstein principle of higher diffusion of the smaller molecule; the verification of cation-cation and cation-anion aggregation for low water content and/or low temperatures (highlighting the aliphatic chain aggregation in the ion-pair composition for low temperatures), which are progressively disrupted and changed with water addition; and the expected free-diffusion dynamics and rotation for high water content and high temperatures.

It was also possible to conclude about the influence in the calculation of dipolar rotational correlation times of two different mathematical processes, considering or not CSA spin-lattice relaxation mechanism in addition to the dipolar spin-lattice relaxation.

Within the enormous number of future works that can be outlined from this study and idealized for complementing it, it should be referred: the density and viscosity studies (already present in various publications), [74–77] which may provide relevant physicochemical information to complement the diffusion and relaxation data; conductivity studies,[74–77] which provide electrical conductance specially meaningful for ion-pair investigation; and possibly the coupling of NMR to other techniques, preferably ones that include ultrafast detection such as FT-IR and dielectric relaxation spectroscopy.[20]

Further obvious future works consist in the application of this same combined methodology (diffusion and relaxation) to study other ILs, trying to find correlations between results, and ascertain the possibility of universal application of this methodology and maybe even try to find a pattern of behavior within different cation and anion structures that permit better structural and dynamic comprehension of ILs.

Chapter 3 – Exploring Diffusion in Alignment Media

3.1 – Introduction

As it will be largely developed in this chapter, alignment media are usually employed in the NMR stereochemical study of molecules. Because of the partial alignment induced by this media, molecules undergo a soft anisotropic motional manifestation. This anisotropic motion in alignment media concerns not only the reorientational molecular motion, that is partial restricted, but also all molecular motion, which includes the translational motion (diffusion).[107]

In this way, one of main objectives of this thesis was to characterize the self-diffusion behavior of small molecules in different alignment media and to investigate the relation between different degrees of alignment and self-diffusion. Furthermore, the possibility that the results obtained in these media may be extrapolated for different "realities", such as the molecular diffusion behavior in cells is also addressed.

3.1.1 – NMR Residual Dipolar Coupling (RDC) and Alignment Media

Although dipolar couplings, one of the four internal spin interactions, are absent in isotropic liquids because molecular free motion averages them out, and are frequently useless in solids, because of extensive intra and intermolecular anisotropic interactions (too complex), this NMR interaction presents great utility. If the molecules in question are placed in anisotropic liquids, intramolecular dipolar couplings do not average out completely giving origin to what is called the residual dipolar couplings. When placed in an anisotropic liquid molecules have some translational and rotational restrictions; and unlike isotropic liquids, the distribution of all possible molecular orientations is not equal. Briefly, anisotropic liquids in terms of motion can be considered to be in an intermediate position between pure solids and pure liquids, sharing characteristics with both of them.[108]

A mathematical description of dipolar couplings are detailed in Annex 2.1.

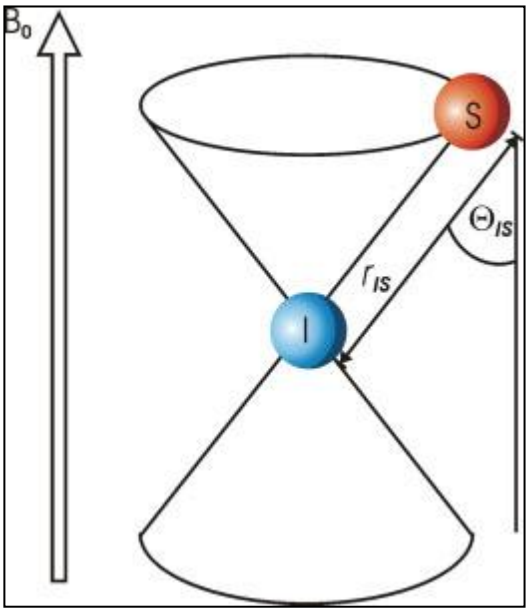

Figure 72 – The two cones covering the possible orientations of the vector connecting the spins I and S, which corresponds to one value of RDC for a given distance r_{IS}. For one bond RDCs, this is equal to the possible orientations of the bond I-S.[108]

Anisotropic liquid conditions are achieved with the so called alignment media, which will be presented later. For convenience, alignment media is the generic term used for all kinds of media that induce partial order to molecules in solution, such as liquid crystals or stretched polymer gels. The molecule takes up a preferred orientation with respect to the magnetic field, tumbling in an anisotropic manner (Figure 72).[108]

Historically, it has been early identified that anisotropic NMR interactions, like dipolar coupling, become directly observable from spectral data and, therefore, gives direct access to important structural information if the molecules are partially oriented in the magnetic field. Although this was recognized in the 1960s-70s[107,109–111], its use for structure determination was limited to few examples because of the problems associated with the necessary alignment of the molecule within the magnetic field. Only strong alignment (high degree of order) mainly with nematic liquid crystals[112–115] (Figure 73), leading to large dipolar couplings (kHz range) relative to scalar coupling (Hz range) and therefore complex spectra, or alignment due to magnetic (dia- and paramagnetic) alignment[116–119], were possible.

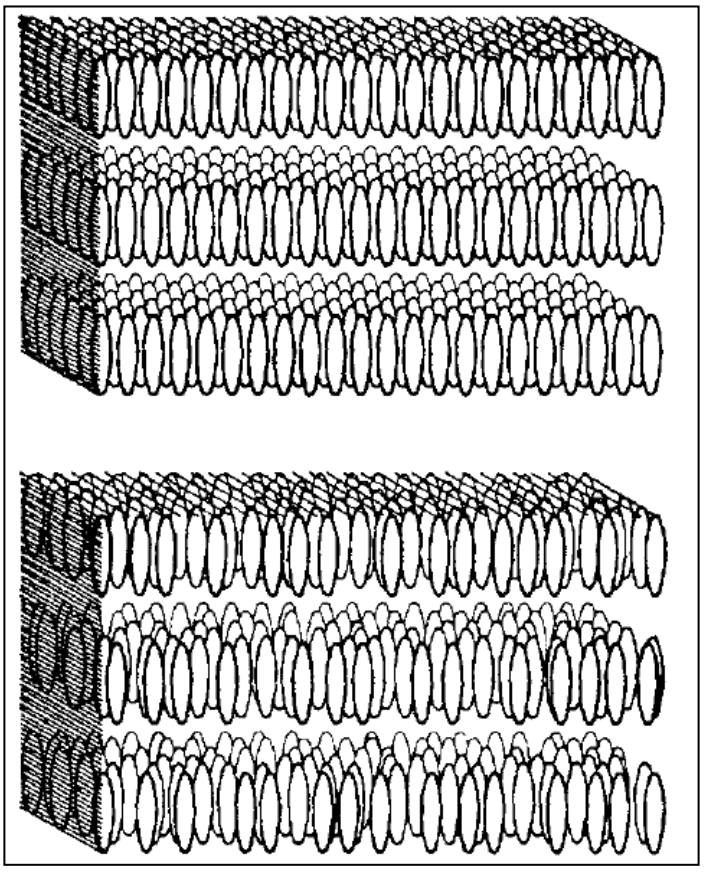

Figure 73 – Idealized representation of the molecular arrangement in nematic liquid crystal phases.[107]

In the 1980s a second technique for alignment appeared, that was strain-induced alignment in a gel (SAG)[120] (Figure 74). The technique was extensively used to study the properties of polymer gels by means of high-resolution deuterium NMR[121], but only lately gel alignment was used to induce RDCs in molecules dissolved into the gel (in 2000s)[122,123]. SAG allows the unrestricted scaling of alignment over a wide range and can be used for aqueous as well as organic solvents, depending on the polymer used (Figure 74). The first example for organic solvents was the RDCs measurement in stretched polystyrene (PS) gels swollen in $CDCl_3$.[124]

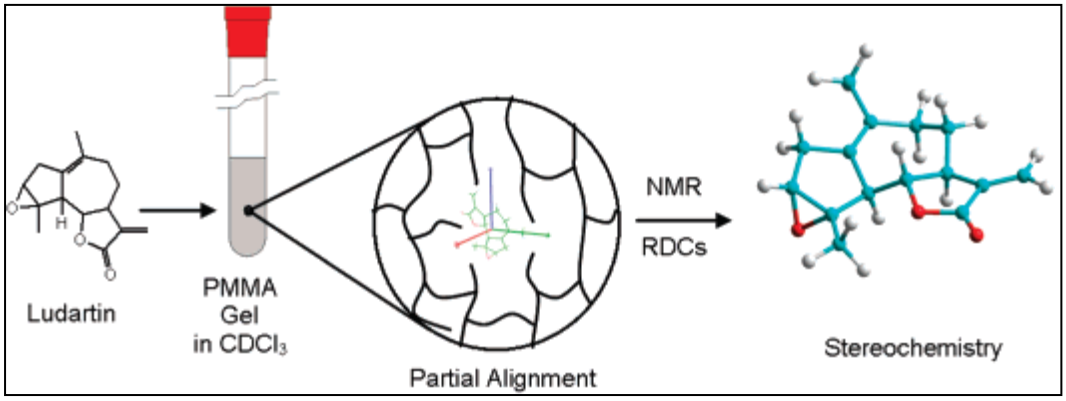

Figure 74 – Representation of the methodological process for the structure stereochemical acquisition using strain-induced alignment in a gel, namely PMMA.[125]

In the 1990s the situation changed with the appearance of media that induce partial alignment of biological macromolecules[126–133]. With these new alignment media the dipolar couplings could be scaled down from many kilohertz, as was the case with initial nematic liquid crystals, to a few hertz (order of the scalar coupling). Because of the low degree of order (order parameter $S < 10^{-3}$) imposed to molecules results in only a residual part of the dipolar coupling being observed (partial averaging) and therefore being known as Residual Dipolar Coupling (RDC). The information can be easily obtained from high-resolution NMR spectra because of its lower magnitude. The high information content of RDCs, together with the easiness of its measurement, explains the impact of this important NMR parameter on the determination of spatial structure and dynamics of proteins and oligosaccharides in recent years[134–138].

Despite the referred development verified in the alignment media field for biological macromolecules, applications to complicated organic molecules, such as natural products, is still very limited[139,140]. This is due to the fact that alignment media inducing a low degree of order were firstly designed only for water[141,142], a solvent in which most organic molecules are insoluble. In any case, from the 1990s onward, the development of alignment media compatible with solvents distinct from water (chloroform and dichloromethane namely) emerged[143–146]; continuing in the 2000s, particularly with polypeptide liquid crystals[147–151] associated with enantiomeric discrimination[152,153] (Figure 75) and molecular conformation[154,155]. NMR studies in alignment media for biological macromolecules and for small molecules are distinct applications of the same theory, however, the fact that both share largely the same principles and procedures, intersect the two areas and keep them next in the upcoming evolutions.[108,156,157]

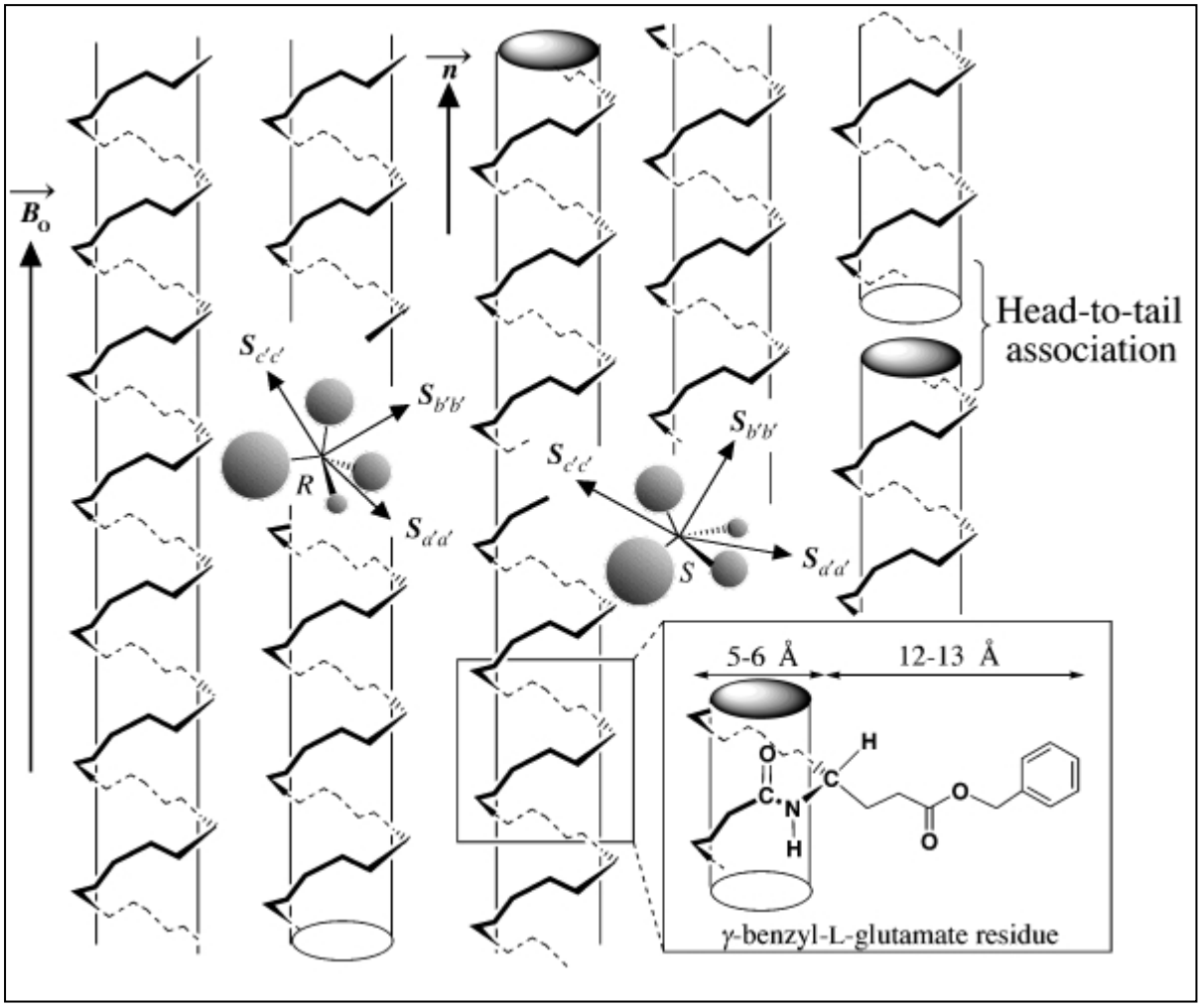

Figure 75 – Representation of the differential ordering effect for two enantiomers dissolved in PBLG liquid crystal phase.[152]

3.1.2 – Alignment Media

In this section the importance and diversity of the alignment media will be presented together with the fundamental characteristics of each alignment media type; the properties and importance of the degree of alignment; and finally some considerations of the whole practical and technical involvement of NMR RDCs, such as sample preparation and measurement methods.

3.1.2.1 – Alignment Conditions

As it was given to understand earlier in this section, the choice of alignment conditions is probably the most important factor in the applicability of the weak alignment media method for organic structure determination. The crucial parameters are the solvent polarity and the degree of alignment

induced by the alignment media. That is the reason for the intense search of appropriate alignment media using different solvents, different orientations and degrees of alignment is still in full restlessness at the moment.[108,124,125,158–166]

One of the fundamental characteristics of the degree of alignment induced in the solute molecule is that, it must be small enough (smaller in size compared with the *J*) so that the contributions of the dipolar interaction in different spin-pairs can be derived from the line splitting ^{1}T (total coupling). The equation that summarizes this relation between dipolar interaction and total coupling observed, for a ^{13}C-^{1}H spin-pair, over one bond is given by equation 22:[108]

$$T_{C-H} = 2 \cdot D_{C-H} + J_{C-H} \quad \textbf{(22)}$$

- $^{1}J_{C\text{-}H}$ is the scalar coupling in hertz.

In this way, the total coupling $^{1}T_{C\text{-}H}$ is can be slightly larger than $^{1}J_{C\text{-}H}$ for a positive residual dipolar coupling $^{1}D_{C\text{-}H}$ or smaller than $^{1}J_{C\text{-}H}$ for a negative $^{1}D_{C\text{-}H}$. This is applicable for other kinds of short or long-range couplings as ^{1}H -^{13}C, ^{1}H-^{1}H or ^{13}C-^{13}C. Worth noting that different notations may be used in the total coupling *T* description: the effective coupling J_{eff}; and an alternative that consists in $T = D + J$, where the line splitting is equal to $D + J$. This has no consequence in structure determination, since it represents only a scaling by a factor of 2.[108]

As it was mentioned above, sign determination may be straightforward if the observed residual dipolar couplings are smaller than the scalar couplings. When there is the case that the degree of alignment is too high, the occurrence of observed one-bond heteronuclear RDCs with bigger or same size to the scalar coupling lead to misinterpretations of the spectra, because of incapable sign determination. Another consequence of too-high degree of alignment is the impossibility to use indirect (F1) detection for the measurement of RDCs, as the cross-peak intensities are poor. When this happens is because there are experimental problems. One is that the heteronuclear transfer step becomes inefficient, since the transfer efficiency depends on matching of the actual coupling with the one set in the INEPT delay (normally 145 Hz for organic samples). The total coupling has to correspond to this requirement in aligned samples. When total couplings vary in wide spectral range frequencies, means that the transfer is poor. Another experimental problem is the broadening of the signal caused by extensive ^{1}H -^{13}C and ^{1}H-^{1}H long-range dipolar couplings. In this cases it is necessary to ascertain if the observed spin systems are still first order. In this way, by adjusting the degree of alignment it is possible to achieve easy and reliable RDCs measurement.[108,147]

As it was said before in this section, coexist nowadays two different methods employed in the alignment of small organic compounds, which are the strain induced alignment in a gel (SAG) and alignment using liquid crystals, which will be discussed further.[108]

3.1.2.2– Strain-Induced Alignment in a Gel (SAG)

Already in the 1980s it has been noticed the effect of introducing molecules, mainly small organic compounds, into polymers subjected to strain, which was the loss of isotropic tumbling dynamics by these probe molecules (Figure 76).[120] At that time the practical application of these results were essentially to achieve polymer structures information.[121] In this case, the polymer is not the target of the investigation, being instead the small organic molecules. To strain the polymer, one dry gel is inserted in an NMR tube and solvent is added (Figure 76). When swelled with solvent the gel should present a diameter larger than the NMR tube diameter, so that when the dry gel is introduced in the NMR tube and the solvent added, the gel may fit the tube walls inducing strain (Figure 76). Exist nowadays numerous gel/solvent combinations for this procedure.[108,122–125,158–160,165]

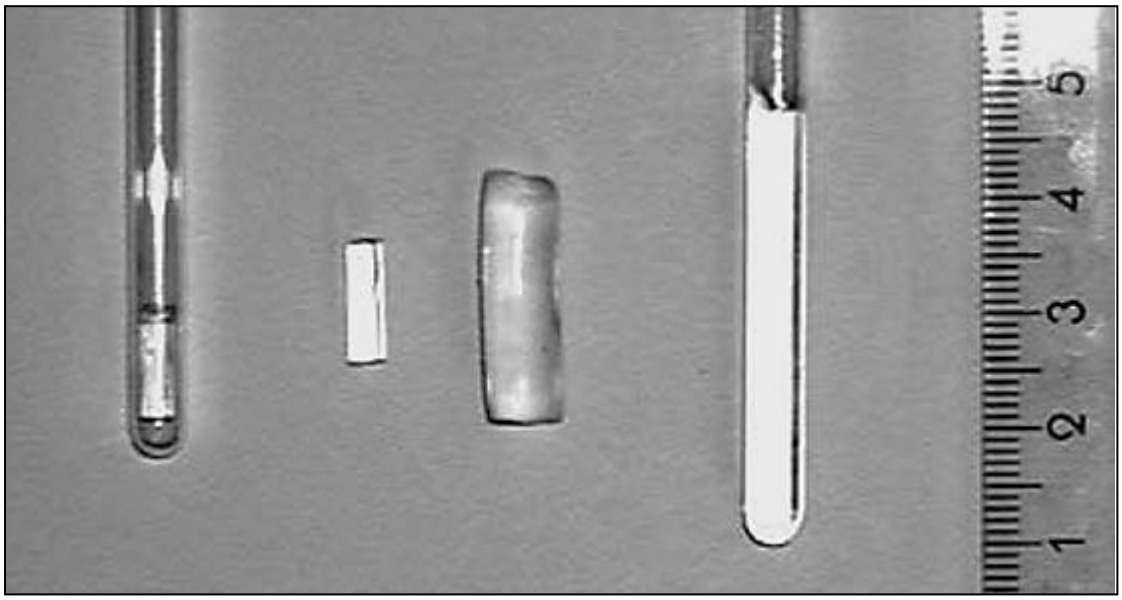

Figure 76 – Representation of the SAG method by using cross-linked polymer gels. In the figure: at left the dry gel into a 5mm-NMR sample tube; followed by the dry gel outside the tube; the swelled gel outside the tube; and the swelled gel into the tube. At right is placed a ruler showing the different length of the gels.[167]

3.1.2.3 – Liquid Crystals Alignment

As it was already revealed, the first conceived nematic liquid crystals had the disadvantage of inducing high degree of alignment and giving origin to NMR spectra dominated by the dipolar couplings.[107,109,111–115] In order to obtain reasonable RDCs, which are the ones that appear as a scalar couplings additional splitting (reduced dipolar couplings), it was necessary to achieve liquid crystals with low degree of alignment (Figure 77).[161] However, it is frequent that this degree of alignment adjustment reveals itself very sensitive to many factors, such as temperature, mechanical handling, solubility, and so on, leading normally to difficult reproducibility.[108]

Polyglutamate/homopolypeptide are nowadays the most widely used lyotropic liquid crystals (Figure 77).[147,149–152] With the solvent mixture these compounds produce either micellar and lamellar phases, as will be seen forward, that are also applied for the measurement of RDCs.[168] In any case, with respect to water soluble compounds, the same alignment media used for biomolecules may be used for this purpose.[127,134,142,168–170108]

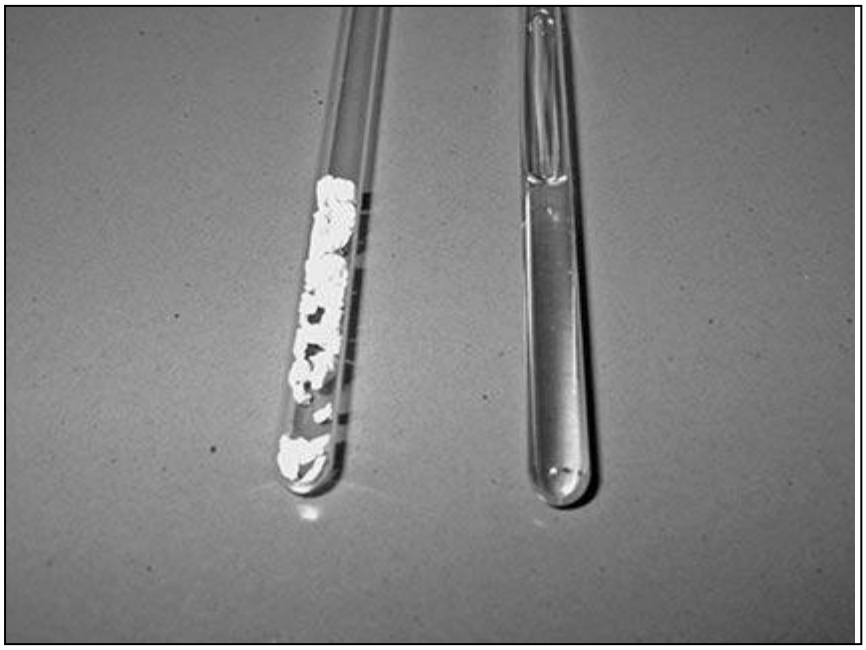

Figure 77 – Representation at left of a typical solid "liquid crystal" into a 5mm-NMR sample tube and at right the lyotropic liquid crystal obtained after preparation ready for use as orienting media.[167]

3.1.2.4 – Paramagnetic Tags

In biomolecular NMR, it have been demonstrated the possibility of using paramagnetic tags or to coordinate paramagnetic metal ions to molecules and consequently achieve alignment.[171,172] These effects was already known since the 1950s and 1960s, but new ones are currently being described.[173] The particularity of this type of alignment consists in the characteristic elevated paramagnetic metal anisotropic magnetic susceptibility, whereas these can be either coordinated or attached to biomolecules.[108,173] The information amount that can be withdrawal from these constraints is able to compensate the inevitable loss of information due to paramagnetic relaxation enhancement.[171] Nevertheless, this approach have not been applied to organic compounds so far.[167]

3.1.2.5 – Changing the Degree of Alignment

Situations there are where the degree of alignment is either higher than the expected, or too lower than the expected. In such cases, it is possible to change the degree of alignment by, for

example, choosing an alignment media inducing different degree. In this way, considering that the alignment media chosen was a SAG one, one possibility offered by this type of alignment is that it is possible to choose the alignment degree by the degree of cross-linking.[124,125,158–160] Higher degree of cross-linking is related with smaller cavities in the gel, and consequently with higher degree of alignment. In contrary, lower degree of cross-linking is related with larger cavities, and consequently lowers degree of alignment. However, it is important to take into consideration that with these media besides the degree of cross-linking, also the temperature influence the degree of alignment. Another factor to take into consideration is the role of the solvent choice, since it may influence the alignment degree and also the orientation of this. This presents to be helpful in cases where the crucial RDCs for structure determination have the same size for one alignment media, and the fact that choosing different alignment conditions with different alignment orientation removes the ambiguity by altering the RDCs values. In any case, this solution has no interest if the RDCs of the compound in question are from axial protons in six-membered rings, since the relation will be always equal. A particular feature of these media is that no influence of the magnetic field strength is verified. SAG gels also offer the possibility of changing the degree of alignment by reversible compression/relaxation of gels (Figure 78).[108,174,175]

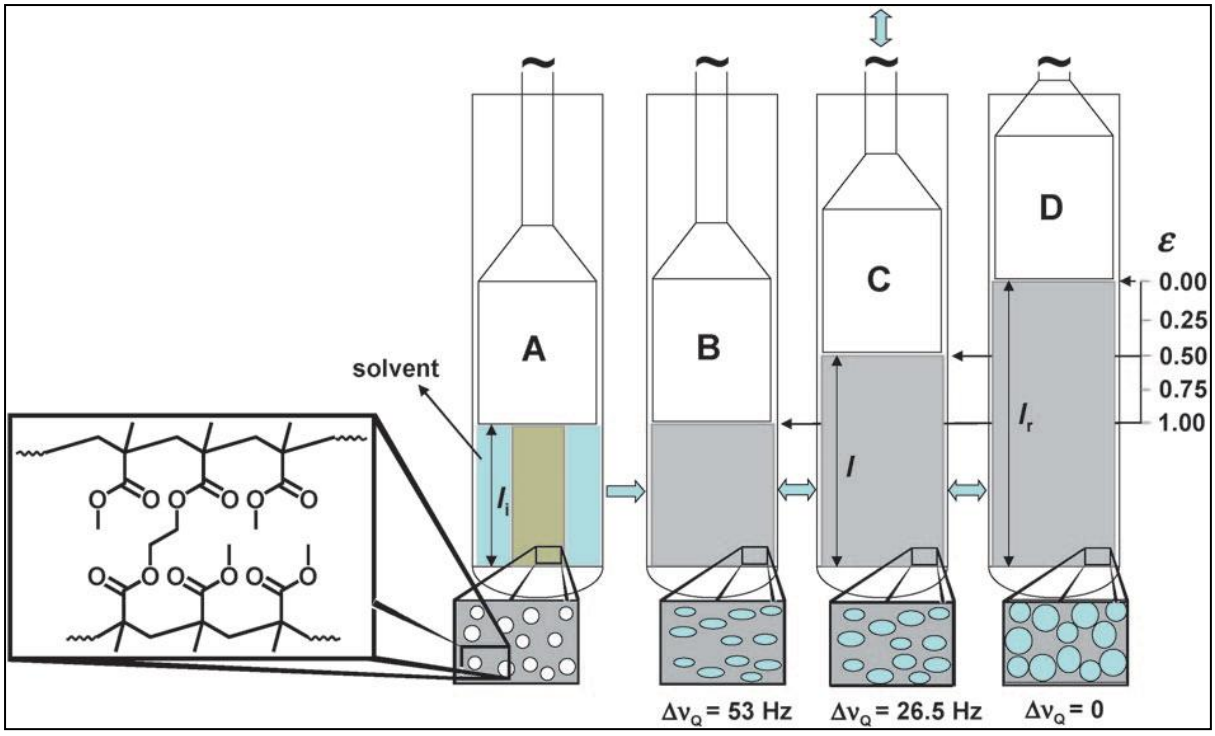

Figure 78 – Representation of the reversible gel compression/stretching experimental setup. At the left (A) the gel is placed into the tube surrounded by solvent and with compression preventing vertical stretching; followed by (B) fitting of the gel on the tube walls due to swelling process; and finally (C and D) the regulation of vertical stretching using a Shigemi plunger allowing the alignment degree selection, followed by ^{2}H quadrupolar coupling splitting.[162]

When it is using lyotropic liquid crystals, a completely different situation is faced. The common resolutions when these alignment media present too high alignment degree are the temperature raising and/or the dilution of the sample. Nevertheless, the dilution of the sample solution is limited,

since from certain concentration value the sample transits from an anisotropic state directly to an isotropic state. In any case, this process is reversible with evaporation of the solvent. If no result is obtained this way, another liquid crystal may be tried.[108,152,176]

3.1.2.6 – Sample Preparation and General Considerations

Besides the sample visual survey, a crucial way to certificate samples homogeneity is to perform a ^{2}H NMR spectra (Figure 79). Samples homogeneity is only guaranteed if no isotropic contribution is verified, which means that no centre signal or hump may be detected. The importance of this homogeneity is related with the credibility or discredit of the results obtained, since it influence all the other physical parameters in solution.[108]

In the case of lyotropic liquid crystals alignment media sample preparation, if the quadrupolar coupling signals (splitting signals) present broad signal width, or the presence of isotropic signal contribution, the sample should be homogenized (Figure 79). One of the practical techniques consists in centrifuging the sample tube until lines in the ^{2}H NMR spectrum become sharp. Although, in the case where the split lines presents to be sharp, but the isotropic signal still appearing, evaporating is the right solution, since probably this situation is due to lower concentration of alignment substrate (Figure 79).[108]

In the case of stretched and compressed polymer sticks (SAG), if an isotropic contribution is present in the spectrum, a possibility to remove the same is to gradually induce compression in the gel, so that it can expand radially and stick to the NMR tube walls. If the isotropic contribution is not removed yet, another polymerization must be done, in a different cast with different radius width.[108]

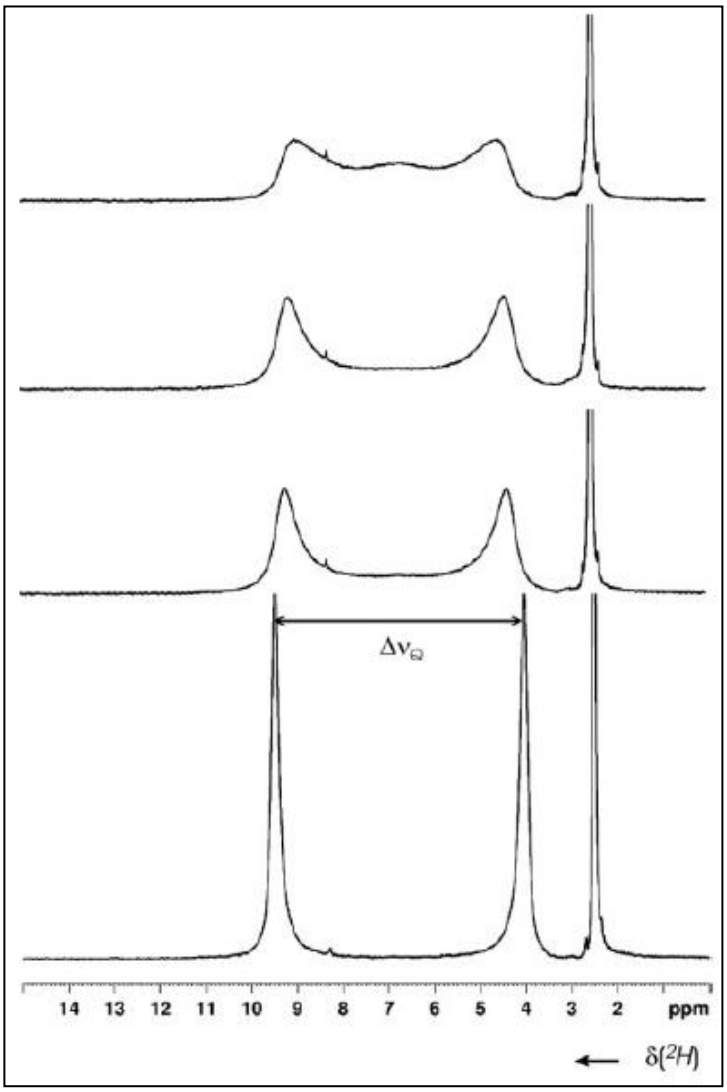

Figure 79 – Representation of ^{2}H NMR spectra of a deuterated solvent illustrating the homogenization process after liquid crystals preparation. From the top to the bottom is observed the central isotropic hump disappearing and the intensity increasing of the anisotropic phase signals.[108]

Considering now the availability and stability of the compound in study, it is important to evaluate carefully which media and which conditions chose, in order to preserve certain "precious" samples. In cases where the samples in study are not "precious", all alignment media hypothesis may be tried and numerous conditions exploited. On the other hand, when handling with "precious" samples, the sample recovery and the possibility of changing the alignment degree after its preparation are priority questions. In dealing with liquid crystals alignment media, a possibility to consider for the recovering of precious samples is the precipitation of the alignment substrate by the addition of solvents to the mixture, in which the solute is soluble but the alignment substrate is not. In dealing with stretched and compressed polymer sticks, recovery of samples is also possible, in this case using extraction by stretching and compressing the gel with large quantities of solvents.[108]

Considering now stability, in the case of stretched and compressed polymer sticks, these gels may present decomposition and deterioration with time, since its polymerization requires use of

radicalar initiator. On the other hand, liquid crystals do not present this handicap, and globally it is not verified great decomposition with time, or even alignment loss.[108]

3.1.3 – Measurement Methods

On the sequence of the process of choosing the proper alignment conditions, the RDCs can be measured.[108]

As previously referred, in order to calculate RDCs two measurements should be performed (see equation 22 in this Chapter, section 3.1.2.1): one in isotropic solution that yields the scalar coupling *J* and one in anisotropic solution that yields the total coupling *T*. The *D* value can be obtained in this way from the difference of the two previously referred. In this process, the *D* value obtaining is only straightforward if the signs of *J* and *T* are already known from measurement or other previously known considerations, as the fact that $^{1}J_{C\text{-}H}$ is known to be positive and $^{1}J_{N\text{-}H}$ is known to be negative for example, since only the absolute values of coupling are verified in the spectrum. When the signs of *J* and *T* are unknown, this fact leads to four possible values of *D*. Such situation is very puzzling, since structural information is coming from *D* and this value depend on determining which of the four values is the right one. In this way, methods that allow determination of the isotropic and total coupling sign present great advantage when compared with those not. Especial cases are when it is using $^{n}D_{C\text{-}H}$ and $^{n}D_{H\text{-}H}$ couplings. Another consideration is related with $^{n}J_{C\text{-}H}$ and $^{n}J_{H\text{-}H}$ small values, which because of large *D* values and opposing sign of *J* and *D*, a zero crossing can frequently be obtained (*D* is larger than *J* and besides cancel it, even surpasses it on the signals splitting).[167]

The measurement methods that allow both the determination of the size and the sign of the scalar and/or total coupling are detailed in Annex 2.2.

3.1.4 – RDCs in Structure Determination

In this section the use of RDCs for structure determination will be shortly presented. As it has been referred before in this work, the use of RDCs aims to provide spatial information about structures, in cases where it is not enabled by other techniques as NOE and ^{3}J coupling. RDCs challenges consist for instance in the determination of relative configuration, assignment of diastereotopic groups, molecular conformation, and so on. In this section three different methods to assign structures based on NMR RDCs it will be presented.[108]

3.1.4.1 – Distinction Based on Similarity of RDCs

One of the major features of the RDCs technique is the fact that only by its size is possible to determine if bonds are parallel or not. Normally RDCs of equal sizes correspond to parallel (and antiparallel) interspin vectors, taken into account that distances (bond length for directly bonded spins) are equal and same nucleus pair is involved (C and H, e.g.). This information is of great utility in six-membered rings, since molecular structure axial protons connected to their respective carbons show RDCs of the same size ($^1D_{C\text{-}H}$) due to their interspin vectors present parallel and antiparallel angular relation. Since equatorial protons present distinct positioning in the molecular structure, i.e. different orientation and relative angles with respect to the axial ones, this feature may be employed in the differentiation of both proton types. In this approach no order matrix (alignment tensor) calculation is necessary. Two main examples of this concept application are the cases of the assignment of α e β isomers of 4,6-*O*-ethylidene-D-glucopyranose,[142] and the relative configuration determination of the dihydropyridone (Figure 80).[149108]

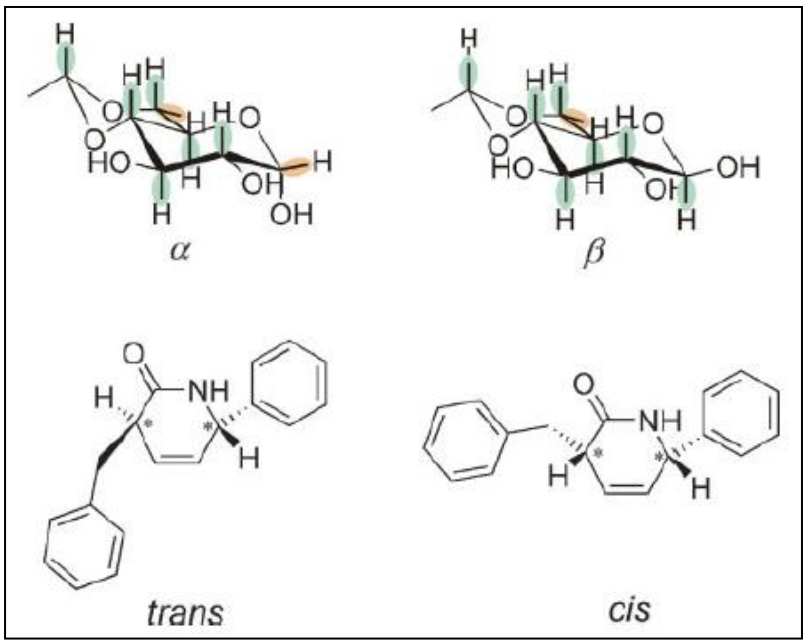

Figure 80 – Representation of *cis* and *trans* diastereoisomers of a dihydropyridone (bottom) and α and β chair three dimensional structures of the 4,6-O-ethylidene-D-glucopyranose (top), indicating the possibility of solving the structures by distinction based on similarity of RDCs.[108]

3.1.4.2 – Assignments Based on Best Fit of Observed Couplings with Trial Structures

Considering that more than five RDCs linearly independent are measured for a rigid compound, a different approach may be used, which uses not only the information of parallel (or antiparallel) bonds but also enables the assignment of diastereotopic groups or relative configurations.[108]

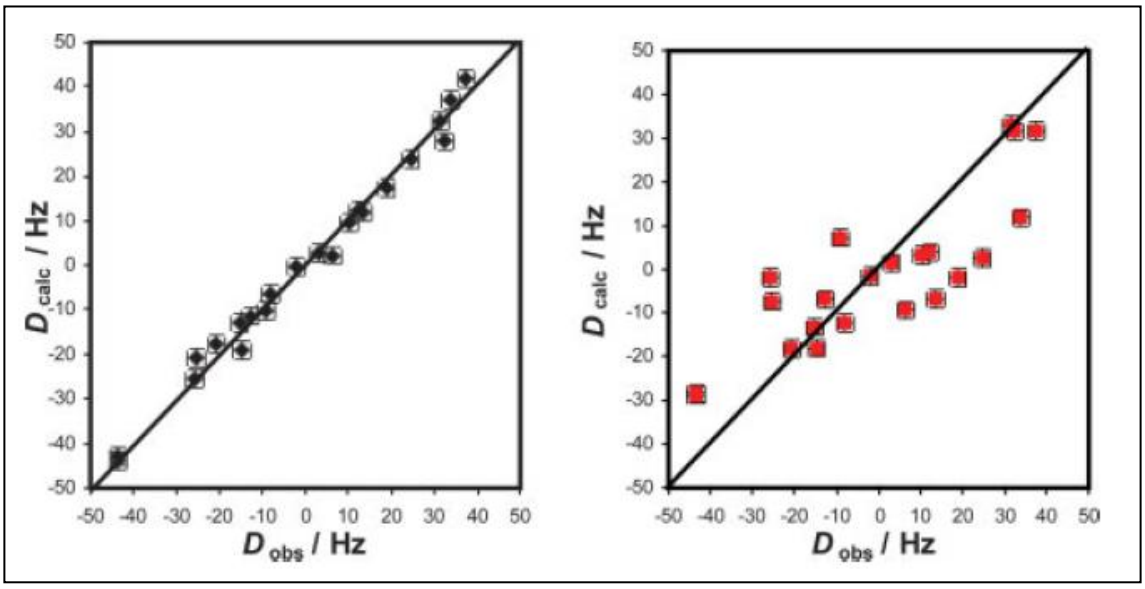

Figure 81 – Comparison of two different relations between D_{calc} and D_{obs} using computational trial structures. At left a good agreement between observed and calculated, and at right a worse agreement between the two.[108]

The particularity of this methodology is that the alignment tensor is not use, but instead a fitting between observed and calculated RDCs is established. The critical feature using this method is the proposed structures selection. If this methodology is to be applied to rigid compounds, which normally present preferred conformations, no problem may arise since good matching is expected to be verified. The process of assignment consists in the consecutive selection of different proposed structures for a set of RDCs. The SVD[177] (singular value decomposition) process conducts each proposed structure to an alignment tensor **A** of the best-fitting, not considering the proposed structures quality. D_{calc} values are then obtained for the best proposed structures fit, which might be in total agreement with the D_{obs} in simple cases of proposed structure correct input. Comparing different outputs it is possible to evaluate the correct input structure. The structure that corresponds to the correct assignment is distinguished from the others by fitting observation (Figure 81). This methodology enables the verification of structural proposals. Considering this methodology, flexible small organic compounds are yet a very difficult task[169], since they mainly encompass several conformers and structural equilibriums.[108]

Examples of this methodology using are the assignment of several diastereotopic protons;[147,148,150,159] and the achievement of rigid compounds relative configuration.[158,178108]

3.1.4.3 – Assignments Based on Prediction of RDCs from the Alignment Tensor

In this more complex methodology the alignment tensor **A** is determined in a first calculation not utilizing all data, but only five RDCs (the set of needed independent RDCs). The alignment tensor **A** properties, obtained by the first calculation, are kept fixed during a second calculation. Therefore,

considering that orientation and degree of alignment are determined for these RDCs set moves up to the second calculation. During second calculation are predicted the RDC values for other "unknown" parts of the molecule, for which RDC values have not been inserted in first calculation.[108]

In the end of the second calculation is obtained a set of RDCs called D_{pred}, which is compared with the RDCs observed D_{obs}. Depending on the fitting of the predicted RDCs with the experimental data, the structural proposal is verified or falsified. This methodology relies on a good structural proposal and may lead to good RDC values estimation.

Briefly, this methodology consists in using RDCs to calculate an alignment tensor, and consequently employ that alignment tensor to predict RDCs for structural proposal. In some cases is possible to predict the alignment tensor from molecular properties of the solute using PALES[179] or MSpin[180] computational software. It has already been shown that it is not only possible to predict RDCs from a known alignment tensor and structural proposal, but also to predict both RDCs and alignment tensor.[108,158]

In sum, this methodology may be regarded as cross-validation method for the RDC experimental (observed) data, since its prediction of RDCs from known alignment tensor and structural proposal. For an accurate cross-validation, structural proposal might be itself very accurate, for good correlation between predicted and observed RDCs. Nevertheless, with this methodology, normally due to little coupling data availability, it is possible to reach a good fit for a wrong structure in the selection procedure, since the fitting process only distinguish between relative fitting qualities, allowing one wrong structure to fit better than other wrong structure.[108]

3.2 – Experimental Section

3.2.1 – Materials

The following sugars were used in this study: D-(+)-glucose, purchased from "Fluka" (purity > 99.0%); D-(+)-cellobiose, purchased from "Fluka" (purity > 99.0%); 1,4-D-(+)-cellotetraose, purchased from "Megazyme" (purity > 95.0%); 1,4-D-(+)--cellohexaose, purchased from "Megazyme" (purity > 90.0%); 1,3:1,4-B-D-glucotetraose, purchased from "Megazyme" (purity > 98.0%); 1,2-D-(+)-sucrose, purchased from "Fluka" (purity > 99.0%); Lysozyme, purchased from TCI Europe (purity > 98.0%).

Commercial solvents used: chloroform, purchased from "Labchem" (commercial); Acetone, purchased from "Labchem" (commercial); methanol, purchased from "Valente e Ribeiro" (commercial).

3.2.2 – Poly(methyl methacrylate) (PMMA) Gel Preparation

The preparation of the cross-linked PMMA gels was based on the preparation protocol developed by Roberto Gil, Chakicherla Gayathri, Nicolai Tsarevsky and Krzysztof Matyjaszewski in 2008[125], with one major modification.

The monomers methyl methacrylate (MMA, 99 %, "Sigma-Aldrich") and ethylene glycol dimethacrylate (EGDMA, 99 %, "Sigma-Aldrich") were purified prior to the experiments by passing the neat liquids through a short column filled with basic alumina, purchased from , in order to remove the polymerization inhibitor. The radical inhibitor 2,2'-Azobis(2, 4-dimethyl valeronitrile) (V-65, 98%) was purchased from Wako, and acetone-d_6, chloroform-*d* and methanol-d_4 (99.8 % of D atoms) were purchased from "eurisotop".

A solution containing MMA (10 ml), V-65 (0.0124 mol %, 2.416 mg) and acetone-d_6 (2 ml) was first prepared. A portion of 10 ml of the stock solution were added to a vial and mixed with EGDMA (0.27 mol %, 40 µl). The resulting solution were transferred to NMR tubes (diameter = 3 or 5 mm, depending on the intended NMR tubes for swelling procedure), which were then capped with rubber septa, and the septa were secured with tape. Each tube was evacuated for short time and back-filled with nitrogen. The cycle was repeated three times, and the NMR tubes were inserted in an oil bath at 50 ºC. The polymerizations were carried out for 5 h, and then the tubes were taken out of the heating bath, the septa were removed and the gels were left to dry slowly at ambient conditions for approximately three weeks. The slow drying is essential for the preparation of uniform rod-shaped gels. When vacuum drying was attempted, the gels were deformed and some of them cracked. When the gels were dry, they shrank and could be easily removed from the tubes. Some tubes had to be broken to take the gels out.[125]

After gel preparation, gel manipulation consists in three steps: first, place the gels in an acetone / methanol solution (50 % v/v), allowing the gels to do the swelling for several hours (one day); second, and without previous evaporation, place the gels in a chloroform solution directly, allowing the inner-gel to exchange the previous mixture for chloroform for several hours (one day); and third, remove the gels from chloroform solution, and let it dry completely until a stiff shrunk rod-shaped gels are formed. At this time, gels are ready to be placed in an NMR tube and swollen with chloroform-D for NMR experiments.

3.2.3 – Copolymeric Poly(acrylamide-based) (PAM) Gel Preparation

The preparation of the cross-linked PAM gels was based on the preparation protocol developed by Peter Haberz, Jonathan Farjon and Christian Griesinger in 2005[160], with some major modifications.

2-(acrylamide)-2-methylpropanesulfonic acid (AMPS, 98 %, "Nzytech"), *N*,*N*-dimethylacrylamide (DMAA, 99 %, "Sigma-Aldrich") and *N*,*N*'-methylenebisacrylamide (BIS, 99 %, "Sigma-Aldrich"), in the proportion of (1:1:0.26) were dissolved in purified water to a total monomer concentration of 1.5 M. The pre-gel solution was inserted into a gel cylinder with an inner diameter of 5.4 mm and polymerized for 15 minutes into a 75 ºC water bath, initiated by ammonium persulphate (0.008 g/ml). The gels were washed once with HCl solution (0.02 M) and at least four times with water, each time for several hours. The swollen gels were left to dry slowly at ambient conditions for approximately three days. The alignment is scalable by varying the diameter of the gel cylinder.[160]

3.2.4 – CpCl-Liquid Crystal Preparation

The preparation of the dilute liquid crystalline phase of cetylpyridinium chloride was based on the preparation protocol introduced by Prosser et al.[181] and enunciated by Kristina Lycknert, Arnold Maliniak and Goeran Widmalm in 2001[182], with no major modification.

Cetylpyridinium chloride (CpCl) was purchased from "Sigma-Aldrich", sodium chloride was purchased from "Panreac", and *n*-hexanol was obtained from "Sigma-Aldrich", all with purity > 98%. The chemicals were used without further purification.[182]

The CpCl / *n*-hexanol / brine (200 mM NaCl in D_2O) sample was prepared by weight to give concentrations of 3.3%, 4.2%, 4.8%, 6.4%, 7.0% and 9.1% (w/w) with respect to the total content of CpCl / *n*-hexanol, where the two components were added in equal amount (of weight).[182]

As an example of the procedure, Cetylpyridinium Chloride-Liquid Crystal (CpCl-LC) 5% (w/w) was prepared starting from dissolving NaCl (11.6 mg) in D_2O (1.0 g) in a magnetically stirred glass vial. When all the NaCl was dissolved, CpCl (26.3 mg) was added while stirring vigorously, and the mixture was heated at 7273 K for six minutes. The mixture was then cooled down to room temperature, *n*-hexanol (25 mg) was added and the mixture was heated again at 7273 K for several minutes (at least one hour) and allowed to cool to room temperature slowly. Stirring was maintained all the time.[182]

The homogeneity of the dilute liquid crystals was checked in the NMR spectrometer by the ^2H quadrupolar splitting of D_2O. Sharp lines of equal height are obtained when the sample is homogeneous.[182]

3.2.5 – Disodium Cromoglycate Preparation

The preparation of the cross-linked DSCG / D_2O phase was based on the preparation protocol developed by Eduardo Troche-Pesqueira, María-Magdalena Cid and Armando Navarro-Vásquez in 2014[163], with no major modification.

Cromolyn disodium salt hydrate (DSCG) ($C_{23}H_{14}Na_2O_{11}\cdot H_2O$; MW=512.33 Da as anhydrous) was purchased from TCI Europe (purity > 98.0%). All reagents were used without further purification.

The DSCG / D_2O phase was formed by dissolving 100 mg of Cromolyn in 0.66 mg of D_2O at 70 ºC K with vigorous stirring, and then letting the solution cool down.

3.2.6 – NMR experiments

All experiments were performed on a Bruker AVANCE III spectrometer operating at 400.16 MHz for the frequency of ^1H, 101 MHz for ^{13}C, and 60.38 MHz for ^2H, equipped with double resonance broad band (BBO) temperature gradient probe with Z-gradients.

^1H diffusion experiments were performed the same way as explained in Experimental Section of Chapter 2.

3.3 – Results and Discussion

As have been previously introduced, in the NMR field, alignment media present its main application at the resolution of structural and stereochemical problems, as it provide the necessary anisotropic conditions that make possible the observation of non-secular parts of NMR internal spin interactions, such as dipolar couplings and chemical shift anisotropy. Nevertheless, the existing diversity of alignment media, namely liquid crystals and polymeric gels, may enclose a huge amount of information and characteristics about physicochemical properties that eventually allow the comprehension of different phenomena in a plethora of different systems, including the biological. In this way, the aim of this study is the investigation of the influence that different alignment media has on solute molecules physicochemical and stereochemical properties, when these are placed in its environment. In this work, the main physicochemical property chosen to follow media influence on molecules has been the NMR self-diffusion. Additionally, NMR residual dipolar couplings (RDCs) have been used for probing the possible effect that the different media could also have on molecular conformation.

Despite the ambitious objectives proposed for this chapter (exploring diffusion in alignment media) in the beginning of the experimental work, which were:

- characterization of different types of alignment media;
- study of the relation between the alignment properties of the media and the translational properties of selected molecular standards;
- approximate conformational determination using residual dipolar couplings;

due to many and lasting experimental difficulties, as well as time limitation, much of the work initially thought remains to be done.

3.3.1 – Integrity, Characterization and Experimental Features of Alignment Media

The experimental difficulties experienced during this work were mainly related with alignment media protocols execution. The obtaining of the different media, not counting the preparation time, required many attempts and some modifications of previous protocols, resulting in long time involved and not used for data acquisition as expected. In addition to the necessary optimization of the established experimental protocols, some logistic and volunteer modifications to original protocols have been made, in some cases in order to make protocols become affordable (low-cost), as the case of PMMA gels where the original protocol demanded the acquisition of a radicalar initiator (V-70) not produced in Europe.

In this sub-section will be shown and discussed the experimental results concerning the characterization and integrity evaluation of the different alignment media. These experimental results consisted in following the gels and liquid crystals preparations by ^{2}H and ^{1}H 1D-NMR experiments, which might indicate the alignment integrity conditions and the content of impurities.

3.3.1.1 – PMMA gels

The PMMA gels alignment media has been the most problematic and lasting (one month drying so they can be removed from polymerization tubes) experimental task. The reason for such is related with the very precise requirements necessary in gel production and to ensure gel utility, which means homogeneity in the alignment conditions, i.e. no isotropic signal existence in the ^{2}H 1D-NMR spectrum. The main problematic features in PMMA gel production are: ensure consistent gel production (initial hard stick, capable of swelling and become elastic) through logistical adaptation of the polymerization conditions; the determination of the right polymerization gel diameter by choosing the right mold for perfect adaptation to NMR tubes (5 mm); and post-polymerization treatment:

1. The consistence of the gel is directly related with its degree of cross-linking, whereas gels with higher degree of cross-linking are harder and gels with lower degree are more flexible. For this specific situation (alignment of small molecules), as has already been introduced, is desired a high degree of cross-linking because of the small size of molecules, so that they express the influence of the involvement and do not move freely. The crucial conditions to optimize in this situation are the polymerization temperature, the polymerization time, the thickness of the mold and the inertness of the atmosphere:
    a. The polymerization temperature is related with the solvent used individual ebullition temperature, which is 56 ºC (acetone), since the solvent presence is essential to create the cavities within the tridimensional reticulated gel, and therefore has approximately (ebullition point in mixtures is altered) 56 ºC as the upmost temperature appropriate for polymerization execution with this solvent. Furthermore, 50 ºC is high enough to reach activation energy for polymerization with the chosen reactants;
    b. The polymerization time is directly related with the chosen temperature, whereas higher temperatures (>50 ºC) will shorten the polymerization time (experimental = 5 hours) and lower temperatures cause the opposite. The extension of the polymerization process for 15 hours lead to gels incapable of swelling, probably due to faster solvent evaporation and/or subsequent cross-linking reactions development;
    c. The thickness of the mold has revealed to be a fundamental feature that has been underestimated during initial attempts. The initial use of large thickness mold tubes in polymerization has demonstrated that polymerization time/temperature is also greatly dependent of this factor. What has been verified was that due to large thickness of

the mold tubes the polymerization process only took place in the solution areas closer to the tube walls, instead of occurring homogeneously, leading to useless polymer gels. This problem was solved with using thinner tubes (NMR commercial tubes, more expensive), instead of cheaper tubes with larger thickness;

d. The inertness of the atmosphere is another important factor of this polymerization, since in this case the process is sensible to molecular oxygen that, when solubilized in solution, reacts with the radicalar specie preferentially to the monomers, and avoids polymerization leading to the appearance of bubbles inside the final gel. This adversity may be overcome with rubber covering and degassing.

2. The determination of the right polymerization gel diameter is directly related to the tube mold used in polymerization process and is crucial to the functionality of the resulting gels. This fact is related with the post-polymerization and analytical procedure, since the gels are expected to swell (horizontal and longitudinally) inside 5 mm NMR tubes leading to perfect fit to the tube walls (avoid molecules not aligned between gel and tube walls), while keeping elasticity. What has been verified is that 5 mm NMR tubes present 4.6 mm of inner diameter and PMMA gels stretch and expand approximately 50% (longitudinally: 2.6 cm to 3.8 cm; horizontally; 2.6 mm to 4 mm) from their dry diameter when swelled without pressure. In this way, the original protocol proposes the polymerization inside 3 mm NMR tubes (2.6 mm diameter gels), ensuring adapted gel shape (cylindrical) and smaller radius than 5 mm NMR tube allowing compressing (the compressing causes the gel to shrink longitudinally and complementary to expand radially, keeping the constant volume). Therefore, if it is desired the ability of compressing, polymerization gel radius should not overcome 3 mm (5 mm NMR tubes present 4.6 mm of inner diameter). If it is not, then 3 mm is the maximum radius for polymerization so that gel fits perfectly the 5 mm NMR tube when swelled.
3. Post-polymerization treatment consists in an indispensable task on this process because of necessary gel integrity. When the dry gels obtained from polymerization were directly placed into chloroform, solvent widely used to solubilize organic molecules, it has been experimentally observed that gels were completely broken, probably due to the high solubility of the gel in chloroform, which causes fast entry of the solvent in gel cavities leading to its burst. In this way, it has been developed a post-polymerization treatment with a mixture of methanol/acetone (50:50) that probably causes a softer initial swelling process (lower affinity of the gel for methanol and acetone), so that when a second swelling in chloroform is made there is no gel degradation.

After gel production with consideration of the previous steps, two NMR standard steps of characterization and integrity evaluation were made, which were the acquisition of ^{2}H and ^{1}H 1D-NMR experiments.

As has been previously introduced, the ^{2}H 1D-NMR spectrum, which allows the detection of solvent ^{2}H nucleus in solution ($CDCl_3$ in this case), is crucial for the determination of the homogeneous anisotropy of the solvent molecules present inside the gel cavities, through the

visualization of the quadrupolar coupling (by the signal splitting) resulting from the non-total-averaging of the non-secular part of the quadrupolar interaction, which along with dipolar coupling and chemical shift spin interactions consist of a tensorial property (value depend on the relative orientation of the molecule with respect to the external magnetic field B_0). In this way, after gel production was always necessary to acquire a ^{2}H 1D-NMR spectrum in order to ascertain that only quadrupolar splitting was observed, and no isotropic central signal was present.

In the way to finally reach a capable execution of PMMA gels, many have been the unsuccessful results. A typical aspect of one detected malfunction produced gel is the ^{2}H 1D-NMR spectrum result shown below in Figure 82.

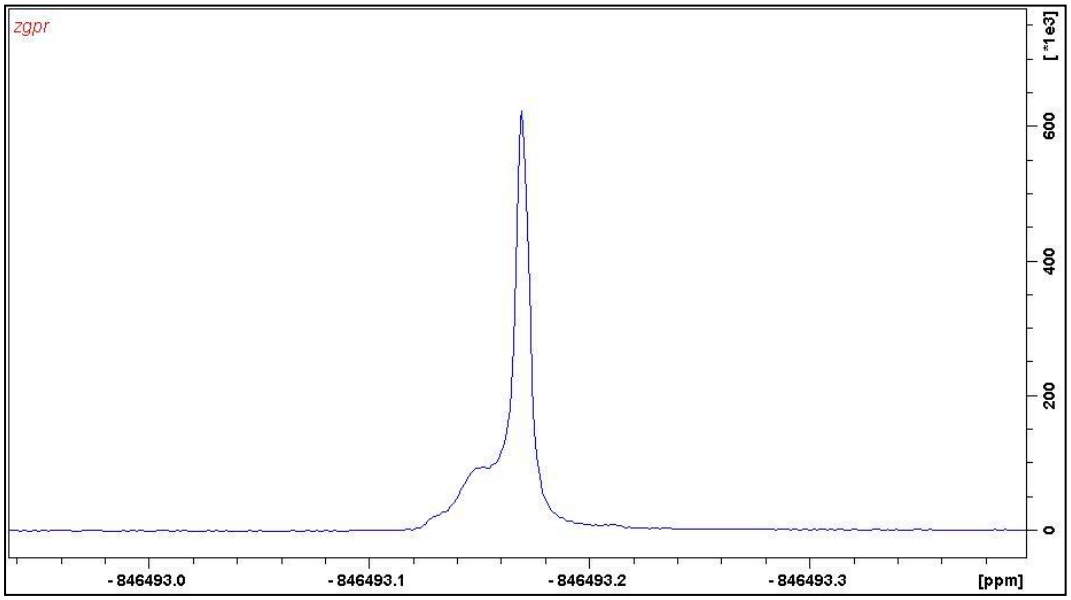

Figure 82 – ^{2}H spectrum representation of a defective prepared PMMA gel, showing intense isotropic signal lateralized at left by an anisotropic hump due to malfunction alignment.

In this spectrum is possible to observe the intense isotropic signal, correspondent to the isotropically reorienting $CDCl_3$ molecules in solution, and at the left of this peak a shoulder that corresponds to the multiple averaged possible orientations that molecules are experiencing into the damaged and dissimilar gel cavities.

On the other hand, an example of a partially successful gel execution process of compression is shown below in Figure 83. It is said partially because a residual isotropic signal was never possible to remove completely, even with the progressive increasing of compression.

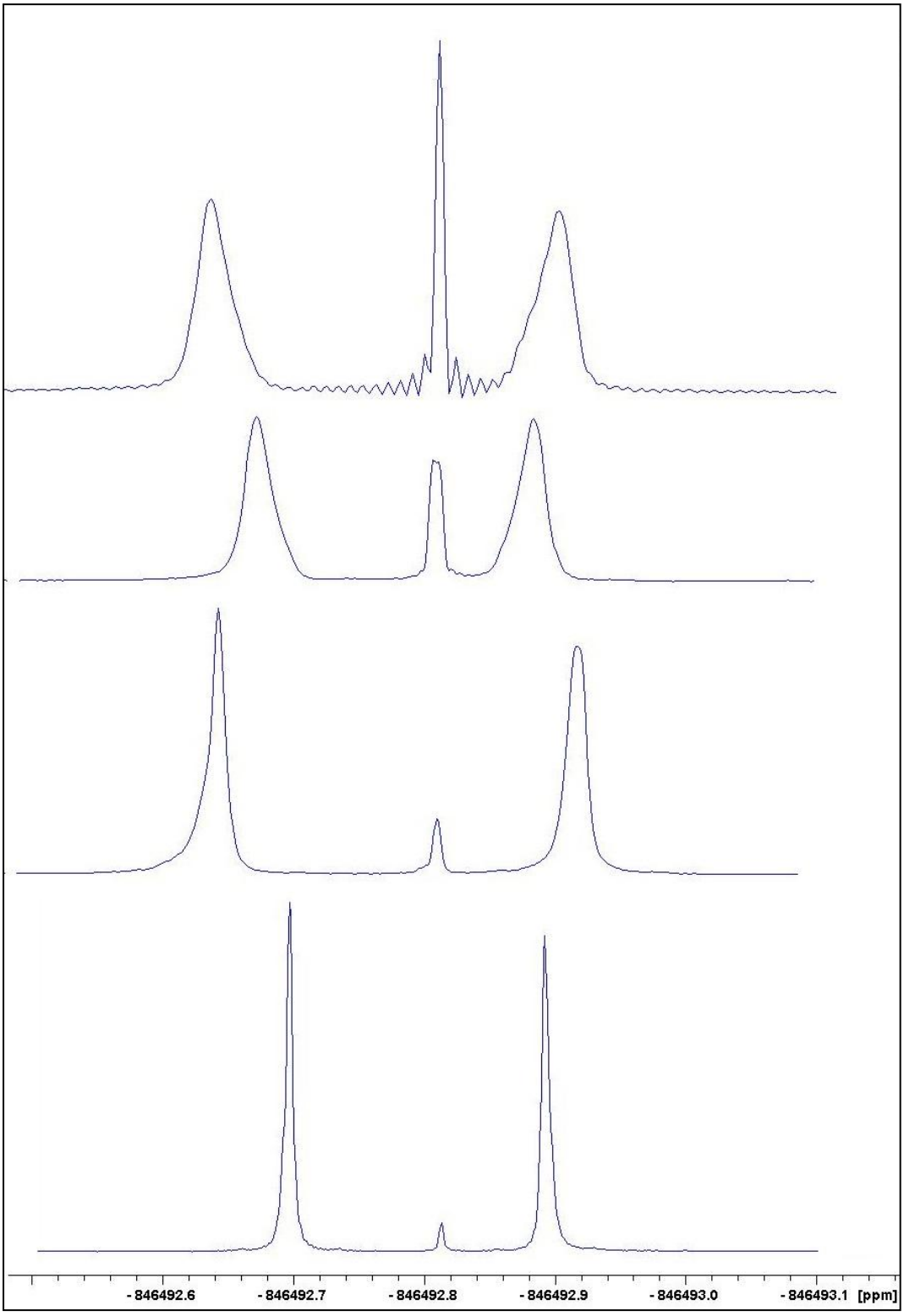

Figure 83 - ^{2}H spectrums representation of a working prepared PMMA gel, showing progressive intensified anisotropic signals lateralizing the central residual isotropic signal. From the top to the bottom is observed the sharpening of the anisotropic signals associated with intensity and quadrupolar splitting increasing (due to alignment increasing), while the opposite is verified for the central isotropic signal. (not the same scale of expansion for all spectrums)

In this case, the ^{2}H 1D-NMR spectrum of the gel obtained initially (top) presents an isotropic signal more intense than the anisotropic quadrupolar splitting, which is consequence of the non-fitting

of the swelled gel to the NMR tube walls due to reduced diameter that leads to an isotropic phase of solvent between the walls of the tube and the gel. As the compression is progressively increased (spectrums below) with recourse of an appropriate piston (Compression Gel Device; from "New Era NMR Supplies and Accessories Catalog"), which is fixed to the tube on the top (Figure 84) and by screwing is pulled downwards compressing the gel, it is possible to observe that the isotropic signal is progressively decreasing its intensity, giving rise to the increasing of the anisotropic quadrupolar signals splitting and intensity. The final spectrum (bottom) reflect a situation where almost every molecule is contained within gel cavities, consequently presenting almost only anisotropic signal resulting from the temporal averaging of molecular preferential orientation (relative to the external magnetic field).

In Figure 84 is presented the necessary equipment for the stretching and compressing of polymeric gels inside NMR tubes, with top regulation.

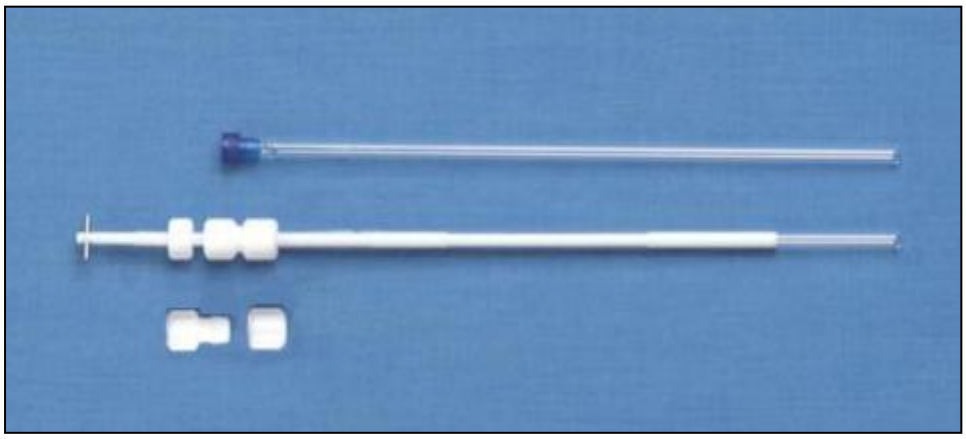

Figure 84 – Representation of the materials needed for a typical strain-induced alignment in a gel experiment and how the plunger may be locked at the desired position. (Reproduced from New Era NMR supplies and accessories catalog)

The NMR tube used can be a regular one, as it is possible to observe (Figure 84), and the other equipment consists in the previously referred "Compression Gel Device" plunger.

The other referred mean of characterization and evaluation of gel integrity, is the ^{1}H 1D-NMR experiment execution. On the other hand, this technique is crucial for the detection and evaluation of impurities presence, such as residual monomer excess (unreacted). In Figure 85 below is represented the following of the gel washing process by ^{1}H 1D-NMR, and is observed the reduction of the impurities (MMA) NMR signals intensity with progressive washing repetitions. The reason for the signals not being completely removed is only because the process was not completely accomplished due to gel degradation with excessive compression. In these spectra it is even possible to observe some reduced intensity broaden signals. These signals correspond to the polymeric gel structure ^{1}H constitution, namely methyl and methylene ^{1}H's of MMA (methyl methacrylate) and EGDMA (ethylene glycol dimethacrylate), which due to reduced mobility (gel rigid structure) present increased relaxation times (as explained before), giving the signals that broaden aspect.

The washing process is executed with recourse of the "Compression Gel Device" plunger, which is used to compress and stretch the gel repeatedly, and sequential addition and removal of chloroform. As chloroform is internalized within gel cavities mechanically, it is removing by solubilization the monomer residual molecules.

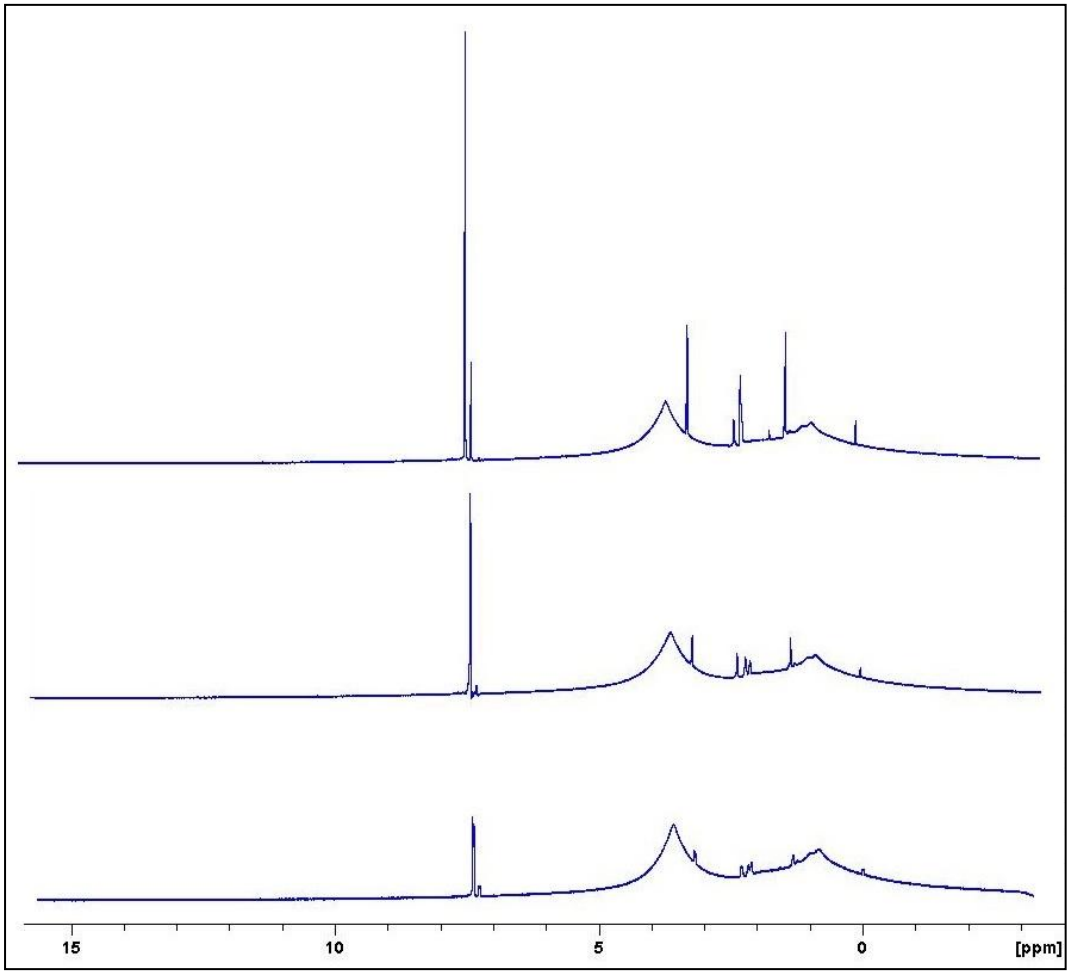

Figure 85 – Representation of several ^{1}H spectrums showing the effect of the successive washings with $CDCl_3$ with stretching and compressing procedure. It is possible to observe the progressive decreasing of the MMA monomer polymerization signals, and the maintenance of the broad polymer signals.

3.3.1.2 – Cetylpyridinium Chloride (CpCl) Lyotropic Liquid Crystal (LLC)

The CpCl/n-hexanol/brine lyotropic liquid crystal (Figure 86 and Figure 87) despite having an apparent quick process of production (one to two hours according to reported procedures), has become several times a lasting process. The reason for such is related with the fact that after liquid crystal production the process requires a period of alignment stabilization. During its production, the liquid crystal non-homogeneous pre-mixture, where CpCl is precipitated and n-hexanol non-miscible, is subjected to elevation of temperature to force the miscibility of the mixture. After the homogenization of the mixture (caused by temperature and stirring), which becomes dull and viscous,

is followed the step of returning to the experimental temperature, which is the room-temperature one. During this last step a crucial feature is the maintenance of the stirring, since it keeps the microscopic homogeneity of the micellar formation (micelles with similar size).

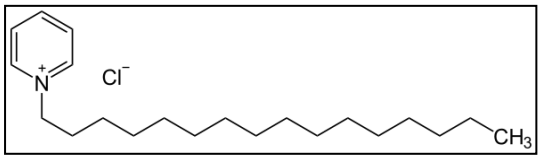

Figure 86 – Representation of the structure of the cetylpyridinium chloride ion-pair.

At this moment is important to highlight the fact that due to cetylpyridinium amphiphilic structure, composed by a polar head and a hydrophobic aliphatic chain, this compound is capable of forming micellar structures in solution (Figure 87) grouping its own aliphatic chains in the centre and exposing its polar head to the outside of the micelle and connect the polar involvement of water, n-hexanol and NaCl ions present in the mixture.

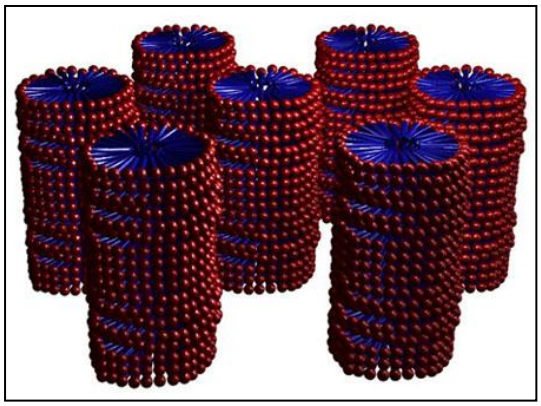

Figure 87 – Representation of the CpCl/n-hexanol/brine micellar formation in lyotropic liquid crystal solution.

This micellar structures formed in regular non-magnetic induced conditions are known to react to induce magnetic conditions forming lamellar phase structures reasoned by its high magnetic susceptibility ($\Delta\chi$), the ones that are verified in the presence of the external magnetic field B_0 and are responsible for the molecular alignment imposition (Figure 88).

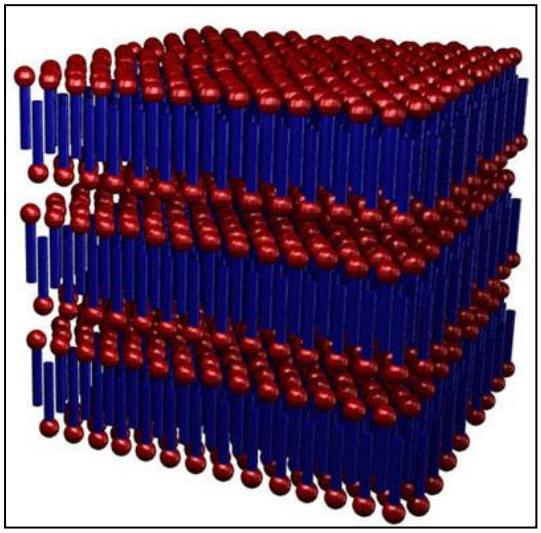

Figure 88 - Representation of the CpCl/n-hexanol/brine lamellar formation in lyotropic liquid crystal solution due to the presence of the external magnetic field.

The importance of a regular micellar size formation is its relation with the degree of alignment induced in molecules solubilized. If heterogeneous micellar formation occurs, different spatial degrees of alignment in solution are verified. One of the techniques used for investigate micellar formation in solution was once again the ^{2}H 1D-NMR spectra. As has been discussed before, through the detection of deuterated molecules (D_2O in this case) alignment in solution, it is possible to infer the homogeneity of micellar formation in the same, as molecules alignment is established by the bulky presence of micelles.

During the process of production of the LLC with previously optimized experimental conditions, it was verified through ^{2}H 1D-NMR spectrums that malfunction lyotropic liquid crystals of cetylpyridinium/n-hexanol/brine mixture were being obtained. The ^{2}H 1D-NMR spectra are presented in Figure 89. Contrary to the malfunctions observed for PMMA gels, in this case it was observed a broadening, total or partial, of the quadrupolar splitting signals. On the top of Figure 89 below it is observed the ^{2}H 1D-NMR spectrum of one total broadening of the quadrupolar splitting signals, which consist in the complete broadening of the signal from the baseline to the top of the signals intensity. In the middle and in the bottom, for opposition, it is verified only the broadening of half of the signal intensity, which means that only from the baseline until half-height of the signal is observed the broadening. This phenomenon is related with the relative molecules population that is oriented with different degrees of alignment, as has been uncovered above. Since it is known that a given splitting corresponds to certain degree of alignment, it is understandable that the broadening, which corresponds to the summation of multiple close different splittings, consists in the presence of multiple degrees of alignment in solution, resulting from the heterogeneous micellar dimension formation.

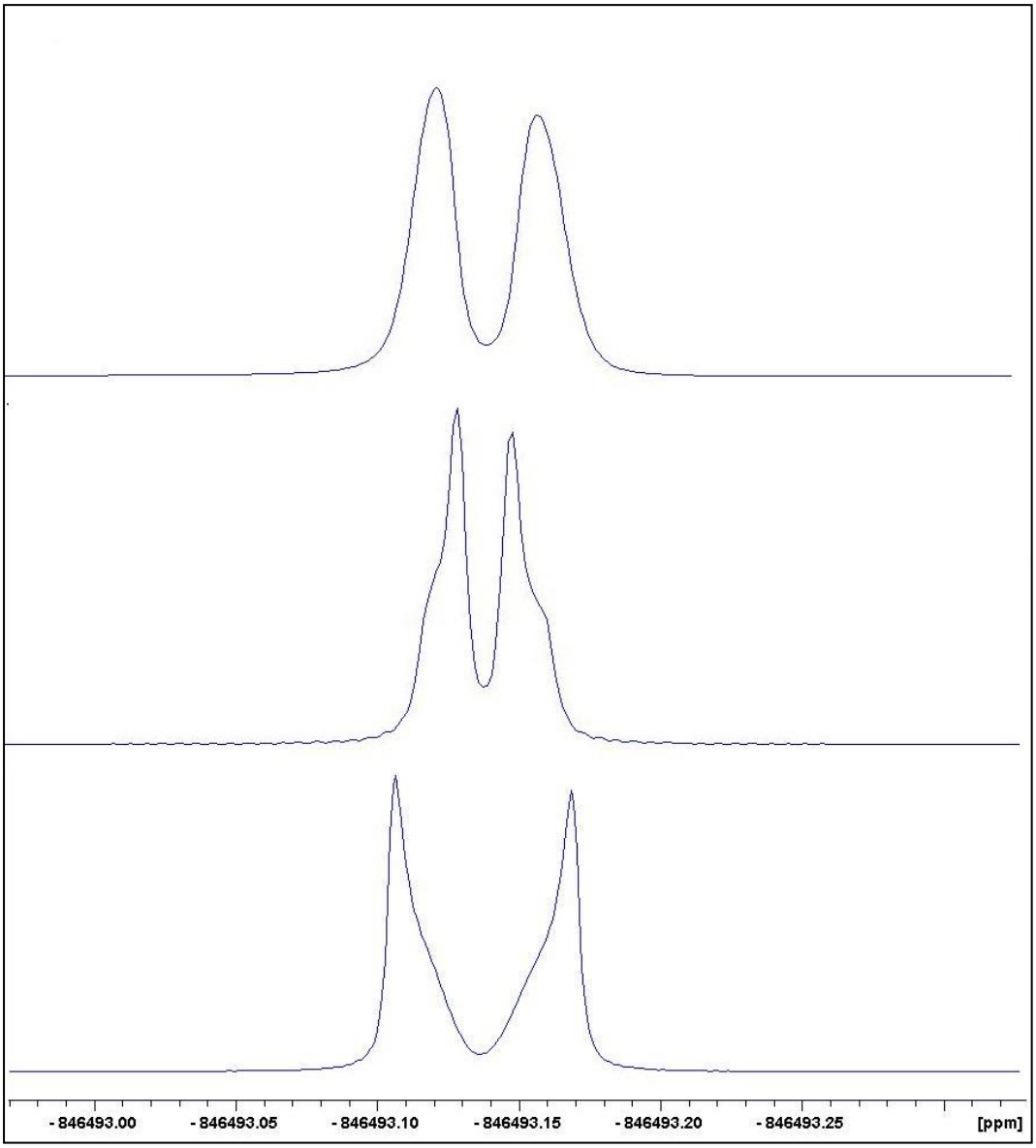

Figure 89 – ^{2}H spectrums of different defective liquid crystal gels.

In the Figure 89 above, at the top spectrum, is observed a regular Gaussian distribution of different degrees of alignment, which probably corresponds to different micellar dimensions, present in solution with a preferential orientation to the one that corresponds to 0.05 ppm or 20 Hz splitting that corresponds to the intermediate degree of alignment. At the middle spectrum is observed that the smaller degree of alignment is preferential in solution (signal peak corresponds to the smaller splitting value, < 0.05 ppm), probably due to higher concentration of smaller size micelles in solution, and the broadening at the bottom of the signal corresponds to larger micelle coexistence. At the bottom spectrum is observed that the higher degree of alignment is dominant in solution (signal peak corresponds to the higher splitting value, > 0.05 ppm), probably due to higher existence of larger size micelles in solution, and the broadening at the bottom of the signal corresponds to smaller micelle coexistence. These results are expected to have great implications in dissolved molecular behavior, specially molecular motion, since is believed that the growing micellar size will affect at least

molecular translational motion, parameter that is desired to study. In this way, if different degrees of alignment exist in solution, probably many diffusion contributions of molecular populations will be verified in the diffusion coefficient single result, and a non-linear decay must be expected.

Another interesting result from CpCl LLC media consisted in the verification of alignment improvement after substrate dissolution. As can be seen in Figure 90, the spectrum below, which corresponds to the ^{2}H 1D-NMR result obtained after substrate dissolution, shows a much better homogeneity of alignment when comparing with the above spectrum obtained before substrate dissolution. This result might be related to one of two questions: first, the reduced possibility of substrate influence on the alignment homogenization; or, on the other hand, the greater possibility of alignment stabilization during the time required for the dissolution procedure, without substrate homogenization interference. The result below in figure 83 was verified for glucose dissolved in CpCl 3% alignment media. The opposite result (homogeneity destabilization; not shown) has been verified for the same alignment (CpCl 3%) for the other studied substrates, namely cellobiose, cellotetraose and cellohexaose, reinforcing the idea that no substrate influenced was induced in alignment media stabilization in the glucose situation. The time required for stabilization was noticed to be a very important factor during all the handling experience with these media, and although it has also been determined that it was a highly variable condition, it was noticed that at least one week was necessary for media stabilizing.

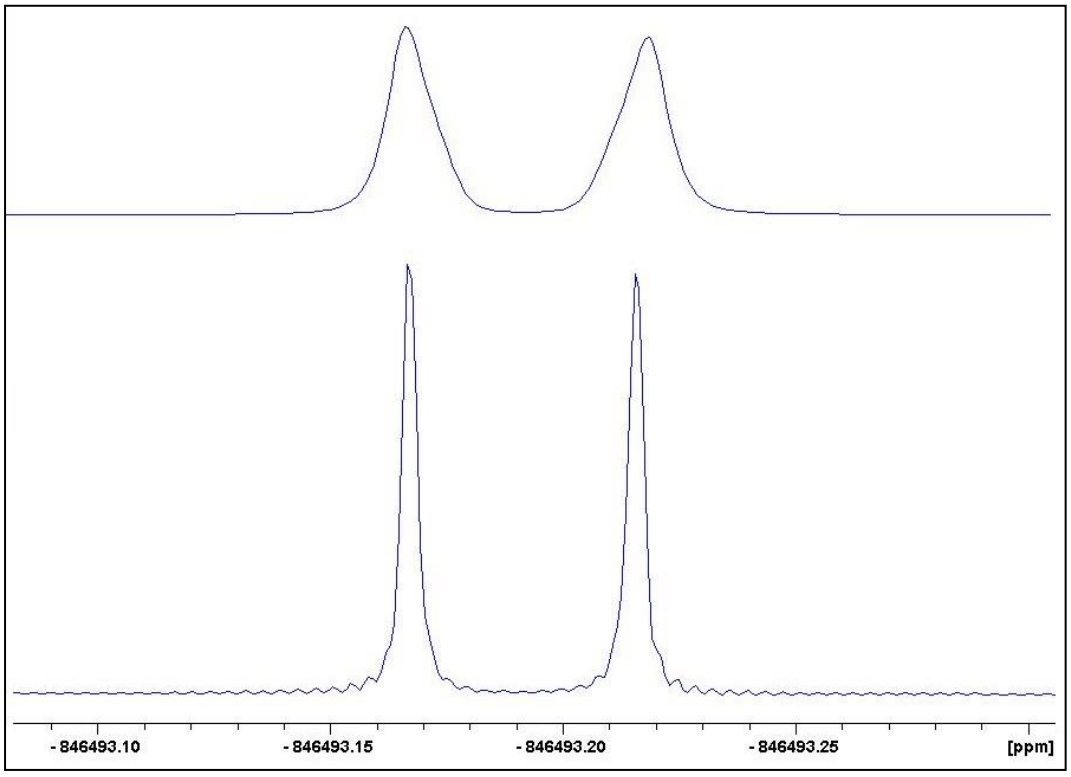

Figure 90 - ^{2}H spectrums of the same liquid crystal before (top) and after (bottom) the addition of substrate (glucose).

3.3.1.3 – Disodium Cromoglycate (DSCG) Lyotropic Liquid Crystal (LLC)

Although DSCG (Figure 91) LLC have not been further used for diffusion and conformation study after media production, a first step characterization was made through the ^{2}H 1D-NMR spectrum acquisition.

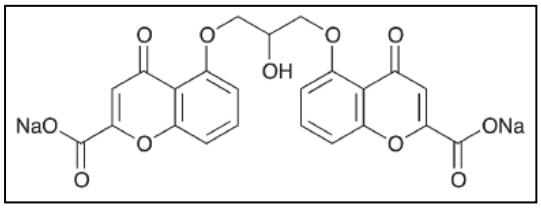

Figure 91 - Representation of the structure of the disodium cromoglycate ion-pair (DSGC).

Disodium cromoglycate salt is a recent discovery in the alignment media investigation, and it forms a liquid crystal phase in water and is one of the cheapest and easiest alignment medium to prepare. Cromolyn, as it is vulgarly known, easily aggregates in solution forming a liquid crystal chromonic phase. This chromonic system is liquid crystalline phased formed by π-stacked columnar aggregation of planar molecules, typically aromatic with hydrophilic groups in the periphery (differently to CpCl). These columnar aggregates provoke the solutes to be trapped between the free space between the columns, as represented below, and performing a disposition of its steric model of alignment that minimizes the steric clashing with the columnar walls, as the parallel disposition of the sugar in relation to the magnetic field represented in the figure below.

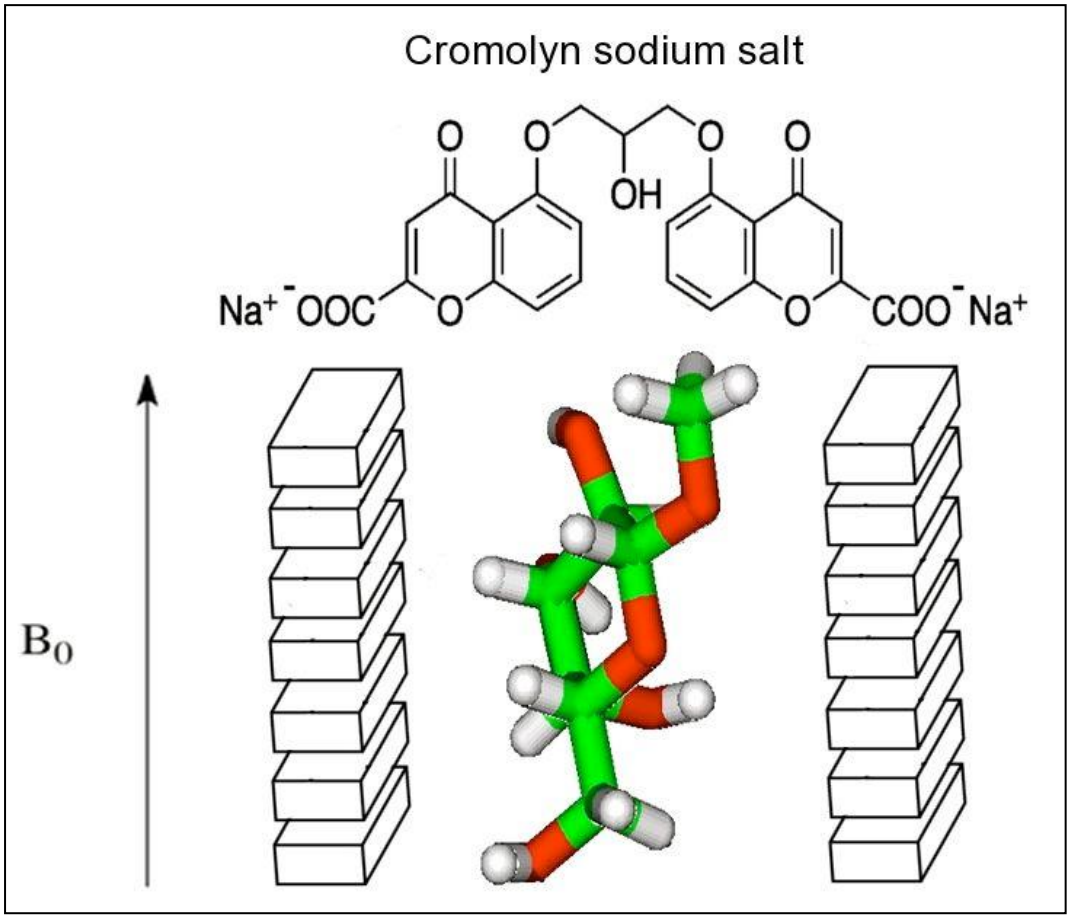

Figure 92 – Representation of the alignment process of methyl-β-D-galactopyranoside in the cromolyn oriented phase.

The ^{2}H 1D-NMR spectrum resulting from this alignment media execution consists in a wide spread quadrupolar splitting of 200 Hz, indicating a highly compacted and orienting alignment media even for the small sized deuterated water in solution. The sharpness of the resulting ^{2}H 1D-NMR spectrum signals indicate the homogeneity of the alignment phase that results in a homogeneity of the aligned molecules, in this case the deuterated water used for the media production.

3.3.2 – Diffusion in Alignment Media

In this sub-section the results of the diffusion study applied to the alignment media CpCl will be presented. The study was done exclusively for this media due to lack of time, since PMMA gels have only been achieved in the end of the experimental work, as have already been referred.

Objectively this study consisted in the determination of diffusion coefficients for different compounds dissolved in different anisotropic CpCl LLC solutions, namely the sugars glucose, cellobiose, cellotetraose and cellohexaose, the protein Lysozyme and the previously studied IL, $BMIMBF_4$, and its comparison with the results obtained for water isotropic solutions.

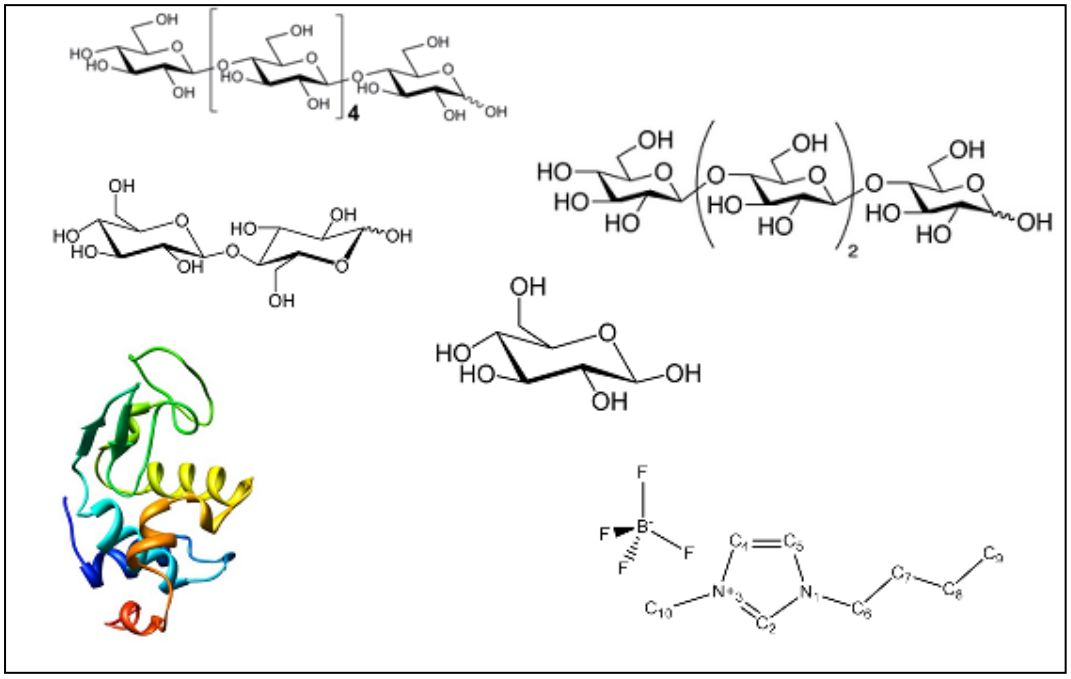

Figure 93 – Structure representation of the different substrates studied in the CpCl/n-hexanol/brine alignment media.

The aim of this study was to study how molecules with different translational molecular behavior are affected in different degree of alignment solutions, namely CpCl 3, 5 and 6 %. The small difference of the solutions concentration is known to induce different alignment conditions and there was an expectation of translational results variability for small condition changes in the media.

Furthermore, the purpose of this study in the context of this entire work, was to understand if the dynamic restrictions imposed by the alignment media on the solute molecules, which are known to generate RDC values appearance that occur in the scale of the pico to nanoseconds time-scale, could also affect diffusion, which occur in the milliseconds time-scale, and be detected by NMR experiments. The RDCs are known to be related with the anisotropic orientation of the solutes in solution during the time averaging of the NMR experiments, which presupposes that if molecules spend more time oriented in a particular direction its translational and rotational motion have been affected in an anisotropic manner. The objective was to detect the influence of this anisotropy in the diffusion behavior of the solutes.

3.3.2.1 – Cetylpyridinium Chloride (CpCl) Lyotropic Liquid Crystal (LLC)

The difference between the CpCl solutions at 3, 5 and 6 % consist in a different micellar size formation in solution for each system, which is expected to influence differently the resulting molecular diffusion coefficients. Two resulting possibilities are previously considered for this study: first, the determination of equal diffusivities for each molecule within the different alignment media degrees,

indicating that no influence of micellar size is affecting the different substrate diffusional properties; and second, the determination of distinct diffusivities for each molecule, which would confirm the practical influence of micellar sizes in substrate properties, and possibly reveal how and when they become significant.

In order to understand the magnitude of the molecular diffusion changes between aligned systems and non-aligned systems, the substrates diffusion coefficients in water solutions were initially measured (Table 3):

Table 3 – Presentation of the different substrates molecular weight and diffusion coefficients in water.

Substrates	**Molecular Weight**	**Diffusion in water (m2/s)**
BMIMBF4	139	6,204E-10
Glucose	180,16	5,101E-10
Cellobiose	342,29	3,465E-10
Cellotetraose	666,58	2,605E-10
Cellohexaose	990,86	2,074E-10
Lyzozyme	14307	7,824E-11

By observing these results is possible to conclude that the diffusion of the different compounds is in accordance to what was predictable by the Stokes-Einstein equation, which means that bigger molecules diffuse slower than the smaller, even for $BMIM^+$, which was expected to present anomalous result due to its ionic feature and the consequent possible interaction with the media subjects, namely CpCl and NaCl.

By plotting the logarithm of the diffusion coefficients versus the logarithm of the molecular weight (MW) (Figure 94) is possible to establish a linear relation, which is normally used to predict diffusion values for unmeasured compounds through a linear regression:

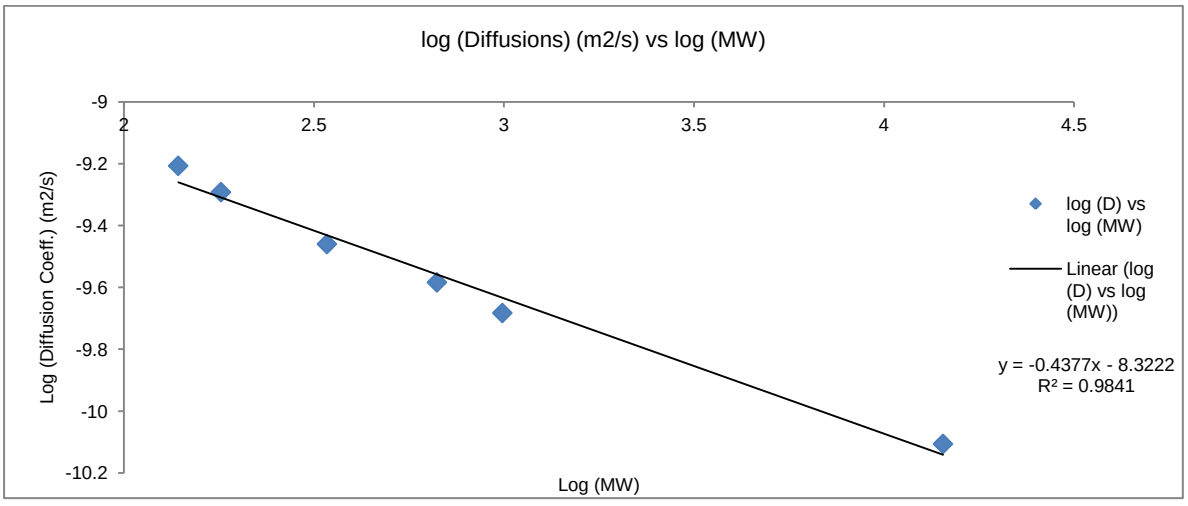

Figure 94 – Representation of the logarithmic relation between the substrates diffusion coefficients and the respective molecular weights in water. A linear regression is established with a R^2 = 0.9841.

Table 4 - Presentation of the different substrates molecular weight, and its diffusion coefficients in water and in different alignment degrees of the same alignment media (CpCl LLC).

Substrates	**Diffusion in water (m^2/s)**	**(Defective) Diffusion in CpCl 3% (< 10 Hz) (m^2/s)**	**Diffusion in CpCl 3% (10 Hz) (m^2/s)**	**Diffusion in CpCl 5% (20Hz) (m^2/s)**	**Diffusion in CpCl 6% (30 Hz) (m^2/s)**	**Molecular Weight**
H_2O	-	6,50E-10	1,36E-09	1,39E-09	1,38E-09	18
Glucose	5.10E-07		4,10E-10	3,85E-10	4,04E-10	180,16
Cellobiose	3.47E-07	9,50E-11		2,85E-10	2,88E-10	342,29
Cellotetraose	2.61E-07	6,86E-11	-	1,89E-10	1,82E-10	666,58
Cellohexaose	2.07E-07	3,48E-11		1,51E-10	1,55E-10	990,86

The diffusion coefficient of the previously mentioned sugars was then measured in different molar percentages of CpCl LLC solutions, corresponding to different alignment conditions, as determined by the ^{2}H NMR quadrupolar splitting (Table 4)

The results obtained indicate that, as in the case of water media, the diffusion coefficients of the different molecules are in accordance with the Stokes-Einstein equation, decreasing with the increasing molecular size. These results also indicate that, as it has been previously hypothesized, in the "good condition" preparations it is verified that the diffusion of the different compounds remains equal for different alignment degrees. This result points out the fact that no influence of the alignment degree is felt on the substrates translational motion behavior, at least for this short range of alignment degrees. Another interesting result consists in the fact that also practically no change is verified between the sugars diffusion coefficient in water and in CpCl LLC solutions, indicating that the global influence of this degree of alignment range (3, 5 and 6 %) is almost negligible for translational motion. Also the water diffusion, along with the sugars, present invariable diffusion through the three alignment degree conditions (3, 5 and 6 %), only presenting value deviation when considering the defective preparation of 3 % CpCl LLC solution, in which the water, just as the sugars, present much slower diffusion coefficient.

The reason for the problematic question of the defective preparation of 3 % CpCl LLC solutions remains somehow a mystery. However, reasons exist to believe that this have been consequence of insufficient time for solution homogenization, prior to substrates dissolution. In practice, it was verified that these preparations were defective through the monitoring by ^{2}H 1D-NMR, being observed different results (splittings) for solutions that came from the same preparation. One reason for such event have only happened in 3 % CpCl LLC preparation, may be the fact that this is the most diluted solution, and for this reason more careful and different conditions might be necessary (different time periods of preparation; or higher temperatures; etc) with liquid crystalline phase formation in order to obtain the desired homogeneity. An example of a defective decay resulting from a defective CpCl LLC preparation may be observed in the figure below:

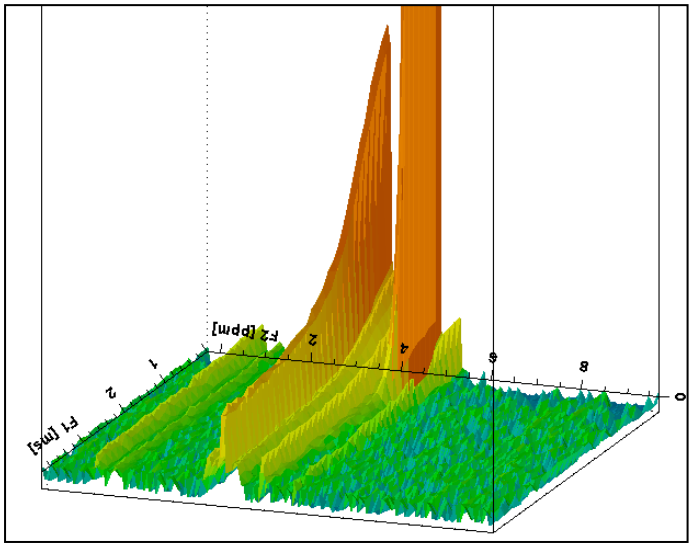

Figure 95 – Representation of a defective decay (of cellotetraose) in a CpCl/n-hexanol/brine liquid crystal.

As may be observed, with exception for the water signal, no other signal presents a single exponential decay, namely cellotetraose and CpCl signals. In fact, after mathematical treatment of the decay data obtained for the non single-exponential signal decays, a bi-exponential decay has been found (data not shown). This result may physically indicate that it is verified by NMR diffusion experiments the contribution of two molecular spin species, one that is diffusing faster, associated with smaller micellar formation regions, and one that is diffusing slower, associated with larger micellar formation regions.

Another good indicative to confirm appropriate CpCl LLC preparations is the ^{1}H 1D-NMR spectrum analysis. Through this spectrum observation becomes possible to evaluate the relative relaxation rate of the alignment media, which is expected to be relaxing very fast and for this reason to present a very broad signal in the ^{1}H 1D-NMR spectrum. On the contrary, in the above spectrum is observed a slower relaxation signal (sharper; at high field of F2 dimension) that in the diffusion experience represented presents almost no decay for the chosen time period, which was expected due to the media properties, such as macroscopic viscosity and microscopic micellar or lamellar aggregates formation.

For opposition, in the next figure is possible to observe a perfect decay of the dissolved $BMIMBF_4$ substance to illustrate a good example of a desired decay. In this pseudo-2D spectrum besides the perfect decay, is also observed a good signal to noise ratio, in opposition to what has been verified in the above situation.

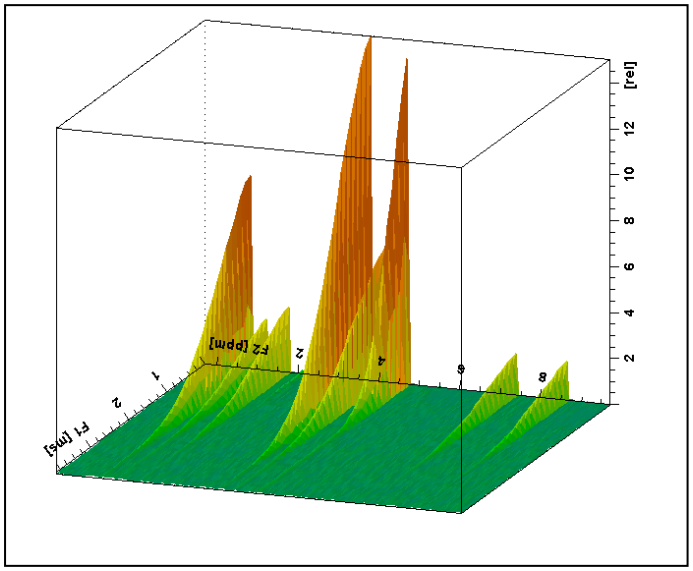

Figure 96 - Representation of effective decay (of $BMIM^+$) in water.

The variation of the diffusion coefficients in the well achieved different alignment degrees (5 and 6 %) represented in the table above, are also shown below versus molecular weight:

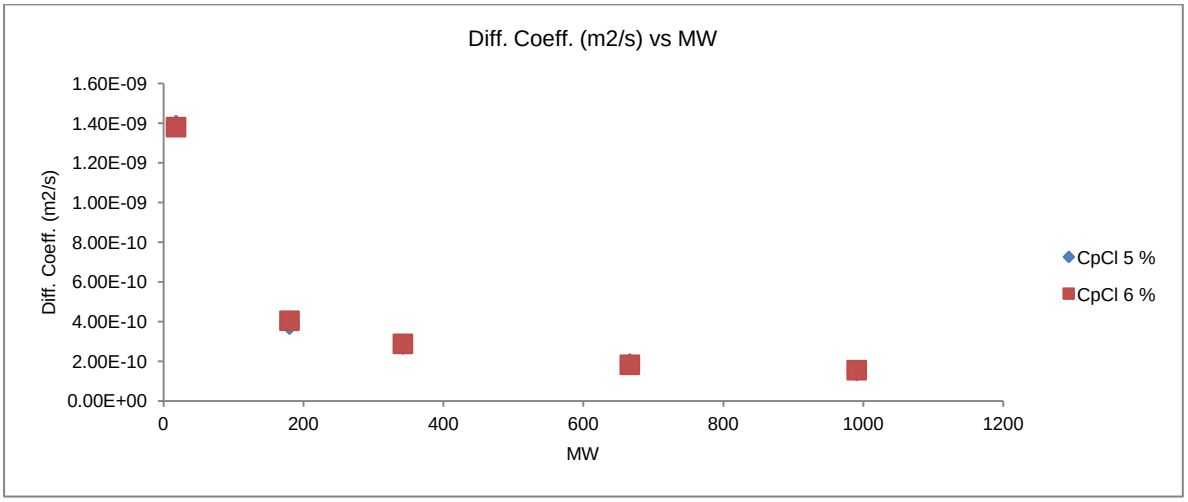

Figure 97 – Representation of the exponential relation between the substrates diffusion coefficients and the molecular weight in the two CpCl/n-hexanol/brine liquid crystal preparations (5 and 7.5 %).

The logarithm relation between diffusion coefficients and molecular weights are again established for these systems, and represented in the figure below. It is possible to observe the high R^2 values associated with the two relations (0.9994 and 0.9983 for 5 % and 6 %, respectively):

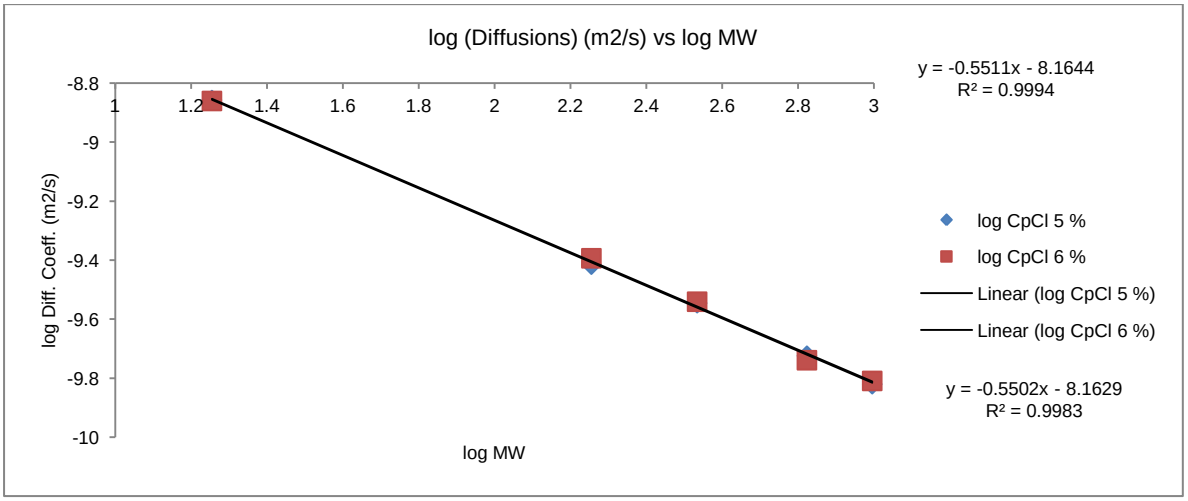

Figure 98 - Representation of the logarithmic relation between the substrates diffusion coefficients and the respective molecular weights in the two CpCl/n-hexanol/brine liquid crystal preparations (5 and 7.5 %). Two linear regressions are established with R^2 = 0.9994 for 5 % and R^2 = 0.9983 for 7.5 %.

At last, another experiment has been performed, which consisted in the testing of the alignment changing with temperature variation, through the monitoring of ^{2}H quadrupolar splitting. This test indicated that the relation of the alignment degree of the solution media with the temperature variation is not linear, progressing in a logarithmical manner.

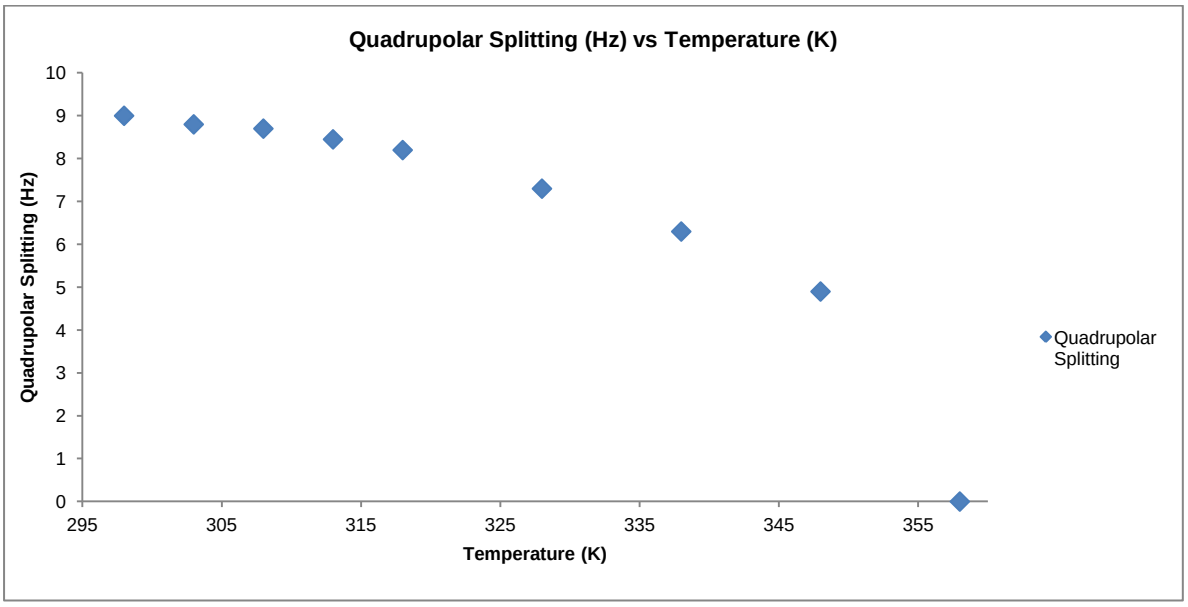

Figure 99 – Representation of the relation between the quadrupolar splitting progression with the temperature variation.

3.3.3 – Conformation in Alignment Media

The conformation study had the purpose of determining the way that the already studied molecules (sugars) react to such media conditions when inserted on it. Although this study was first

planned to determine the conformation of the same sugars studied in the previously discussed diffusion study, so that a correlation between the two results was possible to be carried, due to experimental time limitations these results have not been possible to acquire and process. Nevertheless, we were able to do some acquisition, namely to measure the RDCs, which are known to uncover the relative conformation of molecules in solution, of different sugars such as the sucrose and the β-glucotetraose (G4G4G3G). Again due to time limitations, this study has only been possible to carry out in the already widely discussed CpCl LLC media of alignment.

In the case of sucrose discussion, the results have only been acquired for one degree of alignment media, the 5 % CpCl LLC. On the other hand, for β-glucotetraose (G4G4G3G) the RDCs results from two degree of alignment, namely 5 and 7.5 % CpCl LLC.

The major purpose of this study was the possible understanding of how the different alignment degrees influenced the molecular conformational, in complement to the previous study of how the alignment degree influenced the diffusion motion. Recalling the results obtained from the previous diffusion study, where it was possible to determine that apparently no influence is felt by the molecules with the increasing alignment degree, at least in the alignment range studied, with this conformational study the expectations is that probably the same is verified, and consequently no conformational change will be determined.

3.3.3.1 – Cetylpyridinium Chloride (CpCl) Lyotropic Liquid Crystal (LLC)

3.3.3.1.1 - Sucrose

Table 5 – Sucrose RDC values on CpCl 5%.

Sucrose

	A	B		A	B		A	B
1C (ppm)	62,2	100,3	*3C (ppm)*	77,2	76,8	*5C (ppm)*	84,8	81,5
J (Hz)	298,57	188,74	*J (Hz)*	157,28	157,3	*J (Hz)*	149,67	141,34
T (Hz)	289,36	183,01	*T (Hz)*	147,62	147,24	*T (Hz)*	147,28	147,57
D (Hz)	-9,21	-5,73	*D (Hz)*	-9,66	-10,06	*D (Hz)*	-2,39	6,23
2C (ppm)	114,6	71,9	*4C (ppm)*	75,2	71,5	*6C (ppm)*	62,2	62,2
J (Hz)		149,4	*J (Hz)*	157	141,8	*J (Hz)*	291,06	291,06
T (Hz)		147,51	*T (Hz)*	153,42	147,46	*T (Hz)*	283,05	295,26
D (Hz)	-	-1,89	*D (Hz)*	-3,58	5,66	*D (Hz)*	-8,01	4,2

Observing the sucrose RDCs results in Table 5, it is possible to observe some interesting results. It was expected that the glucose-B ring would be aligned parallel to the external magnetic field

(B_0), as known from literature results. In this way, observing the glucose-B ring RDC values of the axial Hs 2, 3, 4 and 5 it was expected to find equal results in value and in signal, due to its parallel relation.

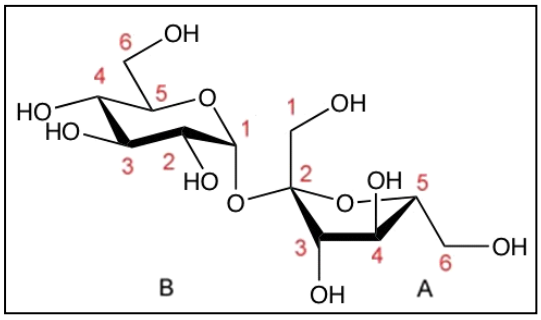

Figure 100 – Representation of sucrose numbering and expected conformation.

Interestingly, although the values of Hs 4 and 5 correspond to the expectations, which were approximately equal positive values (5.66 and 6.23, respectively), since its parallel relation (between C-H bonds; antiperiplanar) and the prediction of parallel orientation of the glucose ring with respect to the external magnetic field, and consequently perpendicular orientation of the ring axial C-H bonds with respect to the external magnetic field. Remember that from 0 º to the magic angle (57.4 º) the RDCs are negative, and from the magic angle to 90 º the RDCs are positive, considering half of the spherical distribution of C-H bonds relation to the external magnetic field.

Anomalously, the Hs 2 and 3 besides presenting negative values (-1.89 and -10.06, respectively), they also present different values to each other. Two eminent explications may arise from this situation: first, errors in the measurement of the two coupling values, the scalar one and the total one (scalar + dipolar; in alignment) resulting in the incorrect determination of the dipolar values; and second, that eventually the glucose ring is really performing a changed conformation (in relation to the one represented in the figure), and its C-H bonds 2 and 3 are pointing equatorially. This hypothesis of changed conformation could be associated to the results obtained for the fructose ring.

Considering now the fructose ring, imagining that its conformation corresponds to the one represented in the figure above, is possible to predict that only the RDC corresponding to the 5 C-H bond would be positive, because of its axial position, and the 3 and 4 ring C-H bonds RDC values would be negative. Taking a look to the Table 5, is possible to observe that oppositely to the prediction the 5 C-H bond present a negative value indicating that is point preferentially parallel with respect to the external magnetic field direction. The 3 and 4 C-H bonds, as expected, present different negative RDC values, which is accordance to their positional conformation and distinct angle. The two hypotheses that arise from the anomalous value of 5 C-H bond are: once again errors in the measurement process; or in second place, the rotation of the fructose ring downwards (considering the figure above) sufficient for the transposition of the 5 C-H bonds from pointing perpendicularly with respect to the magnetic field, to start pointing parallel with respect to the external magnetic field.

In sum, the 1 (equatorial H; RDC negative value), 4 and 5 C-H bonds RDC values of the glucose ring corroborates the represented conformation in the figure above, while the 2 and 3 leave some questions to answer. For the fructose ring, the 3 and 4 C-H bonds RDC values corroborates the represented conformation in the figure above, while the 5 C-H bond suggests a rotation on the fructose ring, also compatible with the values of 3 and 4 C-H bonds RDC values. The 1, of fructose ring, and 6, of fructose and glucose rings, C-H bonds RDC values have no objective interest using this approach, since because of their great mobility the averaged observed with the resulting RDC value may encode several possible positions. One possible conclusion is that in fact the sucrose molecule in these solutions has no linear chain conformation, but adopts a small twisted one.

Despite being very simple and somehow poor, this approach allows the determination of relative positions in sugar rings, as have been introduced earlier in this chapter, and was performed here. Besides that, evaluating linear poly-unit sugars, this approach may be also very interesting to determine the "linearity" of the chain.

3.3.3.1.2 - β-glucotetraose (G4G4G3G)

In addition to the previous sucrose RDCs measurements and analysis, the same have been done for the β-glucotetraose (G4G4G3G), with the advantage that this time it has been done for two different alignment degree values. The expectation for this molecule conformation in solution is that it positions in a parallel manner with respect to the external magnetic field, even knowing that this molecule does not have linear global disposition in water, which is related with its glycosidic bond 1-3.

As has already been seen, a disposition of this type (parallel to the external magnetic field) implies that all the axial Hs of the glucose rings displays positive C-H bond RDC values, and of similar magnitude. The influence of the increment on alignment degree from 5 % to 7.5 % is expected to be observed in terms of magnitude, since it is known that the dipolar coupling value magnitude is dependent on the strength of the alignment (the time duration that the molecule spends in certain position, pointing at certain directions), whereas the sign of the RDC are expected to remain equal due to same pointing direction of the C-H bonds.

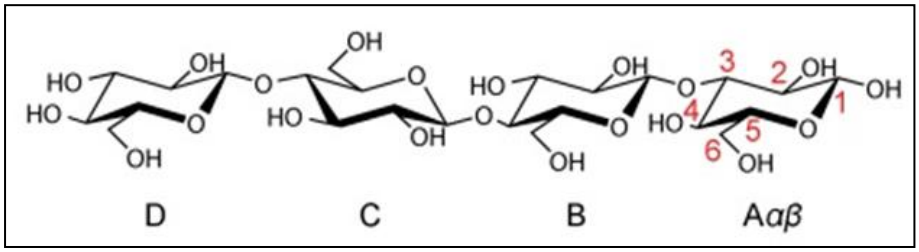

Figure 101 - Representation of β-glucotetraose (G4G4G3G) numbering and expected conformation.

One previous note that is important to consider is the fact that the coupling determination in this case have been much more difficult than in the previous case of sucrose. The reason is the complex spectra exhibited by this compound, which with the addition of couplings (signal splittings) becomes even more complex and harder to attribute. In this way, many C-H bond coupling values obtained are marked with a red box in the table below, in order to signalize the dubious ones.

Table 6 - β-glucotetraose (G4G4G3G) RDC values on CpCl 5 and 7.5%.

G4G4G3G - 5 % CpCl						***G4G4G3G – 7.5 % CpCl***					
	Aα	Aβ	B	C	D		Aα	Aβ	B	C	D
	C1						*C1*				
J (Hz)	186,11	175,36	185,29	175,86	185,92	*J (Hz)*	186,11	175,36	185,29	175,86	185,92
T (Hz)	186	196,33	206,89	206,54	216,48	*T (Hz)*	175,81	217,08	227	226,85	237,41
D (Hz)	-0,11	20,97	21,6	30,68	30,56	*D (Hz)*	-10,3	41,72	41,71	50,99	51,49
	C2						*C2*				
J (Hz)	154,88	144,89	144,67	154,97	155,17	*J (Hz)*	154,88	144,89	144,67	154,97	155,17
T (Hz)	164,45	175,44	175,28	176,01	175,61	*T (Hz)*	185,75	186	195,97	206,17	195,91
D (Hz)	9,57	30,55	30,61	21,04	20,44	*D (Hz)*	30,87	41,11	51,3	51,2	40,74
	C3						*C3*				
J (Hz)	154,64	144,47	155,12	154,9	154,98	*J (Hz)*	154,64	144,47	155,12	154,9	154,98
T (Hz)	165,11	165,11	164,8	164,8	165,01	*T (Hz)*	175,72	175,56	196,27	196,27	175,8
D (Hz)	10,47	20,64	9,68	9,9	10,03	*D (Hz)*	21,08	31,09	41,15	41,37	20,82
	C4						*C4*				
J (Hz)	154,72	165,18	154,97	165,17	154,8	*J (Hz)*	154,72	165,18	154,97	165,17	154,8
T (Hz)	175,46	175,46	175,4	175,4	165,33	*T (Hz)*	185,27	185,27	196,12	196,12	186,53
D (Hz)	20,74	10,28	20,43	10,23	10,53	*D (Hz)*	30,55	20,09	41,15	30,95	31,73
	C5						*C5*				
J (Hz)	154,8	154,73	154,34	154,34	144,54	*J (Hz)*	154,8	154,73	154,34	154,34	144,54
T (Hz)	165,39		165,58	165,58	175,51	*T (Hz)*	186,07	175,67	186	186	196,05
D (Hz)	10,59	-154,73	11,24	11,24	30,97	*D (Hz)*	31,27	20,94	31,66	31,66	51,51
	C6						*C6*				
J (Hz)	299,34	299,5	289,64	299,14	288,8	*J (Hz)*	299,34	299,5	289,64	299,14	288,8
T (Hz)	278,56	289,05	288,94	268,56	278,8	*T (Hz)*	258,31	288,74	278,83	258,21	268,45
D (Hz)	-20,78	-10,45	-0,7	-30,58	-10	*D (Hz)*	-41,03	-10,76	-10,81	-40,93	-20,35
	C6'						*C6'*				
J (Hz)	288,45	299,5	279,28	299,35	289,29	*J (Hz)*	288,45	299,5	279,28	299,35	289,29
T (Hz)	299,06	268,44	278,44	278,94	278,89	*T (Hz)*	185,71	247,64	247,47	247,8	257,68
D (Hz)	10,61	-31,06	-0,84	-20,41	-10,4	*D (Hz)*	-102,74	-51,86	-31,81	-51,55	-31,61

Observing now the resulting values in a global manner, is possible to verify that all the expected axial C-H bond couplings present positive value, confirming its axial position and

additionally confirming that the molecule is standing parallel with respect to the external magnetic field (in a non-linear manner). Considering the fact that these couplings do not present strictly equal values, two possibilities may arise: first, is the possibility of failed measurement of the two splittings, scalar and total, specially supported in this case by the signal confusion that these spectrums presents; and second is the fact that, knowing that the coupling values magnitude are dependent of the degree of restriction, it is possible to assume that such small differences, as 10 and 20 Hz, between the C-H coupling values correspond to small different degrees of restriction of every C-H bond (higher value corresponds to more time spent pointing in certain direction) situated in different positions of the rings.

By observing the table values is possible to establish that globally the carbons 1 and 2 of all the glucose units presents for some reason higher degrees of restriction, while the others present smaller degrees of restriction, interpreting the coupling magnitudes as such. Crucial information are the confirmation of the possibility of distinguish through RDCs if the anomeric H is axial or equatorial, verified by the distinct signal of the two C1 possible configurations of Aα and Aβ, which present negative and positive signal, respectively; and by the same way the possibility of distinction of the two C6 diastereotopic Hs of each unit in some cases.

In sum, is possible to confirm that the sugar β-glucotetraose (G4G4G3G) is standing in a non-linear conformation parallel to the external magnetic field, and that the huge variety of C-H bonds present in every glucose unit show different degrees of restriction through the magnitude of its coupling value. Additionally, is observed the scale up of the magnitude for every coupling from the 5 % to the 7.5 % CpCl solution, which, as already explained, is consequence of the increment on the degree of alignment. Additionally, also refer the possibility of distinguish between anomeric Hs of the two sugar configurations (α or β).

3.4 – Conclusion and Future Works

The main conclusion of this work is that the increasing of the alignment degree of the lyotropic liquid crystal (nematic phase) CpCl/n-Hexanol, in normal conditions, has no huge consequences in the substrates (at least for sugars) self-diffusion and conformation.

In terms of dynamics it is concluded that the anisotropic effect imposed by the alignment media on the solute molecules, which is verified by the RDCs occurrence (pico to nanoseconds time-scale), is not detected in diffusion, at least in the milliseconds time-scale in which arises the diffusion experiments. In this way, in the alignment media studied (CpCl) and in the degrees of alignment selected (3, 5 and 6 %) it appears that the diffusion is totally isotropic in aligned media.

Is also possible to conclude that sugars diffusion follow the Stokes-Einstein equation for diffusion, ordering the increasing diffusion rate as: D-(+)-glucose > D-(+)-cellobiose > 1,4-D-(+)-cellotetraose > 1,4-D-(+)—cellohexaose > Lysozyme, and that a linear relation may be established between the logarithmical values of molecules diffusion and molecular weight.

Is possible to conclude that the sugars diffusion in water and in the alignment media are very close, confirming the almost non-effect of the alignment conditions in diffusion.

Another important achievement was the attaining of the PMMA gel integrity, since because of the utilization of the radicalar initiator V-65 instead of V-70 represents a decrease in global costs.

With this study was possible to determine that the sugars sucrose and β-glucotetraose (G4G4G3G) positioning themselves approximately parallel to the external magnetic field, and possibly present small different degrees of mobility restriction for each C-H bonded carbon within the sugar units, detected by the small nuances of magnitude in RDCs values.

As future work it is logical to propose the repetition of the same experiences and techniques but this time to evaluate a larger range of alignment degrees, to try the detection of any behaviour variation, as with diffusion or with conformation disposition.

Another possible future work was performing this same study on different alignment media type, such as the prepared PMMA gels, or even in another LLC media, such as the prepared cromolyn, presenting also large ranges of alignment degree

A possibility of another study to probe molecular dynamics in alignment media was to perform the same rotational motion study applied for $BMIMBF_4$ in this work, with the objective of detecting the possible effects that these alignment media may induce in molecular correlation times in comparison with the ones verified in water.

Chapter 4 – Conclusions and Future Perspectives

I believe that some global conclusions that can be withdrawn from all this work is that NMR is an invaluable spectroscopic technique that offers almost unlimited possibilities to study matter, specially liquids, and specially its dynamics at the microscopic level.

In this work, techniques that allows the study of diffusion, reorientation and even conformation have been applied with success in determining such specificities, and contributing to the deeper understanding of molecules dynamics in solution, and uncovering many possibilities of future studies based on questions that emerged from this one.

Specifically, with this work it was possible to determine the importance that the alignment media design, preparation and utilization may reveal for not just the conformational comprehension, but also for the diffusion dynamics. Although the somehow frustrating diffusion results from these media experiences, is still exists the possibility of major and significant discoveries arising from this methodology, which consists in a motivation to further develop research on it.

On the other hand, the well established and fruitful methodology to study ionic liquids described herein is an encouraging result and experience to further develop investigation in such field. The possibility of study the whole phase diagram of [BMIM][BF_4] with water, and in addition a large temperature range, consist in one major effort for IL dynamic description, and considering the results obtained it represents a major instrument for investigation that this time resulted possibly in the progressive evaluation of the interesting ion-pair dynamics, which was a primary objective.

This work has contributed not just for producing results, but principally to permit the learning and development of such spectroscopic tool as NMR, and subsequently to dominate panoply of techniques that allowed the obtaining of such results. In this way, it is concluded that the understanding and experience earned consist in an added value that besides the contribution for my physicochemical comprehension of molecules, will enable the progressive deepening of the same in the future.

Possible future works derivative from this work consist easily in the application of such methodologies to different analogous systems, such as: other ionic liquids with close structural relation and similar conditions; the development of new alignment media types, and the investigation of same molecular properties as diffusion and conformation in such systems; and eventually the application of such studies to completely different systems in which are expected interesting results of the same order.

Annexes

A.1 – NMR Relaxation

A.1.1 - Relaxation Measurement Methods

The relaxation methodology approached in this thesis, because of practical application for results purposes, is the inversion-recovery experiments. It is a simple and fundamental experiment that permit the direct obtaining of T_1 values.[4]

A.1.1.1 – Inversion-Recovery – Measurement of T_1

The value of T_1 provides valuable information as to the motion and dynamics of the molecules.[4]

The usual technique for measuring T_1 is called inversion-recovery. The pulse sequence is given by:[4]

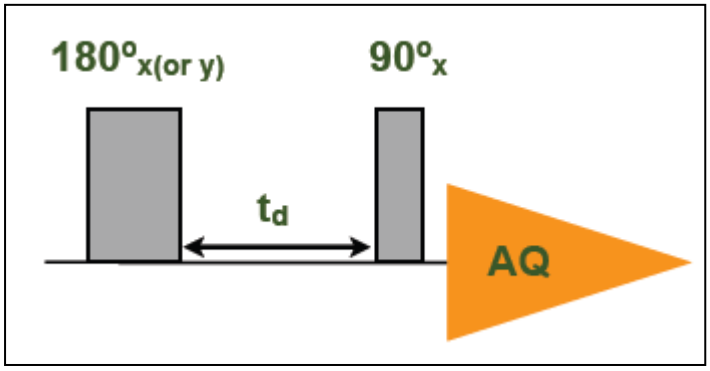

Figure 102 – Inversion-recovery pulse sequence.[4]

It consists of two RF pulses separated by an interval t_d. The use of a single-headed arrow means that the pulse sequence is repeated, with different values of the interval t_d, and the results compiled in a two-dimensional data matrix. Because time variable during the signal acquisition interval is denoted as *t*, then the two-dimensional data matrix may be denoted $s(\tau,t)$.[4]

The pulse sequence given before, hide a number of details. First, for each value of t_d, the pulse sequence and data acquisition are normally repeated many times, adding the signals together in order to enhance the signal over the noise. Second, each repetition of the pulse sequence is separated by a long interval τ_{wait}, during which the spins return to a reproducible thermal equilibrium state. For this to be satisfied, the waiting interval τ_{wait}, plus the signal acquisition period τ_{acq} (within the

latter), must be several times (1-5 times) the relaxation time constant (which imply that it is necessary to have a good guess as to the value of T_1 before determining it this way).[4]

The first pulse in the sequence is a π_x pulse that generates an inverted population distribution. The populations relax back towards thermal equilibrium during the interval τ: their progress is monitored by the second pulse, which converts the population difference into coherences, including the observable (-1)-quantum coherence, which induces an NMR signal:[4]

Although the spin density operator transformations are not shown here, it is known that the observable spin coherence is therefore a function of the interval between the pulses (τ) and the time *t* after the last pulse.[4]

Although this is also not demonstrated, it is known that the spectral peak amplitude is negative for small values of τ, but goes through zero and becomes positive for large values of t_d:[4]

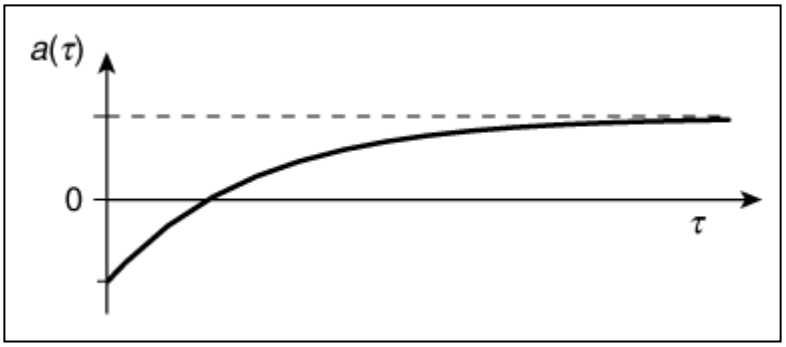

Figure 103 – Peak amplitude as function of τ (equal to t_d).[4]

Whereas the amplitude $a(t_d)$ versus t_d reflects the history of the longitudinal magnetization recovery (each peak amplitude depends on t_d according to the spin-lattice relaxation time constant for the corresponding ensemble *j*), it is possible to calculate T_1 from the following equation (for each ensemble of spins):[4]

$$a_j(\tau) = \frac{1}{2}\mathbb{B}\left(1 - 2e^{\frac{-\tau}{T_1^j}}\right) \quad \textbf{(23)}$$

The data matrix $s(\tau,t)$ is Fourier transformed with respect to *t* giving $S(\tau,\Omega)$.

An experimental data matrix $S(\tau,\Omega)$ for a sample with four different chemical sites is shown:[4]

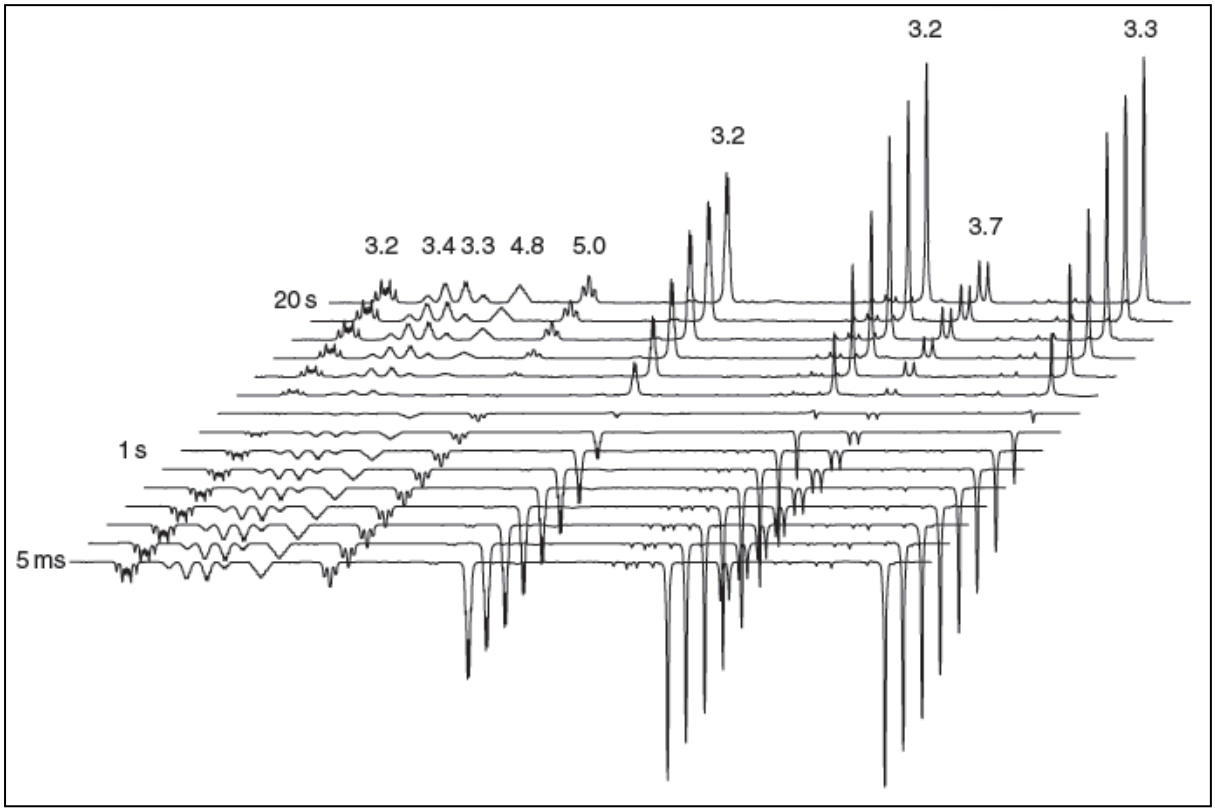

Figure 104 – Inversion-recovery spectra.

The value of T_1 may be extracted from the experimental peak amplitudes $a(t_d)$ by standard methods, for example the values of $\log(a(t_d))$ may be plotted against τ and fitted to a straight line. The slope of the best-fit is the estimated value of $1/T_1$.[4]

A.1.2 – Diffusion-Ordered Measurement Methods

Experiments carried out using a static field that remains systematically inhomogeneous are limited in application, as the line broadening caused by the field inhomogeneity leads to signal overlap and reduces signal-to-noise ratio. The introduction of pulsed field gradients (PFG) allowed spin echo (SE) signals to be measured under high resolution conditions, retaining high sensitivity and allowing signals with different Larmor frequencies to be distinguished. Pulsed field gradient spin echo (PFGSE) experiments have a variety of form, but all share the same basic principals.[9]

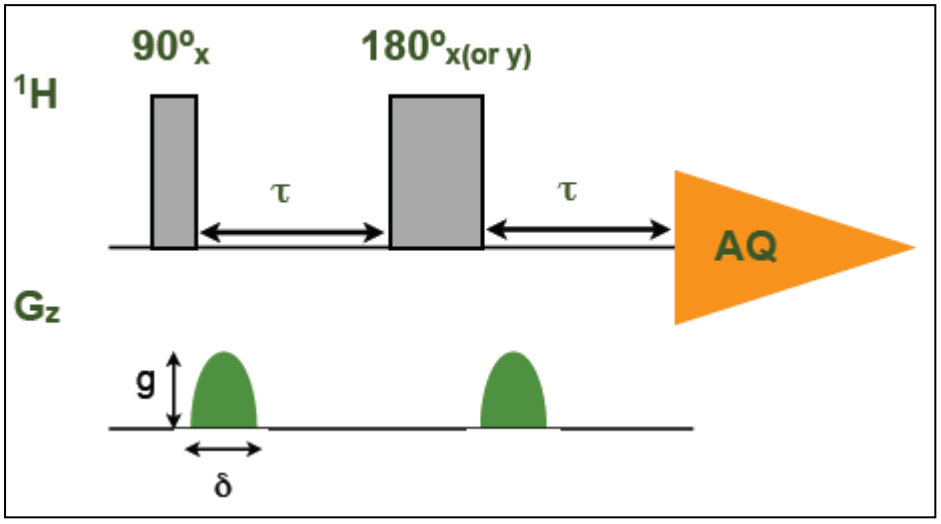

Figure 105 – Pulsed field gradient pulse sequence.

First there is the initial excitation with a $(\pi/2)_x$ that puts the magnetization in the x,y-plane. During the application of the gradient, which is along the direction of the static spectrometer field (B_0), the effective magnetic field for each spin is dependent on its position. Thus, the precession frequency is also position dependent, which leads to the development of position dependent phase angles. The π_y pulse changes the direction of the precession. Therefore, the second gradient of equal magnitude will cancel the effects of the first and refocus all spin, provided that no change of position, with respect to the direction of the gradient, has occurred.[183]

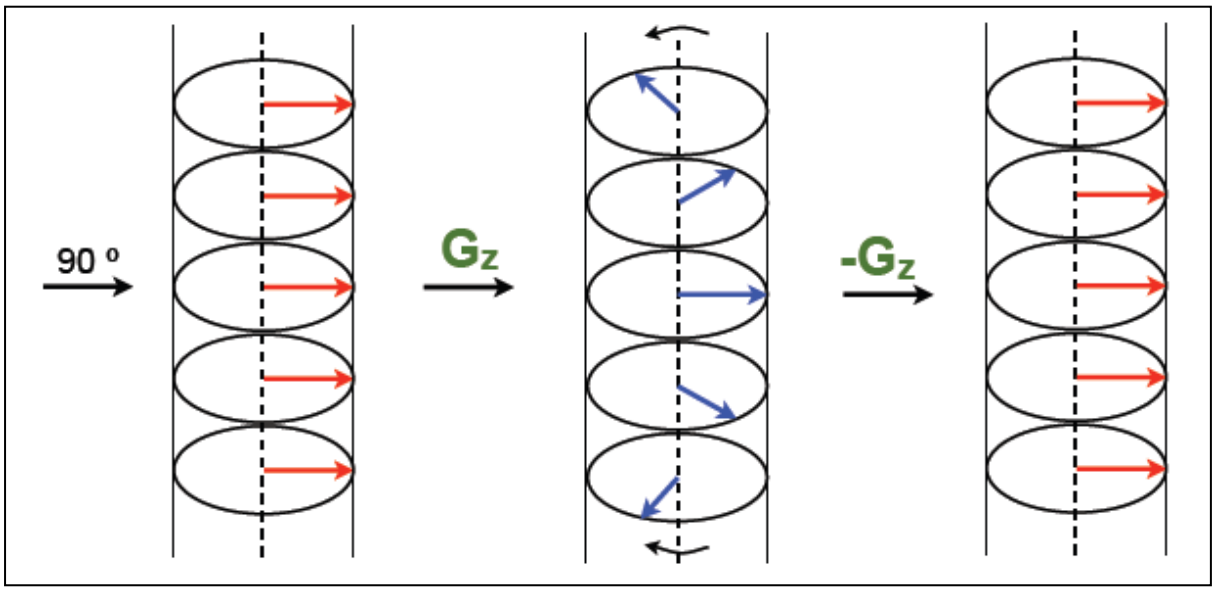

Figure 106 – No diffusion situation.

If there is a change of position, the refocusing will not be complete. This results in a remaining dephasing which is proportional to the displacement during the period *Δ* between the two gradients.[183]

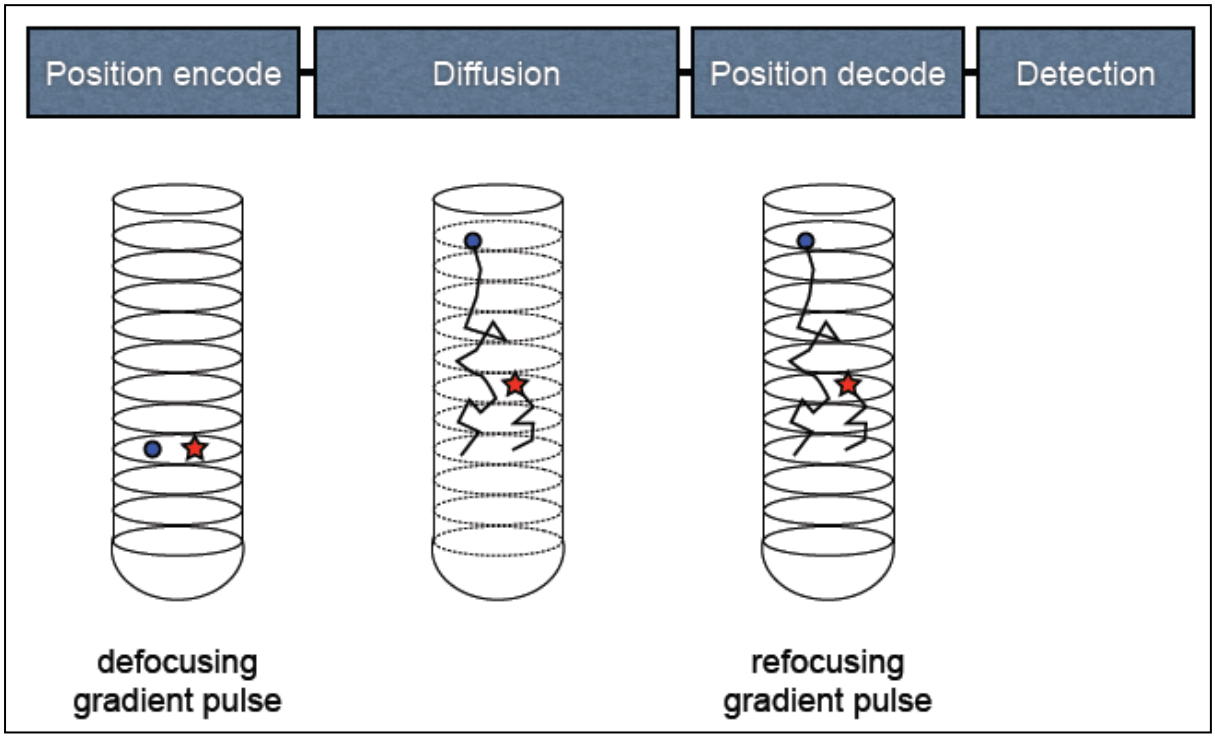

Figure 107 – Diffusion situation.

Since diffusion is a random motion, there is a distribution of gradient induced phase angles. These random phase shifts are averaged over the ensemble of spins contributing to the observed NMR signal. Therefore, this signal is not phase shifted but attenuated, with the degree of attenuation depending on the displacement.[183]

The signal intensity $S(2\tau)$ after the total echo time 2τ is given by:[183]

$$S(2\tau) = S(0)e^{\left(\frac{-2\tau}{T_2}\right)}e^{\left[-\gamma^2 g^2 D\partial^2\left(\Delta-\frac{\delta}{3}\right)\right]} = S(2\tau)_{g=0}e^{\left[-\gamma^2 g^2 D\partial^2\left(\Delta-\frac{\delta}{3}\right)\right]} \quad \textbf{(24)}$$

- $S(0)$ is the signal intensity immediately after the $\pi/2$ pulse;
- g is the strength of the applied gradient;
- δ is the length of the rectangular gradient pulses;
- Δ is the separation between gradient pulses.

Some typical values are: δ in the range of 0-10 ms; Δ in the range of milliseconds to seconds; and g is up to 20 T m^{-1}.[183]

To determine diffusion coefficients a series of experiments is performed in which either g, δ or Δ is varied while keeping τ constant to achieve identical attenuation due to relaxation.

For the determination of D, non-linear regression of the experimental data may be used.

A.2 – NMR in alignment media

A.2.1 – NMR Direct Dipole-Dipole Coupling

Dipolar coupling (or direct dipole-dipole coupling) consist in the direct through-space interaction between two magnetic dipoles (nuclear spins), which alongside with chemical shift, scalar coupling and quadrupolar coupling composes the four internal spin interactions. Out of these four NMR spectroscopic interactions, only two are directly observable in high-resolution NMR spectra of organic compounds in isotropic solutions, which are the isotropic chemical shift (resonant frequency of a nucleus relative to a standard) and the scalar coupling (coupling through chemical bonds connecting two spins). The dipolar and the quadrupolar couplings, plus the anisotropic parts of the former are averaged by the fast tumbling dynamics in solution, as will be seen subsequently, and are noticed only by their contribution to relaxation (for example in Nuclear Overhauser Effect).[4]

Dipolar interaction is easy to physically visualize since it can be consider the representation of two magnetic fields, looping around in the surrounding space, associated to two nuclear spins close to each other, each presenting a characteristic direction according to the spin magnetic moment (vector). The interaction between the two spins is mutual, so each nuclear spin experiences the field generated by the other nuclear spin. This interaction denomination (direct dipole-dipole coupling) is also called this way because the fields between the nuclear spins propagate through the intervening space, without involving the electron clouds. Dipolar coupling may be either intramolecular or intermolecular, and homonuclear or heteronuclear.[4]

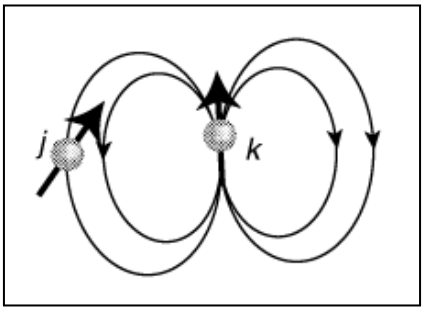

Figure 108 – Dipolar coupling.[4]

A.2.1.1 – NMR Isotropy and Anisotropy

At this point it is important to clarify the meaning of Isotropy and Anisotropy in NMR molecular motion context. In NMR, as in general, isotropy reflect the distribution of something uniformly (*isos* = equal) in all directions (*tropos* = way), while anisotropy reflects the opposite, that is the preferred orientation in some directions. In this context, these terms are directly related to molecular motion (rotational and translational), so that isotropic motion refers to molecules whose motion is free, and individually may experiment all possible orientations in a given time period; and anisotropic motion, on the other hand, refers to molecules whose motion is somehow restricted and thereby some orientations are favored over others in a given time period. Furthermore, in solids every molecule is trapped in their position, so that each molecule presents only a single direction, but together all molecules may combine all possible directions. Many NMR observables are tensorial properties

whose value depends on the relative orientation of the molecule respect to the external magnetic field B_0, as will be seen later.

A.2.1.2 – Quantum Mechanical Approach – Key Equations and Definitions

The full form of the dipolar interaction between I_j and I_k is represented in the potential energy spin Hamiltonian by the following term:[4]

$$\hat{\mathcal{H}}_{jk}^{DD,full} = b_{jk}\left[3\left(\hat{I}_j \cdot e_{jk}\right)\left(\hat{I}_k \cdot e_{jk}\right) - \hat{I}_j \cdot \hat{I}_k\right] \quad \textbf{(25)}$$

- $\mathbf{e_{jk}}$ is a unit vector parallel to the line joining the centers of the two nuclei; the magnitude of the vector e_{jk} is defined to be $e_{jk} \cdot e_{jk} = 1$;

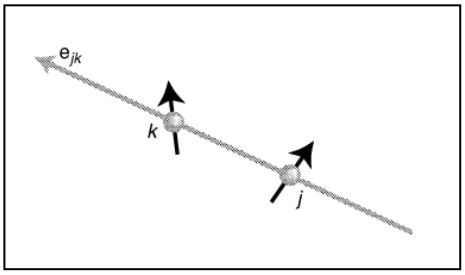

Figure 109 – Internuclear spin vector.[4]

- $\boldsymbol{b_{jk}}$ is the dipolar coupling constant that gives the magnitude of the through-space interaction. Which is given by:[4]

$$b_{jk} = -\frac{\mu_o}{4\pi}\frac{\gamma_j \gamma_k \hbar}{r_{jk}^3} \quad \textbf{(26)}$$

- γ_j and γ_k are the gyromagnetic ratios of the two spins (units of radians per second per Tesla);
- r_{jk} is the spin-spin distance between the two spins (units of meters);
- μ_0 is the magnetic constant, which is equal to 4π x 10^{-7} Hm^{-1} (SI units);
- $\hbar$ is the Planck constant, which is equal to 1.054 x 10^{-34} (units of Joule second).

Equation (2) provides the dipolar coupling in units of radians per second, or Hertz (2π radians per second = 1 Hertz). The interaction goes down according to the inverse cube of the internuclear distance, and scales linearly with the gyromagnetic ratio of each interacting spin.[4]

Dipolar coupling b_{jk} is constant, so it does not depend on molecular orientation. On the other hand, the dipolar spin Hamiltonian in equation (1) is orientation dependent, since the vector e_{jk} changes direction as the molecule rotates. The negative sign in equation (2) indicates that the coupling energy of the interacting spin pair is minimized when both are pointing in the same direction along the internuclear vector.[4]

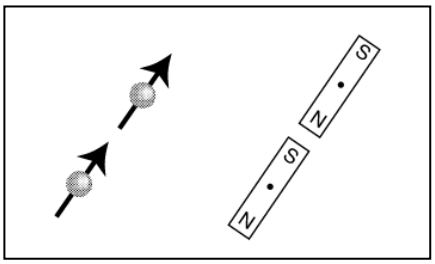

Figure 110 – Polarized magnets.[4]

The dipolar coupling is very useful for molecular structural studies, since it depends only on known physical constants and the inverse cube of the internuclear distance r_{jk}^{-3}. Estimation of this coupling provides a direct spectroscopic way to the distances between nuclei, and so to the geometrical form of the molecule. Measuring many dipolar couplings of spin pairs in a molecule can uncover the molecular structure and conformation unambiguously (NOESY and ROESY experiments make use of this principle).[4]

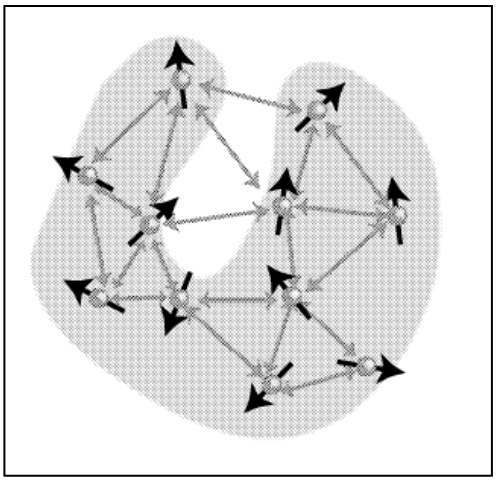

Figure 111 – Many dipolar coupled spins.[4]

A.2.1.2.1 – Secular Dipolar Coupling

The secular approximation in the dipolar coupling context concerns the case where the Hamiltonian is the sum of two terms:[4]

$$\widehat{\mathcal{H}} = \hat{A} + \hat{B} \qquad \textbf{(27)}$$

- *A* and *B* are Hermitian (or self-adjoint) operators (equal to its conjugate transpose, *A** and *B**)

Transposing this principle for a sample containing many "equivalent" spins (equivalent dipolar coupling interaction), where each pair of spins has a dipolar coupling described by equation (1), the dipolar coupling spin Hamiltonian of the whole sample is given by:[4]

$$\hat{\mathcal{H}}_{jk}^{DD,full} = \sum_k \sum_j^{k-1} \hat{\mathcal{H}}_{jk}^{DD,full} \quad \textbf{(28)}$$

Nevertheless, the form of the secular dipolar coupling depends on whether the spins I_j and I_k are of the same isotopic spin species or not. The secular approximation is based on the energy level differences between energy eigenstates, and these energy levels differences depend strongly on whether the spin system is homonuclear or heteronuclear. Recovering the explanation of equation (3), to better understand the difference between the homo- and heteronuclear spin system cases, since *A* is Hermitian it is possible to form an orthogonal basis set from the eigenvectors |*n*> of *A*:[4]

$$\hat{A}|n\rangle = a_n|n\rangle \quad \textbf{(29)}$$

- a_n are the eigenvalues of *A*;
- |*n*> are the eigenvectors of *A*.

Establishing the parallel between operator *A* and a nuclear spin I_j or I_k, *A* eigenvalues a_n may be represented in different energy eigenstates in an energy diagram as follows:[4]

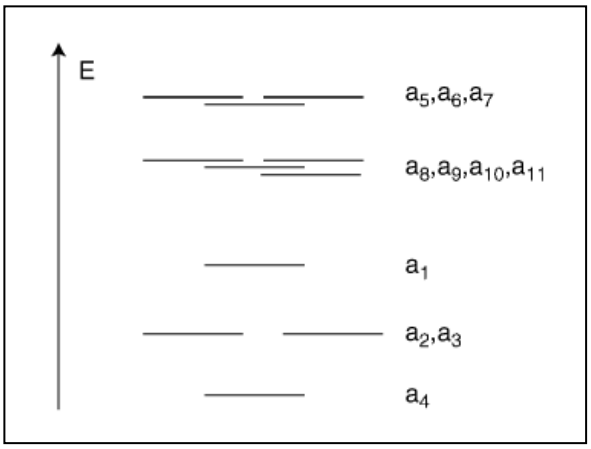

Figure 112 – Energy diagram of eigenstates.[4]

In this way, because the energy differences between eigenstates are characteristic for each nuclear spin (for example ^{1}H, ^{13}C, etc), the secular approximation will be necessarily different for the two cases, homonuclear case and heteronuclear case.[4]

Considering the homonuclear case, then the secular part of the dipolar coupling spin Hamiltonian is given by:[4]

$$\hat{\mathcal{H}}_{jk}^{DD}(\theta_{jk}) = d_{jk}(3\hat{I}_{jz}\hat{I}_{kz} - \hat{I}_j \cdot \hat{I}_k) \quad \textbf{(30)}$$

- d_{jk} is the secular dipolar coupling, that is given by:[4]

$$d_{jk} = b_{jk}\frac{1}{2}(3\cos^2\theta_{jk} - 1) \quad \textbf{(31)}$$

- Θ_{jk} is the angle between the vector joining the spins and the external magnetic field, that is:[4]

$$\cos\theta_{jk} = e_{jk} \cdot e_z \quad \textbf{(32)}$$

As shown in this representation:[4]

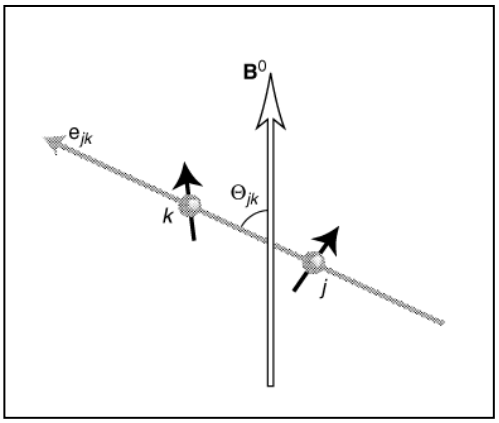

Figure 113 – Internuclear spin vector with respect to the external magnetic field.[4]

Worth noting that the dipolar coupling constant b_{jk} depends only on the distance between the spins and does not depend on the orientation of the spin pair with respect to the magnetic field, while the secular dipolar coupling d_{jk} depends on the orientation and the distance.[4]

Considering the heteronuclear case, then the secular part of the dipolar coupling spin Hamiltonian is given by:[4]

$$\hat{\mathcal{H}}_{jk}^{DD}(\theta_{jk}) = d_{jk}(2\hat{I}_{jz}\hat{I}_{kz}) \quad \textbf{(33)}$$

In both cases, homonuclear and heteronuclear, the secular dipolar coupling d_{jk} depends on the molecular orientation, through the angle Θ_{jk}. The settlement of the angle domain ($3\cos^2\Theta_{jk} - 1$) provides the determination of the opposite sign for the secular dipolar coupling whether the spin pairs are aligned along the field ($\Theta_{jk} = 0$) or the spin pairs are oriented perpendicular to the field ($\Theta_{jk} = \pi/2$). Other significant information is achievable by setting the secular dipolar coupling equal to zero:[4]

$$3\cos^2\theta_{jk} - 1 = 0 \quad \textbf{(34)}$$

Which results in obtaining a value of 54,74 º for Θ_{jk}, that is called the magic angle:[4]

$$\theta_{magic} = arctan\sqrt{2} \cong 54.74^o \quad \textbf{(35)}$$

A.2.1.2.2 – Dipolar Coupling in Isotropic Liquids

In an isotropic liquid the secular part of the intramolecular dipolar coupling averages to zero. This is seen by observing the following integral:[4]

$$\int_0^{\pi} \mathrm{d}\theta_{jk} \sin\theta_{jk}\left(3\cos^2\theta_{jk} - 1\right) = 0 \quad \textbf{(36)}$$

The factor sin Θ_{jk} is necessary in order to reproduce the physical behaviour of nuclear spins in solution, and give all orientations equal probability. The area element on the surface of the sphere is proportional to the sin Θ_{jk} term:[4]

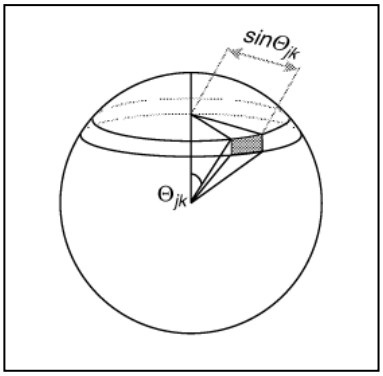

Figure 114 – Sphere surface representation of the area element for orientations equal probability.[4]

The principle idea is that there are only two ways of orienting a spin-spin vector along the magnetic field (up or down), whereas there are many ways of orienting a vector perpendicular to the magnetic field:[4]

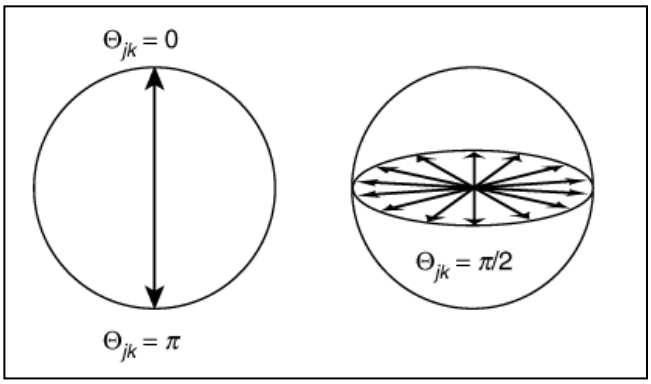

Figure 115 – Parallel and perpendicular orientations.[4]

In the same way, the short-range intermolecular dipolar couplings do average to zero because of the translational and reorientational motions of the molecules. The long-range intermolecular dipolar couplings do not average to zero in isotropic liquids; however these couplings are so small that in most circumstances they may be ignored. The dipolar coupling spin Hamiltonian may be written by:[4]

$$\widehat{\mathcal{H}}_{jk}^{DD} \cong 0 \text{ (in isotropic liquids)} \quad \textbf{(37)}$$

Although the secular part of the dipolar coupling practically disappears in isotropic liquids, it is still possible to exploit the non-secular part of it (b_{jk}) through their effect on the relaxation of the spin system, as it will be unwound in the NOE effect topic.[4]

A.2.1.2.3 – Dipolar Coupling in Anisotropic liquids

In an anisotropic liquid, there is a preferential molecular and translational motion orientation of the molecules.[4]

The intramolecular dipolar couplings do not average out completely in an anisotropic liquid. The dipolar Hamiltonian terms in an anisotropic liquid are given by equation (6) in the homonuclear case, and by the equation (9) in the heteronuclear case, where the secular dipolar couplings are equal to:[4]

$$d_{jk} = b_{jk}\frac{1}{2}\overline{\left(3\cos^2\theta_{jk} - 1\right)} \quad \text{(anisotropic liquids)} \tag{38}$$

The overbar indicates an average over all orientations experienced by the molecules in the anisotropic liquid, weighted by their probabilities.[4]

The rapid diffusion motion in anisotropic liquid still averages out the short-range intermolecular dipolar couplings as in the isotropic liquids. The long-range intermolecular dipolar couplings survive the motional averaging, but are very small and may usually be ignored. The representation of dipolar couplings and molecular orientation in anisotropic liquids can be visualized as in the following diagram:[4]

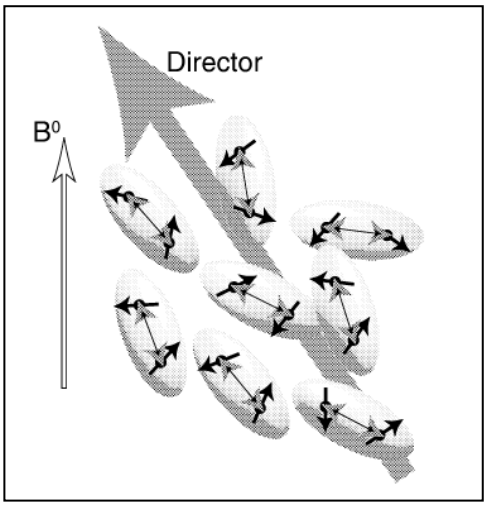

Figure 116 – Dipolar coupling in liquid crystals.

As may be inferred, intramolecular couplings survive while intermolecular couplings are absent.[4]

A.2.2 - Measurement of RDCs

The measurement methods described hereafter will not be classified by their mode of operation (frequency- or intensity-based methods) but by the kind of coupling extracted.[167]

A.2.2.1 – Measurement of $^1D_{C-H}$

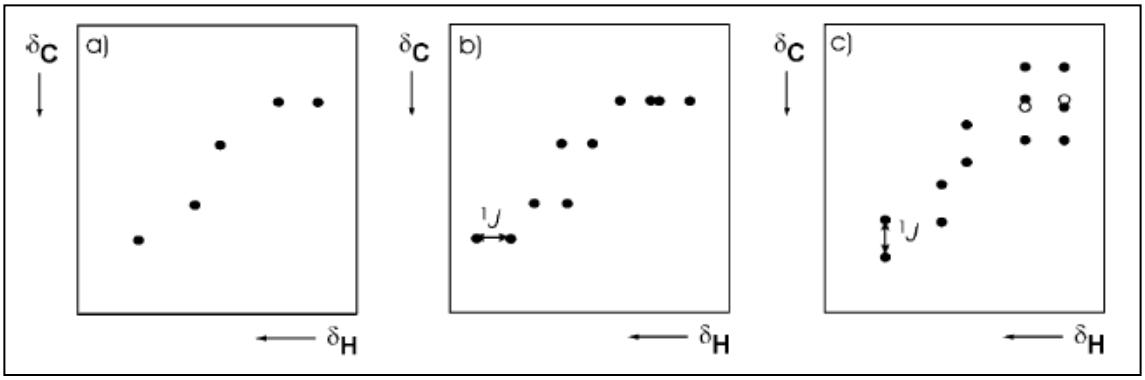

Figure 117 – Representation of a HSQC spectra. a) ordinary decoupled; b) coupled in the direct dimension; c) coupled in the indirect dimension.[167]

As they are the easiest obtained, 1DC-H are by far the most frequently used RDCs. One-bond heteronuclear scalar couplings are usually rather large (1JC-H = 120-250 Hz) and if the degree of order is sufficiently small, the values of 1D are much smaller than 1J, such that the determination of the sign and the size of 1D is straightforward. If T is larger than J, D is positive, and if T is smaller than J, D is negative (as 1JC-H is known to be positive). Thus, in principle, every method for measurement of 1JC-H can be used to obtain 1DC-H, even coupled 13C spectra. However, this cannot be recommended, as measurement times are long, the achievable resolution is low, resonances are prone to overlap and the 1J/DC-H values of diastereotopic protons (within CH2 groups) cannot be assigned to the corresponding 1H chemical shift.[167]

State-of-the-art methods are based on HSQC (heteronuclear single quantum coherence) experiments, from which couplings are extracted from frequency differences either in direct (F2) or indirect dimension (F1).[167]

The arguments for using F2-coupled HSQCs are numerous: experiment times are short, the achievable resolution is maximized and couplings to diastereotopic protons can be extracted easily, as long as signals do not overlap. However, there are also some drawbacks of F2-coupled HSQCs when working with oriented samples. First of all, the proton-proton dipolar couplings (nDH-H) also evolve during acquisition and are therefore observed in the direct dimension together with the 1DC-H couplings that are of interest, which complicates or even impedes extraction of the latter. This problem can be removed by using homonuclear dipolar decoupling during acquisition.[167,184]

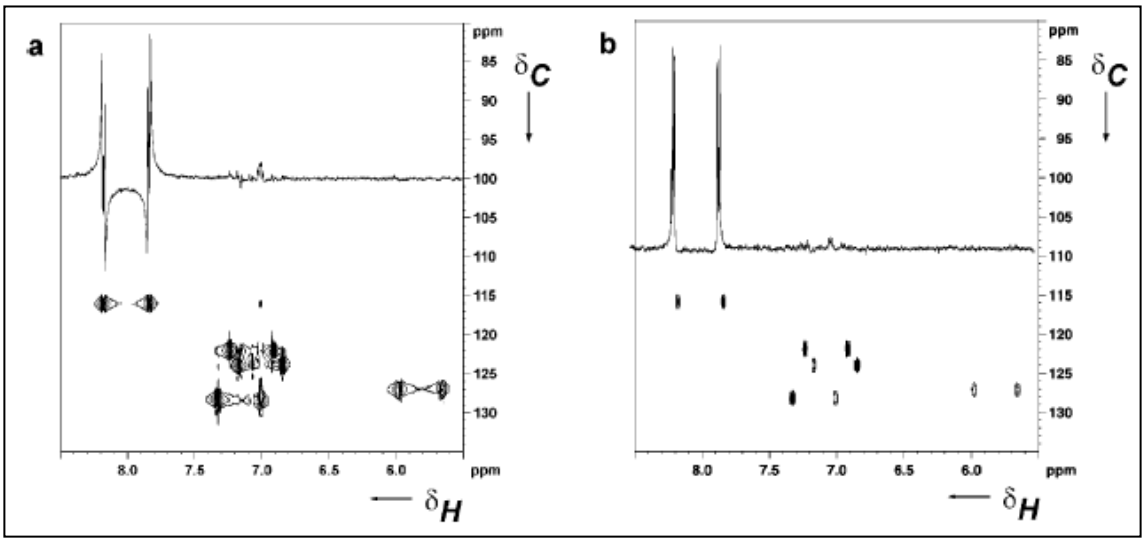

Figure 118 – Mismatching of the magnetisation transfer delay in a direct dimension coupled HSQC spectra.[167]

In all indirectly (F1) detected spectra, magnetization transfer is optimum for an average coupling constant, set to 145-150 Hz. The large spread in the values of T leads to inevitably mismatched transfer delays, which lead to phase distortions in the spectra.[142,148] This problem can be avoided if the magnetization is not converted back into inphase magnetization before detection, but is recorded starting from anti-phase magnetization, leading to anti-phase signals.[185–187] The other possibility to get rid of these dispersive anti-phase distortions is to convert them into non-observable multiquantum magnetization.[186,187] Combining the so-called in-phase and anti-phase spectra even allow the determination of couplings in cases when the signals of diastereotopic protons are overlapping.[167,186]

As a result of the above-stated problems, especially the evolution of proton-proton dipolar couplings in the direct dimension (F2), some groups prefer the extraction of couplings from F1-coupled HSQCs (especially if the orientation is not as small as would be desirable), in which the coupling is extracted from the splitting in the indirect dimension (F1). The obvious drawbacks of F1-coupled HSQCs are the much longer experiment times and much lower resolution (due to the limited number of scans that can be recorded in the indirect dimension). The extraction of couplings to diastereotopic protons is possible only if the difference in couplings is significant; otherwise, the anti-phase centre signals overlap. This overlapping leads to large errors in extracted couplings or even to the cancellation of signals. One less obvious drawback, namely, the evolution of long-range couplings, which broadens the signals, can be removed by modifying the HSQC pulse sequence with a G-BIRD module.[167,188]

This same module has also been used in the corresponding J-modulated experiments (intensity-based method), which allow a much more precise determination of couplings, with the drawback of an enormous increase in experimental time as a series of spectra is recorded.[189] Intensity-based methods are best suited for extremely small D values and have so far been mostly applied for water-soluble compounds. J-modulated experiments have also been used for the very

precise (but not sign-sensitive) measurement of very small proton-proton and proton-carbon long-range coupling.[167,190–192]

References

1. Rabi, I. I., Zacharias, J. R., Millman, S. & Kusch, P. A New Method of Measuring Nuclear Magnetic Moment. *Phys. Rev.* **53,** 318 (1938).

2. Purcell, E. M. Torrey, H. C. and Pound, R. V. Resonance Absorption by Nuclear Magnetic Moments in a Solid. *Phys. Rev.* **69,** 37–38 (1945).

3. Bloch, F. Nuclear Induction. *Phys. Rev.* **70,** 127 (1946).

4. Levitt, M. H. *Spin Dynamics: Basics of Nuclear Magnetic Resonance*. 740 (John Wiley & Sons, 2008).

5. Aue, W. P. Bartholdi, E. and Ernst, R. R. Two-dimensional spectroscopy. Application to nuclear magnetic resonance. *J. Chem. Phys.* **64,** 2229 (1976).

6. Stilbs, P. Molecular Self-Diffusion Coefficients in Fourier Transform Nuclear Magnetic Resonance Spectrometric Analysis of Complex Mixtures. *Am. Chemlcal Soclety* **53,** 2135–2137 (1981).

7. Kevin F. Morris & Charles S. Johnson, J. Diffusion-Ordered Two-Dimensional Nuclear Magnetic Resonance Spectroscopy. *Am. Chem. Soc.* **114,** 3139–3141 (1992).

8. Cabrita, E. J. & Berger, S. DOSY studies of hydrogen bond association: tetramethylsilane as a reference compound for diffusion studies. *Magn. Reson. Chem.* **39,** S142–S148 (2001).

9. Morris, G. A. in *Encycl. Magn. Reson.* (ed. Robin K. Harris, Roderick E. Wasylishen, Edwin D. Becker, Melinda J. Duer, Bernard C. Gerstein, George Gray, Ann E. McDermott, Gareth A. Morris, T. P.) 1–13 (John Wiley and Sons, 2009). doi:10.1002/9780470034590.emrstm0119.pub2

10. Johnson Jr, C. S. Diffusion ordered nuclear magnetic resonance spectroscopy: principles and applications. *Prog. Nucl. Magn. Reson. Spectrosc.* **34,** 203–256 (1999).

11. Price, W. S. Pulsed-Field Gradient Nuclear Magnetic Resonance as a Tool for Studying Translational Diffusion: Part 1. Basic Theory. *Concepts Magn Reson* **9,** 299–336 (1997).

12. Antalek, B. Using pulsed gradient spin echo NMR for chemical mixture analysis: How to obtain optimum results. *Concepts Magn. Reson.* **14,** 225–258 (2002).

13. Price, W. S. Pulsed-Field Gradient Nuclear Magnetic Resonance as a Tool for Studying Translational Diffusion: Part II. Experimental Aspects. *Concepts Magn Reson* **10,** 197–237 (1998).

14. Claridge, T. D. W. *High-Resolution NMR Techniques in Organic Chemistry*. 399 (Pergamon, 1999).

15. Karplus, M. Contact Electron-Spin Coupling of Nuclear Magnetic Moments. *J. Chem. Phys.* **30,** 11 (1959).

16. Haasnoot, C. A. G., de Leeuw, F. A. A. M. & Altona, C. The relantionship between proton-proton NMR coupling constants and substituent electronegativities. *Tetrahedron* **36,** 2783–2792 (1980).

17. Anet, F. & Bourn, A. Nuclear Magnetic Resonance Spectral Assignments from Nuclear Overhauser Effects1. *J. Am. Chem. Soc.* **1010,** 5250–5251 (1965).

18. Armand, M., Endres, F., MacFarlane, D. R., Ohno, H. & Scrosati, B. Ionic-liquid materials for the electrochemical challenges of the future. *Nat. Mater.* **8,** 621–9 (2009).

19. Weingärtner, H. Understanding ionic liquids at the molecular level: facts, problems, and controversies. *Angew. Chem. Int. Ed. Engl.* **47,** 654–70 (2008).

20. Weingärtner, H. NMR studies of ionic liquids: Structure and dynamics. *Curr. Opin. Colloid Interface Sci.* **18,** 183–189 (2013).

21. Plechkova, N. V & Seddon, K. R. Applications of ionic liquids in the chemical industry. *Chem. Soc. Rev.* **37,** 123–50 (2008).

22. Marsh, K. ., Boxall, J. . & Lichtenthaler, R. Room temperature ionic liquids and their mixtures—a review. *Fluid Phase Equilib.* **219,** 93–98 (2004).

23. Dupont, J. On the Solid , Liquid and Solution Structural Organization of Imidazolium Ionic Liquids. *J. Braz. Chem. Soc.* **15,** 341–350 (2004).

24. Iwata, K. & Okajima, H. Local Structure Formation in Alkyl-imidazolium-Based Ionic Liquids as Revealed by Linear and Nonlinear Raman Spectroscopy. 1174–1181 (2007).

25. Łuczak, J., Hupka, J., Thöming, J. & Jungnickel, C. Self-organization of imidazolium ionic liquids in aqueous solution. *Colloids Surfaces A Physicochem. Eng. Asp.* **329,** 125–133 (2008).

26. Smirnova, N. a *et al.* Self-assembly in aqueous solutions of imidazolium ionic liquids and their mixtures with an anionic surfactant. *J. Colloid Interface Sci.* **336,** 793–802 (2009).

27. Bankmann, D. & Giernoth, R. Magnetic resonance spectroscopy in ionic liquids. *Prog. Nucl. Magn. Reson. Spectrosc.* **51,** 63–90 (2007).

28. P. Walden. ethylammonium nitrate. *Bull. Acad. Imper. Sci. St. Petersbg.* **8,** 405–422 (1914).

29. Gabriel, S. and Weiner, J. Ueber einige Abkömmlinge des Propylamins. *Chem. Ber.* **21,** 2669–2679 (1888).

30. Wilkes, J. S., Levisky, J. A., Wilson, R. A. & Hussey, C. L. Dialkylimidazolium Chloroaluminate Melts: A New Class of Room-Temperature Ionic Liquids for Electrochemistry, Spectroscopy, and Synthesis. *Inorg. Chem* **21,** 1263–1264 (1982).

31. Atkins, P. & Paula, J. de. *PHYSICAL CHEMISTRY*. 1085 (W. H. Freeman and Company, 2006).

32. Ohno, H. *Electrochemical Aspects of Ionic Liquids*. 409 (John Wiley & Sons, Inc, 2005).

33. Inman, D. & Lovering, D. G. *Ionic Liquids*. 448 (Springer Science+Business Media New York, 1981).

34. Pandey, S. Analytical applications of room-temperature ionic liquids: a review of recent efforts. *Anal. Chim. Acta* **556,** 38–45 (2006).

35. Liu, J., Jiang, G. & Jönsson, J. Å. Application of ionic liquids in analytical chemistry. *TrAC Trends Anal. Chem.* **24,** 20–27 (2005).

36. Berthod, a, Ruiz-Angel, M. J. & Carda-Broch, S. Ionic liquids in separation techniques. *J. Chromatogr. A* **1184,** 6–18 (2008).

37. Sun, P. & Armstrong, D. W. Ionic liquids in analytical chemistry. *Anal. Chim. Acta* **661,** 1–16 (2010).

38. Singh, V. V. *et al.* Applications of Ionic Liquids in Electrochemical Sensors and Biosensors. *Int. J. Electrochem.* **2012,** 1–19 (2012).

39. Silvester, D. S. & Compton, R. G. Electrochemistry in Room Temperature Ionic Liquids: A Review and Some Possible Applications. *Zeitschrift für Phys. Chemie* **220,** 1247–1274 (2006).

40. Li, X., Zhao, D., Fei, Z. & Wang, L. Applications of functionalized ionic liquids. *Sci. China Ser. B Chem.* **49,** 385–401 (2006).

41. Lu, J., Yan, F. & Texter, J. Advanced applications of ionic liquids in polymer science. *Prog. Polym. Sci.* **34,** 431–448 (2009).

42. Welton, T. & Wasserscheid, P. *Ionic Liquids in Synthesis*. **7,** 776 (Wiley-VCH Verlag GmbH & Co. KGaA, 2008).

43. Hallett, J. P. & Welton, T. Room-temperature ionic liquids: solvents for synthesis and catalysis. 2. *Chem. Rev.* **111,** 3508–76 (2011).

44. Gordon, C. M. New developments in catalysis using ionic liquids. **222,** 101–117 (2001).

45. Zhao, D., Wu, M., Kou, Y. & Min, E. Ionic liquids: applications in catalysis. *Catal. Today* **74,** 157–189 (2002).

46. Olivier-bourbigou, H. & Magna, L. Ionic liquids : perspectives for organic and catalytic reactions. **183,** 419–437 (2002).

47. Zhao, H. & Malhotra, S. V. Applications of Ionic Liquids in Organic Synthesis †. 14–22 (2002).

48. Welton, T. Ionic liquids in catalysis. *Coord. Chem. Rev.* **248,** 2459–2477 (2004).

49. Buzzeo, M. C., Evans, R. G. & Compton, R. G. Non-haloaluminate room-temperature ionic liquids in electrochemistry--a review. *Chemphyschem* **5,** 1106–20 (2004).

50. Ding, J. & Armstrong, D. W. Chiral ionic liquids: synthesis and applications. *Chirality* **17,** 281–92 (2005).

51. Jain, N., Kumar, A., Chauhan, S. & Chauhan, S. M. S. Chemical and biochemical transformations in ionic liquids. *Tetrahedron* **61,** 1015–1060 (2005).

52. Zhu, S. *et al.* Dissolution of cellulose with ionic liquids and its application: a mini-review. *Green Chem.* **8,** 325 (2006).

53. Seoud, O. A. El, Koschella, A., Fidale, L. C. & Dorn, S. Window of Opportunities. (2007).

54. Pu, Y., Jiang, N. & Ragauskas, A. J. Ionic Liquid as a Green Solvent for Lignin. *J. Wood Chem. Technol.* **27,** 23–33 (2007).

55. Greaves, T. L. & Drummond, C. J. Protic ionic liquids: properties and applications. *Chem. Rev.* **108,** 206–37 (2008).

56. Ohno, H. & Fukaya, Y. Task Specific Ionic Liquids for Cellulose Technology. *Chem. Lett.* **38,** 2–7 (2009).

57. Pavlinac, J., Zupan, M., Laali, K. K. & Stavber, S. Halogenation of organic compounds in ionic liquids. *Tetrahedron* **65,** 5625–5662 (2009).

58. Olivier-Bourbigou, H., Magna, L. & Morvan, D. Ionic liquids and catalysis: Recent progress from knowledge to applications. *Appl. Catal. A Gen.* **373,** 1–56 (2010).

59. Keskin, S., Kayrak-Talay, D., Akman, U. & Hortaçsu, Ö. A review of ionic liquids towards supercritical fluid applications. *J. Supercrit. Fluids* **43,** 150–180 (2007).

60. Chowdhury, S., Mohan, R. S. & Scott, J. L. Reactivity of ionic liquids. *Tetrahedron* **63,** 2363–2389 (2007).

61. Hapiot, P. & Lagrost, C. Electrochemical reactivity in room-temperature ionic liquids. *Chem. Rev.* **108,** 2238–64 (2008).

62. Domańska, U. Solubilities and thermophysical properties of ionic liquids. *Pure Appl. Chem.* **77,** 25–29 (2005).

63. Castner, E. W., Wishart, J. F. & Shirota, H. Intermolecular Dynamics , Interactions , and Solvation in Ionic Liquids Ionic Liquids with Aliphatic Cations. 1217–1227 (2007).

64. Endres, F. & Zein El Abedin, S. Air and water stable ionic liquids in physical chemistry. *Phys. Chem. Chem. Phys.* **8,** 2101–16 (2006).

65. Xue, H., Verma, R. & Shreeve, J. M. Review of ionic liquids with fluorine-containing anions. *J. Fluor. Chem.* **127,** 159–176 (2006).

66. Feng, R. Revisiting Characteristics of Ionic Liquids: A Review for Further Application Development. *J. Environ. Prot. (Irvine,. Calif).* **01,** 95–104 (2010).

67. Zhao, D., Liao, Y. & Zhang, Z. Toxicity of Ionic Liquids. *CLEAN – Soil, Air, Water* **35,** 42–48 (2007).

68. Hardacre, C., Holbrey, J. D., Nieuwenhuyzen, M. & Youngs, T. G. a. Structure and solvation in ionic liquids. *Acc. Chem. Res.* **40,** 1146–55 (2007).

69. Russina, O. & Triolo, A. New experimental evidence supporting the mesoscopic segregation model in room temperature ionic liquids. *Faraday Discuss.* **154,** 97 (2012).

70. Suarez, P. A. Z., Einloft, S., Dullius, J. E. L., Souza, R. F. de & Dupont, J. Synthesis and physical-chemical properties of ionic liquids based on l -n-butyl-3-methylimidazolium cation. *J. Chim. Phys.* **95,** 1626–1639 (1998).

71. Wulf, A., Fumino, K., Michalik, D. & Ludwig, R. IR and NMR properties of ionic liquids: do they tell us the same thing? *Chemphyschem* **8,** 2265–9 (2007).

72. Remsing, R. C., Wildin, J. L., Rapp, A. L. & Moyna, G. Hydrogen bonds in ionic liquids revisited: (35/37)Cl NMR studies of deuterium isotope effects in 1-n-butyl-3-methylimidazolium chloride. *J. Phys. Chem. B* **111,** 11619–21 (2007).

73. Noda, A., Hayamizu, K. & Watanabe, M. Pulsed-gradient spin-echo 1H and 19F NMR ionic diffusion coefficient, viscosity, and ionic conductivity of non-chloroaluminate room-temperature ionic liquids. *J. Phys. Chem. B* **105,** 4603–4610 (2001).

74. Tokuda, H., Hayamizu, K., Ishii, K., Susan, M. A. B. H. & Watanabe, M. Physicochemical Properties and Structures of Room Temperature Ionic Liquids. 1. Variation of Anionic Species. *J. Phys. Chem. B* **108,** 16593–16600 (2004).

75. Tokuda, H., Hayamizu, K., Ishii, K., Susan, M. A. B. H. & Watanabe, M. Physicochemical properties and structures of room temperature ionic liquids. 2. Variation of alkyl chain length in imidazolium cation. *J. Phys. Chem. B* **109,** 6103–10 (2005).

76. Tokuda, H. *et al.* Physicochemical properties and structures of room-temperature ionic liquids. 3. Variation of cationic structures. *J. Phys. Chem. B* **110,** 2833–9 (2006).

77. Kazuhide, U., Hiroyuki, T. & Watanabe, M. Ionicity in ionic liquids: correlation with ionic structure and physicochemical properties. *Phys. Chem. Chem. Phys.* **12,** 1648 (2010).

78. Schröder, C. & Steinhauser, O. Using fit functions in computational dielectric spectroscopy. *J. Chem. Phys.* **132,** 244109 (2010).

79. Köddermann, T., Wertz, C., Heintz, A. & Ludwig, R. Ion-pair formation in the ionic liquid 1-ethyl-3-methylimidazolium bis(triflyl)imide as a function of temperature and concentration. *Chemphyschem* **7,** 1944–9 (2006).

80. Daguenet, C. *et al.* Dielectric response of imidazolium-based room-temperature ionic liquids. *J. Phys. Chem. B* **110,** 12682–8 (2006).

81. Mele, A. *et al.* The local structure of ionic liquids: cation-cation NOE interactions and internuclear distances in neat [BMIM][BF4] and [BDMIM][BF4]. *Angew. Chem. Int. Ed. Engl.* **45,** 1123–6 (2006).

82. Lingscheid, Y., Arenz, S. & Giernoth, R. Heteronuclear NOE spectroscopy of ionic liquids. *Chemphyschem* **13,** 261–6 (2012).

83. Carper, W., Wahlbeck, P. & Dölle, A. 13c nmr relaxation rates: separation of dipolar and chemical shift anisotropy effects. *J. Phys. Chem. A* **108,** 6096–6099 (2004).

84. Wahlbeck, P. G. & Carper, W. R. Separation of 13 C Nmr Relaxation Mechanisms in Viscous Solutions. *Chem. Eng. Commun.* **194,** 1160–1168 (2007).

85. Triolo, A., Russina, O., Bleif, H.-J. & Di Cola, E. Nanoscale segregation in room temperature ionic liquids. *J. Phys. Chem. B* **111,** 4641–4 (2007).

86. Fazio, B., Triolo, A. & Marco, G. Di. Local organization of water and its effect on the structural heterogeneities in room-temperature ionic liquid/H2O mixtures. *J. Raman Spectrosc.* **39,** 233–237 (2008).

87. Murgia, S., Monduzzi, M., Lopez, F. & Palazzo, G. Mesoscopic Structure in Mixtures of Water and 1-Butyl-3-methyl imidazolium tetrafluoborate: A Multinuclear NMR Study. *J. Solution Chem.* **42,** 1111–1122 (2013).

88. Bloembergen, N., Purcell, E. M. & Pound, R. V. Relaxation Effects in Nuclear Magnetic Resonance Absorption. *Phys. Rev.* **73,** 679–746 (1948).

89. Murgia, S. & Palazzo, G. Aerosol-OT Forms Oil-in-Water Spherical Micelles in the Presence of the Ionic Liquid bmimBF4. *J. Phys. Chem. B* **113,** 9216–9225 (2009).

90. Feng, S. & Voth, G. a. Molecular dynamics simulations of imidazolium-based ionic liquid/water mixtures: Alkyl side chain length and anion effects. *Fluid Phase Equilib.* **294,** 148–156 (2010).

91. Moreno, M., Castiglione, F., Mele, A., Pasqui, C. & Raos, G. Interaction of water with the model ionic liquid [bmim][BF4]: molecular dynamics simulations and comparison with NMR data. *J. Phys. Chem. B* **112,** 7826–36 (2008).

92. Bagno, A., D'Amico, F. & Saielli, G. Computer simulation of diffusion coefficients of the room-temperature ionic liquid [bmim][BF4]: Problems with classical simulation techniques. *J. Mol. Liq.* **131-132,** 17–23 (2007).

93. Nakakoshi, M. *et al.* Anomalous dynamic behavior of ions and water molecules in dilute aqueous solution of 1-butyl-3-methylimidazolium bromide studied by NMR. *Chem. Phys. Lett.* **427,** 87–90 (2006).

94. Cornellas, A. *et al.* Self-aggregation and antimicrobial activity of imidazolium and pyridinium based ionic liquids in aqueous solution. *J. Colloid Interface Sci.* **355,** 164–71 (2011).

95. Shi, W., Damodaran, K., Nulwala, H. B. & Luebke, D. R. Theoretical and experimental studies of water interaction in acetate based ionic liquids. *Phys. Chem. Chem. Phys.* **14,** 15897–908 (2012).

96. Price, W. *NMR studies of translational motion: principles and applications*. 416 (Cambridge University Press, 2009). at <http://books.google.com/books?hl=en&lr=&id=Lp4gAwAAQBAJ&oi=fnd&pg=PR1&dq=NMR+Studies+of+Translational+Motion+Principles+and+Applications&ots=AcgpvSmPyE&sig=R1pbEE7ucD55XZzUjWIuNHeE4HQ>

97. Murgia, S., Monduzzi, M. & Palazzo, G. Quantification of specific anion binding to non-ionic triton X-100 micelles. *Langmuir* **23,** 1283–1289 (2011).

98. Bowers, J., Butts, C. P., Martin, P. J., Vergara-Gutierrez, M. C. & Heenan, R. K. Aggregation behavior of aqueous solutions of ionic liquids. *Langmuir* **20,** 2191–8 (2004).

99. Wang, W., Lee, D., Leone, A. M. & Murray, R. W. Counterion diffusivity measurements support ion atmosphere relaxation control of electron transfer rates in a semi-solid ruthenium complex molten salt. *Chem. Phys.* **319,** 126–135 (2005).

100. Hayamizu, K. *et al.* Quaternary Ammonium Room-Temperature Ionic Liquid Including an Oxygen Atom in Side Chain/Lithium Salt Binary Electrolytes: Ionic Conductivity and 1H, 7Li, and 19F NMR Studies on Diffusion Coefficients and Local Motions. *J. Phys. Chem. B* **112,** 1189–1197 (2008).

101. Carper, W. R. *et al.* A Bloembergen-Purcell-Pound 13 C NMR relaxation study of the ionic liquid 1-butyl-3-methylimidazolium hexafluorophosphate. *Anal. Bioanal. Chem.* **378,** 1548–1554 (2004).

102. Neuhaus, D. & Williamson, M. P. *The Nuclear Overhauser Effect in Structural and Conformational Analysis*. 656 (Wiley-VCH, 2000).

103. Hayamizu, K., Tsuzuki, S., Seki, S. & Umebayashi, Y. Nuclear magnetic resonance studies on the rotational and translational motions of ionic liquids composed of 1-ethyl-3-

methylimidazolium cation and bis(trifluoromethanesulfonyl)amide and bis(fluorosulfonyl)amide anions and their binary systems including li. *J. Chem. Phys.* **135,** 084505 (2011).

104. Cesare Marincola, F. *et al.* NMR investigation of imidazolium-based ionic liquids and their aqueous mixtures. *Chemphyschem* **13,** 1339–46 (2012).

105. Matveev, V. V *et al.* 13C NMR relaxation and reorientation dynamics in imidazolium-based ionic liquids: revising interpretation. *Phys. Chem. Chem. Phys.* **16,** 10480–4 (2014).

106. Antony, J. H., Mertens, D., Dölle, A., Wasserscheid, P. & Carper, W. R. Molecular reorientational dynamics of the neat ionic liquid 1-butyl-3-methylimidazolium hexafluorophosphate by measurement of 13C nuclear magnetic relaxation data. *Chemphyschem* **4,** 588–94 (2003).

107. Emsley, J. W. & Lindon, J. . C. *NMR Spectroscopy using liquid crystal solvents*. 367 (Pergamon Press, 1975).

108. Thiele, C. M. Use of RDCs in rigid organic compounds and some practical considerations concerning alignment media. *Concepts Magn. Reson. Part A* **30,** 65–80 (2007).

109. A. Saupe, G. E. HIGH-RESOLUTION NUCLEAR MAGNETIC RESONANCE SPECTRA OF ORIENTATED MOLECULES. *Phys. Rev. Lett.* **11,** 462–464 (1963).

110. Saupe, A. Kernresonanzen in kristallinen Flüssigkeiten u n d in kristallinflüssigen Lösungen. Teil I. *Z. Naturforsch.* **19a,** 161–171 (1964).

111. Saupe, A. Recent Results in the Field of Liquid Crystals. *Angew. Chem. internat. Ed.* **7,** 97–112 (1968).

112. Snyder, L. C. Analysis of Nuclear Magnetic Resonance Spectra of Molecules in Liquid Crystal Solvents. *J. Chem. Phys.* **43,** 4041 (1965).

113. Sackmann, E., Meiboom, S. & Snyder, L. C. On the Relation of Nematic to Cholesteric Mesophases. *J. Am. Chem. Soc.* **89,** 5981–5982 (1967).

114. Luckhurst, G. R. Liquid Crystals as Solvents in Nuclear Magnetic Resonance. *Q. Rev. Chem. Soc.* **22,** 179–198 (1968).

115. Yannoni, C. S., Ceasar, G. P. & Dailey, B. P. Nuclear Magnetic Resonance Spectrum of Oriented (Cyclobutadiene) iron Tricarbonyl. *J. Am. Chem. Soc.* **89,** 2833–2836 (1967).

116. Bothner-By, A. A., Domaille, P. J. & C. Gayathri. Ultra-High-Field NMR Spectroscopy: Observation of Proton-Proton Dipolar Coupling in Paramagnetic Bis[tolyltris(pyrazolyl)borato]cobalt(11). *J . Am. Chem. Soc.* **103,** 5602–5603 (1981).

117. Kung, H. C., Wang, K. Y., Goljer, I. & Bolton, P. H. Magnetic Alignment of Duplex and Quadruplex DNAs. *J. Magn. Reson. B* **109,** 323–5 (1995).

118. Luther, T. A. & Heinekey, D. M. Determination of the H-H Distance in Transition-Metal Dihydrogen Complexes: Effects of High Magnetic Fields. *J. Am. Chem. Soc.* **119,** 6688–6689 (1997).

119. BASTIAAN, E. W., MACLEAN, C., VAN ZIJL, P. C. M. & BOTHNER-BY, A. A. High-Resolution NMR of Liquids and Gases: Effects of Magnetic-Field-Induced Molecular Alignment. *Annu. REPORTS NMR Spectrosc.* **19,** 35–77 (1987).

120. Delochet, B. & Samulski, E. T. Short-Range Nematic-like Orientational Order in Strained Elastomers : A Deuterium Magnetic Resonance Study. *Macromolecules* **14,** 575–581 (1981).

121. Edward T. Samulski. Investigations of polymer chains in oriented fluid phases with deuterium nuclear magnetic resonance. *Polymer (Guildf).* **26,** 177–189 (1985).

122. Sass, H. J., Musco, G., Stahl, S. J., Wingfield, P. T. & Grzesiek, S. Solution NMR of proteins within polyacrylamide gels: diffusional properties and residual alignment by mechanical stress or embedding of oriented purple membranes. *J. Biomol. NMR* **18,** 303–9 (2000).

123. Tycko, R., Blanco, F. J. & Ishii, Y. Alignment of Biopolymers in Strained Gels : A New Way To Create Detectable Dipole - Dipole Couplings in High-Resolution Biomolecular NMR. *J. Am. Chem. Soc.* **122,** 9340–9341 (2000).

124. Luy, B., Kobzar, K. & Kessler, H. An easy and scalable method for the partial alignment of organic molecules for measuring residual dipolar couplings. *Angew. Chem. Int. Ed. Engl.* **43,** 1092–4 (2004).

125. Gil, R. R., Gayathri, C., Tsarevsky, N. V & Matyjaszewski, K. Stretched poly(methyl methacrylate) gel aligns small organic molecules in chloroform. stereochemical analysis and diastereotopic proton NMR assignment in ludartin using residual dipolar couplings and 3J coupling constant analysis. *J. Org. Chem.* **73,** 840–848 (2008).

126. Tjandra, N., Omichinski, G. J., Gronenborn, M. A., Clore, G. M. & Bax, A. Use of dipolar 1H-15N and 1H-13C couplings in the structure determination of magnetically oriented macromolecules in solution. *Nat. Struct. Biol.* **4,** 732–738 (1997).

127. Tjandra, N. & Bax, A. Direct Measurement of Distances and Angles in Biomolecules by NMR in a Dilute Liquid Crystalline Medium. *Science (80-.).* **278,** 1111–1114 (1997).

128. Cornilescu, G., Marquardt, J. L., Ottiger, M. & Bax, A. Validation of Protein Structure from Anisotropic Carbonyl Chemical Shifts in a Dilute Liquid Crystalline Phase. *J. Am. Chem. Soc.* **120,** 6836–6837 (1998).

129. SANDERS, C. R., HARE, B. J., HOWARD, K. P. & PRESTEGARD, J. H. MAGNETICALLY-ORIENTED PHOSPHOLIPID MICELLES AS A TOOL FOR THE STUDY OF MEMBRANE-ASSOCIATED MOLECULES. *Prog. NMR Spectrosc.* **26,** 421–444 (1994).

130. Tolman, J. R., Flanagan, J. M., Kennedy, M. a & Prestegard, J. H. Nuclear magnetic dipole interactions in field-oriented proteins: information for structure determination in solution. *Proc. Natl. Acad. Sci. U. S. A.* **92,** 9279–83 (1995).

131. Prestegard, J. H. & Kishore, A. I. Partial alignment of biomolecules: an aid to NMR characterization. *Curr. Opin. Chem. Biol.* **5,** 584–90 (2001).

132. Tjandra, N., Szabo, A. & Bax, A. Protein Backbone Dynamics and 15 N Chemical Shift Anisotropy from Quantitative Measurement of Relaxation Interference Effects. *J. Am. Chem. Soc.* **118,** 6986–6991 (1996).

133. Tjandra, N. & Bax, A. Measurement of Dipolar Contributions to 1 J CH Splittings from Magnetic-Field Dependence of J Modulation in Two-Dimensional NMR Spectra. *J. Magn. Reson.* **124,** 512–515 (1997).

134. Bax, A. & Grishaev, A. Weak alignment NMR: a hawk-eyed view of biomolecular structure. *Curr. Opin. Struct. Biol.* **15,** 563–70 (2005).

135. Prestegard, J. H., Bougault, C. M. & Kishore, A. I. Residual dipolar couplings in structure determination of biomolecules. *Chem. Rev.* **104,** 3519–40 (2004).

136. Giesinger, C., Meiler, J. & Peti, W. Angular Restraints from Residual Dipolar Couplings for Structure Refinement. *Biol. Magn. Reson.* **20,** 163–229 (2003).

137. Blackledge, M. Recent progress in the study of biomolecular structure and dynamics in solution from residual dipolar couplings. *Prog. Nucl. Magn. Reson. Spectrosc.* **46,** 23–61 (2005).

138. Tolman, J. R. & Ruan, K. NMR Residual Dipolar Couplings as Probes of Biomolecular Dynamics. *Chem. Rev.* **106,** 1720–1736 (2006).

139. Gschwind, R. M. Residual Dipolar Couplings — A Valuable NMR Parameter for Small Organic Molecules. *Angew. Chem. Int. Ed.* **44,** 4666–4668 (2005).

140. Yan, J. & Zartler, E. R. Application of residual dipolar couplings in organic compounds. *Magn. Reson. Chem.* **43,** 53–64 (2005).

141. Mangoni, A., Esposito, V. & Randazzo, A. Configuration assignment in small organic molecules via residual dipolar couplings. *Chem. Commun. (Camb).* 154–5 (2003). at <http://www.ncbi.nlm.nih.gov/pubmed/12611012>

142. Yan, J., Kline, A. D., Mo, H., Shapiro, M. J. & Zartler, E. R. A novel method for the determination of stereochemistry in six-membered chairlike rings using residual dipolar couplings. *J. Org. Chem.* **68,** 1786–95 (2003).

143. Canet, I., Lovschall, J. & J. Courtieu. Visualization of enantiomers through deuterium NMR in cholesterics. Optimization of the chiral liquid crystal solvent. *Liq. Cryst.* **16,** 405–412 (1994).

144. Meddour, A., Berdague, P., Hedli, A., Courtieu, J. & Lesot, P. Proton-Decoupled Carbon-13 NMR Spectroscopy in a Lyotropic Chiral Nematic Solvent as an Analytical Tool for the Measurement of the Enantiomeric Excess. *J. Am. Chem. Soc.* **119,** 4502–4508 (1997).

145. Merlet, D., Ancian, B., Courtieu, J. & Lesot, P. Two-Dimensional Deuterium NMR Spectroscopy of Chiral Molecules Oriented in a Polypeptide Liquid Crystal : Applications for the Enantiomeric Analysis through Natural Abundance Deuterium NMR. *J. Am. Chem. Soc.* **121,** 5249–5258 (1999).

146. Canet, I., Meddour, A., Courtieu, J., Canet, J. L. & Salaun, J. New , and Accurate Method To Determine the Enantiomeric Purity of Amino Acids Based on Deuterium NMR in a Cholesteric Lyotropic Liquid Crystal. *J. Am. Chem. Soc.* **116,** 2155–2156 (1994).

147. Thiele, C. M. & Berger, S. Probing the diastereotopicity of methylene protons in strychnine using residual dipolar couplings. *Org. Lett.* **5,** 705–708 (2003).

148. Thiele, C. M. Simultaneous assignment of all diastereotopic protons in strychnine using RDCs: PELG as alignment medium for organic molecules. *J. Org. Chem.* **69,** 7403–13 (2004).

149. Aroulanda, C., Boucard, V., Guibé, F., Courtieu, J. & Merlet, D. Weakly oriented liquid-crystal NMR solvents as a general tool to determine relative configurations. *Chem. Eur. J.* **9,** 4536–9 (2003).

150. Verdier, L., Sakhaii, P., Zweckstetter, M. & Griesinger, C. Measurement of long range H,C couplings in natural products in orienting media: a tool for structure elucidation of natural products. *J. Magn. Reson.* **163,** 353–359 (2003).

151. Aroulanda, C., Lesot, P., Merlet, D. & Courtieu, J. Structural Ambiguities Revisited in Two Bridged Ring Systems Exhibiting Enantiotopic Elements , Using Natural Abundance Deuterium NMR in Chiral Liquid Crystals. *J. Phys. Chem. A* **107,** 10911–10918 (2003).

152. Sarfati, M., Lesot, P., Merlet, D. & Courtieu, J. Theoretical and experimental aspects of enantiomeric differentiation using natural abundance multinuclear nmr spectroscopy in chiral polypeptide liquid crystals. *Chem. Commun.* 2069–2081 (2000). doi:10.1039/b006244h

153. Lesot, P., Sarfati, M. & Courtieu, J. Natural abundance deuterium NMR spectroscopy in polypeptide liquid crystals as a new and incisive means for the enantiodifferentiation of chiral hydrocarbons. *Chem. Eur. J.* **9,** 1724–45 (2003).

154. Sandstrbm, D., Summanen, K. T. & Levitt, M. H. Molecular Order of a Liquid Crystal Investigated by Double-Quantum 13C NMR. *J. Am. Chem. SOC* **116,** 9357–9358 (1994).

155. Sandstrom, D. & Levitt, M. H. Structure and Molecular Ordering of a Nematic Liquid Crystal Studied by Natural-Abundance Double-Quantum 13C NMR. *J. Am. Chem. Soc.* **118,** 6966–6974 (1996).

156. Brunner, E. Residual Dipolar Couplings in Protein NMR. *Concepts Magn. Reson.* **13,** 238–259 (2001).

157. Annila, A. & Permi, P. Weakly aligned biological macromolecules in dilute aqueous liquid crystals. *Concepts Magn. Reson.* **23A,** 22–37 (2004).

158. Freudenberger, J. C., Spiteller, P., Bauer, R., Kessler, H. & Luy, B. Stretched poly(dimethylsiloxane) gels as NMR alignment media for apolar and weakly polar organic solvents: an ideal tool for measuring RDCs at low molecular concentrations. *J. Am. Chem. Soc.* **126,** 14690–14691 (2004).

159. Freudenberger, J. C. *et al.* Stretched poly(vinyl acetate) gels as NMR alignment media for the measurement of residual dipolar couplings in polar organic solvents. *Angew. Chem. Int. Ed. Engl.* **44,** 423–6 (2005).

160. Haberz, P., Farjon, J. & Griesinger, C. A DMSO-compatible orienting medium: towards the investigation of the stereochemistry of natural products. *Angew. Chem. Int. Ed. Engl.* **44,** 427–9 (2005).

161. Bendiak, B. Sensitive through-space dipolar correlations between nuclei of small organic molecules by partial alignment in a deuterated liquid solvent. *J. Am. Chem. Soc.* **124,** 14862–3 (2002).

162. García, M. E. *et al.* Stereochemistry determination by powder X-ray diffraction analysis and NMR spectroscopy residual dipolar couplings. *Angew. Chem. Int. Ed. Engl.* **48,** 5670–4 (2009).

163. Troche-Pesqueira, E., Cid, M.-M. & Navarro-Vázquez, A. Disodium cromoglycate: exploiting its properties as a NMR weak-aligning medium for small organic molecules. *Org. Biomol. Chem.* **12,** 1957–65 (2014).

164. Meyer, N.-C., Krupp, A., Schmidts, V., Thiele, C. M. & Reggelin, M. Polyacetylenes as enantiodifferentiating alignment media. *Angew. Chem. Int. Ed. Engl.* **51,** 8334–8 (2012).

165. Schmidt, M., Sun, H., Leonov, A., Griesinger, C. & Reinscheid, U. M. Chiral discrimination of amines by anisotropic NMR parameters using chiral polyacrylamide-based gels. *Magn. Reson. Chem.* **50,** S38–44 (2012).

166. Trigo-Mouriño, P., Navarro-Vázquez, A. & Sánchez-Pedregal, V. M. Influence of solvent and salt concentration on the alignment properties of acrylamide copolymer gels for the measurement of RDC. *Magn. Reson. Chem.* **50 Suppl 1,** S29–37 (2012).

167. Thiele, C. M. Residual Dipolar Couplings (RDCs) in Organic Structure Determination. *European J. Org. Chem.* 5673–5685 (2008). doi:10.1002/ejoc.200800686

168. Klochkov, V. V, Klochkov, a V, Thiele, C. M. & Berger, S. A novel liquid crystalline system for partial alignment of polar organic molecules. *J. Magn. Reson.* **179,** 58–63 (2006).

169. Thiele, C. M. *et al.* Determination of the relative configuration of a five-membered lactone from residual dipolar couplings. *Angew. Chem. Int. Ed. Engl.* **45,** 4455–60 (2006).

170. Kobzar, K., Kessler, H. & Luy, B. Stretched gelatin gels as chiral alignment media for the discrimination of enantiomers by NMR spectroscopy. *Angew. Chem. Int. Ed. Engl.* **44,** 3145–7 (2005).

171. Bertini, I., Luchinat, C. & Parigi, G. Paramagnetic constraints: An aid for quick solution structure determination of paramagnetic metalloproteins. *Concepts Magn. Reson.* **14,** 259–286 (2002).

172. Wöhnert, J., Franz, K. J., Nitz, M., Imperiali, B. & Schwalbe, H. Protein alignment by a coexpressed lanthanide-binding tag for the measurement of residual dipolar couplings. *J. Am. Chem. Soc.* **125,** 13338–9 (2003).

173. Bertini, I., Luchinat, C. & Parigi, G. Magnetic susceptibility in paramagnetic NMR. *Prog. Nucl. Magn. Reson. Spectrosc.* **40,** 249–273 (2002).

174. Gayathri, C., Tsarevsky, N. & Gil, R. Residual dipolar couplings (RDCs) analysis of small molecules made easy: fast and tuneable alignment by reversible compression/relaxation of reusable PMMA gels. *Chem. Eur. J.* **16,** 3622–6 (2010).

175. Luy, B. *et al.* Orientational properties of stretched polystyrene gels in organic solvents and the suppression of their residual 1H NMR signals. *J. Am. Chem. Soc.* **127,** 6459–65 (2005).

176. Aroulanda, C., Sarfati, M., Courtieu, J. & Lesot, P. Investigation of the Enantioselectivity of Three Polypeptide Liquid-Crystalline Solvents Using NMR Spectroscopy. *Enantiomer* **6,** 281–287 (2001).

177. Losonczi, J. A., Andrec, M., Fischer, M. W. F. & Prestegard, J. H. Order Matrix Analysis of Residual Dipolar Couplings Using Singular Value Decomposition. *J. Magn. Reson.* **138,** 334–342 (1999).

178. Yan, J. *et al.* Complete Relative Stereochemistry of Multiple Stereocenters Using Only Residual Dipolar Couplings. *J. Am. Chem. Soc.* **126,** 5008–5017 (2004).

179. Zweckstetter, M. & Bax, A. Prediction of Sterically Induced Alignment in a Dilute Liquid Crystalline Phase : Aid to Protein Structure Determination by NMR. *J. Am. Chem. Soc.* **122,** 3791–3792 (2000).

180. Navarro-Vázquez, A. MSpin-RDC. A program for the use of residual dipolar couplings for structure elucidation of small molecules. *Magn. Reson. Chem.* **50 Suppl 1,** S73–9 (2012).

181. Prosser, R. S., Losonczi, J. a. & Shiyanovskaya, I. V. Use of a Novel Aqueous Liquid Crystalline Medium for High-Resolution NMR of Macromolecules in Solution. *J. Am. Chem. Soc.* **120,** 11010–11011 (1998).

182. Lycknert, K., Maliniak, A. & Goeran, W. Analysis of Oligosaccharide Conformation by NMR Spectroscopy Utilizing 1 H , 1 H and 1 H , 13 C Residual Dipolar Couplings in a Dilute Liquid Crystalline Phase. *J. Phys. Chem. A* **105,** 5119–5122 (2001).

183. Brand, T., Cabrita, E. J. & Berger, S. Intermolecular interaction as investigated by NOE and diffusion studies. *Prog. Nucl. Magn. Reson. Spectrosc.* **46,** 159–196 (2005).

184. Farjon, J., Bermel, W. & Griesinger, C. Resolution enhancement in spectra of natural products dissolved in weakly orienting media with the help of 1H homonuclear dipolar decoupling during acquisition: application to 1H-13C dipolar couplings measurements. *J. Magn. Reson.* **180,** 72–82 (2006).

185. Enthart, A., Freudenberger, J. C., Furrer, J., Kessler, H. & Luy, B. The CLIP/CLAP-HSQC: pure absorptive spectra for the measurement of one-bond couplings. *J. Magn. Reson.* **192,** 314–322 (2008).

186. Parella, T., Nolis, P. & Espinosa, J. Optimum spin-state selection for all multiplicities in the acquisition dimension of the HSQC experiment. *J. Magn. Reson.* **180,** 39–50 (2006).

187. Marathias, V. M., Goljer, I. & Ii, A. C. B. Simultaneous determination of 1 H – 1 H and 1 H – 13 C residual dipolar couplings in a chiral liquid crystal solvent using a natural abundance HSQC experiment. *Magn. Reson. Chem.* **43,** 512–519 (2005).

188. Feh, K., Berger, S. & Katalin, K. Accurate determination of small one-bond heteronuclear residual dipolar couplings by F1 coupled HSQC modified with a G-BIRD(r) module. *J. Magn. Reson.* **163,** 340–346 (2003).

189. Pham, T. N., Liptaj, T., Bromek, K. & Dusan, U. Measurement of Small One-Bond Proton – Carbon Residual Dipolar Coupling Constants in Partially Oriented 13 C Natural Abundance Oligosaccharide Samples : Analysis of Heteronuclear J CH -Modulated Spectra with the BIRD Inversion Pulse. *J. Magn. Reson.* **209,** 200–209 (2002).

190. Pham, T. N., Liptaj, T., Barlow, P. N. & Uhrín, D. J-modulated 1D directed COSY for precise measurement of proton–proton residual dipolar coupling constants of oligosaccharides. *Magn. Reson. Chem.* **40,** 729–732 (2002).

191. Pham, T. N., Hinchley, S. L., Rankin, D. W. H., Liptaj, T. & Uhrín, D. Determination of Sugar Structures in Solution from Residual Dipolar Coupling Constants : Methodology and Application to Methyl - D -Xylopyranoside. *J. Am. Chem. Soc.* **126,** 13100–13110 (2004).

192. Jin, L., Pham, T. N. & Uhrín, D. Measurement of 1 H – 1 H Residual Dipolar Coupling Constants for Structural Studies of Medium Size Molecules. *ChemPhysChem* **8,** 1228–1235 (2007).